Republic of Iraq
Ministry of Higher Education
and Scientific Research
University of Babylon
College of Materials Engineering
Department of Metallurgical Engineering

# Surface Modification of Ti-13Nb-13Zr Alloy by Electrophoretic Deposition for Orthopaedic Applications

A Thesis
Submitted to Council of the College of Materials Engineering / University of Babylon in Partial Fulfillment of the Requirements for the Degree Doctor of Philosisophy in Materials Engineering / Metallurgical

By

**Nabeel Mohammed Abdulkadhim Radhi**
(M.S.c in Materials Engineering / Metallurgical / 2019)

Supervised by
Prof. Dr.
**Jassim M. Salman Al-Murshdy**

2022 A.D 1444 A.H

بسم الله الرحمن الرحيم

رب اشرح لي صدري ﴿٢٥﴾ ويسر لي
أمري ﴿٢٦﴾ واحلل عقدة من لساني ﴿٢٧﴾
يفقهوا قولي ﴿٢٨﴾

صدق الله العلي العظيم

سورة طه

# Supervisor Certificate

I certify that this thesis entitled **(Surface Modification of Ti-13Nb-13Zr Alloy by Electrophoretic Deposition for Orthopaedic Applications)** was prepared by **( Nabeel Mohammed Abdulkadhim Radhi )** had been carried out under my supervision at the University of Babylon/ College of Material's Engineering/ Department of Metallurgical Engineering in partial fulfillment of the requirements for the degree of Philosophy-Doctorate of Science in Material's Engineering/ Metallurgical .

Signature

Name: **Prof. Dr. Jassim M. Salman Al.Murshdy**

(Supervisor)

Date: / / 2022

# Dedication

*To the martyrs and wounded of the October Revolution*

Nabeel Mohammed

2022

# *Acknowledgments*

First of all, profusely all thanks be for ***ALLAH*** who enable me to achieve this work.

I would like to express my gratitude to my supervisor, ***Prof. Dr. Jassim M. Salman Al-Murshdy*** for his enthusiasm and support. His suggestions, guidance and moral support in difficult times have been essential for completing this work. Special thanks are to my brother ***Asst. Prof. Dr. Ali Mohammed*** for his help and advices.

To my colleague **Noor Al-jaafari** who always being there to give support in difficult times during this study.

I also thank my department, Metallurgical Engineering and my College, Materials Engineering, for their help and good facilities.

Finally I would like to thank the staff of the workshop materials lab. in Babylon University.

*Nabeel Mohammed*

*2022*

# Abstract

The beta alloys have many properties of biocompatibility, osseointegration and superior corrosion resistance, many researchers are looking to develop these alloys to suit the hostile environment of the human body. In this study, after selecting the appropriate conditions (anode electrode, applied voltage, deposition time....etc), (graphene (Gr), Carboxymethyl cellulose (CMC) and the two materials together (ternary coating)) were added to the hydroxyapatite (HAp) suspension coating in addition to the functional gradient of the suspended graphene coating on surface of Ti-13Nb-13Zr alloy via electrophoretic deposition (EPD), due to the compatibility of these materials with the tissues of the human body. Then the effect of the coating layers resulting from these suspended solutions above was studied on each of the microstructure characterization (X-Ray Diffraction (XRD), Scanning Electron Microscope (SEM), X-Ray Fluorescence (XRF) and Light optical microscope), electrochemical tests (Open circuit and Polarization teats), mechanical tests (Wear tests), physical tests (Contact angle, Zeta potential, Surface roughness, and PH) and Antibacterial activity and Cytotoxicity evaluation to verify the extent to which these layers protect the surface of the Ti-13Nb-13Zr alloy.

Positive values of the zeta potential were a clear indicator of the adoption of the cathodic electrophoretic deposition (EPD) process. The pattern of the base alloy revealed the diffraction of the (β and α) phases that matched the JCPDS Card No. (044 - 1294). Can notice the emergence of new peaks due to the effect of the additions ratios (5HAp, 0.5 Gr, and 0.5 CMC ), which also led to a reduction or increase in the angle of the peaks of each of the phases of the titanium alloy (beta and alpha), as well as, the addition of graphene and CMC and in cases of mixing them and the functional gradation of graphene led to an increase in the adhesion strength of the hydroxyapatite layer starting from 4.55MPa for HAp, 7.90MPa for

0.08 CMC, 8.28MPa for (0.08CMC + 0.2Gr) Mix, 9.76MPa for 1 Gr up to 10.12MPa for functional gradient (FG). This was proved when the adhesion strength of the above coating layers was increased after immersing the coated specimens for a maximum of 6 days.

The contact angle values are ranged from 14.3° for (1 CMC + 0.2Gr), 20.5° for 1 Gr, and 32.3° for FG, the excessive roughness, porosity, and cracks on the surface of the CMC coating immediately lowered the contact angle of this layer from 54.6° for the base alloy to 11.2° for 0.5 CMC. The high wear resistance for adding graphene, with volume losses ranging from $0.00614cm^3$ to the Ti-13Nb-13Zr uncoated alloy at 25 mint to $0.001344cm^3$ to 1Gr at the same time under a load of 15 N, the high hardness of the graphene coating can be expected from its high wear resistance when compared to other additives.

When compared to the other additions, the greatest value of OCP (-26.1mV) in the negative direction of the 0.08 Gr addition shows a decrease in the corrosion rate for this coating layer, going from 0.0781mm/y for the Ti-13Nb-13Zr uncoated alloy to 0.00312mm/y for 0.08Gr. All the additives used (Gr, CMC, mix of them, and FG) are anti-bacterial, as the largest zone of inhibition when suspension solution of G2 (45mm) was when attacking the positive bacteria Staphylococcus aureas (S. aureas). MTT assay is the most common method used for assessing the cytoxicity (loss of viable cells), G2 (0.2Gr) specimen exhibited the nearly 100% of the cell viability, while C1 and base alloy without coating specimens presented the least cell viability in comparison to other specimens. The cell viability for the specimens was obtained in the order of higher to lower:

G2 > F > M2 > C1 > Base alloy without coating.

The best results were achieved when G2 (0.2Gr) was added to the hydroxyapatite coating (H), hence this ratio is regarded the optimal ratio in this study for the aim of enhancing the surface of the Ti-13Nb-13Zr alloy.

# Table of Content

## CHAPTER THREE
## EXPERIMENTAL WORK AND PROCEDURE



## CHAPTER FOUR
## RESULTS AND DISCUSSION

## *List of Latin Symbols*

| Symbol | Meaning | Units |
|---|---|---|
| E | Elastic modulus | GPa |
| T | Temperature | °C |
| W | Weight | g |

## *List of Greek Symbols*

| Symbol | Meaning | Units |
|---|---|---|
| α | Alpha phase | - |
| β | Beta phase | - |
| ρ | Density | g/cm³ |
| ζ | Zeta Potential | mV |
| θ | Contact Angel | Degree |

## *List of Subscripts & Superscripts*

| Symbol | Meaning | Units |
|---|---|---|
| W∘ | weight of uncoated substrate | g/cm³ |
| $W_c$ | weight of the coated substrate | g/cm³ |
| $I_{corr.}$ | Corrosion Current Density | µA/cm² |
| $E_{corr.}$ | Corrosion Potential | mV |
| Wt | Weight percentage | % |
| $K_{IC}$ | Fracture Toughness | MPa $m^{1/2}$ |

## *List of Abbreviations*

| Symbol | Meaning |
|---|---|
| A | Area |
| ASTM | American Society For Testing And Materials |
| ALP | Alkaline Phosphatase |
| BMD | Bone Mineral Density |
| BCC | Body Centere Cubic |
| EPD | Electrophoretic Deposition |
| E.coli | Escherichia coli |
| BG | Bioactive Glass |
| CR | Corrosion Rate |
| CH | Chitosan |
| CMC | CarboxyMethyl Cellulose |
| CP-Ti | Commercially Pure Titanium |

| | |
|---|---|
| CVD | Chemical Vapor Deposition |
| PVD | Physical Vapor Deposition |
| EDS | Energy-Dispersive Spectrometry |
| FT-IR | Fourier Transform Infrared |
| FBG | Fine Particle Size |
| FG | Functional Gradient |
| CBG | Coarse Particle Size |
| GDC | Gadolinium Doped Ceria |
| Gr | Graphene |
| GO | Graphene Oxide |
| HCP | Hexagonal Close Packed |
| HER | Hydrogen Evolution Reaction |
| OER | Oxygen Evolution Reaction |
| ISO | International Organization for Standardization |
| JIS | Japanese Industrial Standard |
| mm/y | millimeters per year |
| mV | Millivolt |
| LD | Lethal Dose |
| LOM | Light Optical Microscope |
| LCA | Lithocholic Acid |
| LDH | Layered Double Hydroxides |
| OCP | Open-Circuit Potential |
| OES | Optical Emission Spectrometer |
| PTFE | Polytetrafluoroethylene |
| PMMA | Poly(Methyl Methacrylate) |
| PPy | polypyrrole |
| PEEK | Polyether Ether Ketone |
| PVA | Polyvinyl Alcohol |
| PBS | Phosphate Buffer Saline |
| Rp | Polarization Resistance |
| rpm | Revolutions per minute |
| SS | Stainless Steel |
| UHMWPE | Ultrahigh-Molecular-Weight Polyethylene |
| USSP | Ultrasonic Shot Peening |
| UTS | Ultimate Tensile Strength |
| HAp | Hydroxyapatite |
| HR | Hardness Rockwell |
| TNZT | Ti–35Nb–7Zr–5Ta |

| | |
|---|---|
| TNTZ | Ti–29Nb–13Ta–4.6Zr |
| TMZF | Ti-12Mo-6Zr-2Fe |
| TNZF | Ti-28Nb-13Zr-0.5Fe |
| TS | Tensile Strength |
| SBF | Simulated Body Fluid |
| SCE | Standard Calomel Electrode |
| S. aureus | Staphylococcus aureus |
| SEM | Scanning Electron Microscopy |
| Wd | Deposition weight |
| XRD | X-Ray Diffraction |
| XRF | X-Ray Fluorescent |
| YSZ | Yttrium Stabilized Zirconia |
| YS | Yield Strength |

# *List of Figures*

## CHAPTER ONE
## INTRODUCTION



## CHAPTER TWO
## THEORETICAL PART AND LITERATURE SURVEY

## CHAPTER THREE
## EXPERIMENTAL WORK AND PROCEDURE

## CHAPTER FOUR
## RESULTS AND DISCUSSION

# *List of Tables*

## CHAPTER ONE
## INTRODUCTION



## CHAPTER TWO
## THEORETICAL PART AND LITERATURE SURVEY



## CHAPTER THREE
## EXPERIMENTAL WORK AND PROCEDURE

## CHAPTER FOUR
## RESULTS AND DISCUSSION

# CHAPTER ONE

# Introduction

# CHAPTER ONE

# INTRODUCTION

## 1.1 General View

This section offers a summary of the subjects of this thesis and an introduction to the reason for this work and a clarification of the study's goals.

The bone may be an advanced tissue that unendingly undergoes dynamic biological reworking. This distinguishing characterization of bone supports its capability to change itself to heal the damage. Nevertheless, once bone damage surpasses a serious non-medicinal volume, external involvement is demanded to complete self-cure to bridge the defect. The better choice is to employ autograft ( the tissue which belonged to the patient). Nonetheless, the morbidity related to a second operative wound is influenced by autograft tissue harvesting. Tissue from an allograft (get from another body) is an alternative option, but it carries the hazard of transmissible sickness and is dependent on logistical factors (restricted availability). The limitations of autograft and allograft tissue used required increased study efforts to recognize materials of biomimetic and structures proper for skeletal repair without the deep problems [1].

## 1.2 Implant Characteristics

A modern-day implant's property requirements can be broadly classified into three important features [2]:

- The material used in the prosthesis must be compatible with the human body.
- The implant must have the desired balance of physical and mechanical properties to function properly.
- The device must be relatively simple to manufacture, reproducible, consistent, and meet all technical and biological specifications.

## 1.3 Metals Used in Biomedical

Stainless steels, CoCr-alloys, and alloys with Ti-based are generally applied in joint replacements. These three major alloy groups have a long history of use in joint replacements [3]. Many of these alloys have been standardized by employing both international and national standards, such as the (ISO), (ASTM), and (JIS) [4].

The type of metal used in biomedical applications is determined by the implant application. Table (1.1) summarizes the metals commonly used for different implant divisions. Figure (1.1) depicts a collection of implants used in the human body [5, 6].

**Table (1.1):** Division of Implants and Metals Used [5].

| Division | Example of implants | Type of metal |
|---|---|---|
| Cardiovascular | Stent and Artificial valve | 316L SS, CoCrMo, Ti, Ti6Al4V |
| Orthopaedic | Bone fixation (plate, screw, pin), Artificial joints | 316L SS, Ti, Ti6Al4V CoCrMo,Ti6Al4V, Ti6Al7Nb |
| Dentistry | Orthodontic wire Filling | 316L SS, CoCrMo, TiNi, TiMo, AgSn(Cu) amalgam, Au |
| Craniofacial | Plate and screw | 316LSS, CoCrMo, Ti, Ti6Al4V |
| Otorhinology | Artificial eardrum | 316L SS |

## 1.4 Titanium as a Biomaterial

Titanium alloy refers to the use of titanium as a matrix for the addition of other elements. Titanium is a novel structural material with superior all-around characteristics, as shown in Table (1.2) [7].

**Table (1.2):** Titanium Properties [7].

| Property | Typical value |
|---|---|
| Density (g/**cm$^3$**) | 4.5 |
| Melting Range (°C) | 1668 |
| Elastic modulus (GPa) | 116 |
| Tensile Strengths (MPa) | 550 |

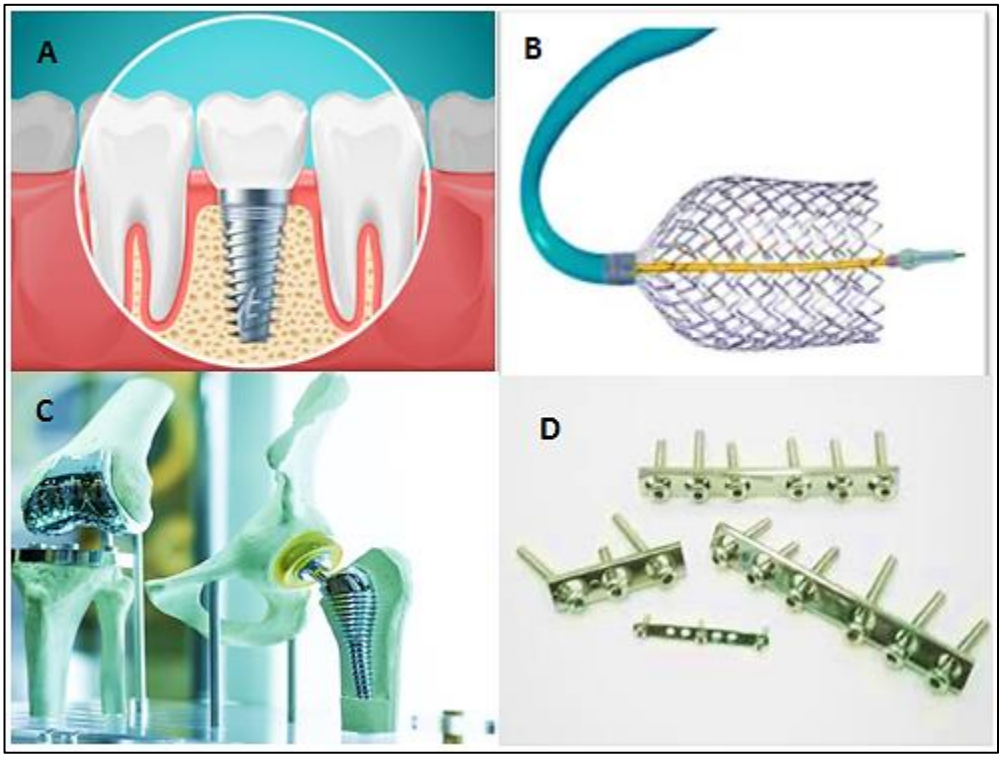


**Figure (1.1):** Shows a Set of Implants Where: (A) Dental Implants Showing Anchors and Dental Prostheses, (B) Endovascular Nitinol Stent, (C) Knee and Hip Implant Components, (D) Bone break fixing Plate and Screw [6].

Because of the above, titanium alloys have grown in the field of flight, aerospace, alchemical, shipbuilding, medical, and extra manufacturing sectors. Titanium has a density of (4.5 g/cm$^3$) which is only 60 percent of the density of iron. As a result, The significance of Ti- alloy materials has been acknowledged by many countries around the world, titanium alloy materials are being researched, developed, and supported by practical applications [7,8].

There has been a dramatic change in the use of titanium, as well as the number of new alloys and product forms chosen by medical implant designers. The "Metallurgical Materials" Subcommittee has developed several new ASTM standards for titanium-based alloy biomaterials since the early 1990s. These consensus standards will be listed in the following chapter [9].

## 1.5 Objective of the Present Study

The aim of the current work is improve the hydroxyapatite layer by adding two materials, one of them is ceramic (graphene) and the other is polymeric (carboxymethyl cellulose) in different proportions (0.08, 0.2, 0.5 and 1g) to the hydroxyapatite suspension solution. In addition to, mixing the two additions together, and most importantly, conducting Functional gradient, which will give excellent results. These suspended solutions of the above additives are coated by electrophoretic deposition to obtain a super-protective layer on the surface of the Ti-13Nb-13Zr beta alloy to simulate fluids hostile to the human body.

## 1.6 The Organization of the Thesis

The current thesis has been divided into five chapters and it can be out lined as follows:

**Chapter One:** gives a general overview of metallic implants used in the human body and their history from the first used in the human body until the present time. In addition to that, the applications of implants and their Properties. The objective of the work is also present in this chapter.

**Chapter Two:** deals at the beginning of this chapter with the bone structure, auxiliary tissue in bone formation and Installation of joints and their types. There will be a focus on the criteria of selection implantable metals such as biocompatibility, wound healing, toxicity, wear and corrosion behaviour, the types of Ti alloys, development of low young's modulus titanium alloys, and it will also talk about beta alloys (Ti-13Nb-13Zr). Then there will be a detailed focus on the Surface Modifications and their methods, especially on electrophoretic deposition. At the end of this section, there was also a proper literature review.

**The Third Chapter** focuses on the experiments and details the circumstances in which the experiments were conducted. This chapter

accurately describes the mechanical and chemical tests( in vivo and vitro) of the samples of basic materials used in this study.

**Chapter Four:** records all results of the used tests. And discuss the behavior test obtained from each alloy ( coated or uncoated) and compare it with the others.

**Chapter Five:** gives a brief account of the conclusions and objectives that have been accomplished in this study. Moreover, some important recommendations could be applied in many future researches.

# CHAPTER TWO

# Theoretical part and Literature Survey

# CHAPTER TWO
# THEORETICAL PART & LITERATURE SURVEY

## 2.1 Introduction

Deals at the beginning of this chapter bone structure, auxiliary tissue in bone formation and Installation of joints and their types. There will be a focus on the criteria of selection implantable metals such as biocompatibility, wound healing, toxicity, wear and corrosion behaviour, the types of Ti alloys, development of low young's modulus titanium alloys, and it will also talk about beta alloys (Ti-13Nb-13Zr). Then there will be a detailed focus on the Surface Modifications and their methods, especially on electrophoretic deposition. A suitable literature review was also presented at the end of this chapter.

## 2.2 Inception

Supporting body weight, aiding mobility, safeguarding organs, encouraging mineral homeostasis, forming the blood supply, and storing triglycerides are all functions of bone. The hierarchical and anisotropic structure of bone tissue is closely linked to its numerous activities. Disease and trauma are common causes of bone loss. As a result, artificial medical devices and regenerative medicine are growing and becoming more popular in clinical settings, although completely understanding the intricate function of sophisticated bone structure is challenging. The first step in achieving this aim is to get a thorough grasp of the structure and function of bones [10].

## 2.3 Bone Tissue

### 2.3.1 Bone Structure

Bone comes in various shapes and sizes, including long, flat, short, and irregular, and the sizes and shapes vary from person to person. The

mature human skeletal system comprises around 206 bone components (213 bones in some references)[11]. Bone is arranged hierarchically and anisotropically at multiple levels due to its diverse tasks ranging from load support to mineral control such as calcium and phosphorus (Figure 2.1) [12].

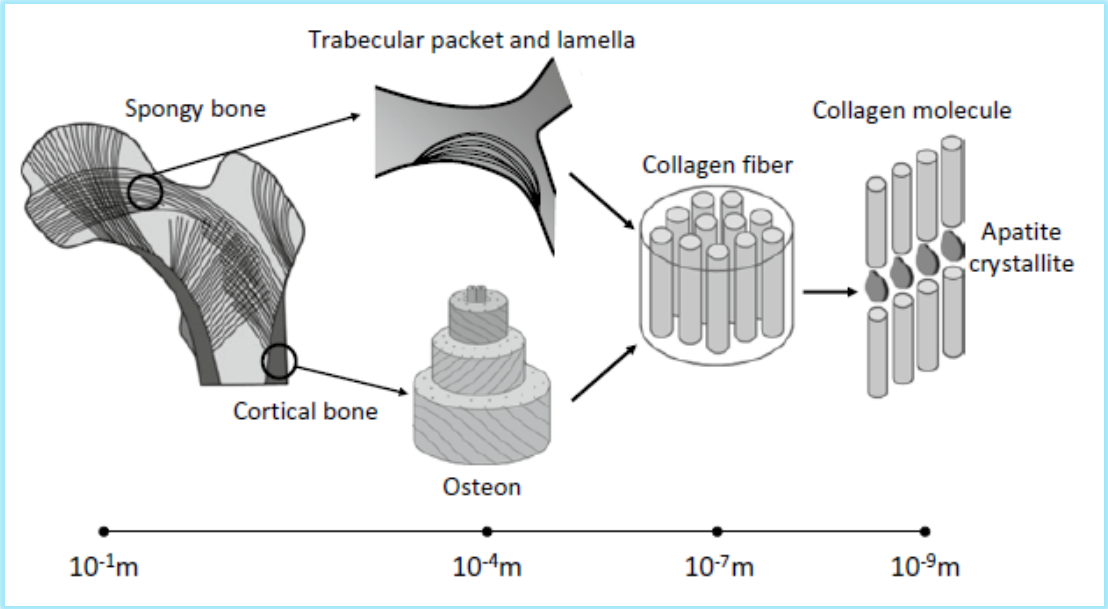


**Figure (2.1):** From the Particle to the Organ Level, the Hierarchy of Bone is Depicted Schematically[12].

Cross-linked type I collagen and the mineralized ingredient HAp provide bone with its strength and flexibility at the nanostructural level. The HAp is made up of hydroxyapatite $Ca_{10}(PO_4)_6(OH)_2$. Bone cells also serve a vital function in the body and contain extremely minute quantities of protein, cytokines, and hormones [13]. Bones are divided into cortical and spongy, primarily responsible for load support and turnover. Because it contributes to vital mineral homeostasis through the bone marrow, the relative ratio of spongy bone surface area to volume is larger than that of cortical bone [14,15]. The anatomical median section of the human proximal femoral bone is shown in Figure 2.2[16].

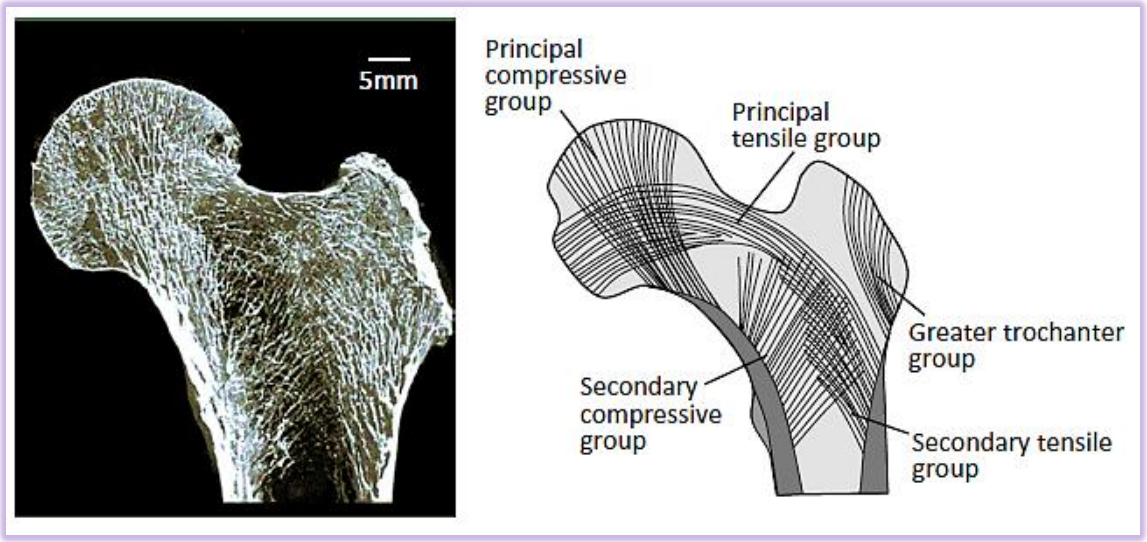


**Figure (2.2):** A Classic Trabecular Structure in the Proximal Region of a Human Tibia is Seen in this Diagram. The Trabecular Extension Orientations are Highly Associated with the Vivo Multiple Structural[16].

Bone is a highly porous, lively tissue with a complex structure that is difficult to replicate artificially. For sustaining functional degeneration of bone or bony joints, bone replacement materials or an artificial joint including metal are employed. Artificial materials and bone, however, have a considerable divergence in microstructure and function. As a result, mechanical safety and joint mobility must be prioritized in bone healing and artificial joint replacement, which may only result in partial bone function recovery. In addition, a bone regeneration technology that can restore original bone tissue is being developed [17].

In orthopaedic surgery, bone mineral density (BMD) and bone mass are used to diagnose and treat patients. As a result, innovative biomaterials and biodevices for bone formation and replacement should consider bone tissue's hierarchical and complex organization with anisotropic microstructure [18,19].

### 2.3.2 Bone Cells

Other bone-related cells, such as mesenchymal stem cells, interact with the three major bone cell types, osteoblasts, osteoclasts, and osteocytes(Figure 2.3) [20,21].

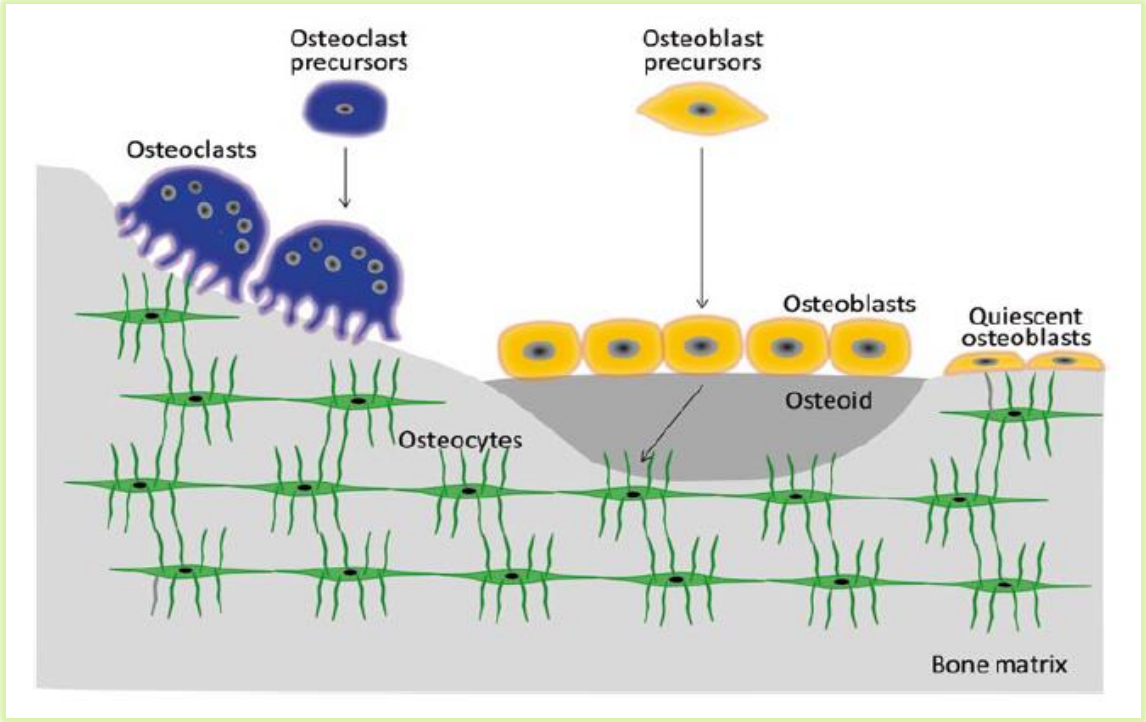


**Figure (2.3):** Bone Cells are Involved in the Modeling and Remodeling of Bones [20].

### 2.3.3 Spontaneous Healing and Bone Disease

Small flaws can be spontaneously repaired when a bone fracture occurs. Regarding macroscopic changes, Figure 2.4 depicts the mending phase of general bone fractures. The healing of a bone fracture is divided into three stages: inflammatory, reparative, and remodeling [22].

- A hematoma occupies the fractured area during **the inflammatory phase**, and osteonecrosis develops owing to osteocyte necrosis and extinction near the damaged end of the bone and the periosteum and bone marrow destruction. The hematoma is evacuated, inflammatory granulation tissue develops, and osteoclasts destroy necrotic bone in an inflammatory response (Figure 2.4a)[23].
- The soft callus and the ensuing hard callus phase make up **the reparative phase**. The hematoma is eliminated and replaced with granulation tissue during the soft callus phase when capillary blood vessels invade, and cells penetrate the hematoma(Figure 2.4b). Endochondral and intramembranous ossification are two types of hard

callus ossification that occur via cartilage. When the fixation in the bone fracture location is strong enough, intramembranous ossification occurs, dependent on mechanical stability[22,23].

- Immature bone is substituted for lamellar bone during **the remodelling phase**, and the bone shape is progressively rectified to the original shape, accompanied by the creation of marrow cavities (Figure 2.4c). The healing process is complete since the bones have finally fused (Figure 2.4d). When the release of functional proteins is accompanied by bone rebuilding, the process moves forward [23, 24].

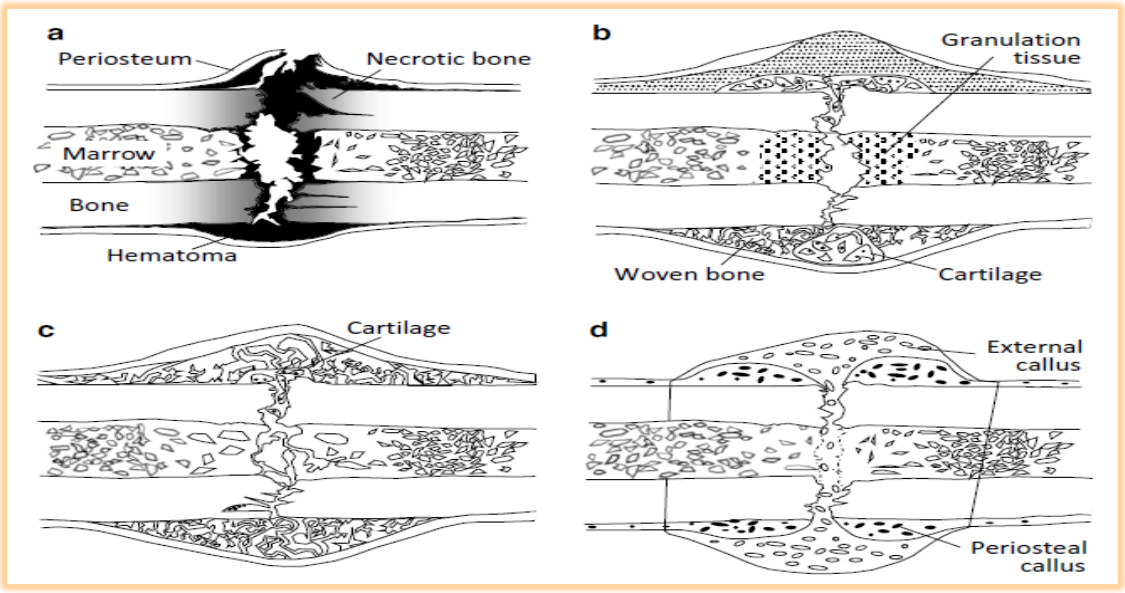


**Figure (2.4):** A Classic Fracture Healing Procedure Involves (a) An Inflammatory Process, (b) A Reparative Step, (c) A Remodelling Stage, and (d) Bone Joining by the Creation of an Exterior Callus[22].

## 2.4 Structure of Joint

### 2.4.1 Anatomical Classification

A joint is a point where two bones meet. Immovable, amphiarthrodial, and diarthrodial joints are the three types of gross joints[25].

### 2.4.1.1 Immovable Joint

The fibrous synarthrosis, packed with thick collagenized fibrous tissue, such as the skull structures, is the Immovable joint (Figure 2.5a ). There is no mobility in this joint. The epiphyseal plate which includes the cartilage plate is also classified into the immovable joint[25].

### 2.4.1.2 Amphiarthrodial Joint

The intervertebral disc and the symphysis pubis are amphiarthrodial joints characterized by restricted movement (Figure 2.5b). The syndesmosis is an amphiarthrodial joint in which the bone connects to the ligament, such as the distal tibiofibular joint and the forearm's interosseous membrane[26].

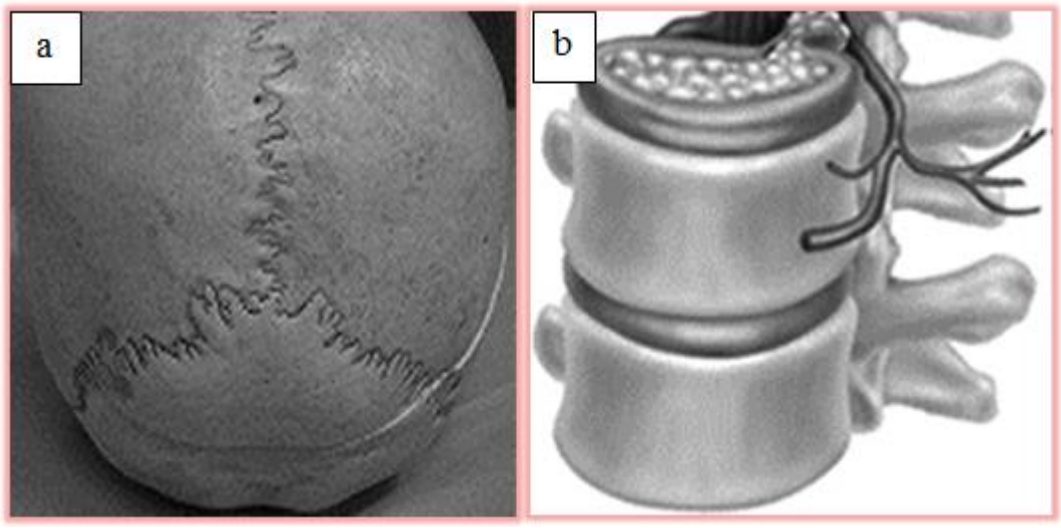


**Figure (2.5)**: (a) Structure of Skull are Cannot be Moved Joint, (b) A Kind of Joint that is Made up of Multi Disc [26].

### 2.4.1.3 Diarthrodial Joint/Synovial Joint

The diarthrodial joint, cavitated to generate a freely moving connecting unit between two bones, is the most common [27]. The diarthrodial joint serves the following purposes: (1) the capacity of the articulating surfaces to move over each other freely, (2) the ability to retain stability during motion, and (3) a suitable distribution of stress across the tissues that make up the joint to avoid injury. The four functional categories

of diarthrodial joints are ball-and-socket joint, hinge joint, saddle joint, and pivot joint [27].

- ***Hinge Joint***

Hinge motion shows angular motion in one plane, particularly extension and flexion, as seen in the humeroulnar and knee joints. Because the medial femoral condyle and lateral femoral condyle have distinct forms, the knee joint operates not only as a hinge joint but also as a sliding joint on the contact surface (Figure 2.6a )[28].

- ***Pivot Joint***

Pivot joint shows only uniaxial rolling motion, such as proximal radioulnar joint surrounded by the annular ligament (Figure 2.6b)[29].

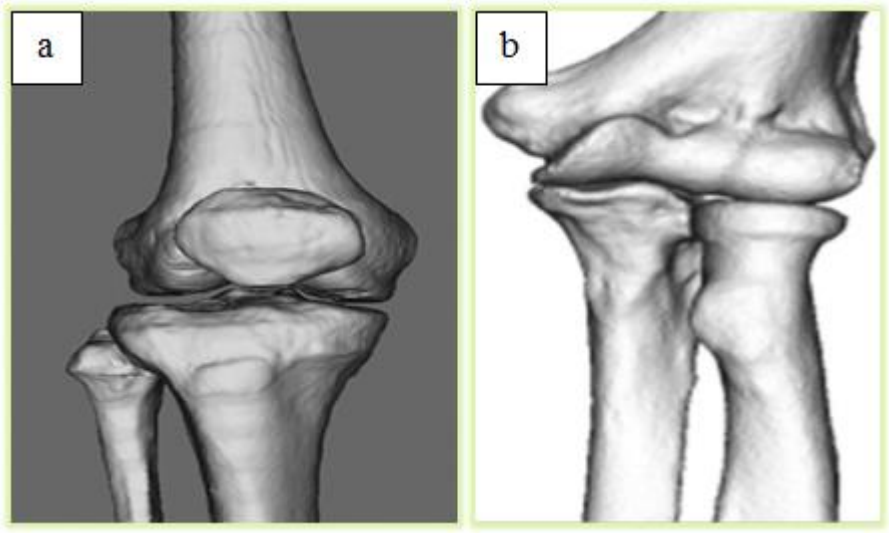


**Figure (2.6):** Diarthrodial Joint (a)Hinge Joint (Knee Joint), (b) Pivot Joint (Proximal Radioulnar Joint) [29].

- ***Ball-and-Socket Joint***

Ball-and-socket joints, such as the hip joint (femoral head and acetabulum) and shoulder joint (concave bony fossa), are made up of a hemispherical bony head and a concave bony fossa (humeral head and glenoid cavity). Because of the triaxial motion, this joint has a wide range of motion [30].

The hip joint has a vast range of motion, including extension, flexion, external rotation, and internal rotation and is anatomically a ball-

and-socket joint (Figure 2.7a ). The hip joint serves as a weight-bearing point as well [30].

- ***Saddle Joint***

Saddle joint shows large angular motion, not rolling motion, such as the carpometacarpal joint (Figure 2.7b) [31].

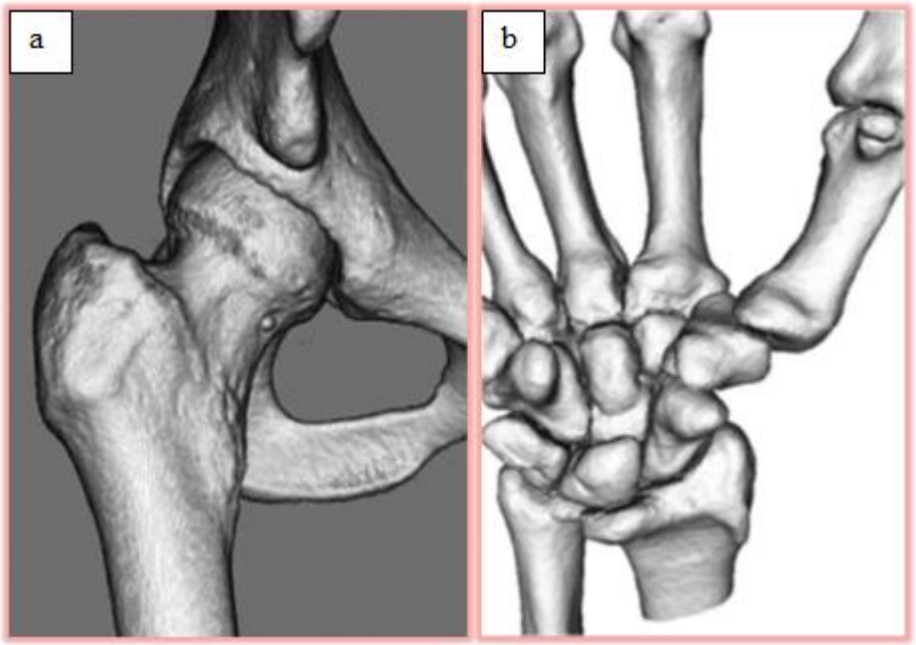


**Figure (2.7):** Diarthrodial Joint (a) Ball-and-Socket Joint (Hip Joint), (b) Saddle Joint (Carpometacarpal Joint) [31].

## 2.5 Biometals Implants and Its Properties

The ability to pick a metal implant material that is biocompatible and that is not poisonous to the surrounding biological system is a must. The implantation of metals such as aluminium, iron, copper, nickel, zinc, carbon steel, silver, and magnesium into the human body has been studied for over a century. These metals were eliminated because they were too reactive in the body to be implanted for a long time[32].

When stainless steel was introduced to general engineering in the early 1900s as a new corrosion-resistant material, it was soon used for surgical purposes. However, because of its high carbon content (0.08 per cent) and low molybdenum content, the 18-8 stainless steel that was

originally employed showed intergranular corrosion and extensive pitting[33].

Cobalt-chromium and cobalt-chromium molybdenum alloys were initially introduced and used in dentistry and orthopaedic applications around the same period because of their corrosion resistance. Titanium and its alloys are the most corrosion-resistant implant materials currently in use. Titanium alloys were initially utilized in the 1960s, and their popularity has continued to expand since the mid-1970s and continues to increase. Several titanium alloys give optimum strength and corrosion resistance, including Ti-6Al-4V, Ti-5Al-2.5Fe, and Ti-6Al-7Nb. The major advantage of titanium and its alloys is the non-reactivity of the passive film that is formed; the main disadvantages are its susceptibility to fretting as well as oxygen diffusion during fabrication, causing embrittlement [34,35].

As demonstrated in Table 2.1 [35,36], most metal alloys are used in medical equipment and industrial alternatives. Table 2.2 shows the mechanical characteristics of the alloys described in this thesis [36,37].

**Table (2.1):** The most Important Biomedical Metals and Alloys and their Applications [37].

| Material | Major Application |
|---|---|
| 316L Stainless Steel | cranial plates, orthopaedic fracture plates, dental implants, spinal rods, joint replacement prostheses, stents, catheters |
| Cobalt-Chromium alloys | orbit reconstruction, dental implants, orthopaedic fracture plates, heart valves, spinal rods, joint replacement prostheses |
| Titanium, Nitinol, Titanium alloys (Ti-6Al-4V, Ti-5AL-2.5 Fe, Ti-6Al -7Nb) | cranial plates, orbit reconstruction, maxillofacial reconstruction, dental implants, dental wires, orthopaedic fracture plates, joint replacement prostheses, stents, ablation catheters |

**Table (2.2):** Healthy Bone and Implant Alloy Mechanical and Physical Characteristics [36].

| Material | Tensile Strength $(MN/m)^2$ | Yield Strength $(MN/m)^2$ | Vickers Hardness (Hv) | Young's Modulus $(GN/m)^2$ | Fatigue Limit $(GN/m)^2$ |
|---|---|---|---|---|---|
| 316L SS | 650 | 280 | 190 | 211 | 0.28 |
| Wrought Co-Cr Alloy | 1540 | 1050 | 450 | 541 | 0.49 |
| Cast Co-Cr Alloy | 690 | 490 | 300 | 241 | 0.30 |
| Ti-6Al-4V | 1000 | 970 | --- | 121 | --- |
| Human Bone | 137.3 | --- | 26.3 | 30 | --- |

## 2.6 It Should not have Happened

### 2.6.1 Corrosion Behaviour

A patient had a primary complete hip replacement and a prosthesis inserted. Radiographs taken seventy months after surgery revealed a damaged prosthetic neck (Figure 2.8). A similar instance was recorded 85 months after surgery for the same type of prosthesis. The parts consisted of a wrought CoCrMo alloy head (ASTM F799) coupled to a CoCrMo stem. The fractures occurred in the neck just distal of the head-neck taper. Both patients were overweight with an active life, but the mechanical characteristics of the neck part should have been sufficient to support their weight. However, Something went wrong [38].

A cross-section of the taper revealed corrosive fluid penetration at the grain boundaries. The fracture was likewise seen to follow the grain boundaries (Figure 2.8(1)a); (1)b indicates the commencement of the fracture[38,39].

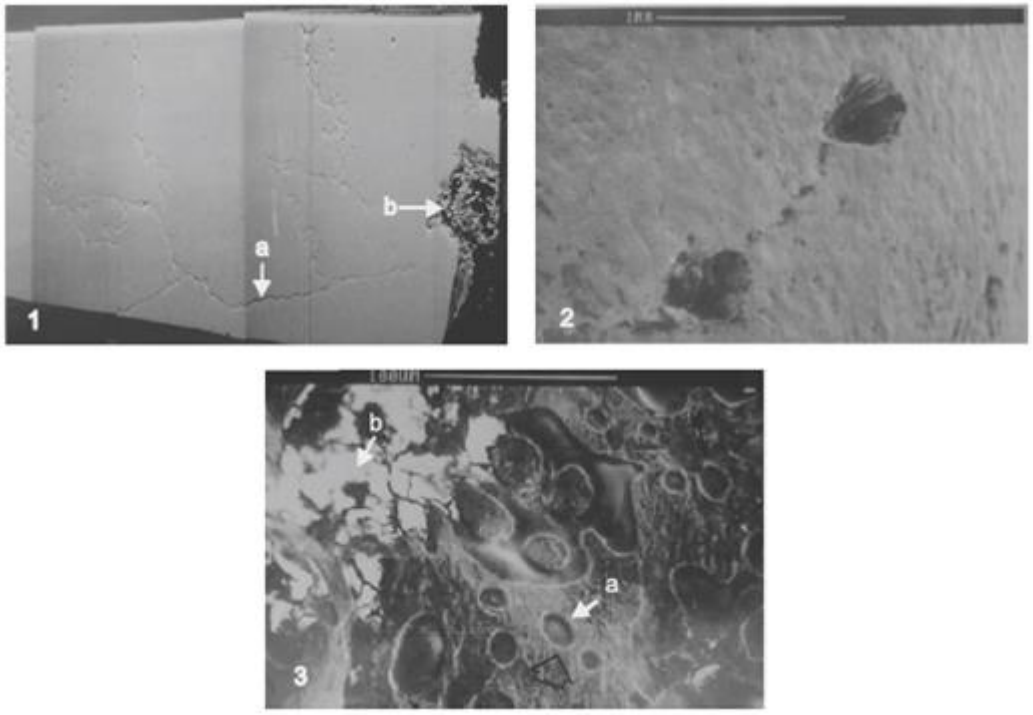


**Figure (2.8):** (1) intergranular Cracks May be Seen in the Cross - Sectional Area (a) throughout the neck, Whereas (b) Reveals the Rupture Start Point.(2) Micrograph of the free fracture surface. (3) Micrograph of the fracture surfaces: (a) pores; (b) non-conducting debris[38].

### 2.6.1.1 Styles in Corrosion

Don't like things when corrode, it happens when an unfavorable potential difference acts as a driving factor and the reaction advances at a discernible rate. Different "styles" of corrosion might emerge due to the potential difference being developed in unusual ways. In the 1960s, when hip implantology was growing, implant producers broke fundamental corrosion protection standards by mixing non-compatible metals. Due to some devastating consequences in the following decades, great research efforts were devoted to the problem and the degradation of biomaterials in general[40].

- ***General or Uniform Attack and Galvanic Corrosion***

In general, uniform corrosion is defined as a result of small spatially and temporarily randomly distributed anode and cathode zones on macroscopically homogeneous metal substrate[41].

Despite their high protective oxide layer, stainless steel, CoCr alloys, and titanium show small but sizeable uniform attack. The process definitely a combination the chemical dissolving of the passive layer and galvanic corrosion of either the uncovered or almost accessible metal substrate. Chemical and electrochemical reactions are heterogeneous processes with a solid and liquid phase, as well as absorbed oxygen $O_2$ and any other biological component capable of assisting attack to start[42].

- ***Localized Corrosion***

Corrosion seen in one place might result from an wrong environment at the far end of a metal piece. Metals serve as electric current highways. Excessive corrosion can cause implant devices to fail prematurely, losing their mechanical qualities before the human tissues have had the time to recover. The term "localized corrosion" refers to a group of family members with distinct appearances [43].

### 2.6.2 Intoxicated by Implants

The poisoning is closely related to Stoke and what happened in his schoolboy laboratory where he experimented with mercury. His professional work on hydrides and the development of high vacuum apparatus and other instruments implying the use of mercury in Breslau (now Wroclaw) and Berlin developed further his erethism or chronic mercurialism. He suffered from headaches, dizzy spells, memory loss and catarrh. After one of his collaborators had a tooth abscess in 1924, a toxicologist finally discovered that his collaborator’s as well as Stock’s disease was due to mercury poisoning. From that time on, Stock began his research on mercury poisoning and contamination, which were to span the final 20 years of his life. From this work emergedwhat is called the second amalgam war [38].

The first amalgam war took place in the 1840s between the American Association of Dental Surgeons and those dentists who insisted on using

the new techniques of making fillings with dental amalgam. The next war was Stock's one. His fight against amalgam was based on his analytical determinations of mercury content in urine of patients having amalgam fillings [38].

### 2.6.2.1 Toxicity

By definition, essential elements do not have intrinsic toxicity. The supply and subsequent concentration in the body may, however, be deficient, in excess, or, beyond simple excess, harmful and toxic. Intrinsically, toxic elements show a negative response to any concentration, the end of the response curve being possible death. Tables are published for toxicity levels commonly expressed as Lethal Dose. LD50 is the administered amount of an element in a specified form for which 50% of the test animals die, of course, forensic investigators of today are well acquainted with deliberate administration of lethal doses. Acute poisoning is only reported for accidental ingestion by children, intoxication during industrial accidents or in agriculture (thallium(TI), arsenic(As), methylmercury ($CH_3Hg$)) [44].

### 2.6.2.2 Trace and Essential Trace Elements

All metal ions, except calcium, iron, potassium, sodium, and magnesium, are present in the body as trace elements. Table 2.3 lists the necessary components. The average total quantity of the element contained in an adult is listed in the second column. The molar concentration in plasma is listed in the third column, and the average daily quantity consumed by an adult is listed in the fourth column[45].

**Table (2.3):** Concentration of Essential Elements in Humans. The Ions are Listed as they are Expected to Occur at pH 7 [45].

| Element | Total | Plasma | Daily allowance |
|---|---|---|---|
| $Na^+$ | 100g | 141 mM | 1-2 g |
| $K^+$ | 140g | 4 mM | 2-5 g |
| $Mg^{2+}$ | 19g | 0.9 mM | 0.7 g |
| $Ca^{2+}$ | 1000g | 2 mM | 0.8 g |
| $Cr(OH)^+$ | 6 mg | 0.5 µM | 0.1 mg |
| $MoO_4^{2-}$ | 9 mg | 0.05 µM | 0.3 mg |
| $Mn^{2+}$ | 12 mg | 0.2 µM | 4 mg |
| $Fe^{2+}$ | 4.2g | 20 µM | 10-20 mg |
| $Co^{2+}$ | 1 mg | 0.1 µM | 3 µg |
| $Ni^{2+}$ | 1 mg | 0.1 µM | 170 µg |
| CuO | 72 mg | 18 µM | 3 mg |
| $Zn^{2+}$ | 2.3g | 20 µM | 15 mg |
| Si | | | 10-26 |
| $HPO_4^{2-}$ | 780g | 2 mM | 1 g |
| $SO_4^{2-}$ | 140g | 1 mM | ---- |
| $HSeO_3^-$ | 5 mg | 2 µM | 0.1 g |
| $F^-$ | 2.6 g | 10 µM | 2 mg |
| $Cl^-$ | 95 g | 103 µM | 2-4 g |
| $I^-$ | 30 mg | 0.5 µM | 0.15 µg |

A remark about silicon. This element is not taken up in current tables of essential elements. Its absence in the body should be quite strange as it is the second most abundant element in earth's crust (about 28%).

The paper by Edith Carlisle in Science in 1970 . The author advanced strong evidence that silicon element is actively involved in bone formation at bone forming sites of the body, particularly in osteoid tissue. At the edge of the trabeculae with Ca contents ranging from 0.1 to 2.0%, the Si content ranges from 0.08 to 1.0%, and similar Si contents are found in periosteal areas for 0.5–15%Ca. At higher Ca contents, Si content vanishes [45].

### 2.6.2.3 Sensitivity to Metal Implants

Cobalt, nickel or chromium sensitivity affects 10–15 per cent of the general population, with Ni having the greatest sensitivity (>10 per cent) as the Figure (2.9)[46].

**Figure (2.9):** Sensitivity to Chromium 2 Months after Implantation of a Femoral Component Made of a Co–Cr Alloy [46].

Patients with well-performing implants have a prevalence of metal sensitivities to one or more of Ni, Co, and Cr that is nearly double that of the general population (25 vs 10%) and four to five times that of patients with poorly functioning implants (60 per cent). It should be noted, however, that linking patients to well- or poorly-functioning prostheses does not prove causation since many criteria were not stated (preexisting allergenicity etc.). The outcome is as such not unexpected: wear and corrosion provoke anyway more metal dissolution than well-fixed prostheses [47].

### 2.6.3 Friction and Wear Failure

Surface damage or material removal from surfaces in contact and motion with each other is referred to as wear. Material may be damaged on the surface, transported from one surface to another, or broken loose as a wear particle [48].

The wear qualities of an implant material are critical, particularly in joint replacements. Wear is impossible to describe without first grasping

the concept of friction between two materials. When two solid materials contact, they touch only at the tips of their highest asperities (microscopic protuberances). Therefore, the real contact area is much smaller than the apparent surface area. For ductile materials, the real area of contact increases as the applied load (P) increases. Due to the creation of plastic junctions, ductile materials can be pressure welded, as illustrated in Figure 2.10. When two materials slide over one other with or without a lubricating coating, the plastic junctions are the primary source of adhesive friction. The resistance to the shear failure of the plastic junction results in a frictional force[48,49]. Therefore, the sliding force (F) will be simply proportional to the shear yield strength (k) of the junctions and the contact area (A) [48]:

$$F = A\,k \qquad (2.1)$$

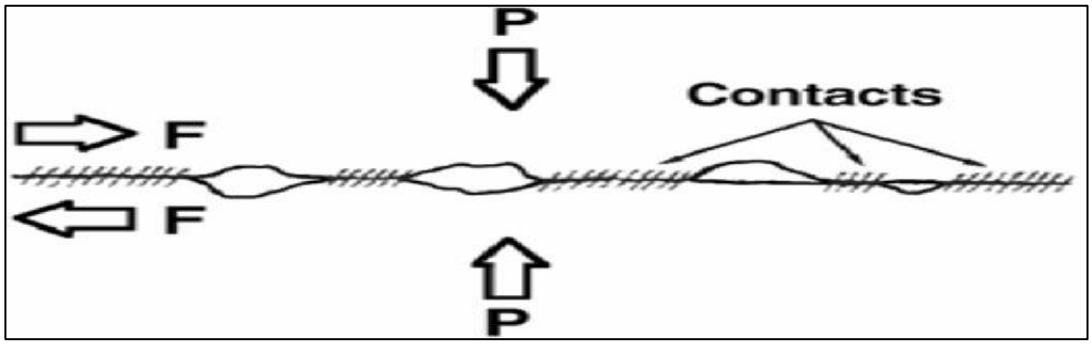


**Figure (2.10):** In this Diagram, two surfaces under pressure for ductile materials [50].

If metals in contact are similar, wear is higher than if they are dissimilar. Specifically, the lower the mutual solid solubility of the metals, the lower the wear [49].

Dissimilar metals are troublesome in biomaterials because corrosion happens when dissimilar metals are put in an aqueous, saline environment such as the body. Furthermore, metal wear is accelerated in corrosive environments. Low friction and wear can be seen at polymer–metal contacts; however, low friction does not always imply low wear. For example, Teflon (PTFE, polytetrafluoroethylene) has a low friction coefficient but wears quickly. Teflon was used in the early stages of

implant development; however, it was found ineffective due to excessive wear. UHMWPE (ultrahigh-molecular-weight polyethene) is now the material of choice for joint replacement implants. Although polymers cannot sustain as much contact stress as metals, they are suitable for use in joint replacements in this regard [50].

Wear debris in hip replacement implants can cause tissue reactions such as fibroblast-like cell growth and activated macrophages. PMMA and UHMWPE are inert in the bulk; however, tiny particles of these materials irritate cells. Tissue reactivity to wear debris plays a role in bone resorption and implant loosening, common causes of joint implant failure [50,51].

Metal-on-metal designs in joint replacement implants have lower wear rates than metal-on-polymer designs and are thus considered an alternative. However, since the new designs and better congruent head and socket designs are relatively new, only early and midterm clinical results are available, and no long-term results. Elevated levels of metal ions due to wear debris have been observed in patients with these implants, but it is not yet known if there is a health risk [51,52].

## 2.7 Titanium Alloys for Biomedical Applications

From the standpoint of osteogenesis, titanium and its alloys have the highest biocompatibility of among all of the known metallic biomaterials. Titanium alloys are also considered to be suitable alternatives to stainless steels and Co–Cr alloys, which are currently used commercially as biomaterials in implant devices. This is primarily attributable to the typically low Young's moduli of titanium alloys, which is effective in both inhibiting bone resorption and enhancing good remodeling as the load transfers through both the implant and bone when the Young's moduli of the two materials are closely matched [53]. Titanium alloys also have the benefit of having a low density, titanium alloys have a density of around 4.5 g/cc, about half that of Co–Cr alloys and stainless steel. Titanium alloys

provide many other advantages, are resistant to in vivo corrosion, pitting attack, and crevice corrosion[54,55].

The contact of tissue with titanium implants is with the oxide surface layer. Wear debris is composed mainly of $TiO_2$. A serious chemical effort is needed to dissolve this oxide but, the body is an efficient chemical war machine. The attack is occasionally wear-assisted in load bearing implants and, in case of long-term implants, the body has ample time to act [56].

Titanium alloys are generally grouped into α-type, (α + β)-, and β-type titanium alloys according to their primary constitutional phase(s). The α-type titanium alloys are composed of single-phase α-microstructures, and the β-type titanium alloys are composed of single-phase β-microstructures. The (α + β)-type titanium alloys are composed of two-phase α + β-microstructures. The α- and β-phases consist of the hexagonal closed-packed (HCP) and body-centered (BCC) structures, respectively, the latter possessing a lower atomic density. These characteristics are depicted in Figure 2.11. The Young's modulus is typically smaller in β-type titanium alloys than in α- or (α + β)-type titanium alloys, and so β-type titanium alloys have been the focus of researchers aiming to produce titanium alloys with as low a Young's modulus as possible[57,58].

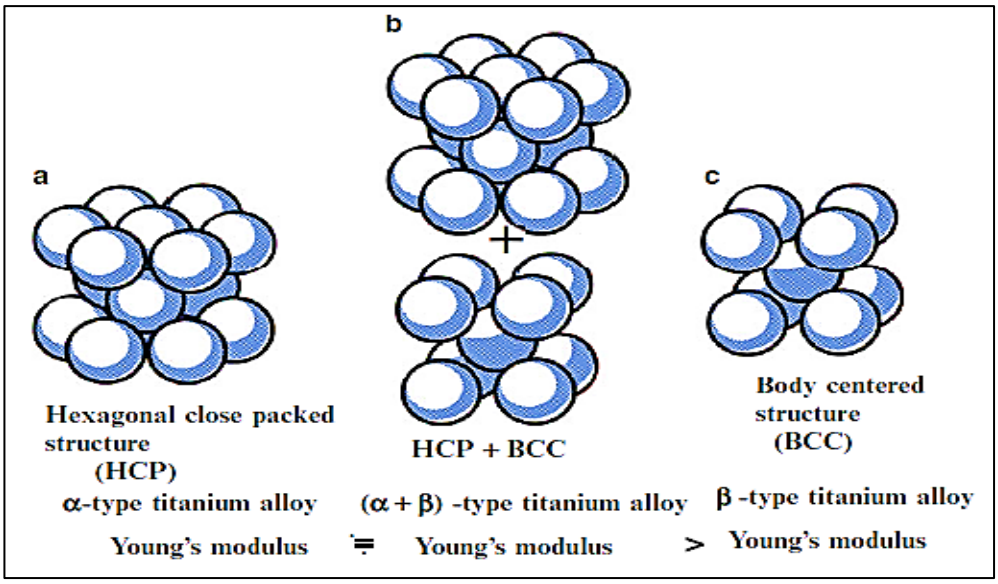


**Figure (2.11):** Schematic Explanation of α-, (α + β)-, and β-Type Titanium Alloys Based on Crystal Structure [58].

Table 2.4 tabulates strength and ductility properties of most of the titanium biomaterials used and being considered by manufacturers of medical devices. Although some of these alloys have undergone different heat treatments, the heat treatments are in common use, and rather wide ranges of strength and ductility can be achieved as shown by these data. Although tensile strength of the (α + β) Ti-6Al-7Nb alloy (600MPa) is beat to the β- Ti-13Nb-13Zr alloy (500MPa), the β -Ti alloys is superior to both α and α + β- Ti alloys in terms of Yield Strength and modulus of elasticity[59].

**Table (2.4):** Mechanical Properties of Selected Titanium Biomaterials[60].

| Alloys | E(GPa) | YS(MPa) | UTS(MPa) | TS(MPa) |
|---|---|---|---|---|
| **Ti-6Al-4V (Alpha\ Beta)** | 110-114 | 828-869 | 895-930 | 400 |
| **Ti-6Al-7Nb (Alpha\ Beta)** | 105 | 795 | 860 | 600 |
| **Ti-13Nb-13Zr (near-Beta)** | 79-84 | 836-908 | 973-1037 | 500 |

E: Modulus of elasticity; YS: Yield Strength; UTS: Ultimate Tensile Strength; TS: Tensile Strength

### 2.7.1 Development of Low Young's Modulus Titanium Alloys

If the Young's modulus of an implant is higher than that of the cortical bone, then the load is preferentially transferred to the implant. This phenomenon is referred to as stress shielding, and it is especially true in the case of load-bearing implants, such as those used for replacing failed hard tissue (cortical bone). When stress shielding occurs, it results in bone resorption and poor bone remodeling, which are the leading causes of implant loosening and refracture of the bone after implant extraction. The Young's moduli of β type titanium alloys are typically smaller than those of the other metallic biomaterials, such as stainless steels and Co–Cr alloys, as well as those of α- and (α + β)-type titanium alloys. Various low-modulus β-type titanium alloys have been developed for biomedical applications as shown in Table 2.5 [61,62]. Those low-modulus β-type

titanium alloys which contain the most biocompatible elements are Ti–35Nb–7Zr–5Ta (TNZT: TiOsteum), Ti–29Nb–13Ta–4.6Zr (TNTZ), and Ti–36Nb 2Ta–3Zr–O (gum metal), exhibit Young's modulus values of approximately 55, 60, and 70 GPa, respectively. Note, however, that these values are still much higher than that of cortical bone (10–30 GPa). Nb, Ta, and Zr are relatively safe elements for the human body based on reported cytotoxicity and thus a means of lowering the Young's modulus of the Ti–β type titanium alloy system is desirable[36].

The Young's modulus, along with other variables such as fracture toughness, tensile strength, elongation to failure, fatigue life, fretting fatigue life, wears characteristics, and so on, must be regulated in structural biomaterials used in implants that replace hard tissue. These variables are broadly referred to as mechanical biocompatibilities, and fatigue strength is one of the most crucial from an implant's endurance standpoint. When the lowest Young's modulus is reached in β-type titanium alloys, the mechanical biocompatibilities are often inferior[36].

### 2.7.2 Ti-13Nb-13Zr nearβ-Type Titanium Alloy

The selection of elements is a vital phenomenon in designing beta Ti alloys because an improved beta phase stability can only be achieved using beta stabilizing elements. Among other β stabilizers, the eutectoid elements such as iron (Fe), manganese (Mn), chromium (Cr) etc. are strong β stabilizers, inexpensive and can improve mechanical and fatigue strength upon addition of even very small quantities in Ti alloys. Further, zirconium (Zr) is also a compatible element to Ti because it resides in the same group of the Periodic Table. In addition, Zr possesses excellent corrosion resistance ability and especially high Zr quantities can improve mechanical strength when alloyed with Ti. on the other hand, Nb not only increases the corrosion resistance of Ti with a fast repassivation rate but also exhibits excellent biocompatibility [63].

Among the new alloys of research interest based on titanium, the near-β Ti–13Nb–13Zr alloy appears as an option to be taken into account for biomedical implant applications because of its toxic free alloying elements, high corrosion resistance and good biocompatibility. This alloy contains unique combination of Nb and Zr alloying elements, that is expected to have superior corrosion resistance over the other α+β type alloys. During spontaneous passivation, it releases fewer metal ions because of minor alloying elements which are less soluble than those of Al and V. There is also development of dense passive oxide layer that gives better protection [64,65].

**Table (2.5):** Representative Low-Modulus β-Type Titanium Alloys for Biomedical Applications [36].

| Beta type Ti-alloy | ASTM standard | ISO standard | JIS standard |
|---|---|---|---|
| Ti-13Nb-13Zr | ASTM F1713 | --- | --- |
| Ti-12Mo-6Zr-2Fe (TMZF) | ASTM F1813 | --- | --- |
| Ti-15Mo | ASTM F 2066 | --- | --- |
| Ti-15Mo-5Zr-3Al | --- | --- | JIS T 7401-6 |
| Ti-45Nb | AMS 4982 | --- | --- |
| Ti-35Nb-7Zr-5Ta (TNZT) | Task force F-04.12.23 | --- | --- |

### 2.7.2.1 Phase Diagram and transformations in Ti-13Nb-13Zr alloy

The estimated Ti-Nb phase diagram (for 13 wt.% Zr) is shown in figure 1, based on the ternary Ti-Nb-Zr phase diagram. Ti-13Nb-13Zr have a lower beta transus (137 °C) than Ti-6Al-4V (1000 °C). The estimated beta transus for air-cooling and the martensite transformation starting temperature (Ms) for water quenching are also shown in Figure 2.12. The metastable phases can form either on quenching from the β phase field or during heat treatment. Metastable phases that form in the order of increasing content of β stabilisers are hexagonal martensite (α′), orthorhombic martensite (α″), omega phase (ω), and phase separated β

phases (β and β′). These phases have different mechanical properties. Thus, a low modulus Ti alloy can be produced by stabilising the β phase. In particular, the formation of ω phase has to be avoided due to its highest elastic modulus [66, 67].

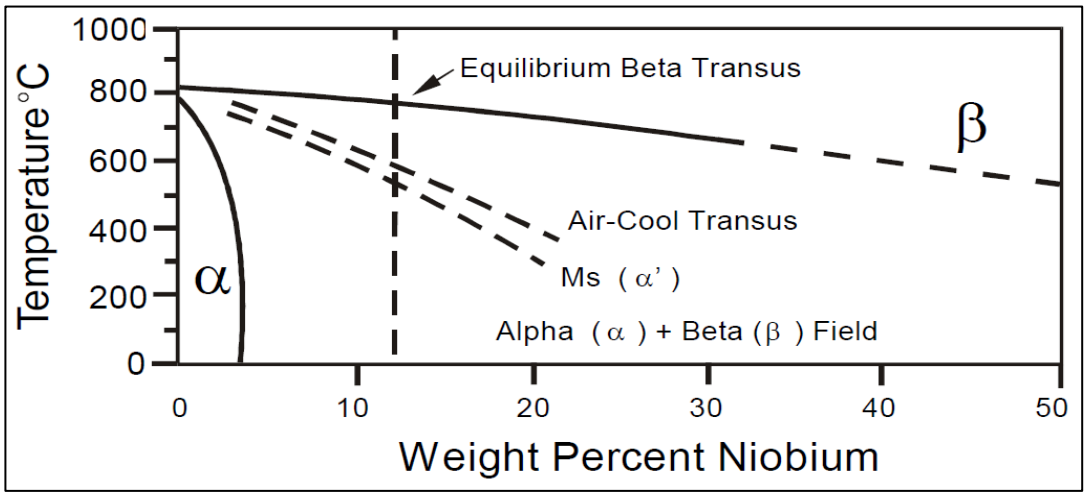


**Figure (2.12)**: The estimated Ti-Nb phase diagram for 13 wt.% Zr based on the ternary Ti-Nb-Zr phase diagram [67].

## 2.8 Functional Gradient Materials

In the 1980s, Functionally Graded Materials (FGM) was first proposed by Japanese scholars. It was originally designed to solve the huge temperature difference caused by the overheating of the outer surface of the spacecraft while keeping the internal temperature unchanged. Functionally graded materials combine the best of different materials to achieve their good performance. Once introduced, this concept has aroused worldwide exploration and expanded it into many fields such as metal-ceramic, metal-polymer, and ceramic-polymer and so on. In general, FGMs exhibit regular gradient changes both in the macro and the micro-scale (including uniform variation and layering variation). Therefore, FGM has many physical and chemical properties. Gradient structure can effectively enhance the strength, toughness, wear resistance and other properties of a particular region of the material, the material life and application performance of a qualitative leap, and even become a composite material development direction [68, 69].

### 2.8.1 Functionally Graded Material Preparation Method

The functionally graded material is prepared through the diffusion and bonding of different materials between atoms, so as to achieve the purpose of permanent connection and good performance. At present, there are many reports about the preparation methods of functionally graded materials, but from the fundamental principle, we can summarize them as physical combination method, chemical combination method and physical and chemical synthesis method. The physical combination method, as shown in Table 2.6, refers to the layering of materials by controlling the variation of the movement direction and velocity of liquid particles with different sizes and shapes under the action of gravity, centrifugal force, electric field force and magnetic field force[70].

The chemical bonding method, as shown in Table 2.7, refers to the use of sintering, deposition and other methods to make the material changes in the molecular level, in the new phase and the resulting old gradient structure, so as to achieve the desired performance[70, 69].

Physical and chemical combination of law, as shown in Table 2.8, refers to the combination of physical and chemical synthesis, so that the material in the reaction process while taking advantage of its physical and chemical properties, to achieve the connection of materials, so that the gradient derived from each phase derived from the combined method[A].

**Table (2.6):** Physical methods [69].

| Method | Specific content |
|---|---|
| Wet powder coating method | The raw material powder is added into a dispersant to make a suspension, and then the suspension is sprayed onto the substrate. By controlling the spraying rate, a gradient composition of the composition can be obtained. The method of spraying a greater impact on impurities, coating adhesion is not easy to control. |
| Directional solidification method | In the process of solidification, coercive measures are used to make the material appear in a specific direction during solidification and finally obtain a grain structure with a specific orientation, so as to achieve a gradient structure. The method is complicated, and the two parameters of the temperature gradient and the solidification rate in the solidification process are not easily controlled. |

| | |
|---|---|
| Centrifugal casting method | Centrifugal force field using different density particles in the centrifugal force to move in different directions in order to achieve structural stratification. The method can prepare large-scale and high-density gradient materials, but does not work well for preparing high-melting-point ceramic system functionally graded materials. |
| Settlement casting method | Add a certain size of the powder particles in the melt, under the action of gravity, through the settlement parameters and subsequent cold processing to form a gradient structure of the material. The method is complicated process, long working hours. |
| Filling casting method | First, a melt is injected into the cavity, and then the second melt is injected into the first non-condensed melt to achieve gradient connection between the two melt under the effect of thermal convection. |

**Table (2.7):** Chemical methods [69, 71].

| Method | Specific content |
|---|---|
| Electrodeposition method | Under the action of electrolysis or chemical reaction, different active particles undergo chemical reduction reaction at the same time and deposit on the surface of the substrate to form a coating. Process equipment is simple, easy to operate, easy to control the accuracy, low cost, but only for the preparation of thin foil FGM body. |
| Laser cladding method | The mixed powder is sprayed onto the substrate to control the laser heating power and other parameters to melt the substrate surface to produce a molten pool, and then the powder is added to react to form a gradient structure after cooling. FGM can be prepared film and body, wide adaptation; but the preparation process is complex, expensive equipment. |
| Reactive infiltration method | The preform reacts with the infiltrated material through a chemical reaction to couple the solute distribution at the interface, thereby forming a gradient structure. The method has the advantages of short preparation period and close size forming. |
| Self-propagating high temperature synthesis | The reaction of the material itself is continued by the heat release of the material itself, and it has a good prospect for the preparation of large size and complex materials. This method has the advantages of high efficiency, less energy consumption, rapid reaction and high purity of the product. |

**Table (2.8):** Combination of physical and chemical methods [69]**.**

| Method | Specific content |
|---|---|
| Powder metallurgy method | The raw material powder is arranged in order according to a predetermined order, then pressed and shaped through a molding process, and finally a functionally graded material is obtained through a densification process such as sintering. High reliability, suitable for the preparation of simple shape FGM parts, but the supply and demand is complex and the cost is high. |
| Vapor deposition method | Divided into physical vapor deposition and chemical vapor deposition, the principle is the use of active gaseous substances deposited on the substrate surface film, forming a gradient structure. The method has the advantages of rapid deposition speed, flexible process, and high gradient material binding. However, due to the volume limitation of the deposition chamber, only small-sized materials can be prepared. |

| | |
|---|---|
| Plasma spraying method | The raw material powder is added into the plasma jet, and the high temperature of the plasma is used to melt or partially melt the raw material powder during jetting, so that a gradient film structure is sprayed onto the substrate. The method is suitable for the gradient coating of complex geometrical devices, but the bonding strength between the gradient coating and the matrix is not high, and the coating has the defects of uneven microstructure, loose porosity and rough surface. |
| Grouting method | The raw material powder is poured into a liquid to form a suspension, and then the suspension is injected into the cavity, to be cooled and dried, and then hot-pressed to form a gradient structure. The process is suitable for mass production of gradient materials. |

## 2.8.2 Functionally Graded Materials Applications

Functionally graded materials have been used in many fields such as aerospace, nuclear energy, biology, electromagnetism, optics, energy and other fields through the ingenious combination of inorganic and organic materials such as metals, ceramics and plastics[69].

### 2.8.2.1 Aerospace Field

Functionally graded materials with high temperature resistance, thermal shock resistance, thermal fatigue resistance and corrosion resistance can be applied to heat-resistant surface of space shuttle and aircraft engine parts. Spacecraft engine combustion chamber wall at work, the side need to withstand high temperature and thermal erosion above 2000K, the material has excellent heat and heat insulation properties, while the other side will have low temperature liquid hydrogen cooling, the material proposed Low temperature and high thermal conductivity requirements[69,71].

### 2.8.2.2 Nuclear Energy Field

The high strength, heat resistance and corrosion resistance of FGM provide a reliable guarantee for the development of next generation nuclear industry. Nuclear power generation, nuclear power and the storage of nuclear weapons are extremely dangerous. Once the accident is triggered, it will have serious consequences. Therefore, imperative to ensure its safety, functionally graded materials show great superiority in the construction

materials of nuclear furnaces and inner wall materials of nuclear furnaces, which greatly protects the safety of the nuclear industry[69].

#### 2.8.2.3 Biological Field

The gradient material is common in nature, such as the shell of layered structure, the hard and tough animal skeleton, and the layered human skin. The medical development of FGM makes medical assistance to patients more timely and effective. The functionally graded material has the characteristics of high specific strength, high specific modulus, abrasion resistance and biocompatibility. Based on this, the artificial joint developed makes the artificial prosthesis and the patient's own skeleton have strong binding force and reliable Durable, showing good biocompatibility, but also has good self-healing and repair of regenerative properties. With its superior properties, FGM has a good application prospect in the biomedical fields, such as artificial bones, teeth, and heart[72].

#### 2.8.2.4 Electromagnetic Field

In the electromagnetic field, the gradient structure has the piezoelectric gradient function and the electromagnetic gradient function, and can be used to make electromagnetic shielding materials, ceramic filters, ultrasonic oscillators, etc. And the application of functionally graded materials on disks, permanent magnets, electromagnets and oscillators can reduce the mass and size of the corresponding devices and improve their performance[71].

#### 2.8.2.5 Optical field

Improving the mechanical and optical properties of glass has become an important direction in the field of development, by adding rare earth elements and materials with different refractive indices to the functionally graded material, the optical properties of the glass can be changed according to the environment. The relevant scholars have successfully prepared materials such as glass lasers, optical fiber lenses, anti-reflection films, and discolored glass[69, 71].

#### 2.8.2.6 Energy Sector

Functionally graded materials also have special properties based on heat resistance, corrosion resistance and thermal shock resistance. In particular, the development of various special function graded materials has made FGM play an important role in the energy field. For example, in the aspect of power generation system, the application of gradient thermoelectric energy conversion material makes the emitter not cracked in the high temperature working environment of 1860°C and greatly reduces the thermal stress of the system[69].

## 2.9 Surface Modifications

Surface can be defined as the outermost face, the exterior boundary or the outermost layer of atoms of the material. Interface is the boundary region between two adjacent phases, such as between solid and liquid. Atoms and molecules forming the surface will govern the surface properties of that material, because they will be in contact with the host atoms and molecules or their immediate. Surfaces of the bulk materials are different because the number of dangling bonds is less as compared to the smaller particles of the same volume [73].

Surface characteristics are related to a material's surface, such as surface tension, surface energy, adsorption, corrosion and degradation resistance, wear resistance, and adhesion. Surface qualities influence a material's reactivity, solubility, and other properties[73, 74].

As defined by Williams, a biomaterial is a non-viable material used in a medical device, intended to interact with biological systems. Surface properties, to a large extent, define success or failure of a biomaterial. The surface properties of biomaterials that are important for acceptance in the host include chemical structure, hyprophilicity/ hydrophobicity, the presence of ionic group, surface morphology and topography [75].

The attachment of various ligands or molecules to a surface to produce distinct physical, chemical, or biological characteristics is known as a surface modification. Surface modification is used in biomaterials to increase interfacial qualities such as wettability, protein and ligand adsorption, and roughness, all of which help to improve the biomaterial's effectiveness [76].

### 2.9.1 Surface Modifications Methods

Surface modification can be accomplished by physically or chemically altering surface atoms/molecules or depositing a layer on top of the surface. A polymer layer, an organic layer, or a thin coating of another material might be used. Figure 2.13 depicts a variety of surface modification techniques. A specific approach can be used depending on the substrate's surface and the modification's requirements [77].

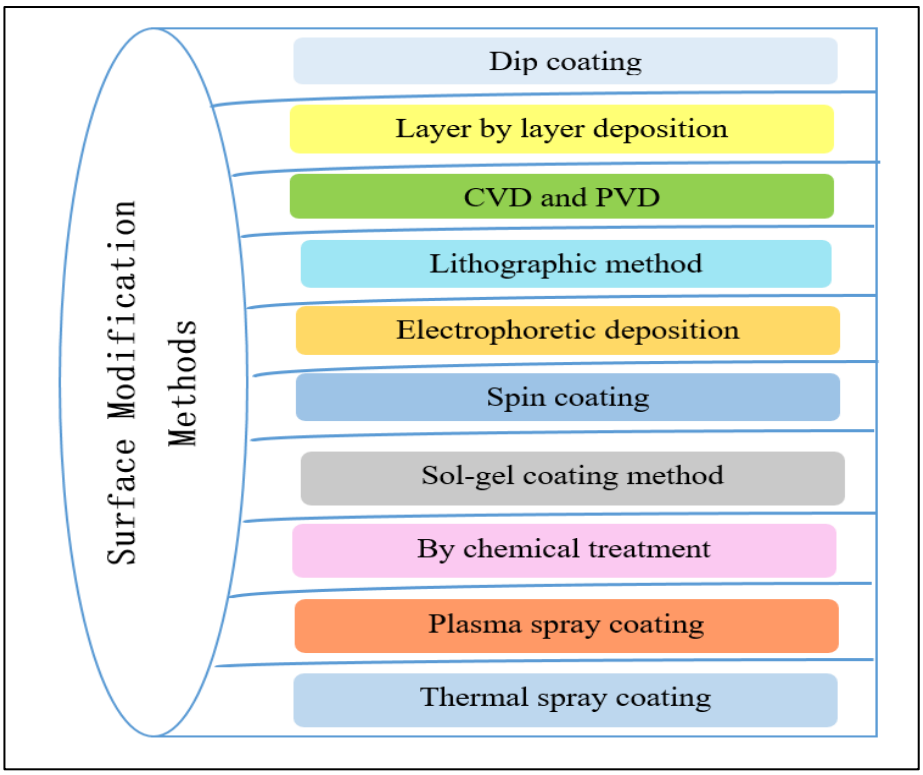


**Figure (2.13):** Schematic Diagram Showing Different Surface Modifications [77].

## 2.10 Electrophoretic Deposition

Electrophoretic deposition is technique of an electrochemical manner for the combination of two basic processes called electrophoresis and deposition. In the first process, an electric field is applied between two electrodes and suspended particles in a suitable solution charging moving toward the oppositely charged electrode. In the second process, where the particles accumulate at the deposition electrode and create a relatively uniform and homogeneous film [78,79,80].

This technique enables the production of unique microstructures and nanostructures as well as novel and complex material combinations in a variety of macroscopic shapes, dimensions and arrangements starting from micron-sized to nanosized particles. If the suspension colloidal including metals, polymers, ceramics, glass after deposition in the form of a fine powder (for example, less than 30 microns), it can be applied in the EPD for them easily. Then, heat-treatment is needed to remove porosity and to densify the deposit or in some cases there is no need for heat treatment according to the additives to the suspension coating [78, 80].

### 2.10.1 Types of Electrophoretic Deposition

Two kinds of EPD are known according to the surface charge of the suspended particles. If the particles are positively charged, they will move towards the electrode with the opposite sign, the cathode, and this process is called cathodic EPD. While, if the spread particles are negatively charged, they will be attracted by the positively charged electrode, the anode, and this process is named anodic EPD (Figure 2.14) [81].

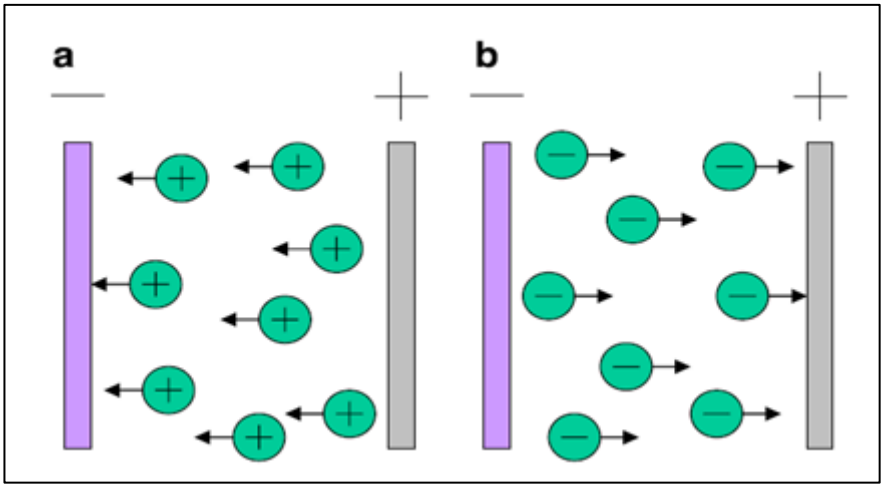


**Figure (2.14):**Schematic Illustration of Electrophoretic Deposition Process (a) Cathodic EPD and (b) Anodic EPD [81].

### 2.10.2 Electrophoretic Deposition Advantages

There are important reasons for concern in EPD, not only on its high versatility to be used with different materials and combinations of materials but also because EPD is a cost-effective and because it requires simple supplying equipment and infrastructure. Therefore, the main advantages of the EPD are[78,80,81]: Process simplicity, low equipment costs, deposition uniformity, the ability to coat complex shaped substrates, the EPD procedure is performed at room temperature, the deposits are high pure, applicability in medical application, the ability to generate thick composite films, and there is no phase transition during the coating process.

The coating thickness that EPD can produce varies greatly, ranging from 0.1 µm to more than 100 µm. The typical thickness of coatings achieved by various process techniques is shown in Figure 2.15. It demonstrates EPD's flexibility by demonstrating its ability to generate a wide range of coating thicknesses[82].

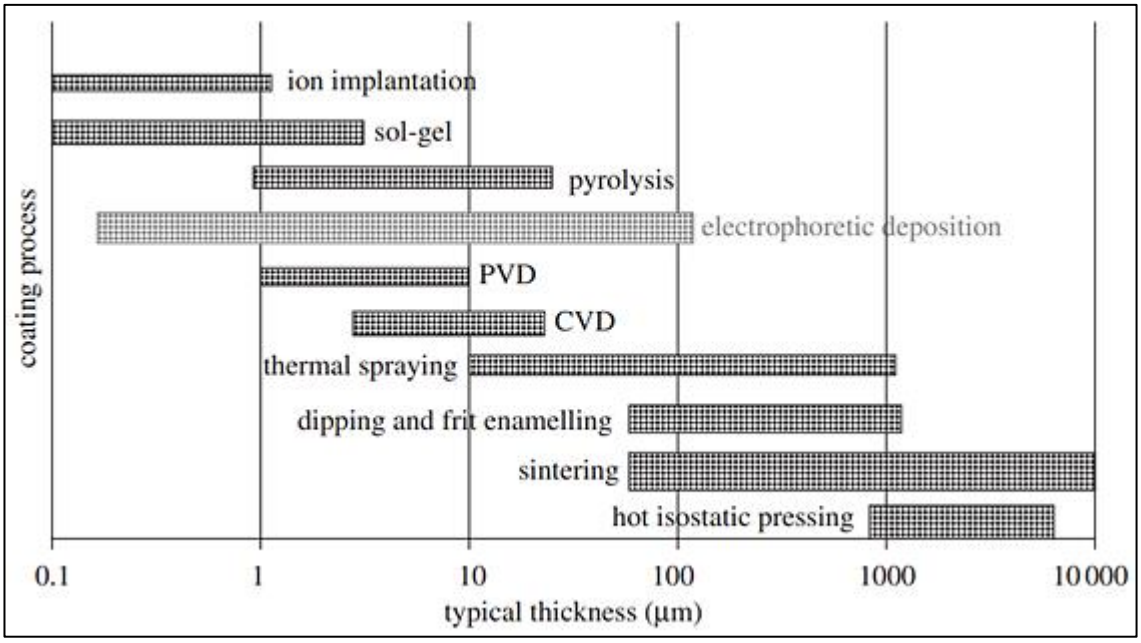


**Figure (2.15):** Typical Thickness of Coatings Obtained by Different Process Methods [82].

## 2.11 Factors Influencing the Film Formation

Figure 2.16 shows the sketch of EPD process. With application of an electric field, the ionically charged particles suspended in the suspension move to the oppositely charged electrode and then deposit onto it. The driving force exerted on the particles is the interaction between the electric field and the surface charge of particles. The drag force consists of the sluggish drag force from the liquid, the force exerted by the electric field on the counter-ions in the double layer and the distortion in the double layer caused by a displacement between the center of the negative and positive charge. Hence, the deposition behavior of charged particles is influenced by two groups of parameters: those related to the suspension, such as zeta potential, electrolyte conductivity, and those associated with the deposition process including voltage and deposition time [78].

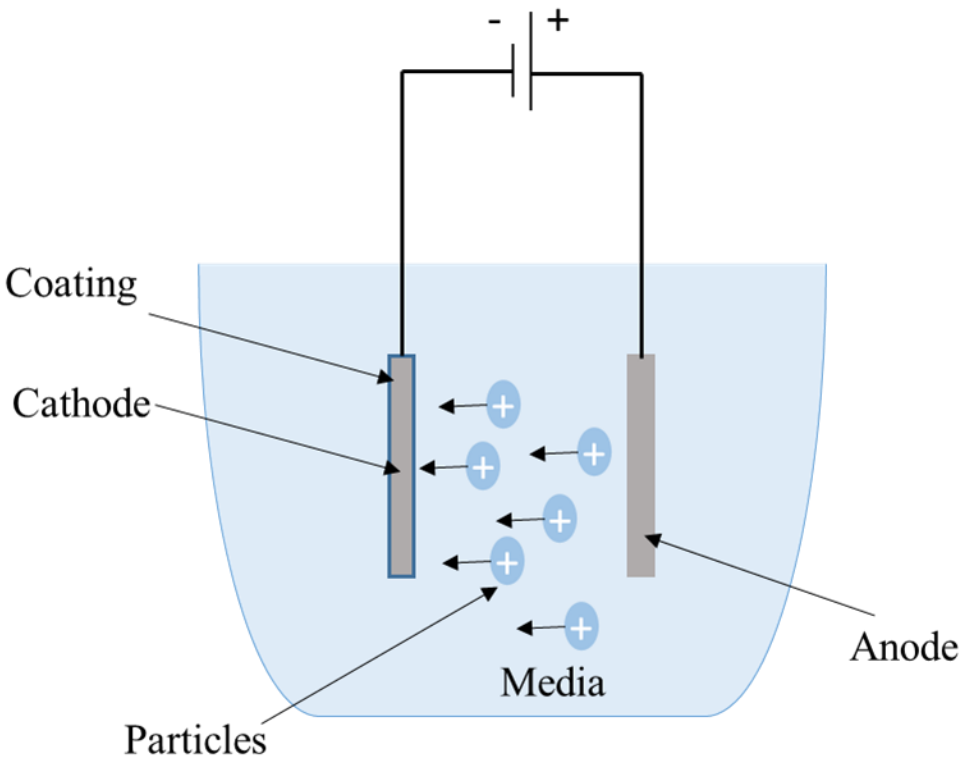


**Figure (2.16):** Sketch of the EPD Process[81].

## 2.12 Factors Related to the Suspension

### 2.12.1 Zeta Potential

Zeta potential can be defined as the potential difference between the dispersion medium and the stationary layer of fluid attached to the dispersed particle and is usually denoted by using the Greek letter zeta (ζ). The zeta potential indicates the suspension's stability as well as the direction of particle movement. Various charging agents, such as acids and bases, or some surface charge modifier, such as iodine, can be used to change the zeta potential [83].

### 2.12.2 Solvent

Water outperforms every organic solvent in terms of cost, flammability, and toxicity. Unfortunately, the electrolysis of water which occurs at low voltages is inevitable under an electric field strength high enough to obtain an intact and reasonable film. The electrochemical reactions are shown in the following equations:

$$\text{Anode: } 2H_2O - 4e^- \rightarrow O_2 + 4H^+ \text{ -----(2.2)}$$

$$\text{Cathode: } 2H_2O + 2e^- \rightarrow H_2 + 2OH^- \text{ -----(2.3)}$$

The bubble evolution associated with the hydrogen evolution reaction (HER) (Eq. (2.3)) or oxygen evolution reaction (OER) (Eq. (2.2)) during deposition reduces the deposit's homogeneity and quality[84, 78]. Table 2.9 summarizes some of the most common solvents used in the electrophoretic deposition.

**Table (2.9):** Physical Properties of Solvents [84].

| Solvents | Density (kg/L) | Melting Point (˚C) | Boiling Point (°C) | Dielectric Constant | Viscosity (CP)=$10^{-3}$ (Ns $m^{-2}$) | Specific Conductivity (S/cm) |
|---|---|---|---|---|---|---|
| Pentanol | 0.8122 | -79 | 138 | 13.90 | 3.62 | $8.08\times10^{-7}$ |
| Butanol | 0.8098 | -90 | 118 | 17.24 | 2.54 | $2.37\times10^{-6}$ |
| Propanol | 0.7827 | -90 | 82 | 18.45 | 2.04 | $1.01\times10^{-6}$ |
| Iso-Propanol | 0.8020 | -126 | 97 | 20.28 | 1.94 | $1.11\times10^{-5}$ |
| Acetone | 0.7856 | -95 | 56 | 20.86 | 0.31 | $4.05\times10^{-7}$ |
| Ethanol | 0.7731 | -114 | 78 | 24.64 | 1.09 | $5.36\times10^{-5}$ |
| Methanol | 0.7872 | -98 | 32 | 32.88 | 0.56 | $3.32\times10^{-4}$ |
| Distilled Water | 0.9982 | 0 | 100 | 80.40 | 0.89 | $5.50\times10^{-6}$ |

### 2.12.3 Particle Concentration

Particle concentration plays an important role in the properties of the film, including the film composition in a multi-component EPD. In a multi-component EPD, each component's deposition rate is independent; the deposition rate increases as particle concentration increases [85]. Although the deposition rate is theoretically proportionate to the solid loading, numerous tests failed to obtain a linear relationship between the deposition rate and particle concentration. Moreno et al.[86] discovered that the green density of $Al_2O_3$ films deposited from aqueous suspension increases with solid content, whereas Guo et al.[87] observed that the solid loading shows no visible effect on the packing density of yttrium stabilized zirconia (YSZ) deposit obtained from the organic suspension when all other parameters are

kept constant. Because bubble evolution in aqueous suspensions is much more violent than in organic suspensions, this discrepancy might be attributed to the differing characteristics of the solvents.

### 2.12.4 The Conductivity of the Suspension

The conductivity of the suspension is a key factor and needs to be considered in EPD experiments. Particle motion is extremely low when the suspension is too conductive, and when the suspension is too conductive, the particles charge electronically , and the stability is lost. Whereas the conductivity of the suspension increases with temperature and electrolyte (dispersant) concentration; however, not all conductivity values are useful for electrophoretic deposition, and a narrow band of conductivity range exists at varying dispersant dosage and temperature in which the deposit is formed. The forming possibilities are limited since the conductivity beyond this band is inadequate for EPD. This acceptable conductivity range, on the other hand, is likely to vary depending on the different systems. The applied current, on the other hand, can boost the conductivity zone suited, ensuring the EPD process' success [83].

## 2.13 Factors Related to the Operation

### 2.13.1 Applied Voltage

Normally, the amount of deposit increases with the increase in applied voltage. The increasing thickness from 60 V to 100 V was ascribed to the increase of the driving force. However, when the voltage was 120 V or higher, the thickness declined, and the density of the deposit deteriorated due to the violent bubble evolution. Besu's [88] work showed that a moderate electric strength (25–100$Vcm^{-1}$) always resulted in more uniform films. In contrast, a higher electric strength (>100 $Vcm^{-1}$) reduces the quality of the film as the deposition process is disturbed by the violent bubble evolution.

### 2.13.2 Deposition Time

A linear relationship is observed between deposition time and applied voltage at the initial deposition time. However, after a prolonged deposition time, the deposition rate will become slower and close to zero. Wang et al.[89] found the deposit weight of ZnO coating on copper initially increased proportionally by time, then attained a plateau after a certain time under constant voltage (20, 60 100 V). In contrast, the deposition rate remains constant under constant current [90].

### 2.13.3 Electron Transfer Kinetics of Substrate

In addition to the preceding parameters, the electron transfer kinetics of the substrate also influences the deposition rate. Hu et al.[91] found the deposition rate of gadolinium doped ceria (GDC) on PPy coated yttrium stabilized zirconia (YSZ) was slower than that on graphite when other parameters are fixed (Figure 2.17). In this suspension, the particles are positively charged because of the absorbed $H^+$ ions. The reduction of $H^+$ ions at the cathode is an electrochemical process that requires two stages, as indicated below:

$$H^+_{bulk} \xrightarrow{transport\ process} H^+_{surface} \xrightarrow{charge\ transfer\ process} \frac{1}{2}H_2$$

($H^+_{bulk}$ and $H^+_{surface}$) Denote the presence of $H^+$ ions in the suspension's bulk and near the cathode, respectively.

When the PPy coated YSZ was used as the cathode, the rate of charge transfer process was slower than that of the transport process and the reduction of $H^+$ ions was surface reaction controlled. In contrast, the reduction of $H^+$ ions was mass-transfer controlled when using a graphite cathode. Under the same constant voltage, the deposition rate on the graphite electrode was faster than that with the PPy coated YSZ both because of the latter electrode's higher resistance and its slower charge transfer kinetics for water reduction.

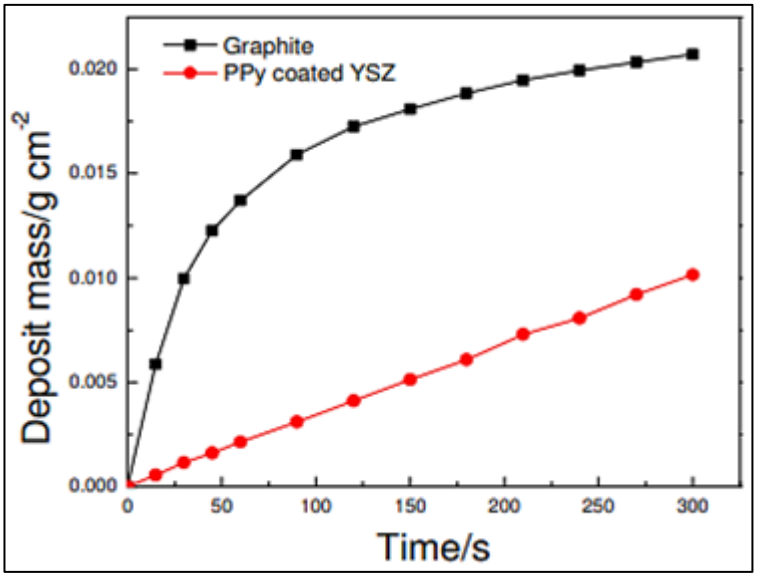


**Figure (2.17):** The Deposit Mass Per Unit Area as a Function of Time under Constant Voltage (60 V) [91].

## 2.14 Some Materials Used to Improve Coatings

### 2.14.1 Hydroxyapatite (HAp)

#### 2.14.1.1 Overview

Hydroxyapatite (HAp) is the calcium phosphate with the chemical formula $Ca_{10}(PO_4)_6(OH)_2$; it is one of the widely utilized bioceramics widely used as a biomaterial for bone replacement. HAp is appealing because of its biocompatibilities, osteoconductivity, noninflammatory and mechanical properties and wide application potential as bone fillers, bone tissue engineering scaffolds, implant coatings, soft tissue repair, and drug delivery systems. Hydroxyapatite accounts for the inorganic component of bone tissue by 60-70%. The mineral phase in human bone is composed of molecules consisting essentially of phosphorus and calcium with the molecular formula $Ca_{10}(PO_4)_6(OH)_2$ and belongs to the group of calcium phosphate compounds as shown in Figure (2.18)[92, 93].

This bioceramic is highly compatible with native bone due to its bio-mimicking characteristic properties. Several synthetic methods were extensively reported for the preparation of HAp. Although many synthetic methods have been developed for preparing HAp with specific

characteristics, it remains challenging because of the possibility of forming toxic intermediate products. HAp can be synthesized by the sol-gel method, hydrothermal reaction, co-precipitation reaction, and mechano-chemical methods[94].

**Figure (2.18):** HAp-Coated Femoral Stem of Hip Surgery Implants[94].

### 2.14.1.2 Crystal Structure of HAp

Hydroxyapatite (HAp) has a hexagonal crystal structure with the molecular formula $Ca_{10}(PO_4)_6(OH)_2$, and the structure of Hydroxyapatite nanoparticles (nanoHAp) has two distinct binding sites. For example, nanoHAp have negatively charged phosphate anions($PO_4^{3-}$) at both ends and positively charged calcium cations ($Ca^{2+}$) on the sides, as shown in Figure (2.19). HAp is an essential mineral for human bones, which consist of 70% low-crystalline or amorphous apatite, 30% collagen, and bone marrow cells[95].

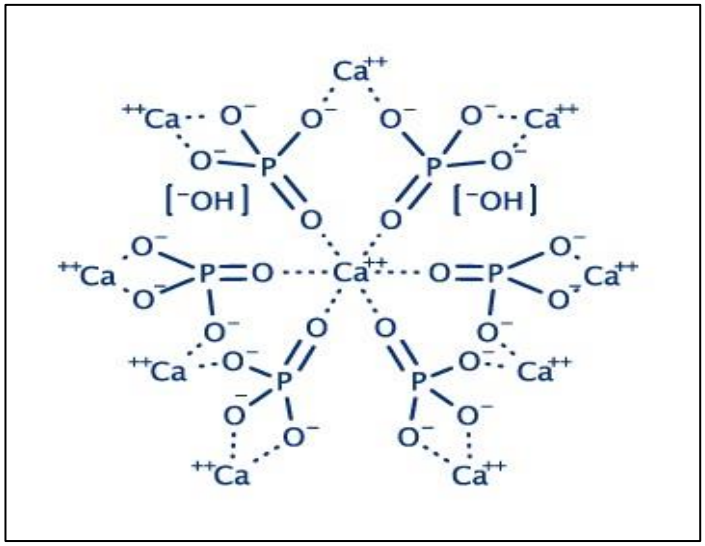

**Figure (2.19):** The Crystalline Structure of HAp [95].

### 2.14.1.3 Properties and Advantages of HAp

Table 2.10 presents the values published for the mechanical and physical properties of HAp, in addition to some advantages of HAp. The bending, compressive, and tensile strength values of HAp lie in the ranges 38–250, 120–900, and 38–300 MPa, respectively. The large scatter is due to many factors, such as the random strength distribution and the effects of residual microporosity, grain size and ion impurities. With increasing Ca/P ratio, the strength increases, reaches a peak at Ca/P of 1.67, and sharply decreases for Ca/P > 1.67. Young‘s modulus of HAp varies from 35 to 120 GPa, depending on the residual porosity and impurities. Dense HAp ceramics exhibit superplasticity at temperatures between 1000 and 1100°C due to grain boundary slip[96].

The mechanical properties of bone depend largely upon the humidity, mode of the applied load, the direction of the applied load and the location of the bone within the human body. Although HAp exhibits valuable properties as a biomaterial (regards biocompatibility, bioactivity, osteoconductivity, and direct bonding with bones), its mechanical properties are poor, as indicated by its poor fracture toughness ($K_{IC}$ is 0.7 to 1.2 MPa $m^{1/2}$). As a consequence, this severely restricts its field of

application in orthopaedics. However, it remains an excellent candidate for coating metallic prostheses or filling small bone defects[96,97].

**Table (2.10):** Principal Properties of HAp[96].

| Property | Value | Property | Value |
|---|---|---|---|
| Density | 3.16 g/$cm^3$ | Poisson's ratio | 0.27 |
| Decomposition temp. | >1000 °C | Fracture Energy | 2.3-20 J/$m^2$ |
| Dielectric constant | 7.40-10.47 | Fracture toughness | 0.7-1.2MPa.$m^{1/2}$ (decrease with porosity) |
| Thermal conductivity | 0.013 W/cm.K | Fracture hardness | 3-7 GPa (dense HA) |
| Melting point | 1614 °C | Biocompatibility | High |
| Tensile strength | 38-300MPa (dense HA) ~3MPa (porous HA) | Biodegradation | Low |
| Bending strength | 38-250 MPa (dense HA) 2-11 MPa (porous HA) | Bioactivity | High |
| Compressive strength | 120-900 MPa (dense HA) 2-100 MPa (porous HA) | Osteoconduction | High |
| Young's elastic modulus | 35-120 GPa | ----- | ----- |

### 2.14.1.4 Applications of HAp

The interaction between inorganic materials and protein molecules is of pivotal interest in biomaterials, biomineralization, biosensors, biochemistry, and industry. As mentioned earlier, HAp crystals have two binding sites, i.e. calcium cations ($Ca^{2+}$) and phosphate anions($PO_4^{3-}$), owing to their chemical composition and specific orientation. A description of some of the most important applications is given below[98, 99, 100]:

- ***HAp as a Coating Material***

  To restore a damaged bone, it is imperative to design a bone implanting material that can be used to cure the bone defect and reconstruct the bone. There are several difficulties in fabricating suitable bone implant materials. For example, the first difficulty commonly appears in synchronizing between the implanting material and bone during the bone remodelling process (resorption and

reparative process). The implanting material should not have any adverse effects on the immune system. However, the implanting materials sometimes resorb before the osteogenesis, rendering the material ineffective. In other cases, infections due to the implants result in disease and even death, which are very costly to the patient and society. Owing to these reasons, it is necessary to devise a way to design and fabricate suitable bone tissue regenerating implants[98, 101]

Recently, a technique was used where an implant is coated with a biocompatible and bioactive material to enhance the compatibility and bioactivity of the implanting material. The most common coating agent used is HAp. Furthermore, coating the implanting material surfaces (as titanium alloys) with HA enhances the osteointegration with bone.

- ***HAp as a Drug Delivery Carrier***

The rough surface and the "P" and "Ca" sites of HAp facilitate protein binding during the mineralization process. The importance of the rough surface has been confirmed by the interaction of amino acids with HAp. Use HAp nanorods /nanoparticles as a drug delivery carrier for various proteins (growth factors) and drugs. For example, the drug-loaded/modified HAp nanorods/nanoparticles were blended with a polymeric solution to carry the drug-loaded HAp to the target site[100].

- ***HAp-Based Composite Materials***

In most polymeric composites, HAp has been used as an enforcer to provide mechanical strength and bioactivity to the composite material. The importance of HAp in bone tissue regeneration has been reported extensively. Various researchers have fabricated HAp/polymer scaffolds as a drug delivery carrier, improved bone

tissue regeneration (grafting proteins and drugs on the surface of HAp) and treatment of various bone defects such as osteoporosis[98,99].

- ***HAp-Based Ceramics in Bone Tissue Regeneration***

  Due to the similarity between HAp and inorganic cement of natural bone, HAp has been used in pristine, composite, or ceramic forms for bone tissue regeneration. To achieve the desired goal (safe and satisfactory bone regeneration), the selected materials for an implant should have similar properties to those of natural bone. Several HAp bioceramics have been prepared to mimic natural bone. However, as mentioned above, the implants must provide an environment close to the natural one. For example, besides other factors, the implant must have a mechanical strength close to the bone[98, 100].

Besides its implanting material, HAp has been used in gene delivery, cancer therapy and as a bio-imaging tool. Gene therapy is a long-recognized promise for the treatment of a wide range of incurable diseases through the replacement of the missing or defective genes, catalyzing the destruction of cancer cells, causing the cancer cells to revert to normal tissue, promoting the growth of new tissue or stimulating regeneration of the damaged tissue. However, this promise remains unfulfilled, primarily since the lack of a safe and competent vehicle for the delivery of genes [98].

### 2.14.2 Graphene (Gr)

#### 2.14.2.1 Overview

A reinforcing material, such as graphene (Gr), has good mechanical capabilities and may be added to the HAp coating to make it appropriate for usage in the physiological environment of the body under high mechanical strain. Gr has also been reported to improve the HAp coating's

corrosion resistance. Composite coatings, such as HAp-carbon, are thought to provide a novel way to compensate for HAp's poor mechanical capabilities [102]. The features, properties and applications of graphene can be described below (Table 2.11).

**Table (2.11):** Comparison of Graphene and Carbon Nanotubes.

| No. | Graphene | Carbon nanotube | Ref. |
|---|---|---|---|
| **1.** | **Crystal Structure** | | 103, 104 |
| | Crystalline carbon materials, monolayers of 2D carbon atoms arranged in a honeycomb network, giant aromatic macromolecule in which each carbon atom is bound to three adjoining carbon atoms via two single and one double covalent bond, as shown in the figure below. 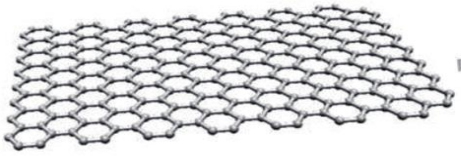 | In crystalline carbon materials, most of the physical properties of carbon nanotubes derive from graphene; carbon atoms are densely organized in a regular sp2-bonded atomic-scale honeycomb (hexagonal) pattern, and sp2 hybridization of carbon builds a layered construction with weak out-of-plane bonding of the van der Waals form and strong in-plane bounds as shown in the figure below. 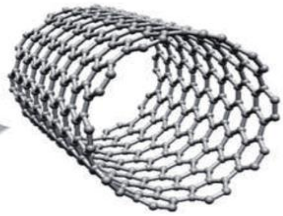 | |
| **2.** | **Properties** | | 105, 106 |
| | Gr is well-known for its exceptional mechanical properties, such as exceptional structural rigidity, a fracture strength of 130 GPa, an elastic modulus of 32 GPa. It exhibits high electrical conductivity ($10^4$ s/cm), ultra-high thermal conductivity (5300 W/mK), and excellent electron mobility (250,000 $cm^2$/Vs) at room temperature, where each carbon atom contributes to this system by one unbound electron freely moving through the crystal. The other | As far as the properties of carbon nanotubes are concerned, they vary depending on the conditions under which they are synthesized. The surprising properties of CNTs are due to their one-dimensional conductivity, high mechanical strength and high thermal conductivity. It has been observed that Young's modulus value for the MWCNTs is 1200 GPa as compared to the SWCNTs is 1054 GPa, and the | |

| | | | |
|---|---|---|---|
| | significant properties are a large specific surface area of 2630 $m^2$/g, the unusual carrier transport velocity which reaches up to 40 GHz, the charge carrier concentration of 1.4 × $10^{13}$ $cm^{-2}$, and a high-current carrying capacity of up to $10^9$ A/$cm^2$. Optical transmittance of 97.7% has confirmed these superior optical properties. | tensile strength value for the MWCNTs is 150 GPa which is a value similar to the SWCNTs. It has also been observed that the Electrical conductivity value for the SWCNTs is 1× $10^6$S/m and the density for MWCNTs is 2.6 (g/$cm^3$). All these properties largely depend on the structure of the carbon nanotubes. | |
| **3.** | **Advantages** | | 107 |
| | Excellent conductivity, fast charged carrier mobility, good mechanical strength, high optical transparency, good mechanical inertness, low toxicity toward human osteoblasts, excellent antibacterial properties and its potential to initialize apatite mineralization. | Large surface area, high electrical conductivity, and good chemical inertness. | |
| **4.** | **Limitations** | | 107 |
| | Low surface area arising from the easy aggregation, low quantities of defective sites. | Low quantities of defective sites. | |
| **5.** | **Applications** | | 106, 108 |
| | Bio-imaging, Drug delivery, Phototherapy, Combination therapy, sensors, and Tissue engineering, are the most important applications of graphene. | Electrochemical system applications, Applications in electric double layer capacitance, Applications of nanotubes in chemical sensors, Medicinal applications, Nanoporous membrane systems, Nanoprobes and sensors are the most important applications of carbon nanotubes. | |

### 2.14.3 Carboxymethyl Cellulose (CMC)

#### 2.14.3.1 Fundamental Structure of CMC

CMC is an anionic linear and long-chain compound that consists of glucopyranosyl units with a high molecular weight providing strength and structural integrity in biocoatings. CMC is the most important water-soluble cellulose derivative, with many applications in the food industry and the one that is produced in greater quantity on a commercial level; Figure 2.20 represents the Fundamental structure of the CMC[109].

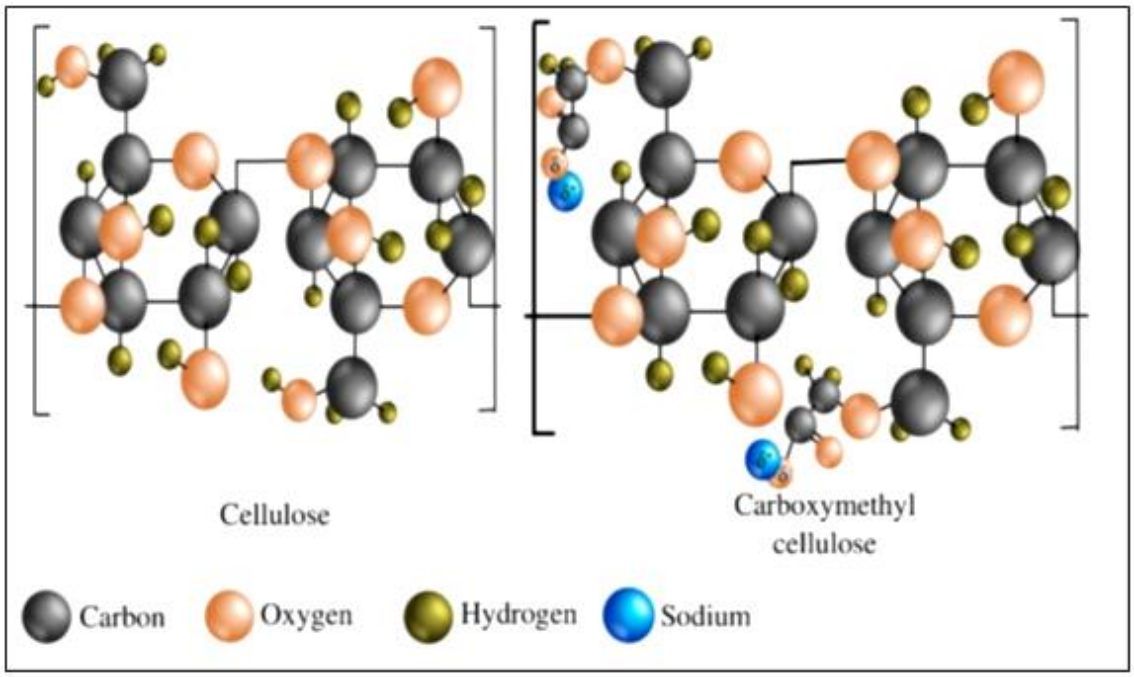


**Figure (2.20):** The Fundamental Structural Difference Between Cellulose and Carboxymethyl Cellulose (CMC)[110].

#### 2.14.3.2 Properties and Advantages of CMC

Different characteristics of CMC depend on its molecular weight, the number of carboxyl groups per hydroglucose unit and the distribution of the substituents along the polymer chains; below are some of the CMC Properties and Advantages[111].

1. CMC-based coatings have water binding and moisture sorption due to the abundant hydroxyl and carboxylic groups in CMC structure.
2. CMC hydrogel has high water content and could be applied as a filler owing to its polymeric structure and high molecular weight.

3. CMC coatings exhibit excellent oxygen, aroma and oil barrier properties, owing to CMC's tightly packed, ordered hydrogen-bonded network structure and low solubility.
4. CMC edible coatings show anti-senescence properties delaying the ripening process in some climacteric fruits.
5. The coatings are also applied onto the harvested fruits to provide barriers against gas exchange between fruit and environment, successfully utilized for adjusting oxygen and water transfer.

### 2.14.3.3 Applications of CMC

- ***Application in Textile Industries***

  CMC has recently been developed as a very effective thickening agent in paints and textile varnishes for its better water-absorbing property[112].

- ***Application in Food Industries***

  CMC is frequently used in the food industry as an auxiliary agent due to its excellent properties, such as being odourless, tasteless, noncaloric, physiologically inert, forming a clear solution without opacity [113].

- ***Application in the Water Treatment Process***

  CMC-based materials have been mainly used thus far for the removal of various organic-inorganic dyes, inorganic ionic pollutants (both anions and cations), and various radioactive species from polluted waters in different experimental conditions[113].

- ***Biomedical Application***

  Due to the characteristic surface properties for facile cell adhesion, low cytotoxicity, excellent biocompatibility, biodegradability, and cell viability, CMC materials have found a wide range of applications in the biomedical. CMC-based

biomaterials have been widely used in tissue engineering, wound dressing, bio-sensing, bioimaging, bone regeneration, drug delivery, and various biomedical technology fields. However, all of these fields are interrelated with each other[112, 113].

- ***Application of CMC in Pharmaceutical Industries***

  Among them, CMC and its derivatives (composite/ copolymer) have received ample attention for use in pharmaceutical products due to its properties such as biocompatibility, long half-life in vivo, high stability and drug binding capacity, pH-sensitivity (for the presence of carboxy group), and best reliable carrier[112].

### 2.14.4 Chitosan (CH)

#### 2.14.4.1 Fundamental Structure of CH

Chitosan has attracted great attention in many research fields as it is a biopolymer that contains linear amino polysaccharides of glucosamine and N-acetyl glucosamine units. Naturally, it is available with the following properties white, hard and inelastic. It is obtained by alkaline deacetylation of chitin extracted from the anthropoid exoskeletons, as well as from the cell walls of some fungi (Figure 2.21). Due to $–NH_2$ and –OH groups present in the structure, it is an effective biosorbent for various contaminants[114].

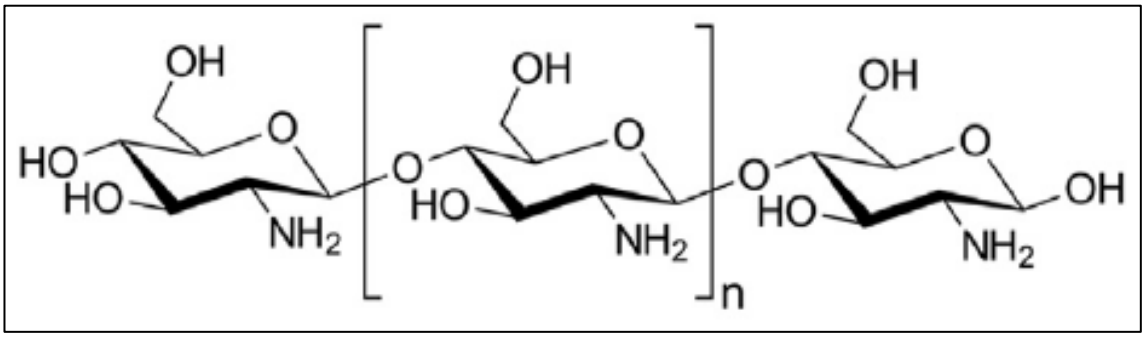


**Figure (2.21):** Chemical Structures of Biopolymer Chitosan[114].

### 2.14.4.2 Properties of CH

- ***Chemical Properties***

  Solubility in various aqueous media/solution viscosity, multifunctionality, polyelectrolyte behaviour, polyoxysalt formation, flexibility; ability to form gel, membrane, film, beads, etc.; metal chelation, optical properties[115].

- ***Biological Properties***

  Nontoxicity, biodegradability, biocompatibility, cytocompatibility, antimicrobial, antioxidant, anticholesterolemic, anti-inflammatory, analgesic, hemostatic, mucoadhesion, adsorption enhancer, granulation and scar formation[115].

### 2.14.4.3 Applications of CH

The applications of chitosan in the biomedical field can be shown below (Figure 2.22) [116].

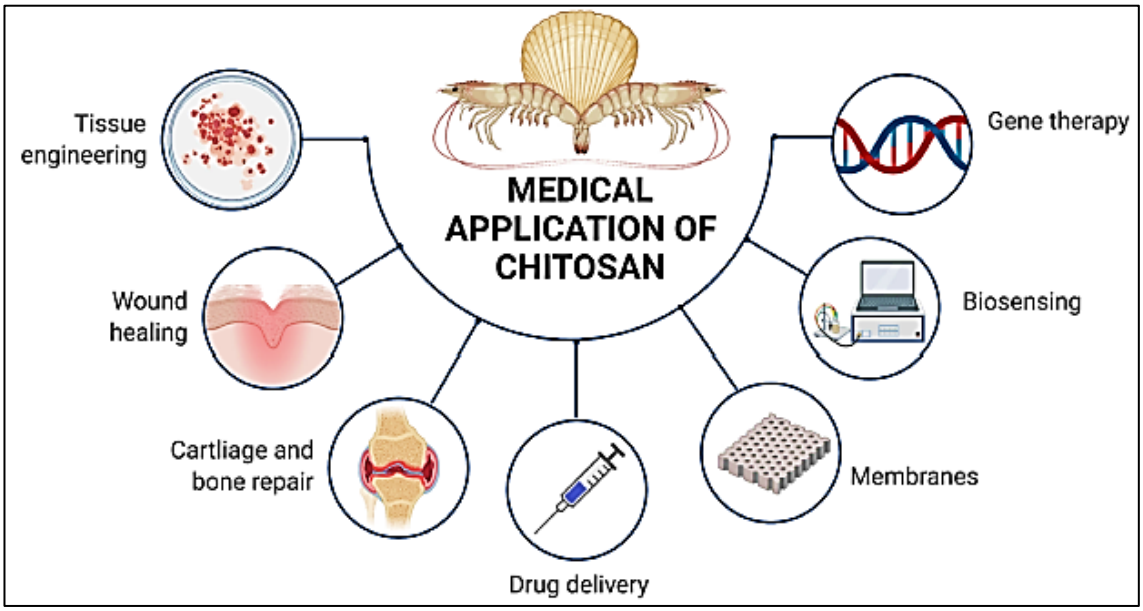


**Figure (2.22):** Schematic Diagram of Medical Application of Chitosan[116].

## 2.15 Literature Survey

The previous literature review revolved around the use of biocompatible coatings to improve the surface of the various bio-alloys used inside the human body, which studied the effect of coatings on the properties (biological, mechanical, physical and chemical) by using different coating parameters, type and method that make the implant better biocompatible.

So the literature review was divided into three Sections the first one was about using the same Ti-alloy used in this thesis (Ti-13Nb-13Zr) but modified with a different method, and the second section was about using the same surface modification (EPD) which used in this thesis on different alloy, the last section dealing with using the (Ti-13Nb-13Zr) and (EPD) method.

### 1. The (Ti-13Nb-13Zr) with a Different Modified Method

*In* ***2020 Kumar, P et al.*** **[117]** In this study, the near-beta Titanium alloy Ti–13Nb–13Zr was subjected to two different solutionizing temperatures (660°C and 900°C) and quenched ( water quenching and subzero quenching). Elastic modulus was decreased with an increase in cooling rate from solution temperature. The samples solutionized at 900°C and quenched at sub-zero temperature contained $\alpha^{=}$ martensite along with $\alpha^{-}$ and β phases, and these lowered the elastic modulus. Among all the heat-treated samples, the one solutionized at 900°C and quenched at sub-zero exhibited the lowest elastic modulus of 59 GPa and adequate tensile properties for the application as bioimplants.

*In* ***2020 Ossowska, A et al.*** **[118]** The purpose of this research was to characterize the effect of two-stage anodization performed for 30 min in phosphoric acid in the presence of hydrofluoric acid in the second stage Ti –13Nb–13Zr alloy. The research results demonstrate that two-stage oxidation affects several features and, in particular, improves mechanical

and chemical behaviour. The XRD results in both rutile and anatase appearance in the oxide layers. The nanoindentation tests show that the presence of nanotubular structure significantly increases hardness and Young's modulus and decreases plastic work. The contact angle measurements show an increase in wettability for both coatings, and the MTT assay revealed a bit higher number of bacteria on surfaces of coatings in second stage compared to the first stage and Ti–13Nb–13Zr.

*In **2021 Ja˙zd˙zewska et al.*** **[119]** analyzed the influence of laser modification (laser beam frequency f = 25 Hz and laser beam power P = 1000 W during a laser pulse with duration t = 1 ms) on mechanical and residual stress properties of the obtained surface layers for samples made of pure grade IV titanium and the titanium alloys Ti-6Al-4V and Ti-13Nb-13Zr. The obtained results showed increased values of tensile stresses after laser modification: the highest value was found for the Ti-6Al-4V alloy at 6.7434 GPa and the lowest for pure grade IV titanium at 3.742 GPa. After laser and heat treatment, a stress reduction was observed, with a significant increase in the hardness of the tested materials, with the highest value for Ti-6Al-4V alloy at 27.723 GPa.

*In **2021 Kumar, P et al.*** **[120]** investigated the effect of surface modification, imparted by ultrasonic shot peening (USSP) for different durations of 15–120s, on electrochemical corrosion resistance of the near β Ti-13Nb-13Zr alloy in Ringer's solution, at room temperature. By electrochemical impedance spectroscopy and potentiodynamic polarization tests. There was maximum passivation in the 30 s of USSP treatment, which decreased with an increase in USSP duration. The improvement in the corrosion resistance from USSP was due to grain refinement and the associated compressive residual stresses in the surface region.

*In **2022 Mao et al.*** **[121]** studied the influence of Cu content on the elastic modulus and antibacterial property of Ti-13Nb-13Zr-xCu (x = 3, 7 wt.%) alloys. The results have demonstrated that the antibacterial

performance and the elastic modulus were significantly improved, but the corrosion resistance deteriorated with increased copper content. Ti-13Nb-13Zr-3Cu with a low modulus of 73 GPa and an antibacterial rate of over 90% against Staphylococcus aureus (S. aureus) exhibited great potential as a candidate for implant titanium in the future.

## 2. The (EPD) Method with Different Alloys

*In 2018* ***Kadhim M. J et al.*** **[122]** The present work was designed on producing nanohydroxyapatite layers using electrophoretic deposition (EPD) on 316L stainless steel substrate. The EPD coatings were prepared by the deposition of hydroxyapatite (HA)-chitosan nanocomposites on different substrate roughness (polish surface, 220 grit SiC grind, and sand blast surfaces). Depositions were performed using the suspensions of HA nano particles (3 g/L) in the mixture of alcohol and distilled water (ethanol, 5 vol. %water and containing 0.5 g/L of chitosan dissolved in 1 vol.% acetic acid. Coatings were achieved on the cathode at constant voltage, time and temperature (90 V, 5 min and 40 °C respectively). The results showed the deposited coatings on sand blasted substrate has less porosity compared with the polish surface and 220 emery paper SiC grinding substrate respectively. The coating on the sand blasted substrate showed higher nanoroughness (122 nm), better adhesion bonding (removal area 15%) and higher thickness layer (12 µm) than that of the polish substrate and 220 emery paper SiC grinding substrate.

*In* ***2018 Fatih E. et al.*** **[123]** studied the improvement of the electrophoretic deposition (EPD) and suspension parameters for generating nanostructured PEEK-hydroxyapatite (HAp) coatings on 316L stainless steel substrates for biomedical application. The result shows that increasing the quantity of HAp enhanced bioactivity while lowering coating adhesion strength. After three days of incubation in simulated bodily fluid (SBF), apatite-like layer development was visible on coatings with a high HAp concentration.

*In **2020 Seungwan Ryu et al.*** **[124]** investigated the effect of the size of graphene oxide (GO) nanosheets (large GO (lGO): 20 ± 5 μm, medium size GO (mGO): 5 ± 3 μm, and small size GO (sGO): 1 ± 0.5 μm) on the anti-corrosion properties, three kinds of GO nanosheets were coated on the surface of two-dimensional (2D), steel (Fe) plates and 3D Fe rods via cathodic EPD processes. As the size of the coated GO sheets increased, a smoother and thicker coating layer was formed on the Fe plate, which resulted in better corrosion resistance. In addition, novel EPD equipment with multi-electrodes has been developed to coat GO sheets onto 3D metal structures. The sGO were coated on a 3D Fe rod using the EPD equipment with multiple electrodes, improving the corrosion resistance while maintaining the high electrical conductivity.

*In **2020 Shirin Khanmohammadi et al.*** **[125]** developed composite coatings of 75%(hydroxyapatite whiskers)WHA-25% (fine bioglass) FBG and 50%WHA-50%(coarse bioglass) CBG as precedent optimized compositions on anodized titanium substrate. An enhancement of 58% was obtained for the adhesion strength of FBG-based coating due to the interlocking of titania nanotubes with fine bioglass particles entering the voids of nanotubes, which was only 32% for CBG particles. The microstructure of the coatings demonstrated no changes by anodizing the substrate, while the thickness of the coatings reduced significantly owing to the decreased deposition kinetics. The enhancement of the bactericidal effect and cellular behaviour of the coatings indicated the positive impact of the underlaid nanotubes compared with bare titanium.

*In **2021 Abbass M. K. et al.*** **[126]** The aim of this work is to optimize EPD variables (voltage, time, and focus) using alternating current through the Taguchi Design of Experiment (DOE). Coating Nano hydroxyapatite (Nano-HA) on a Ti6Al4V substrate depends on thickness and roughness, then characterization of a coating layer to determine the optimum state.

Hydroxyapatite (HAp) powder was deposited on a Ti-6Al-4V alloy substrate by electro-deposition with ethanol as a solvent under AC current. The value of the optimum conditions for deposition of the HAp layer which is a simultaneous thickness and maximum coating mass, was predicted at a sedimentation voltage of 40 V, 2 min sedimentation time and 1 g / L for the concentration of the suspended solution at room temperature. In addition, close agreement was observed between the experimental results and the expected results. For the solution at room temperature, the results obtained with the highest value of the coating thickness of 41at the surface roughness of 0.94 and the contact angle of the alloy before coating is 67.489º reduced to. 38.132º after plating, which indicates an increase in the harmony of the metal implant and biocompatibility.

*In* ***2021 Ehsan Vafa et al.*** **[127]** investigated the properties of the composite coating (polyvinyl alcohol (PVA) reinforced natural chitosan (CH)/ bioactive glass (BG)) with different PVA concentrations (15, 20 and 25 wt.%) in the composite suspension on 316L stainless steel by using electrophoretic deposition (EPD) process. The result shows an increased corrosion resistance of 25 wt.% PVA of composite coating indicated more bio-stability of the composite coated in-vitro compared to 15 wt.% and 20 wt.% PVA composite coated. The decomposition rate of coats shows that the composite coating with 20 wt.% PVA coating is proposed as the best bioactivity and hydroxyapatite (HA) forming ability compared to 15 wt.% and 25 wt.% PVA coating. Likewise, the adhesive test indicates more adhesively in the composite with 20 wt.% PVA composite than others.

*In* ***2021 Filip Macia¸g et al.*****[128]** studied the effect of electrophoretic deposition parameters on the microstructure and adhesion of zein coatings to commercially pure titanium (CP-Ti) Grade 1 sheet substrate. It was found that the zein content and the ratio of water to ethanol of the solution used for EPD, as well as the process voltage value and time, significantly influence the morphology of coatings. The deposits

obtained from the solution containing 150 g/L and 200 g/L of zein and 10 vol % of water, and 90 vol % of ethanol, about 4–5 µm thick, were dense and homogeneous. The coatings showed the highest adhesion to the as-received and anodized substrates due to the presence of a thick $TiO_2$ layer on their surfaces and the presence of specific surface features. Coated titanium substrates showed slightly lower electrochemical corrosion resistance than the uncoated ones in Ringer's solution. The coatings showed a well-developed surface topography compared to the as-received substrate and demonstrated hydrophilic nature.

**3. The (Ti-13Nb-13Zr) Alloy was Modified Using (EPD) Method.**

*In* ***2017 Bartmanski, M. et al.*****[129]** focused on the determination of the effects of both EPD voltage for nanohydroxyapatite coating (15 and 30 V) and the decoration of nanoHAp coatings with nanosilver(60 V and a deposition time of 5 min) on the microstructure and physical, chemical, and mechanical properties of thin nanoHAp coatings for Ti-13Zr-13Nb alloy. The thickness of the undecorated coatings was found to be 2.16 and 5.14 µm for applied EPD voltages of (15 and 30V), respectively. The release rate of silver nanoparticles into an artificial saliva solution increased with exposure time and EPD voltage. The corrosion current, between 1 and 10 nA/$cm^2$, was significantly higher for undecorated nanoHAp coatings and close to that of the substrate for decorated nanoHAp coatings. The hardness of the undecorated nanoHAp coatings obtained at 15 and 30 V of EPD voltage attained (0.2245 ± 0.036 and 0.0661 ± 0.008 GPa), respectively.

*In* ***2018 Moskalewicz, T. et al.*****[130]** investigated the microstructure and coating properties for Electrophoretic Deposition of Composite Alumina/Polyetheretherketone ($Al_2O_3$/PEEK) Coatings on the Ti-13Nb-13Zr Alloy. Scanning and transmission electron microscopy investigation of the coating microstructure revealed the presence of uniformly distributed $Al_2O_3$ and their agglomerates within the PEEK matrix. Micro-scratch tests

indicated that the coatings are characterized by excellent adhesion to the substrate. The $Al_2O_3$/PEEK coatings significantly improved the wear resistance and reduced the coefficient of friction of the Ti-13Nb-13Zr alloy during dry sliding compared with a polymer PEEK-coated alloy. The coatings increased the corrosion resistance of the alloy in Ringer's solution. The coatings were also found to be cytocompatible with MG-63 osteoblast-like cells.

*In* ***2020 Singh et al.*****[131]** investigated the Ti-13Nb-13Zr alloy was electrophoretically coated (EPD) with pure hydroxyapatite (HA), pure iron oxide ($Fe_3O_4$) and HA-$Fe_3O_4$-chitosan (Cs) coatings by altering the concentration of $Fe_3O_4$ at three different levels (1, 3 and 5 wt%). The morphology of the composite coating indicated porous nature with an average 10 ± 0.2 μm coating thickness, which was examined by scanning electron microscopy (SEM). The HA-1wt% $Fe_3O_4$ composite coating exhibited the preeminent corrosion resistance with the lowest $I_{corr.}$ and the highest $E_{corr.}$ value as a contrast to HA-3wt% $Fe_3O_4$ and HA-5wt% $Fe_3O_4$ coatings. Additionally, in vitro bioactivity test found that the composite coating enhanced the apatite formation ability, and the composite HA-Cs bioactive coating incorporated with $Fe_3O_4$ is a promising candidate for biomedical applications.

### 2.14.1 Summary of Literature Survey

The following Table (2.12) summarizes the closest literature to the thesis using the (Ti-13Nb-13Zr) alloy modified by the (EPD) method.

**Table (2.12):** Summarizes the Materials, Solutions, Parameters, and Sintering Circumstances Utilized in the Closest Literature to the Thesis.

| No. | Authors | Coating materials | Solution suspension | Coating parameters | Sintering treatment | Ref. |
|---|---|---|---|---|---|---|
| 1 | ***Nabeel, M. (thesis)*** | nanoHAp, nanoGr and nanoCMC | Ethanol | 40 V and 60s | avoidance sintering step because the composite coating was stable, and no change was found in XRD patterns. | \\ |
| 2 | ***Bartmanski, M. et al.*** | nanoHAp + nanosilver | Ethanol | (15 and 30 V) for nanoHAp and (60 V and a deposition time of 5 min) for nanosilver | 800 °C for 120 min | [129] |
| 3 | ***Moskalewicz, T. et al.*** | Alumina/ Polyetherether ketone ($Al_2O_3$/PEEK) | Ethanol | The voltage of 30, 40, 50, 60, and 70 V was applied and the deposition time of 10, 20, 30, 40, 50 and 60 s | 20 min at a temperature of 350◦C | [130] |
| 4 | ***Singh, S. et al.*** | hydroxyapatite (HA), pure iron oxide ($Fe_3O_4$) and HA–$Fe_3O_4$–chitosan (Cs) | Ethanol | 15 V and 6 min | without | [131] |

# CHAPTER THREE

# Experimental Work

# CHAPTER THREE
## EXPERIMENTAL WORK AND PROCEDURE

## 3.1 Introduction

This chapter will explain all of the materials utilized in this project to make composite materials through EPD-Coating, as well as their properties and the technique for specimen preparation, testing, and assessment. The experimental portion of this research involves the selection of bioceramic and biopolymeric materials for use in the EPD process, as well as the base alloy, specimens, and suspended preparation, as well as a discussion of the EPD - coating method, apparatus, and conditions. A flow diagram of the current work is shown in Figure 3.1.

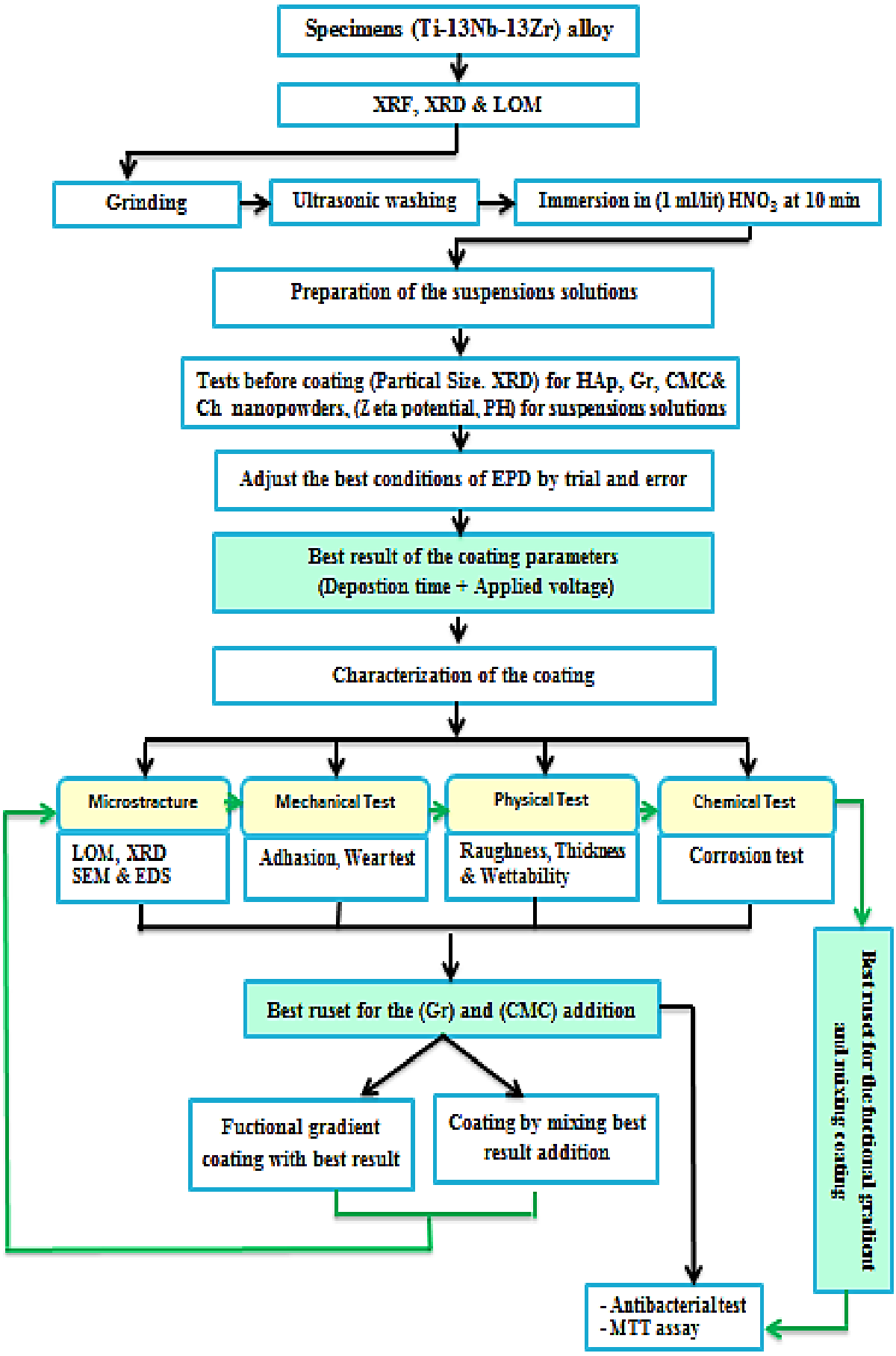


**Figure (3.1):** Flow Chart of the Procedure Used in this Work.

## 3.2 Materials used

### 3.2.1 Base Alloy

Table 3.1 illustrates the chemical composition of Ti-13Zr-13Nb alloy used in the study. The chemical analysis was carried out using X-Ray Fluorescent (XRF) test available in the Ministry of Science and Technology in Baghdad- Iraq.

**Table (3.1):** Chemical Composition(wt%) of Ti-13Zr-13Nb Base Alloy.

| Elements | Concentration (%) |
|---|---|
| **Zr** | **15.22** |
| **Nb** | **13.45** |
| **Fe** | 0.1155 |
| **Mo** | 0.077 |
| **Zn** | 0.0527 |
| **Mn** | 0.0387 |
| **Cu** | 0.0432 |
| **Ti** | **Balance** |
| **Residual Element** | 0.13505 |
| **Sum of Concentration** | 100% |

Light optical microscope (LOM) have been used to get the microstructure of the etched specimens. The specimens have been etched ( the Kroll's solution prepared as etching solution of 10 ml HF, 15 ml $HNO_3$ and 75 ml $H_2O$) [132] to reveal the grain boundaries in the microstructure. Pores of different size are irregular but have been rounded. The most common types of features in the microstructure in metallic materials are the boundaries between crystalline grains and /or the boundaries between different solid phases in multiphase alloys.

The metallography can give a simplified idea about the relationships between the microstructure of the material and the microscopic properties because the size and the shape of grains have a direct effect on the behavior of the material. The microstructure reveals that Ti-13Nb-13Zr alloy consist mainly of one phase (β) and a little bit of the (α) phase. Where

it is considered an alloy (near-β) structure at room temperature as shown in Figure (3.2).

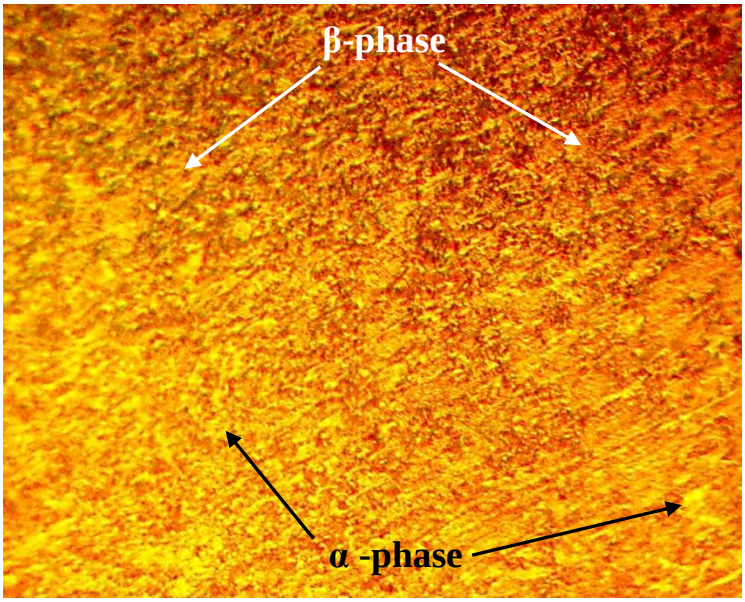


**Figure (3.2):** Microstructure for Ti-13Nb-13Zr Alloy.

### 3.2.2 Suspension Materials

The particle size distribution of (Hydroxyapatite, Graphene, and CarboxyMethyl Cellulose) was determined using Bettersize2000 laser particle size analyzer (Bettersize instrument Ltd) illustrates in Table 3.2. which is located in the laboratories of the department of Ceramics and Building Materials /Faculty of Material Engineering/ University of Babylon.

**Table (3.2):** Chemical Analysis of Suspension Materials.

| No. | Main component | Purity % | Average Particle size (nm) |
|---|---|---|---|
| **1.** | Hydroxyapatite $Ca_{10}(PO_4)_6(OH)_2$ | 99.89 | 44.701 |
| **2.** | Chitosan (CH) | 99 | 57.16 |
| **3.** | Graphene (Gr) | 99.9 | 28.94 |
| **4.** | CarboxyMethyl Cellulose (CMC) | 98 | 488.3 |

Figures (3.3), (3.4), (3.5), and (3.6) illustrated the XRD patterns for (Hydroxyapatite, Chitosan, CarboxyMethyl Cellulose and Graphene) powders respectively. The shown patterns matched to the standard patterns for mentioned powders [133,134,135,136] .

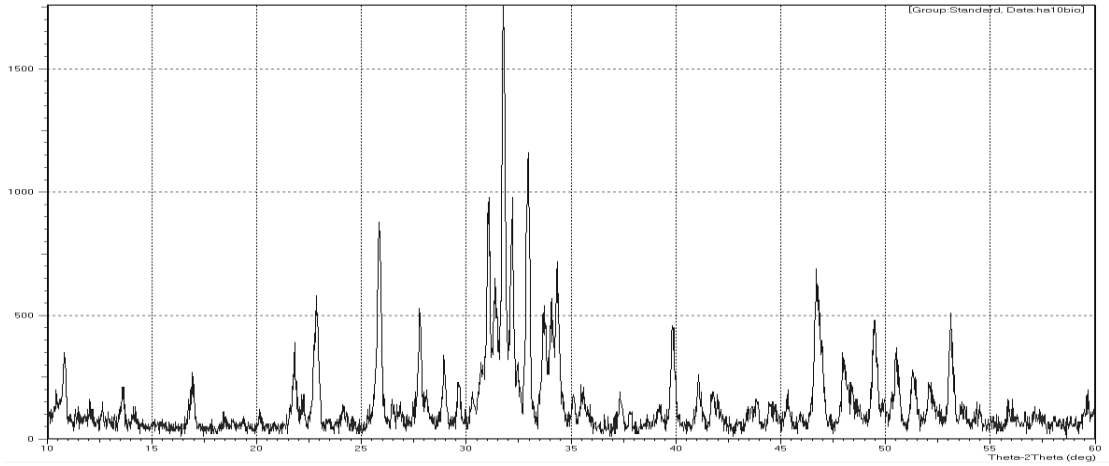


**Figure (3.3):** XRD Patterns for Hydroxyapatite (HAp) Powder.

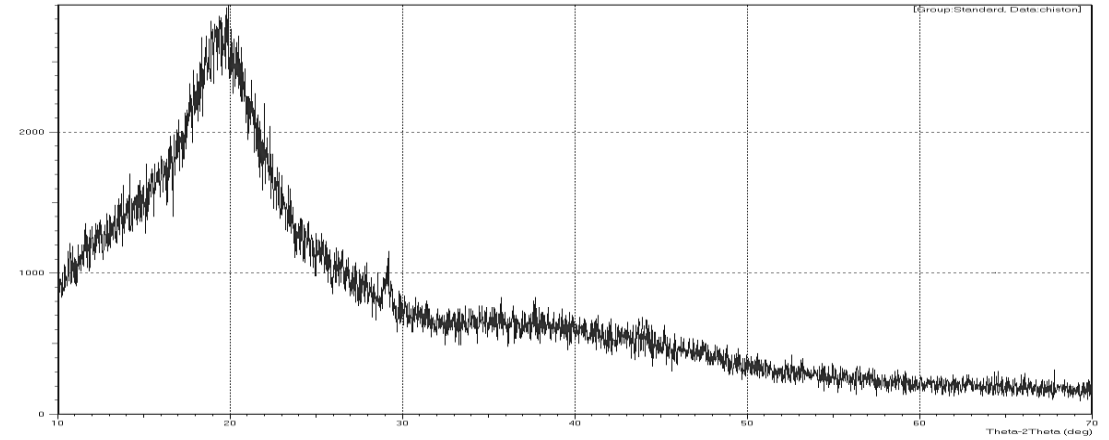


**Figure (3.4):** XRD Patterns for Chitosan (CH) Powder.

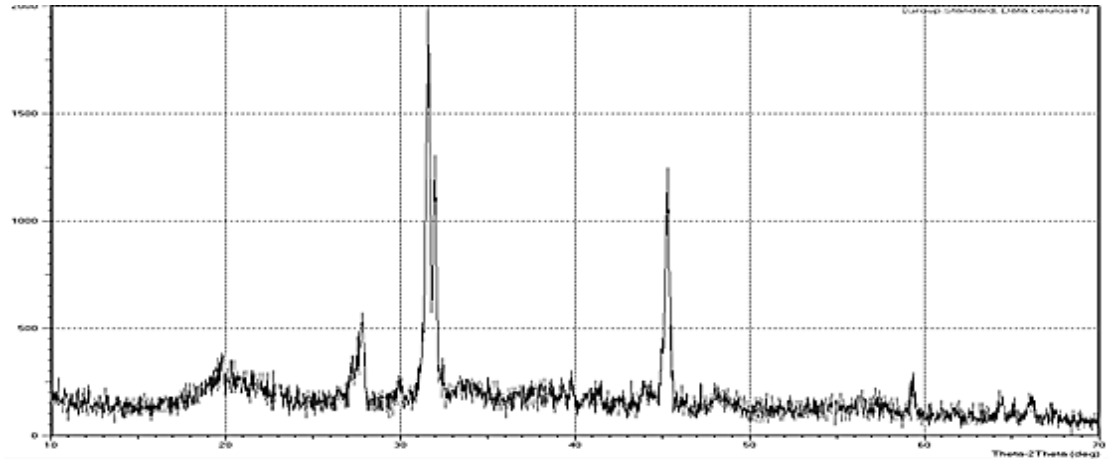


**Figure (3.5):** XRD Patterns for CarboxyMethyl Cellulose (CMC) Powder.

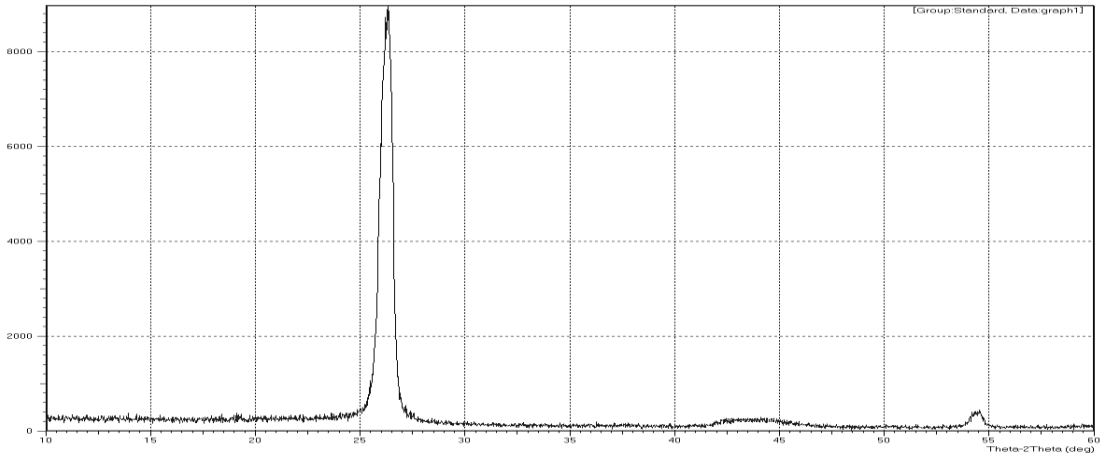


**Figure (3.6):** XRD Patterns for Graphene (Gr) Powder.

## 3.3 Suspension Preparations

Suspension solutions were prepared as follows:

a) HAp-Suspension solution

Chitosan (0.5 g/L) was dissolved in 1 % acetic acid and stirred at room temperature for 24h (solution 1). HAp solution was prepared by dissolving HAp nanoparticles into (ethanol with purity >99%) by stirring at room temperature with constant amount of (5) vol% for 60 min (solution 2). After that, (solution 1) was gently added to (solution 2) and add (1 ml/lit) percentage of nitric acid ($HNO_3$) used as a dispersant agent and the mixture was magnetically stirred for 24h followed by 20 min ultrasonication step (solution 3) (Figure (3.7)).

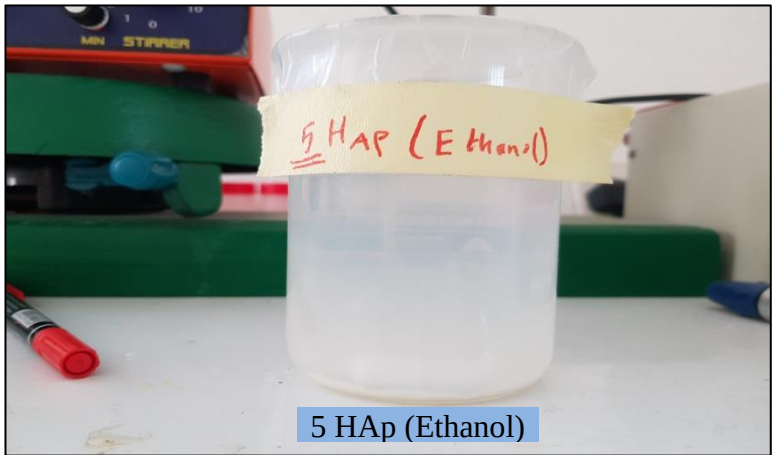


**Figure (3.7):** Solution 3, HAp-Suspension Solution.

b) (HAp-Graphene)-Suspension solution

Different amount of (0.08, 0.2, 0.5 and 1 g/L) from Graphene nanopowder was slowly added to (solution 3) and the mixture was magnetically stirred for 24h followed by 20 min ultrasonication (solution 4) (Figure (3.8)).

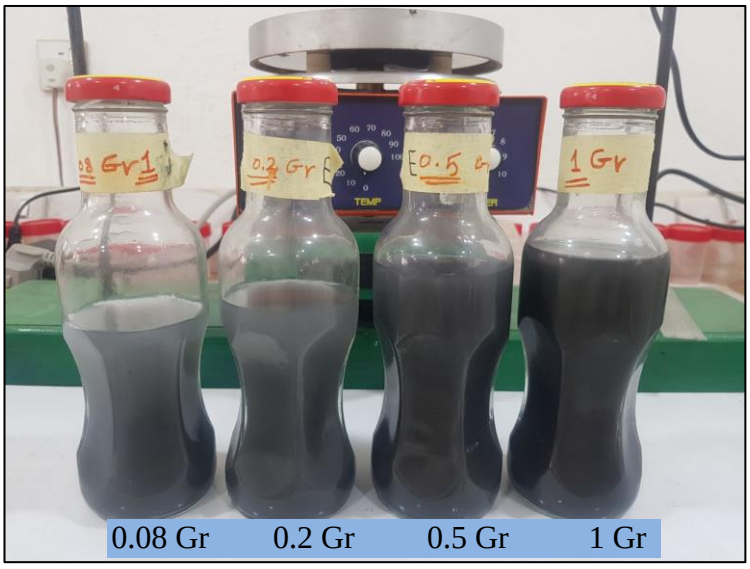


**Figure (3.8):** Solution 4, (HA-Graphene)-Suspension Solution.

c) (HAp- CarboxyMethyl Cellulose)-Suspension solution

Since CarboxyMethyl Cellulose is an insoluble polymeric substance in ethanol as the ubiquitous solvent for EPD, it was not possible to directly add CMC to the solution. Therefore, at first, different amount of (0.08, 0.2, 0.5, and 1 g/L) from CMC was resolved in 1ml distilled water by stirring for six hours until the solution became transparent as shown in Table (3.3), and at the end, CMC was completely mixed with (solution 3) and the mixture was magnetically stirred for 24h with 5min ultrasonication per hour (solution 5) (Figure (3.9)).

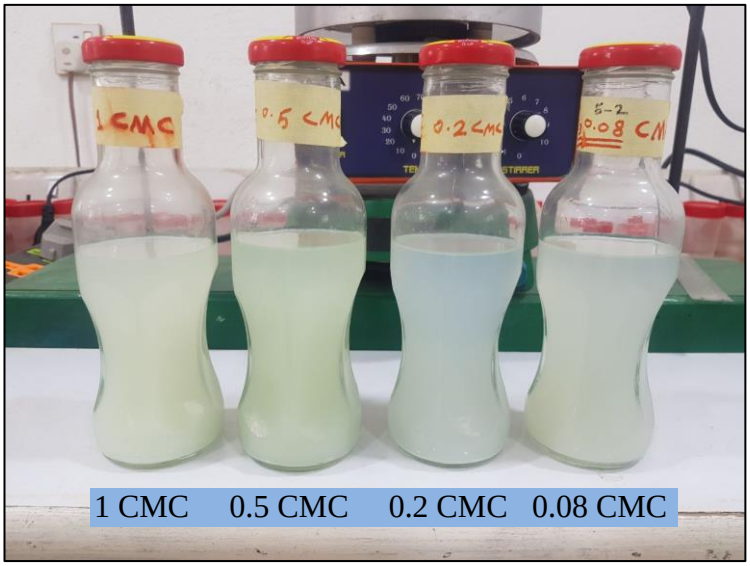


**Figure (3.9):** Solution 5, (HA- CarboxyMethyl Cellulose)-Suspension Solutions.

d) (HA-CMC-Gr)-Suspension solution

One of the percentages of the better material (0.08, 0.2, 0.5, or 1 g/L ) from ( Gr or CMC) is added to different percentages of the worst materials (0.08, 0.2, 0.5, and 1 g/L) from (Gr or CMC), Where a percentage (0.2 g/L) of graphene was added to (solution 5) in different percentages and the mixture was magnetically stirred for 24h followed by 20 min ultrasonication step (solution 6) (Figure (3.10)).

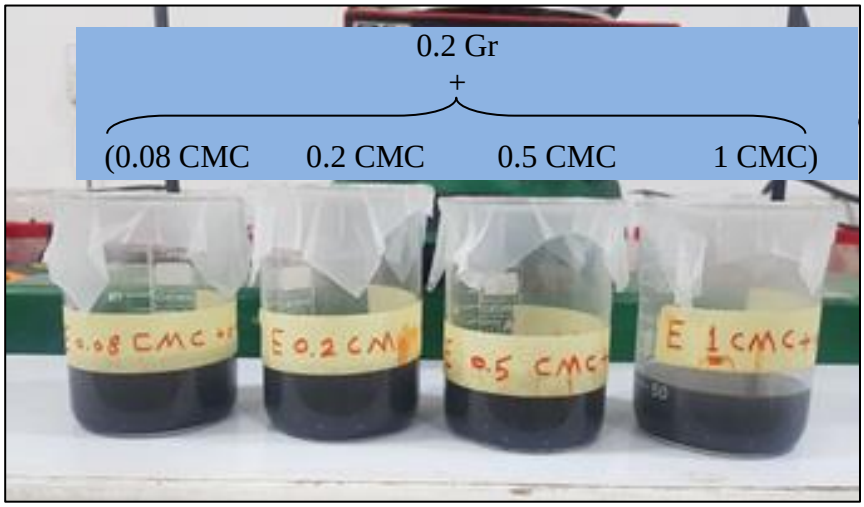


**Figure (3.10):** Solution 6 (HA-CMC-Gr)-Suspension Solutions.

**Table (3.3):** The main Components of Each Suspension Solutions Used in the EPD Coating.

| NO | Component coating | HA (g/lit) | Chitosan (g/lit) | Gr (g/lit) | CMC (g/lit) | Distilled water (ml) |
|---|---|---|---|---|---|---|
| a) | HA | 5 | 0.5 | - | - | - |
| b) | HA-Gr | 5 | 0.5 | (0.08, 0.2, 0.5 & 1) | - | - |
| c) | HA-CMC | 5 | 0.5 | - | (0.08, 0.2, 0.5 & 1) | 1 |
| d) | HA-CMC-Gr | 5 | 0.5 | 0.2 | (0.08, 0.2, 0.5 & 1) | 1 |

To achieve a homogeneous dispersion of the particles, all solutions above, aged for 24hr at room temperature to allow fully charging of particles dispersed to produce a stable suspension. Before use, the suspension was stirred for another 20min.

The Table (3.4) below shows the codes for each of the additives percentage used in this thesis to be used in discussing the results.

**Table (3.4):** Codes, Coating Material and Proportions for Each Additive Used.

| Sample Code | Material of coating | percentage of coating material (g) |
|---|---|---|
| **B** | Base without coating | ---- |
| **H** | Hydroxyapatite (HAp) | 5 |
| **$G_1$** | HAp-Graphene (Gr) | 0.08 |
| **$G_2$** | HAp-Graphene (Gr) | 0.2 |
| **$G_3$** | HAp-Graphene (Gr) | 0.5 |
| **$G_4$** | HAp-Graphene (Gr) | 1 |
| **$C_1$** | HAp-Carboxymethyl cellulose (CMC) | 0.08 |
| **$C_2$** | HAp-Carboxymethyl cellulose (CMC) | 0.2 |
| **$C_3$** | HAp-Carboxymethyl cellulose (CMC) | 0.5 |
| **$C_4$** | HAp-Carboxymethyl cellulose (CMC) | 1 |

| | | | |
|---|---|---|---|
| **Ternary coating** | **$M_1$** | HAp- (Gr + CMC) | (0.2 + 0.08) |
| | **$M_2$** | HAp- (Gr + CMC) | (0.2 + 0.2) |
| | **$M_3$** | HAp- (Gr + CMC) | (0.2 + 0.5) |
| | **$M_4$** | HAp- (Gr + CMC) | (0.2 + 1) |
| **F** | | Functional Gradient HAp- Graphene (Gr) | 0.08 Gr<br>0.2 Gr<br>0.5 Gr<br>1 Gr<br>Base |

## 3.4 Specimens Preparations

a) The Ti-13Zr-13Nb alloy was used as test specimens in this study, This specimens were cut into dimension of (13 diameter * 5 mm thickness) by wire cutting machine (Figure 3.11) at University of Technology/Baghdad as shown figure (3-2). Figure (3.12) shows the dimensions of the specimens used in EPD coating, it was prepared up to 200-250 samples for the purpose of conducting coating process.

**Figure (3.11):** Wire Cut Machine.


**Figure (3.12):** Dimensions of the Ti-13Zr-13Nb Specimen.

b) Because of the high sensitivity and accuracy of the electrophoretic deposition process, the specimens used in this process were abraded using silicon carbide (SiC) papers (180–1000 grits) and washed completely with distilled water and, then pure acetone, followed by ultrasonically cleaned with acetone for 20 min. Then it was immersed in a solution of (5 ml) of nitric acid ($HNO_3$) for 10min and finally, washing specimens distilled water and dried with hot air.

c) The samples were weighted before and after coating process. The deposit yield (deposit mass per unit area) was determined knowing the area of the deposit for (13 diameter * 5 mm thickness) , as shown in Equation 3.1.

$$W_d = (w_c - w_o) / A \quad \ldots\ldots\ldots\ldots\ldots\ldots 3.1$$

Where:

$\boldsymbol{W_d}$ **:** Weight of Deposition

$\boldsymbol{w_o}$ **&** $\boldsymbol{w_c}$ **:** Represent the weight of the uncoated and coated substrates respectively.

**A:** Represents the deposit area,

## 3.5 Experimental Procedure for EPD

a) A Ti-13Zr-13Nb alloy was used as a cathode electrode and counter electrode (stainless steel 316L) as an anode. The counter electrodes were washed with acetone and then dried.

b) The electrodes were immersed vertically in a 50 ml beaker containing the suspension. The distance between the electrodes in the EPD cell was kept constant at10mm.

c) The EPD was performed with different deposition times and voltages, (which are explained in Chapter four) using DC-Power supply (S-1500-150, Freq:50HZ±20%, DC OUT: 150V 10A, China) ( Figure 3.13).

d) HA-Gr-Chitosan, HA-CMC-Chitosan, and HA-Gr-CMC-Chitosan composite were deposited on Ti-13Zr-13Nb alloy by EPD at room temperature. After the termination of the EPD process, a jack was used to slowly lower the suspension and remove the coated electrode out of suspension in order to prevent the detachment of the wet deposit.

e) The samples were dried 24 hours in atmosphere after the completing EPD process.

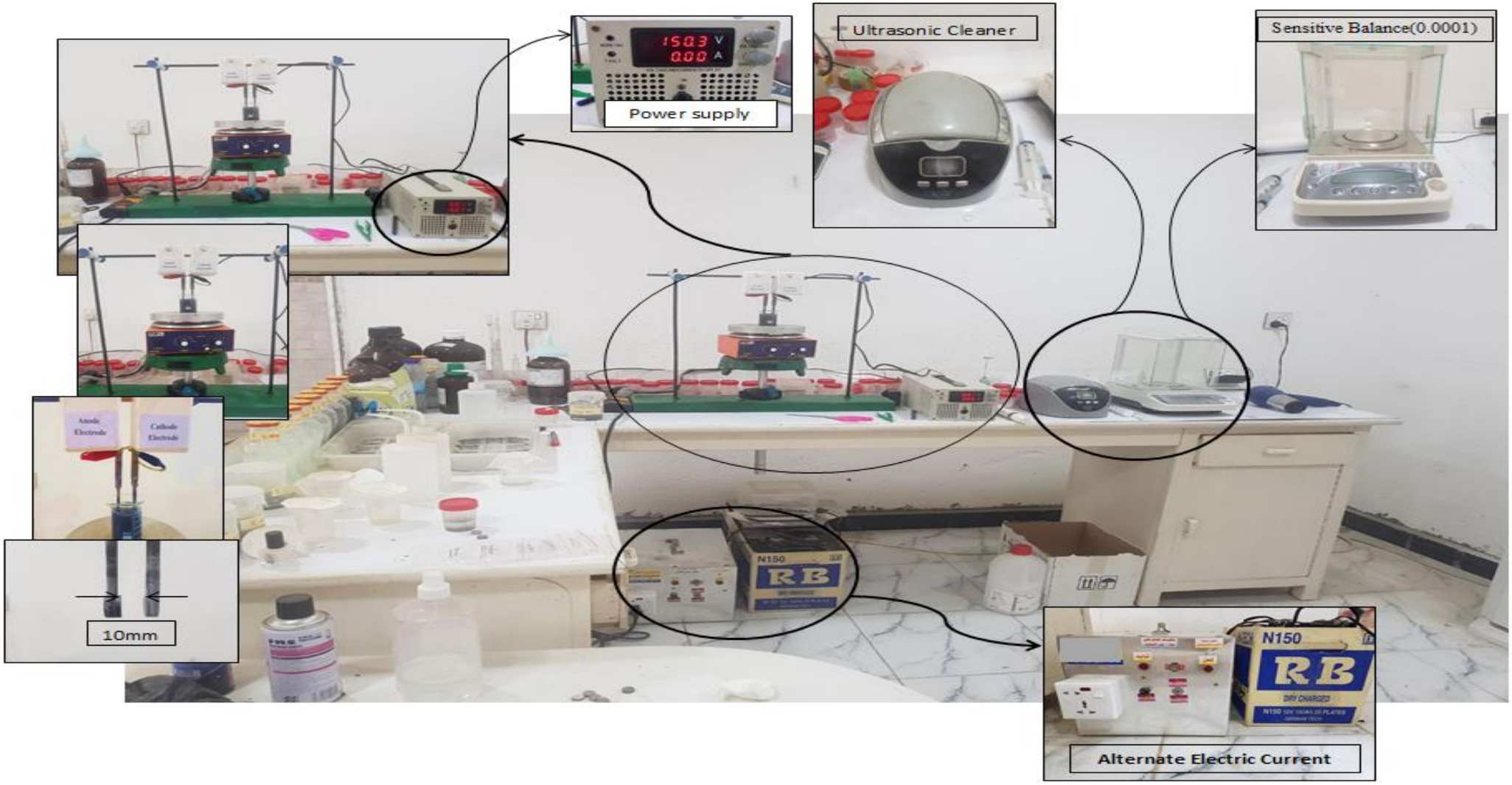


**Figure (3.13):** Shows the Devices Used in the EPD Coating.

## 3.6 Test and Characterization

### 3.6.1 Light Optical Microscope (LOM)

The microscopic structure was studied using optical microscopy in order to identify the existing phases and to see the shape and size of the grains, after grinding, polishing, and etched in a solution (swab) for base substrate before coating, coating thickness (cross-section), wear test results and after corrosion test. After coating, visual observation is considerably a serious and important step to evaluate the produced layer from EPD operation. However, visual observation results are confirmed using a light Optical microscope, It is also considered as the basic evaluation for that all samples which did not result in satisfactory coating layers were disregarded by LOM. While work continued on those samples considered to be satisfactory  This test was done at specimens preparation laboratory, the microscope is type (BEL PHOTONICS). Located in the Laboratories of the Department of Metallurgical - University of Babylon (Figure 3.14).

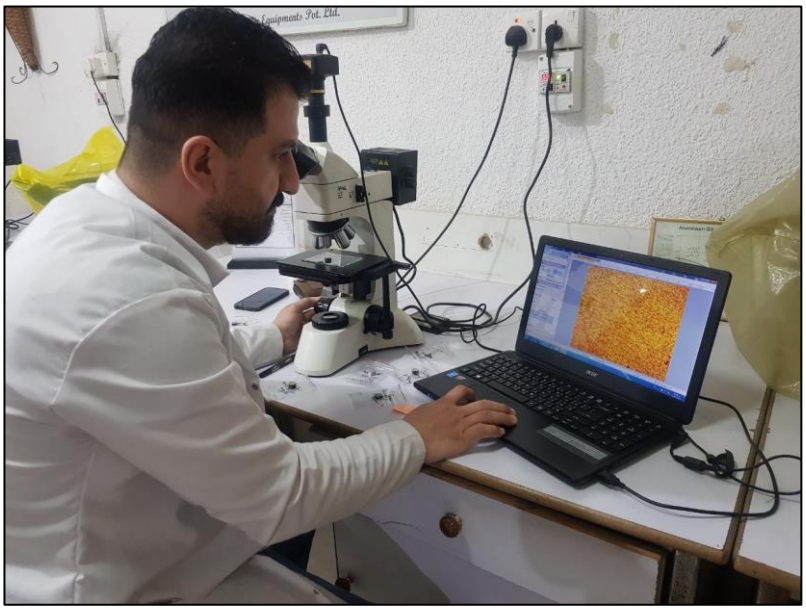

**Figure (3.14):** Light Optical Microscope (LOM).

### 3.6.2 Field Emission Scanning Electron Microscopy (FESEM)

For the purpose of obtaining surface morphology, a field emission scanning electron microscope (FESEM) was used. The sample is imaged

through a high-pack of electrons. An Energy Dispersive X-ray Spectrometry (EDX) detector combined with FESEM was employed to detect the elemental distribution of the selected liners in the FESEM image. The samples were coated with a gold layer of around 15 nm (model Q150T, QUORUM) before the observation to avoid sample charging during imaging. This test was done in University of Tehran (Amirabad)/ Iran by using FESEM type (TESCAN Mira 3) (Figure (3.15)).


**Figure (3.15):** Scanning Electron Microscopy.

### 3.6.3 X-Ray Diffraction (XRD)

The XRD test was conducted at University of Tehran (Amirabad)/ Iran (type XRD-PW1730 philips/ USA) as shown in Figure (3.16), where the phase purity present in the coating was tested by X- Ray diffraction (XRD). The diffractograms were gained by utilizing a X-ray diffract meter. The XRD generator with Cu aim at 40 KV and 30 mA, scanning speed (5°) per minute was used. The scanning. rate was (10 – 80).


**Figure (3.16):** X- Ray Diffraction Type XRD-PW1730/ Philips.

### 3.6.4 Zeta Potential

In order to ensure the homogeneity of the coatings and the stability of the suspensions, they were studied in terms of zeta potential. Laser Doppler Velocimetry (LDV) procedure was used to calculate Zeta prospective and electrophoretic movement (Brookhaven Instruments, Center of Nano Technology and Advanced Materials, University of Technology). Prior to zeta latent measure, the suspensions were magnetic and ultrasonicated stirred for 10 min.

### 3.6.5 The Wettability

The hydrophobicity or wet-ability for the coated and uncoated samples of Ti-13Nb-13Zr alloy were measured using the contact angel (θ) of droplet on solid surface used Hank's solution, which is an important index to quantitatively evaluate the wettability of solid surface ,the optical contact angle equipment type CAM 11O-O4W (Figure (3.17)) which was attached with CCD camera was used to measure contact angle, and the contact angle measurement was taken immediately after the droplet was placed on the solid surface by a 1 μL pipettor. In individual contact angle

measurements between each test liquid and each solid surface, each contact angle was measured 3 times.

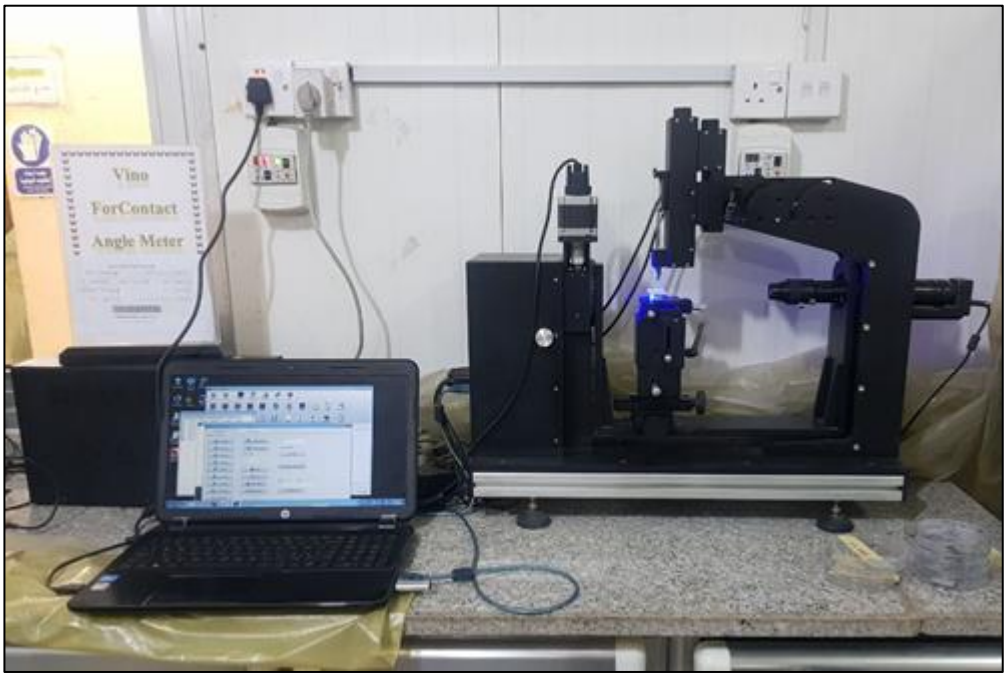


**Figure (3.17):** Contact Angle Measurement Device.

### 3.6.6 Adhesion Test

Coating adhesion to the implant surface plays an important role in medical applications, especially for long-term use purposes. To measure the adhesion strength between the coating and the alloy substrate, pull-off test was conducted according to the ASTM-D4541 standard as shown in Figure (3.18) located in the Metallurgical laboratory in the Laboratories of the Department of Metallurgical Engineering - University of Babylon, for the samples coated with HAp, HAp-CMC, HAp-Gr, HAp-CMC-Gr and FG. Also, this test was conducted after immersing the coated samples in Hank's solution for the purpose of simulating the hostile environment of the human body. Specimens coated are immersed in small plastic containers with 100mL of Hank's solution Table (3.5), these smaller containers are immersed in a larger container containing water at 37°C (±2) for (1, 3, and 6) days with a continual electric current for the duration of the immersion as shown in Figure (3.19).

**Figure (3.18):** Pull-off Device.

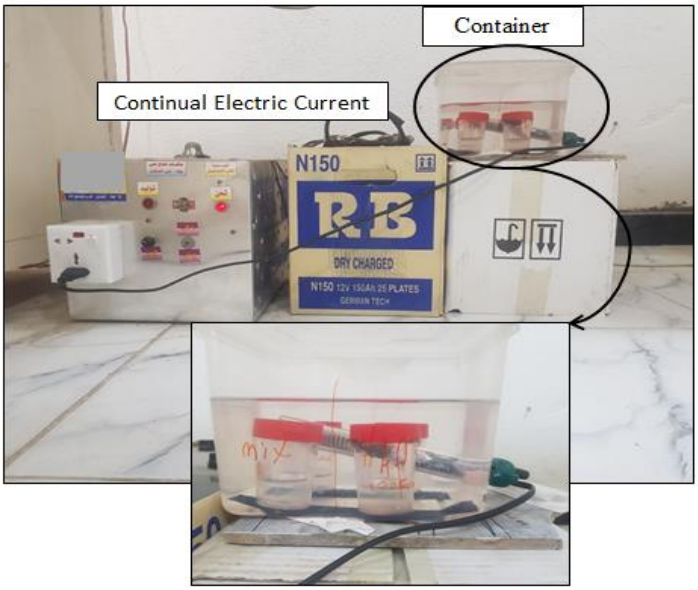


**Figure (3.19):** The Incubator to Keep the Temperature at 37˚C(±2).

## 3.6.7 Corrosion Test

### 3.6.7.1 Electrochemical Test

Because of the importance of the Ti and its alloys and their use as an implants within the human body, corrosion tests should be done on specimens to determine the behavior of corrosion of specimens in the human body. The electrochemical evaluation of the corrosion behavior of Ti-13Zr-13Nb alloy with the HAp, HAp-Gr, HAp-CMC, HAp-Gr-CMC, and FG coating in addition to the uncoated substrates was performed, this test was done in Corrosion Laboratory in the Laboratories of the

Department of Metallurgical Engineering - University of Babylon. In this test was used Hank's solutions is illustrated in Table (3.5) [137]. The pH of Hank's solution at 37±2°C was 7.4.

**Table (3.5):** Chemical Composition of Hank's Solution [137].

| No. | Constituents | (g/L) |
|---|---|---|
| 1 | KCl | 0.4 |
| 2 | $CaCl_2$ | 0.14 |
| 3 | $NaHCO_3$ | 0.35 |
| 4 | NaCl | 8 |
| 5 | $MgCl_2.6H_2O$ | 0.1 |
| 6 | Glucose | 1 |
| 7 | $Na_2HPO_4.2H_2O$ | 0.06 |
| 8 | $KH_2PO_4$ | 0.06 |
| 9 | $MgSO_4.7H_2O$ | 0.06 |

The electrochemical Tests was conducted at temperature 37±2°C on the all specimens. The test was performed as shown:

1. Calculation of the OCP (open circuit potential), the experimental arrangement for the measurement of open circuit potential is shown in Figure (3.20). A 500 ml capacity glass electrolytic cell is used. The tests are carried out with the specimens immersed in Hank's solution. Through the standard calomel electrode (SCE), the working electrode potential can be measured.

   A voltmeter is connected between the working electrode and the reference electrode. For each specimen from (0 up to 200min) open circuit potential measurements were performed. The first record was taken immediately after immersion then the voltage was monitored for the intired period of test at an interval of (5min).

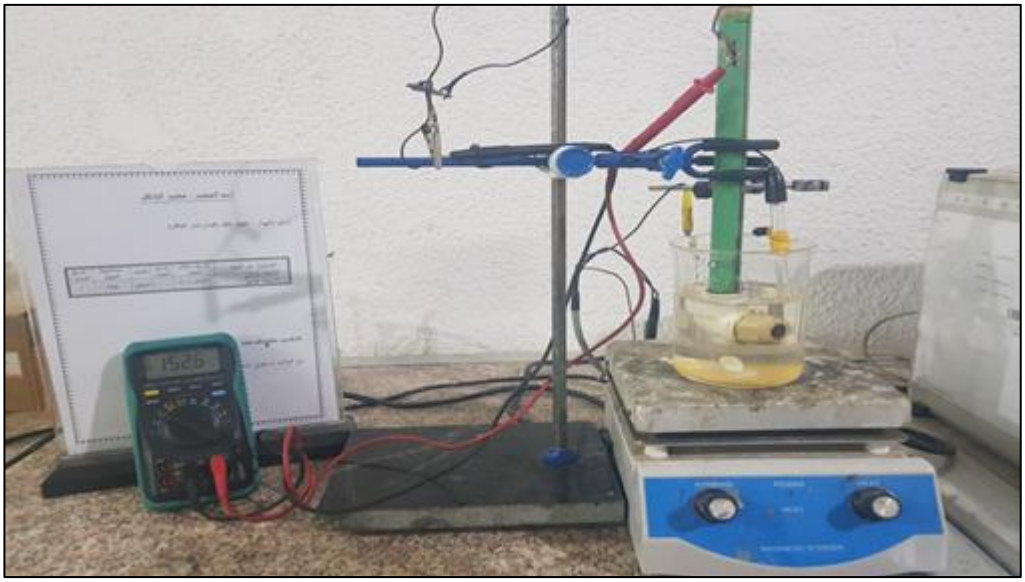

**Figure (3.20):** Open Circuit Potential Measurement.

2. Potentiodynamic polarization, electrochemical tests were carried out in three-electrodes cell and containing electrolytes similar to Hank's solution. The counter electrode was Pt electrode and the reference electrode was SCE and working electrode specimen according to the American Society for Testing and Materials (ASTM). The potentiodynamic polarization curves were plotted and both corrosion current density( $I_{corr.}$)and corrosion potential ($E_{corr.}$)were estimated by Tafel plots by using anodic and cathodic branches. The electrochemical system used is shown in Figure (3.21).

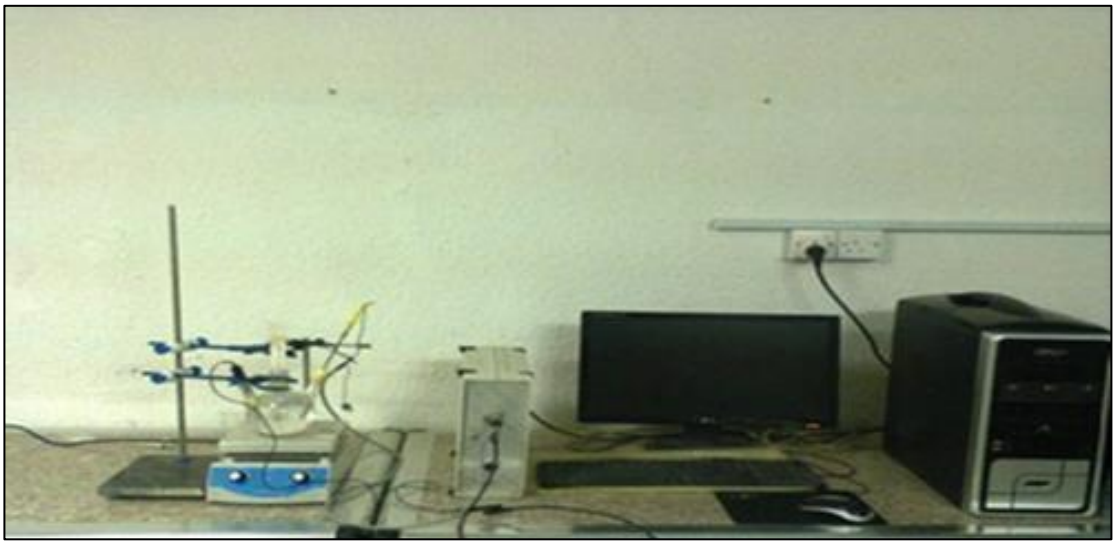

**Figure (3.21):** The Electrochemical System.

The test was started by using 0.4 mV /s as the scanning rate from 250 mV bottom the (OCP) and continued test up to 250 mV above the (OCP). The double cycle polarization technique was used. The measurements were carried out in Hank's solution at 37°C in a Pyrex glass cell with a Pt counter electrode. The potential was controlled with reference to a saturated calomel electrode, and the same OCP used in polarization test . Each experiment was carried out at least three times and mean values of $E_{pit}$ and $E_{prot.}$

### 3.6.7.2 weight loss Test

The corrosion rate was calculated for all samples before and after coating by used weight loss test according to the American Society for Testing Material G1-03 (Metals, 2017)[138].

The corrosion rate (CR) of coatings and substrate alloy was calculated using the following equation[139, 140]:

$$\text{Corrosion Rate } (C_R) = \frac{8.76 \times 10^4 \times W}{A \times T \times D} \quad (mm/y) \text{ - - - - - - - - (3.2)}$$

Where:

$C_R$ : Corrosion rate,
mm/y : Millimeter per year,
W : Mass loss in grams,
T : Time of exposure in hours,
A : Area in $cm^2$, and
D : Density in $g/cm^3$.

## 3.6.8 Wear Test

The dry wear tests studied by using micro-tester (pin-on-disk) type MT 4003 version 10 is located in the Laboratories of the Department of Metallurgical Engineering - University of Babylon as shown in Figure (3.22), using (150 rpm) and constant radius (6mm) with different sliding distance and the loads were (5, 10 and 15N). Before starting the test, the specimen (13mm diameter * 5mm thickness) is weighed using a sensitive

balance (0.0001). After the time (5, 10, 15, 20 and 25 min), the specimen test is weighted and the volume loss had determined according to equation (3.3). The test method had been covered according to (ASTM G 99-05, 2010)[141].

$$\textbf{\textit{Volume loss}} = \frac{\boldsymbol{weigth\ loss(g)}}{\rho(\frac{\boldsymbol{g}}{\boldsymbol{cm^3}})} \quad \text{..... (3.3)}$$

Where:
Weight loss (g)= quantity loss after( 10, 15, 20, 25 and 30 min).
$\rho$ (g/cm³) = theoretical density.

**Figure (3.22):** Pin-on-Disk Wear Instrument.

### 3.6.9 The Thickness of the Coating Measurement

The thickness of the coating was measured by (COATING THICKNESS GAUGE, MODEL: TT260) in the laboratories of the Faculty of Materials Engineering, Department of Polymers and Petrochemical Industries as shown in Figure 3.23. Each measurement was repeated five times. In order to verify the accuracy of thickness, a cross section was made to measure the thickness. The sample was in a vertical position, mounted in a cold mounting resin and subsequently gently grinded of the sample with 1000 grit SiC paper. Micrographs of these samples have then been obtained by optical microscope.

**Figure (3.23):** Coating Thickness Gauge.

### 3.6.10 Roughness Measurement.

In this work, the surface roughness was measured before and after coating. It was measured by surface roughness tester (HSR210, SaluTron, made in Germany) available in the laboratories of the College of Materials Engineering, Department of Metallurgy at the University of Babylon as shown in Figure 3.24.

**Figure (3.24):** Surface Roughness Measurement.

### 3.6.11 Antibacterial Test

The surface of biomaterial was exposed to the risk of initial microbial colonization and bacterial attack. The antibacterial activity of Ti-13Nb-13Zr alloy without coating, HAp-Gr, HAp-CMC, ternary coating, and functional gradient as specimens coated and solutions suspensions (the proportions of additives will be determined later) was investigated to evaluate whether the coated layers is antibacterial or not.

The antibacterial activity was studied by using the inhibition zone method. An antibacterial kinetic test with bacterial strains of Escherichia coli (E.coli, Gram-negative) and Staphylococcus aureus (S. aureus, Gram-positive) [142] was prepared at the University of Babylon-College of Science - Department of biology. For the bacteria preparation, the E.coli and S. aureus grown on agar and placed in the incubator for 24 h at 37 °C. Specimens were immersed in 5 ml of phosphate-buffered saline (PBS) shown in Table 3.6 for 24 hours then the bacteria spread on a petri dish where the suspensions and specimens (After removing the samples from PBS solution) were placed in four different regions on it and incubated. After the incubation, the inhibition zones were measured using normal ruler.

**Table (3.6):** Shows the Composition of PBS Solution[143].

| No. | Constituents | (g/l) |
|---|---|---|
| 1 | NaCl | 8.0 |
| 2 | KCl | 0.2 |
| 3 | $Na_2HPO_4$ | 1.42 |
| 4 | $KH_2PO_4$ | 0.24 |
| 9 | Deionized water | Balance |

### 3.6.12 MTT Assay

#### 3.6.12.1 General principles

MTT assay is one of the most effective method to check the cell viability of cell line, to evaluate safe, and efficient amount of the drug.

MTT assay is a colorimetric assay for assessing cytotoxicity or cytostatic activity. Under defined condition, NADPH dependent cellular oxidoreductase enzymes reflects the number of viable cells. The MTT enters the cells and passes into the mitochondria, This enzyme reduce the tetrazolium salt MTT(3-(4,5 Dimethyl thiazol-2-Yl)-2,5-Diphenyltetrazolium Bromide) in a insoluble formazan product (it is artificial chromogenic product formed by reduction of the tetrazolium salt by dehydrogenase and reductase) which have purple color, the cells are soluble in organic solvents like DMSO, acidified isopropanol will be the solvents to make the soluble of insoluble formazan as show in Figure (3.25). The obtained color will be processed for OD and reads the obtained data.

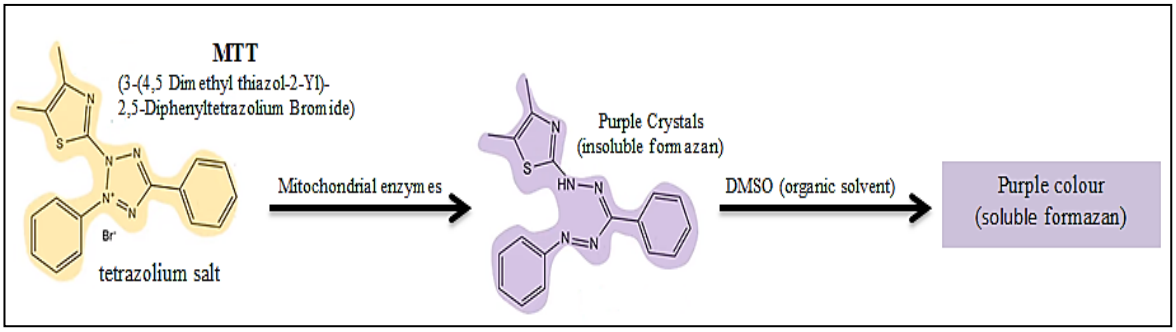


**Figure (3.25):** The Principle Procedure of MTT Assay[134].

### 3.6.12.2 Procedure of MTT Assay on Coating Specimens to Check Cell Viability

The biocompatibility of ( HAp-Gr, HAp-CMC, ternary coating, functional gradient, and base alloy without coating) coatings (the proportions of additives will be determined later) was assessed using Human osteoblast like (MG-63) cells line was obtained from the Pasteur Institute (Tehran, Iran). The osteoblast cultures were designed according to the protocol of ISO 10993:5[144].

The cells were grown in Dulbecco's modified Eagle's medium (DMEM; Gibco, Life Technologies, Waltham, MA, USA) supplemented with 10% fetal bovine serum (FBS; BioWest SAS, Nuaille, France) and 1%

PSF (antibiotic antimycotic solution, Sigma-Aldrich®, St. Louis, MO, USA)) mix and incubated at 37 C in a $CO_2$ atmosphere.

After obtaining the osteoblast culture, the cells were treated with 0.25% trypsin (Gibco, Invitrogen, Waltham, MA, USA) and 0.1% ethylenediaminetetraacetic acid (Merck, Darmstadt, Germany) in phosphate-buffered saline (PBS) at 37°C. The all specimens were sterilized at 180C for 2 hr in the vacuum oven and then placed in plates Petri dishes, for osteoblast cell implantation at a set density of 100,000 cells/$cm^2$. The cells were cultured on the surfaces of the specimens in "as-prepared" condition. The cultures were evaluated for cell viability at 24, 48, and 72 h (MTT assay). The control cell culture was grown on a Petri dish (DMEM solution without metal extract was used as the control).

The cell viability was determined using the standard colorimetric assay MTT (3-(4, 5-dimethylthiazol-2-yl)-2,5-diphenyltetrazolium bromide) reduction test. The absorbance was quantified by measuring the wavelength at 595 nm using a TECAN spectrophotometer. In order to quantify the data, the value of the absorbance obtained for the control cell culture (culture grown on Petri dish) was set as 100% viability and the other absorbance values were transformed to a % of viability in relation to the control sample. For the in vitro experiments, three independent experiments were performed, each with three replicates. The data are presented as means standard deviation (SD).

# CHAPTER FOUR

# Results and Discussion

# CHAPTER FOUR

# RESULTS & DISCUSSION

## 4.1 Introduction

Experimental results have been demonstrated in this chapter which involve the properties related to the coating layers (nanoHAp, nanoHAp+ nanoGr, nanoHAp+ nanoCMC, ternary coating, and FG) deposited on the Ti-13Nb-13Zr alloy specimen that were deposition by electrophoretic deposition. The microstructure examination from light optical microscope, SEM and EDS, phase's analysis from XRD technique, Zeta potential, surface roughness, content angle, corrosion test, dry sliding wear test, Antibacterial test, and Cytotoxicity evaluation results have been cleared and discussed at same voltage and time.

## 4.2 Coating Process Parameters

### 4.2.1 Electrodes Materials

To obtain a suitable anode electrode for coating the cathode electrode represented by Ti-13Nb-13Zr alloy with the suspended solutions mentioned earlier in Chapter Three requires experimenting with many materials which have been used in a lot of research in this field, including the three electrodes (graphite, stainless steel -316L and Ti-13Nb-13Zr titanium alloy, which are shown in Appendix 'A' Figure 8). All these electrodes were tested with a suspension solution containing hydroxyapatite powder (5 HAp) with time and voltage shown in Figure (4.1) which have been adopted. To reach the electrode that gives a homogeneous and regular coating layer and maintains the efficiency of the suspension solution that has been adopted in all coatings process parameters. When conducting coating experiments using a graphite electrode, it was found that it contaminated the suspended solution from the coated first specimen as shown in Figure (4.2). Therefore, despite the good results achieved by this

electrode, it was excluded because it causes loss and consumption of suspended solutions. According to the results that were reached for the re-coating experiment using both Ti-13Nb-13Zr alloy and stainless steel -316L electrode, it was found that the best results in terms of coating quality were using the last electrode (stainless steel -316L electrode).

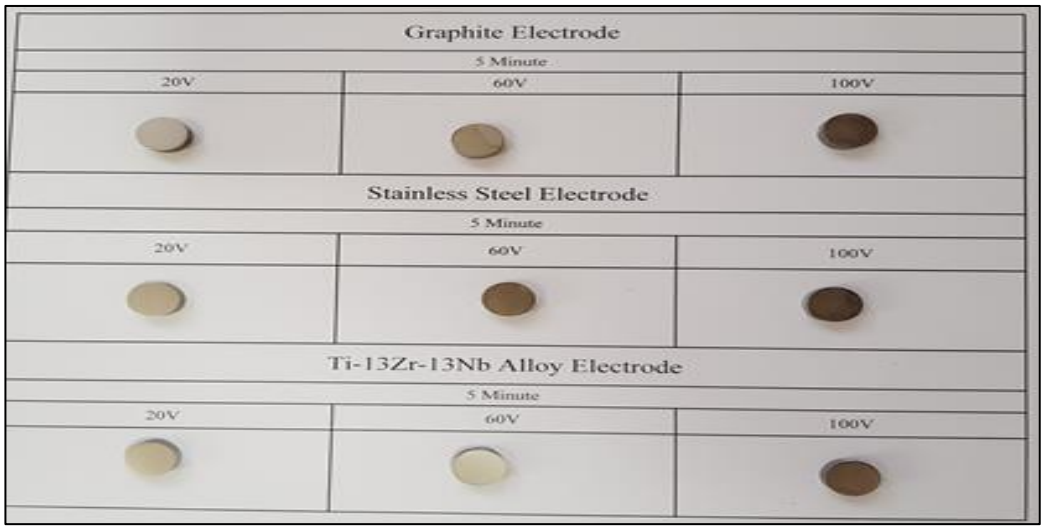


**Figure (4.1):** The Voltage and Time Used with the Three Electrode Material.

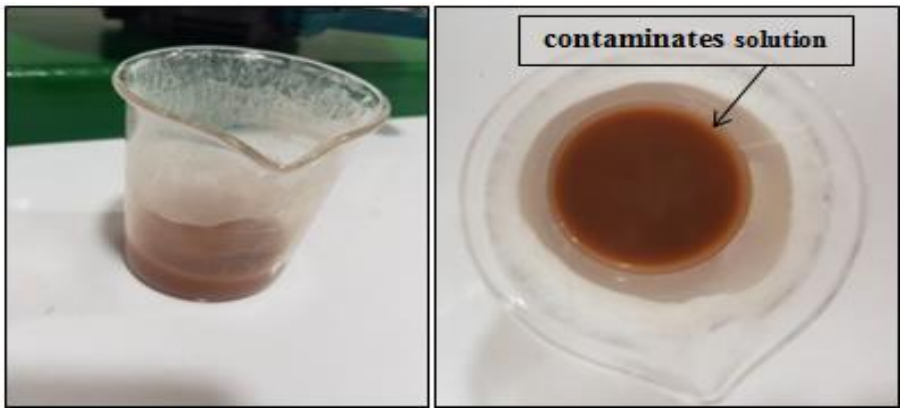


**Figure (4.2):** The Coating Solution with Graphite Electrode.

### 4.2.2 Time and Voltage parameters

In order to choose the best conditions for coating process parameters (time, voltage) and after studying many of research, it was found that there is a discrepancy in the choice of voltage and time. the voltage ranged (10-110)V and the time from (10) seconds to (7) min [129, 130, 131]. Therefore to achieve the best results for coating parameters the researcher decided to experiment with all conditions of time and voltage to reach the best results.

This was done through two-stage. The first stage tested the conditions (1-7) min and (50-100)volt, as shown in Figure (4.3a). These conditions were excluded, because the coating layer that was deposited on the surface of the Ti-13Nb-13Zr alloy at these conditions was unsatisfactory in terms of its irregularity and inhomogeneity, except for rarely. In addition to peeling off part of this layer as a result of the high thickness, which ranged between (132 to 233) which results from long time and high voltage, which led to the removal of the coating layer easily when conducting the adhesion test (pull-off test)

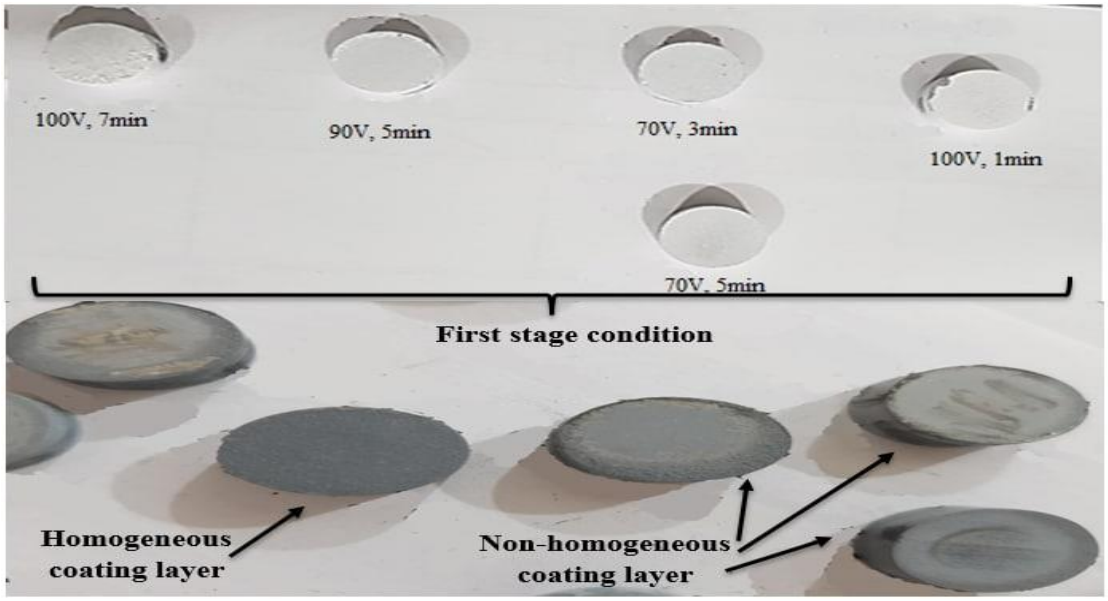


**Figure (4.3a):** First Stage Condition and State Coating Layer Surface.

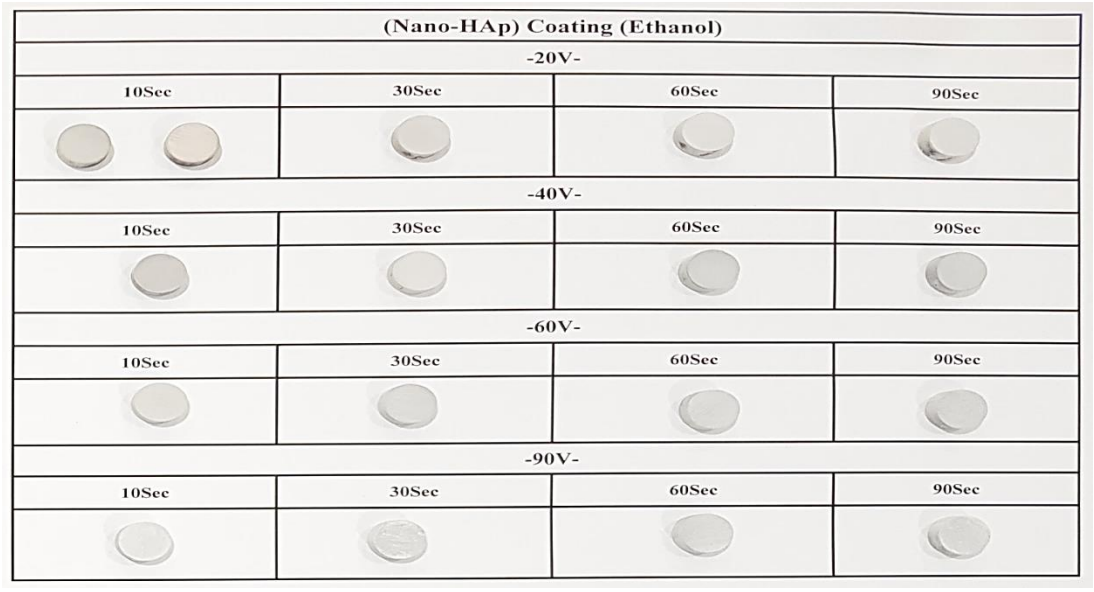


**Figure (4.3b):** Second Stage Condition and State Coating Layer Surface.

In the second stage, which consists of (20-90)volt and (10-90) seconds as shown in Figure (4.3b) the coating layer shows homogeneity and uniformity. so the conditions (40V, 60S) were chosen as the best volt and time for the coating process that was after the pull-off test on all samples. which noted that it's have the highest values of adhesion with all addition (HAp, Gr, CMC) and this was proven by measuring the thickness of the coating layer, as it appeared that this condition had the lowest coating thickness as can be shown in the Table (4.1). Except the (1CMC) for failure to obtain a coating layer under all conditions. This can be attributed to the high percentage of CMC that led to the difficulty of dealing with it during the mixing and coating process. The high flow amount of CMC particles toward the cathode, which led to the irregular accumulation of particles on the surface of the cathode, causing a very weak adhesion of this layer and then separation of large parts of the coating layer from the surface of the alloy before removing it from the solution as can be shown in Figure (4.4).

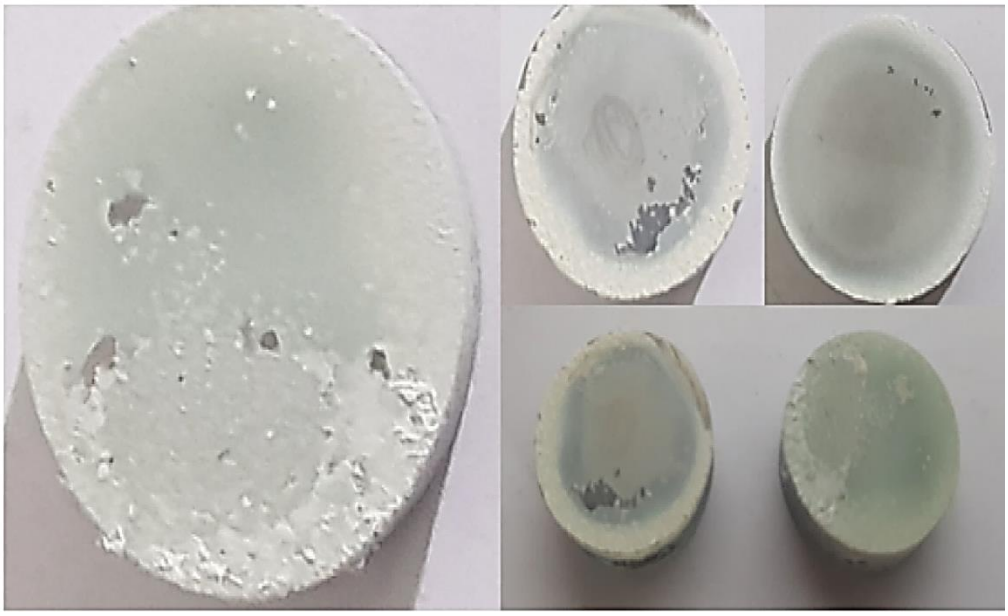

**Figure (4.4):** 1 CMC Coating on Ti-13Nb-13Zr Alloy.

**Table (4.1):** The adhesion strength (MPa) (Pull-Off Test) Result for the Second Stage Condition with (Hydroxyapatite, Graphene, and Carboxymethyl Cellulose) Coatings.

| **Hydroxyapatite** | | | | | | | | | | | | | | | | |
|---|---|---|---|---|---|---|---|---|---|---|---|---|---|---|---|---|
| **Parameters / percentages** | **20 V** | | | | **40 V** | | | | **60 V** | | | | **90 V** | | | |
| | **10 s** | **30 s** | **60 s** | **90 s** | **10 s** | **30 s** | **60 s** | **90 s** | **10 s** | **30 s** | **60 s** | **90 s** | **10s** | **30 s** | **60 s** | **90s** |
| **5** | 5.1 | 5.2 | 4.4 | 3.7 | 6.3 | 6.4 | 7.3 | 7 | 3.4 | 3.1 | 2.3 | 1.4 | 1.2 | 0.94 | 0.82 | 0.5 |
| **Graphene** | | | | | | | | | | | | | | | | |
| **0.08** | 9.6 | 9.9 | 9.1 | 7.8 | 8.1 | 8.9 | 13.3 | 10 | 6.3 | 5.8 | 5.1 | 4.5 | 3.8 | 2.7 | 2.2 | 1.7 |
| **0.2** | 9.7 | 9.5 | 8.1 | 7.5 | 10.2 | 12.4 | 15.2 | 13 | 6.1 | 5.5 | 5.3 | 3.3 | 3.1 | 2.2 | 1.8 | 1.3 |
| **0.5** | 8.1 | 7.7 | 8.2 | 7.1 | 7.3 | 8.6 | 12.3 | 10.1 | 4.8 | 3.2 | 1.8 | 1.1 | 2.5 | 2.3 | 2.4 | 1.3 |
| **1** | 9.8 | 6.5 | 5.7 | 2.4 | 8.1 | 8.3 | 8.5 | 8.5 | 5.1 | 2.5 | 4.3 | 1.2 | 1.1 | 0.9 | 0.8 | 0.9 |
| **Carboxymethyl Cellulose** | | | | | | | | | | | | | | | | |
| **0.08** | 6.2 | 6 | 5.4 | 2.8 | 8.2 | 8.9 | 9.2 | 9 | 5.1 | 5.5 | 4.7 | 3.2 | 2.7 | 2.1 | 1.2 | 0.8 |
| **0.2** | 6.9 | 5.4 | 4.6 | 3 | 7.3 | 9.5 | 9 | 9.2 | 4.7 | 4.2 | 3.5 | 1.3 | 2.2 | 1.8 | 0.9 | 0.6 |
| **0.5** | 4.7 | 4.2 | 3.5 | 2.8 | 7.6 | 6.3 | 7.8 | 7.1 | 2.4 | 1.5 | 1.1 | 0.9 | 1.3 | 0.8 | 0.8 | 0.5 |

For studying the effect of voltages and deposition time on the coating thickness and the deposition weight on the surface of the (Ti-13Nb-13Zr) alloy, the coating thickness was measured for all samples coated with (graphene, CMC) as shown in Figure (4.5), it can be observed that the coating thickness increases with the increase in applied voltage during coating Kumari et.al [145] also proves it, the coating thickness gradually increases from 49.9 µm at 20 V in G1 to its highest value of 125.6 µm at 90 V in G4 (Figure 4.5 A), while these values increase for CMC coating (Figure 4.5 B) to about 62.5 µm at 20 V in C1 to the highest value for coatings that reach 138. 6 µm at 90 V in C3.

In both CMC and graphene coatings, an increase in the thickness of the coating can be observed with an increase in the percentage of addition, but slightly, as shown in the values of 40 V in the Figures below (Figure 4.5 A, B).

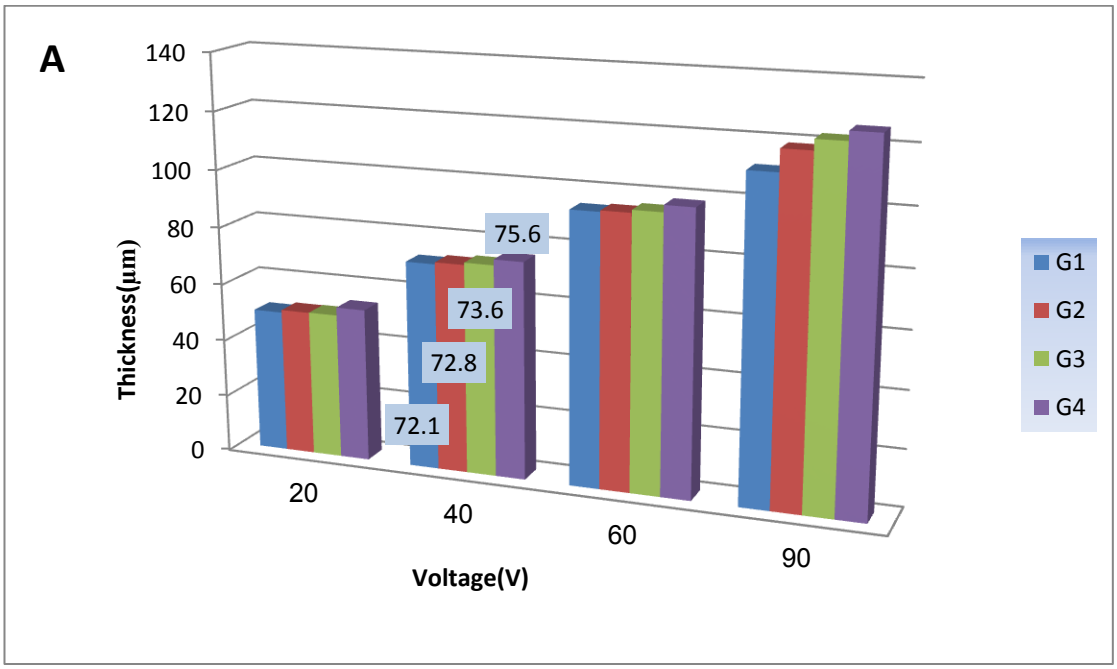

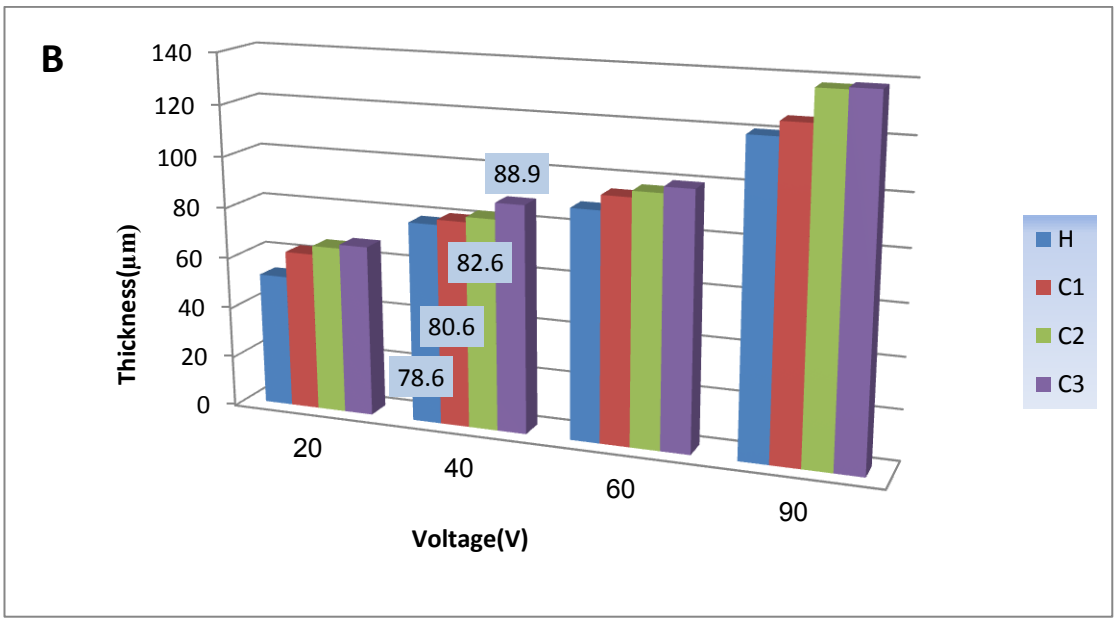


**Figure (4.5):** Effect of Applied Voltage on Coating Thickness in Ethanol at 60 Sec, (A) Gr and (B) H and CMC.

Figure (4.6 A, B) shows the deposition weight of the coating (graphene, CMC) on the (Ti-13Nb-13Zr) alloy with the applied voltages at the constant time (60 s) during the coating process, which can notice the same effect of the applied voltage on the coating thickness, so the deposition weight increases with the increase in the applied voltages, increase in the deposition weight can be shown with an increase in the percentage of adding of both graphene and CMC (Figure 4.6 A, B) respectively, especially at 90 V, which increases from (0.0000043191 g/cm$^2$ at G1) for 20V to (0.000012766 g/cm$^2$ at G4) for 90V and almost the same increase when adding CMC, which increases from (0.0000044681 g/cm$^2$ at C1) for 20V to (0.0000182979 g/cm$^2$ at C3) for 90V.

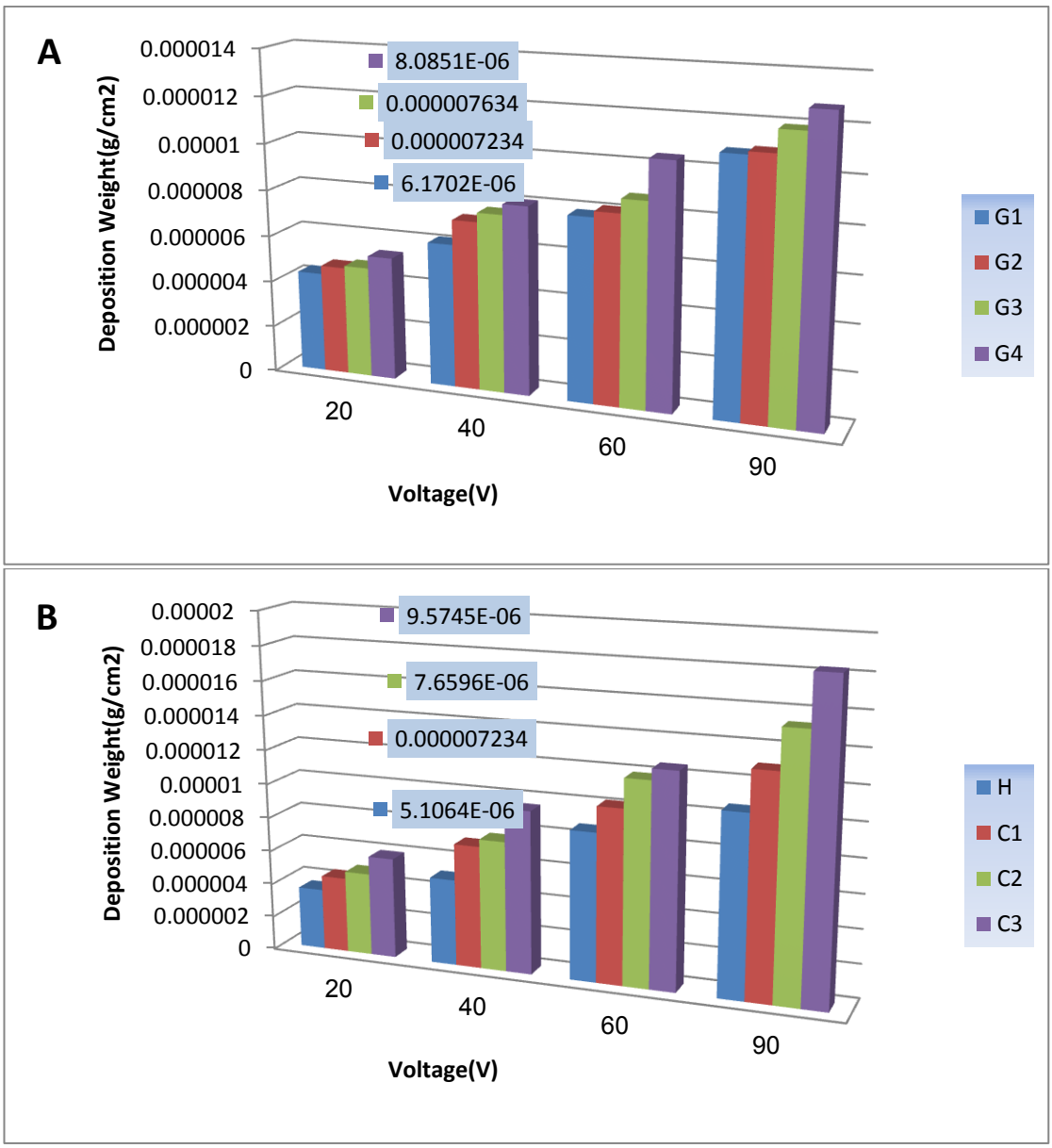


**Figure (4.6):** Influence of Applied Voltage on Deposition Weight at 60 Sec, (A) Gr and (B) H and CMC.

Figures (4.7 A,B) and (4.8 A,B) indicate that the influence of deposition time on each of the coating thicknesses and the deposition weight of the coating with constant applied voltage at (40) V creates a slight increase in each of them.

Whereas the coating thickness at 10 seconds in G1 is 71.3 µm, increases to 72.3 µm at 90 seconds, as well as for the rest of the addition ratios Figure (4.7A). For the addition of CMC, it increases from 73.2 µm at 10 seconds in C1 to 75.6 µm at 90 seconds, as well as for the rest of the additions Figure (4.7B).

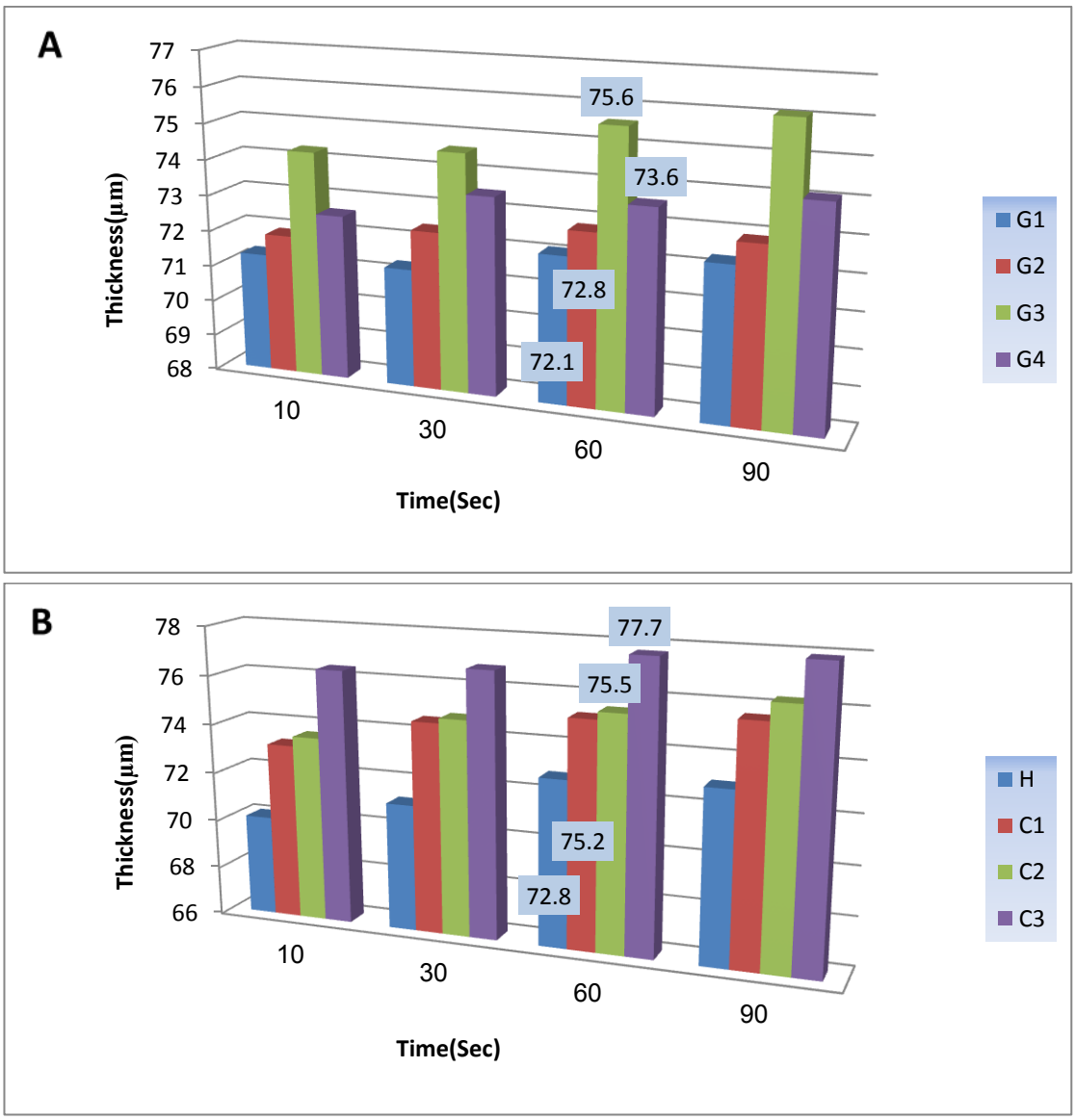


**Figure (4.7):** Effect of Deposit Time on Coating Thickness at 40V, (A) Gr and (B) H and CMC.

In both additions, the deposition weight increases slightly as the deposition time increases, as shown in Figures (4.8 A and B), so the deposition weight increase from (0.0000025532 g/cm$^2$) at 10 second to (0.0000076 g/cm$^2$) at 90 second in G1 and from (0.000003617 g/cm$^2$) at 10 second to (0.0000085106 g/cm$^2$) at 90 second in C1 ,as well as for the rest of the addition.

Can be noted the slight increase in coating thickness vs. deposition time when the percentage of addition increases from G1 to G4 and from C1 to C3 (Figure 4.7A, B). Similarly, when measuring deposition weight vs. deposition time (Figure 4.8A, B), there is a slight increase as the percentage

of addition for CMC increases. In the case of graphene, the deposition weight and coating thickness increases slightly from G1 to G3 following that, it decreases at G4 due to graphene saturation of the coating solution, resulting in the opposite result.

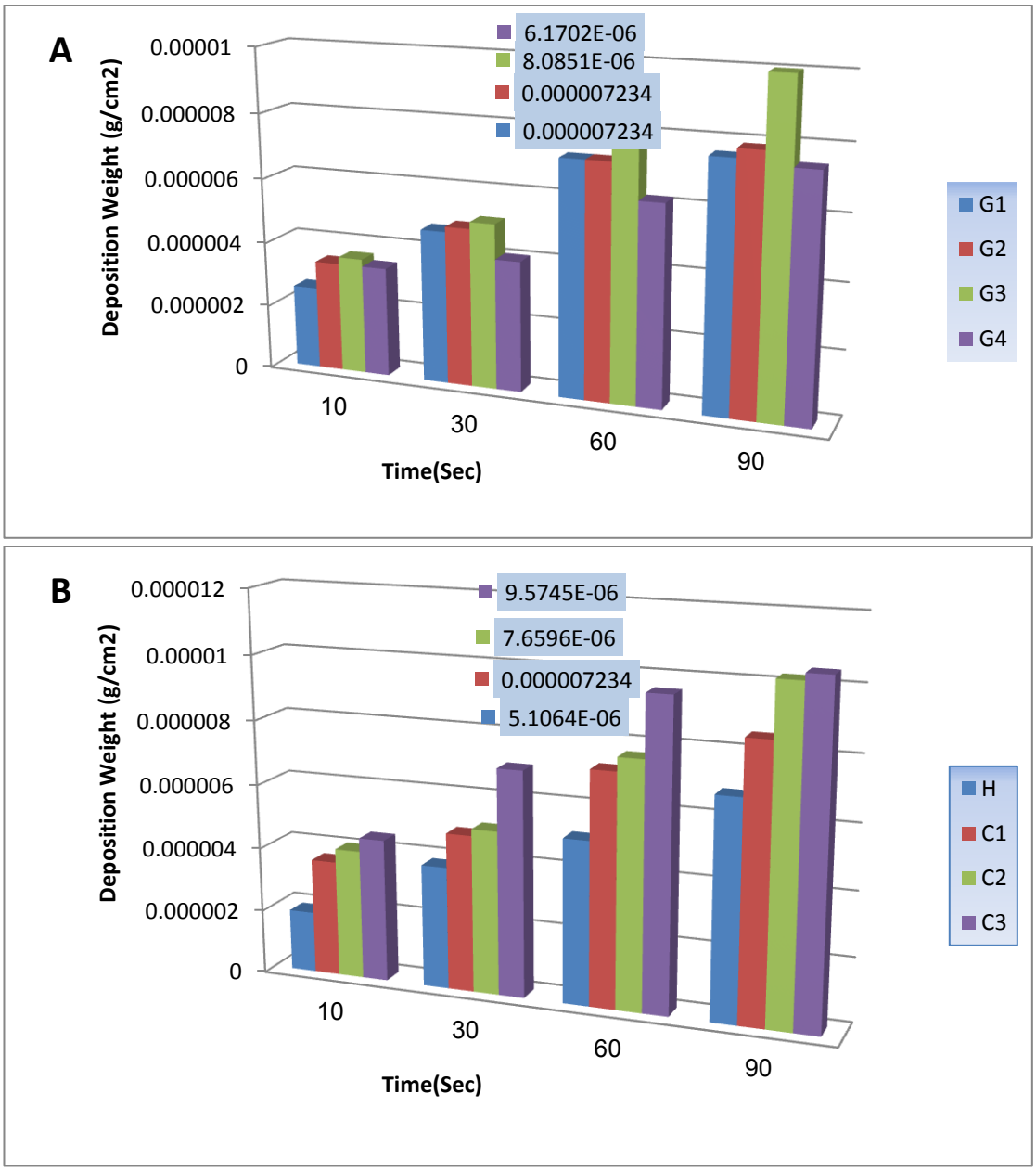


**Figure (4.8):** Effect of Deposition Time on Deposition Weight at Applied Voltage of 40V, (A) Gr and (B) H and CMC.

As previously noted, the thickness of the coating increases as the applied voltage and deposition time increase; however, at high voltages and times, particularly (90 V, 90 s), the thickness of the coating will be non - uniform in all areas of the coating layer. This was observed when examining the thickness of the coating (cross-section) in several areas from

the coating layer, particularly the CMC coating; this is attributed to the fast movement of the suspension particles during coating process and the formation of hydrogen bubbles on the surface of the Ti-13Nb-13Zr alloy, which resulted in non-homogeneous deposition [146]. The Figure (4.9) below depicts the thickness of the coating for various additives.

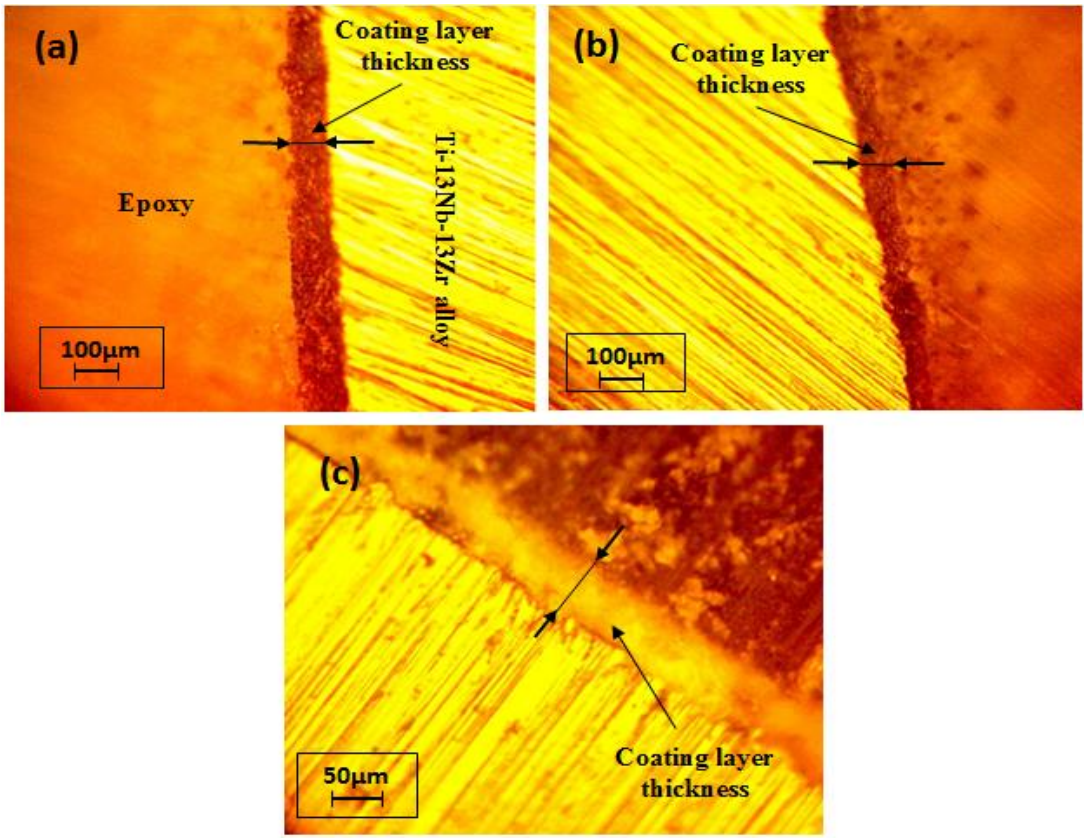


**Figure (4.9):** The Coating Thickness in 40V at 60 Sec **(a)** for 0.08CMC, **(b)** for 0.08Gr, **(c)** for HAp.

## 4.3 X-ray Diffraction Analysis

Figure 4.10 shows the XRD pattern of the coated specimens in addition to the base alloy without coating. The pattern of the base alloy in (Figure 4.10a) revealed the diffraction of the beta and alpha phases that matched the JCPDS Card No. (044 - 1294) where no impurity phase was obtained for this alloy. when the coatings are deposited on the base alloy, can notice the emergence of new peaks due to the effect of the additions ratios (5HAp, 0.5 Gr, and 0.5 CMC ), which also led to a reduction or increase in the angle of the peaks of each of the phases of the titanium alloy (beta and alpha), which ultimately depends on the effect of the addition.

Zunyu et. al [147] It can be seen that the Ti-13Nb-13Zr alloy mainly consists of β -Ti and α -Ti, but the Ti-13Nb-13Zr-10Cu alloy is mainly composed of β -Ti, α -Ti, and Cu-containing phases. It is implied that the main phase of Ti-13Nb-13Zr-10Cu alloy is still the β -Ti phase. After the addition of Cu, the peaks of Ti slightly shift to bigger angles. It could attribute to the incorporation of Cu into Titanium, leading to the lattice expansion of Titanium.

The pattern of HAp coating in (Figure 4.10b) revealed the recognition of the HA phase, especially at 2θ=13.3° and 26.55°, which is consistent with JCPDS Card No. (09–432). The existence of the amorphous phase was not recognized in HA coating and there was no other phase present in the coating this agrees with Rad et al. [148] fabricated HA coating on the Ti–13Nb–13Zr substrate by EPD. In (Figure 4.10C), the graphene coating, it can be noticed that the intensity and 2 theta of the hydroxyapatite peaks and substrate alloy increased, which could be attributed to the interaction of graphene with the phases of the substrate alloy, which led to the formation of carbides, and thus led to the appearance of hydroxyapatite peaks with more clarity. The addition of CMC (Figure 4.10d), led to a decrease in the intensity of the hydroxyapatite peaks, which can be attributed to the dissolution of CMC in water and thus its association with the free bond of hydroxyapatite (-OH).

The XRD analysis revealed no observation referring to chitosan (Ch) peaks indicating that it was collected in the semi-crystalline form. The disappearance of Ch peaks may be attributed to the presence of HA, Gr, and CMC affecting the intermolecular hydrogen bonds of Ch between –OH and $–NH_2$ groups, and that agrees with Hou et al. [149]. The prior investigations on chitosan-based coatings showed that the anchoring of chitosan with HA gives stability and mechanical strength to the composite coatings. The avoidance of the usually required sintering step endorsed that

the composite coating was stable in nature and no structural change in crystallinity was found in XRD patterns.

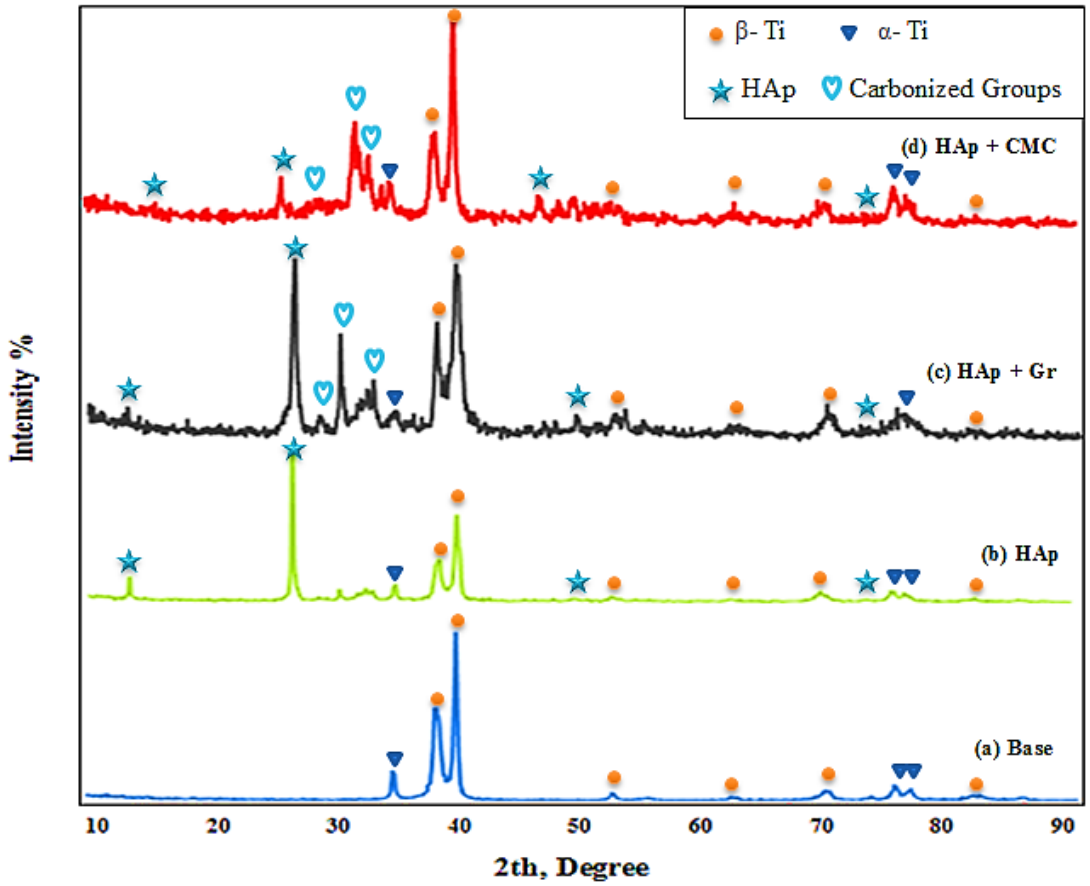


**Figure (4.10):** XRD Pattern of EPD on Ti–13Nb–13Zr Alloy: (a) Substrate Alloy, (b) HAp, (c) HAp + Gr, and (d) HAp + CMC.

## 4.4 Zeta Potential Test

Table (4.2) shows the zeta potentials of the different suspensions containing nanoparticles of (HAp), (CMC), (Gr) and (Mix) as well as the pH values in the presence and absence of nitric acid ($HNO_3$). As can be seen, the zeta potentials ( $\zeta$ ) of all four suspensions present positive values at pH indicated for each of them, indicating that the particles are positively charged, which also predicts particle cathodic deposition. In the four nano additions, the zeta potential is increased by adding (0.08) Gr to the hydroxyapatite which enhances the surface charge and zeta potential. As mentioned in the results shown in Table 4.2, the pH values decrease with the addition of nitric acid (7.2 for hydroxyapatite before adding the acid to 2.1 after adding), which indicates higher zeta values than before adding

nitric acid, there is a very close correlation between pH and zeta where the lower the pH the higher the zeta values [150]. Therefore, from these results, the effects of adding (CMC, Gr and Ternary coating) on the stability behavior of suspensions containing hydroxyapatite are clear and predicts cathodic process, indicating that the ethanol suspension is suitable for EPD.

**Table (4.2):** Zeta Potentials and PH of Various Suspensions after and before Addition $HNO_3$.

| Type of Suspensions | Zeta Potential (mV) after Adding $HNO_3$ | PH | |
|---|---|---|---|
| | | Before Adding $HNO_3$ | After Adding $HNO_3$ |
| **HAp** | 48 | 7.2 | 2.1 |
| **HAp-Gr** | 55 | 6.3 | 1.6 |
| **HAp-CMC** | 45 | 7.5 | 2.2 |
| **HAp-Gr-CMC** | 43 | 7.9 | 2.4 |

## 4.5 Adhesion strength

The adhesion strength of the coating layers for (HAp, HAp-Gr, HAp-CMC, Ternary coating and functional gradient F) was measured before and after immersion for (1, 3, and 6) days in Hank's solution at 37°C by using the pull-off test (ASTM-D4541) as shown in Table (4.3). The adhesion strength of graphene coatings after immersion increases with the increase of the immersion period and the addition percentage compared to the rest of the layers, while CMC layers and Ternary coatings, where decreases with the increase in both of the immersion period and the addition percentage. The highest adhesion resistance obtained was (10.12 MPa before immersion) among all layers, when the functional gradient (F) was performed, which increased to (11.24 MPa) after one day of immersion, and (20.75 MPa) after 6 days of immersion.

**Table (4.3):** Adhesion Resistance for (1,3, and 6) Days of All Coatings.

| Specimens | Adhesion Strength (MPa) | | | |
|---|---|---|---|---|
| | Without Immersion | 1 Day | 3 Days | 6 Days |
| **HAp** | 4.55 | 10.36 | 12.87 | 9.95 |
| **G1** | 9.18 | 10.5 | 10.39 | 17.83 |
| **G2** | 9.21 | 10.59 | 14.79 | 18.78 |
| **G3** | 9.53 | 11.25 | 15.22 | 19.21 |
| **G4** | 9.76 | 11.83 | 15.32 | 20.98 |
| **C1** | 7.90 | 7.54 | 5.36 | 2.73 |
| **C2** | 7.32 | 6.57 | 4.66 | 2.61 |
| **C3** | 6.63 | 5.35 | 3.18 | 2.13 |
| **M1** | 8.38 | 8.33 | 8.41 | 8.13 |
| **M2** | 8.12 | 7.53 | 7.51 | 7.08 |
| **M3** | 6.36 | 5.81 | 5.30 | 4.88 |
| **M4** | 5.10 | 5.71 | 4.34 | 3.72 |
| **F** | 10.12 | 11.24 | 20.28 | 20.75 |

The increase in the adhesion strength of the graphene coating is related to the fact the graphene caused that the HAp particles to stick together more strongly on Ti-13Nb-13Zr substrate, in addition to, there were no large agglomeration in the graphene coating, and therefore the coating was more dense and cohesive compared to the HAp, CMC, and Ternary coating layers. These results are consistent with the results of the SEM, where it is possible to notice the significant improvement that occurred in the surface of the coating layer by adding graphene when deposited on Ti-13Nb-13Zr substrate (as show later Figure 4.13 B and D). Because of the cracks on the surface of the CMC coating layer as shown in the images of FESEM (Figure 4.15), in addition to the high porosity, which led to a decrease in the adhesion strength of all proportions of CMC

additives due to the penetration of the immersion liquid (Hank's solution) in those cracks, which in turn led to Weakening the adhesion of the HAp particles to each other on the surface of the Ti-13Nb-13Zr alloy for all periods of immersion. For the graphene coating, the high bonding strength it gives to the HAp particles and the uniformity and regularity of the coating layer led to an increase in the adhesion strength of the layer on the surface of the Ti-13Nb-13Zr alloy after the three immersion periods.

## 4.6 Surface Roughness

Figure (4.11) below can observe the surface roughness values for all the samples that were examined.

The highest surface roughness value was achieved when added different percentages of CMC, starting from (C1) (0.986 nm) up to the highest value among all samples (C4) is (1.766 nm). While the highest roughness for the mixing samples was (1.455 nm) for the sample (M4). The surface roughness of the (HAp) sample is (0.644 nm) above the roughness of the (Ti-13Nb-13Zr) alloy is (0.455 nm), but it remains less than the surface roughness of all other additions.

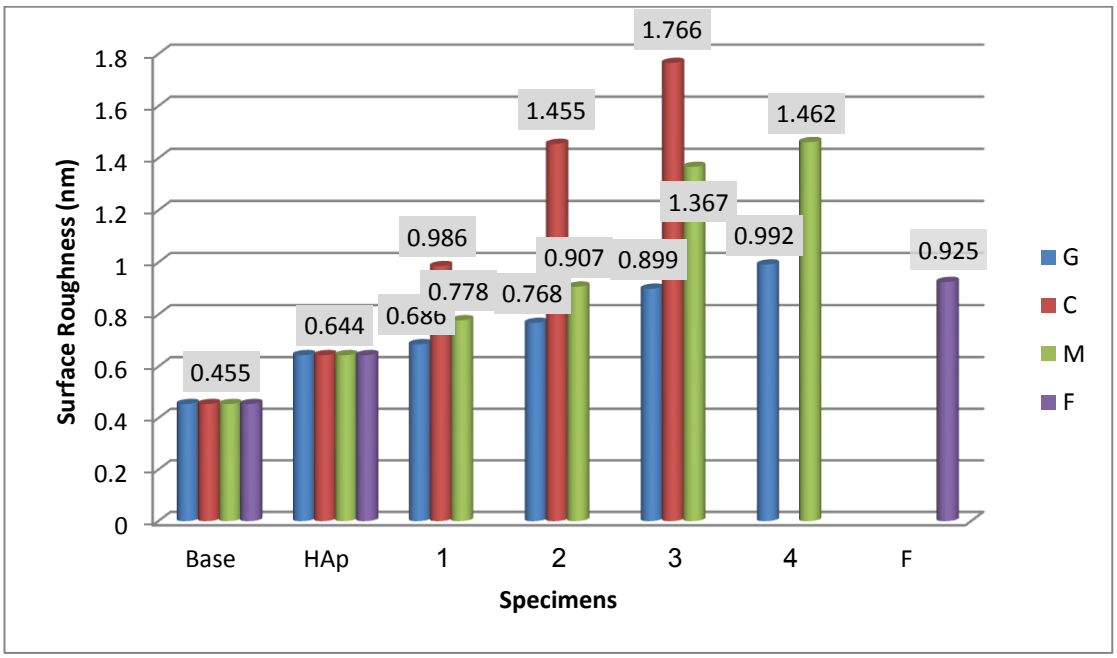


**Figure (4.11):** Surface Roughness Values (Ra) µm for (G, C, M, and F) Coatings.

By surface roughness measurement, the (C3 and M4) biocoatings is the optimal option among others. It was pointed out that the rapid adhesion of the osteoblast cells onto the implant surface can be achieved by increasing the surface roughness, which may provide a substantial improving in contact area with the bone. Roughness acts as a driving force for osseointegration due to the high surface energy of the rough surface as well as the improvement of contact between the bone and implant [151].

## 4.7 Wetting Behavior Test

Contact angle is a measure of the degree of wettability, which plays a pivotal role in controlling cell adhesion and proliferation, as shown in Figure (4.12), the contact angle values (for the coated and uncoated samples) showed different results showing the extent to this layer is hydrophilic or hydrophobic inside the human body.

The surface of non-coated (Ti-13Nb-13Zr) sample had a higher aqueous contact angle of 54.6˚ indicating a less hydrophilic surface compared to the coated samples, but, in case of get various ratio from (Gr and CMC), it can be noted decreasing in contact angle till the drop becomes more splay over the surface, it means high in absorption as (20.5°) for (G4) and (11.2°) for (C3), and sometimes without contact angle value as shown in Table (4.3). Same condition above was noted also in percentage of (Mix and FG) which reaches to (14.3°) for sample (M4) and (32.3°) for (F).

The decoration of nanoHAp coatings with CMC leads to a significant decrease in contact angle. It is well known that the wettability of metals is lower than that of polymers and ceramics; this is clearly shown in the presence of a relatively small amount of nanoCMC and nanoGr. The low contact angles for all specimens may be attributed to their porous surface structure. Contact angles are measures of wettability; their low values correspond to anticipated high biocompatibility. On the other hand, the best

values of contact angle for cell attachment were assessed at 55° and for bone regeneration at 35° to 80° [152], these values are higher than those recorded here.

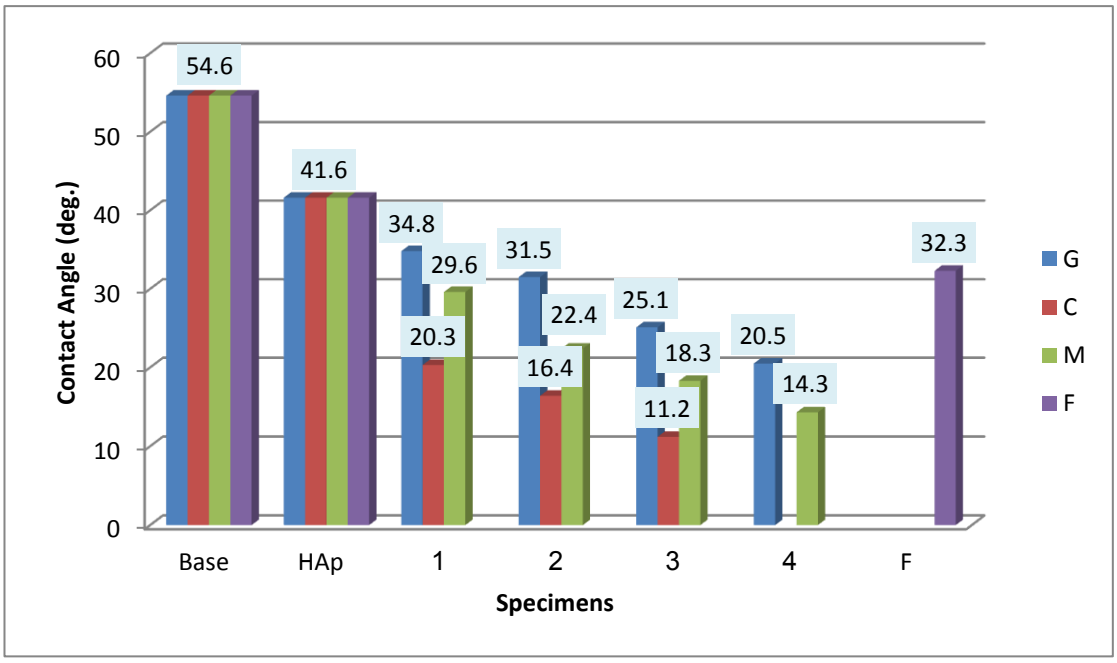


**Figure (4.12):** Photometric Quantification of Contact Angle Θº Bound to the Different Coating Surfaces.

The (nanoHAp-nanoCMC) coating are regarded to be hydrophilic due to the high porosity and roughness, as mentioned previously, in addition to the cracks that were observed in the CMC coating, which allow liquids to penetrate to the lower layers of the coating, which leads to a significant decrease in the contact angle. on the other hand, prevent the Hank's solution droplets from penetrating the interior of the (nanoHAp-nanoGr) coating, resulting in an increase in the contact angle.

**Table (4.4):** Contact Angle of (Ti-13Nb-13Zr) and Coated Specimens Using Hank's Solution.

| Specimens | Base | HAp | G4 | C3 | M4 | F |
|---|---|---|---|---|---|---|
| Degrees |  **54.6 °** |  **41.6 °** |  **20.5 °** |  **11.2 °** |  **14.3 °** |  **32.3 °** |

The best results mentioned in the above Table (4.4) do not mean that they are the best results for the rest of the tests, because of the presence of developed cracks with the increase of the percentage of addition, porosity,

roughness and surface topography that make the subsequent results do not match the results of the contact angle in terms of the best results.

## 4.8 Surface Morphology Analysis

### 4.8.1 Surface Morphology of Coating

SEM images for the surface morphology of samples coated with (graphene, CMC, and hydroxyapatite) at various magnifications are shown in Figure (4.13).

As shown in Figure (4.13 A), the number of microcracks present on the surface of the hydroxyapatite coating is reduced when graphene and functional gradient (FG) (Figure 4.13B & D) are added compared to adding CMC and Ternary Coating (Figure 4.13C & E) , Furthermore, no surface flakes or cracks were observed on the surface of the graphene coating that can be seen on the surface of the hydroxyapatite and CMC coatings, and the higher roughness of the CMC coating can be observed compared to the graphene coatings.

These cracks can be attributed to high ethanol evaporation and quick drying of the coatings due to the formation of thermal stresses caused by the difference in thermal expansion of the CMC coating and the base alloy, which is one of the most important causes of cracks on the coating's surface.

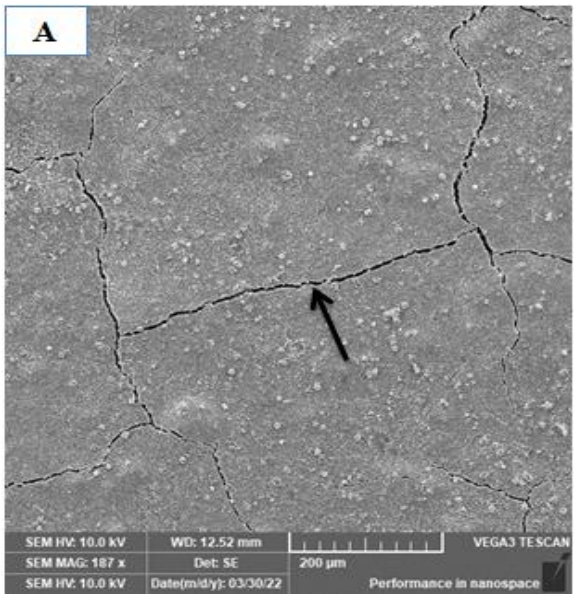

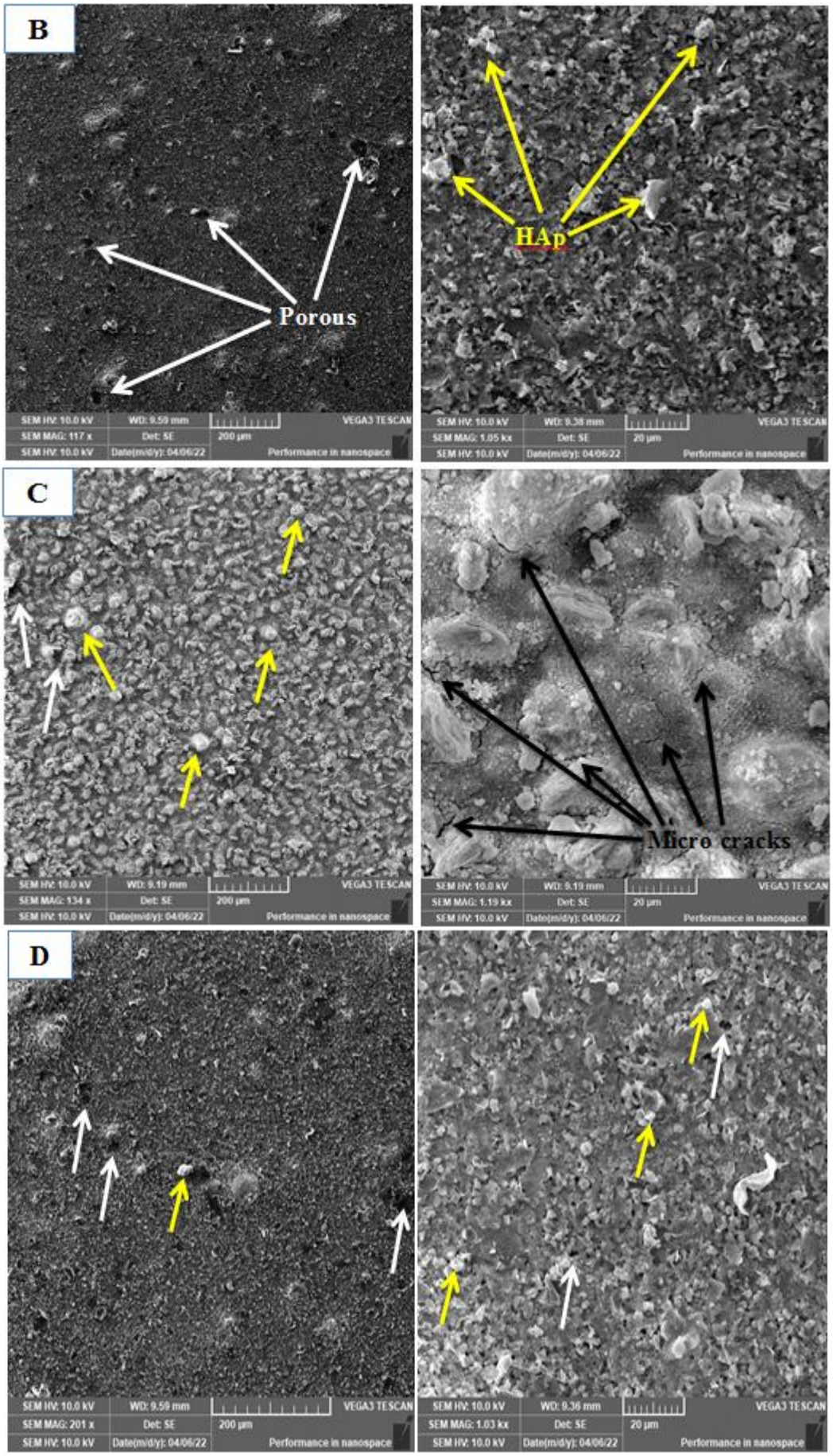
B
Porous
HAp
C
Micro cracks
D

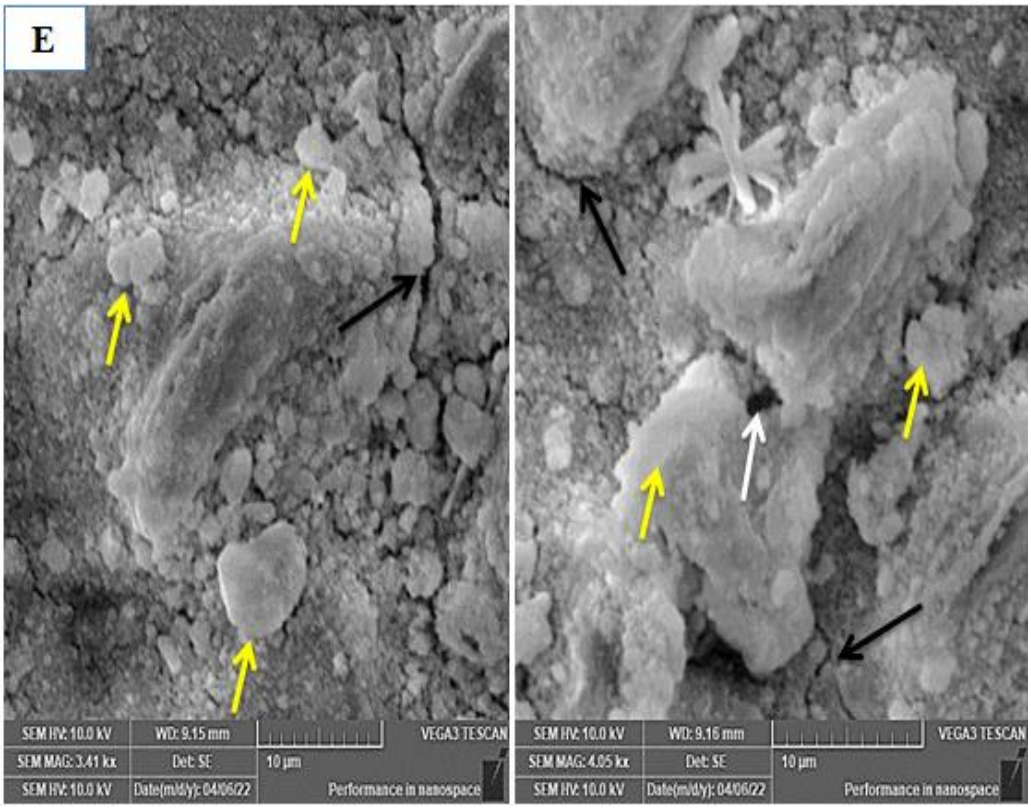


**Figure (4.13):** Coating Surface Morphology By the FESEM of (A) HAp Coating, (B) Gr Coating, (C) CMC Coating, (D) FG Coating, and (E) Ternary Coating Deposited By EPD Method in 40V at 60sec.

### 4.8.2 Surface Morphology of Coating after Immersion 6 Days

The procedure's purpose is to immersion the coated specimens to test the coating layers under harsh conditions that simulate, to some extent, the hostile environment of the human body that would destroy these layers for a long period.

The immersion of the coated specimens in Hank's solution (which contains salts that would be hostile to the coating layers) in itself is a great challenge to know the behaviour of these layers (HAp, Gr, CMC, and ternary coatings) and their resistance to the harsh conditions that surround them.

FESEM images of specimens showed grain boundaries and pores of different sizes, as indicated in Figures (4.14) to (4.17). The coating conditions were constant for all coatings (40V, 60S). The effect of additions on the structure of the hydroxyapatite coating after immersion for

6 days can be observed in terms of the distribution of pores, cracks and surface roughness, especially the addition of graphene in the Figure (4.14), which shows the uniform distribution of graphene, which gave an integrated structure that corresponds With the results of roughness and contact angle previously mentioned.

It can be concluded that immersion of the coated specimens in Hank's solution for 6 days (which can be considered an accelerated period simulating the living of these coated implants inside the human body) did not affect the microstructure and did not weaken the adhesion of this layer on the substrate alloy as mentioned previously but rather increased its strength and stability based on the coexistence of the Hank's solution with coating layers within the specified period.

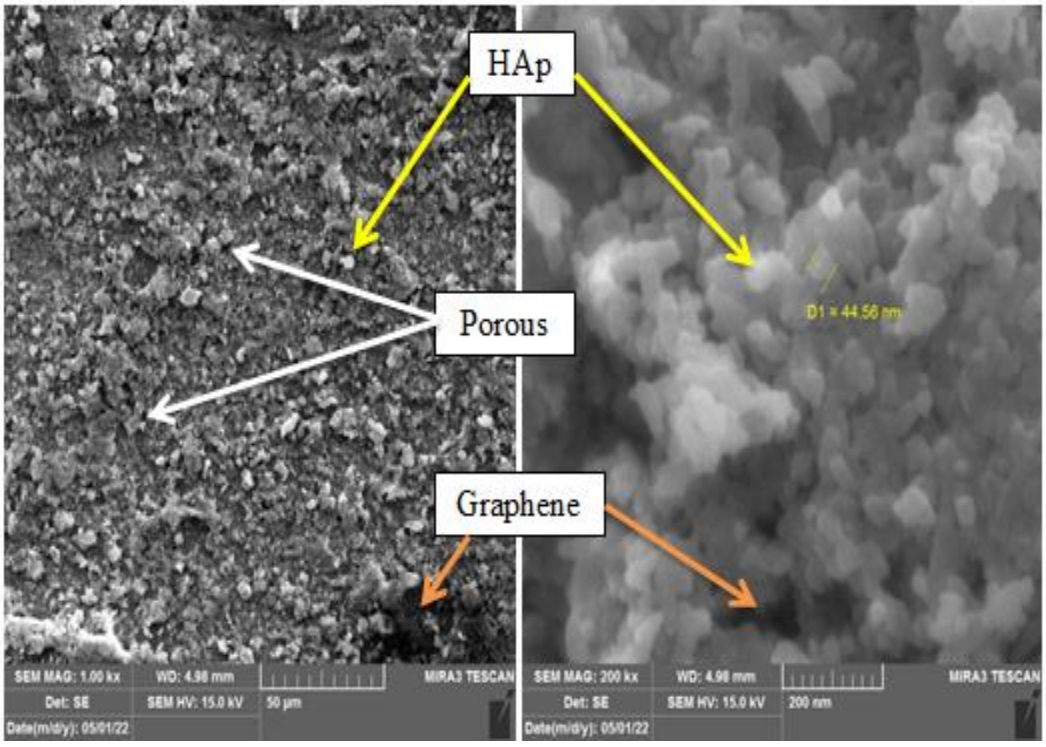


**Figure (4.14):** FESEM Images for Graphene Coating (G2-Specimen) after 6 Days Immersion.

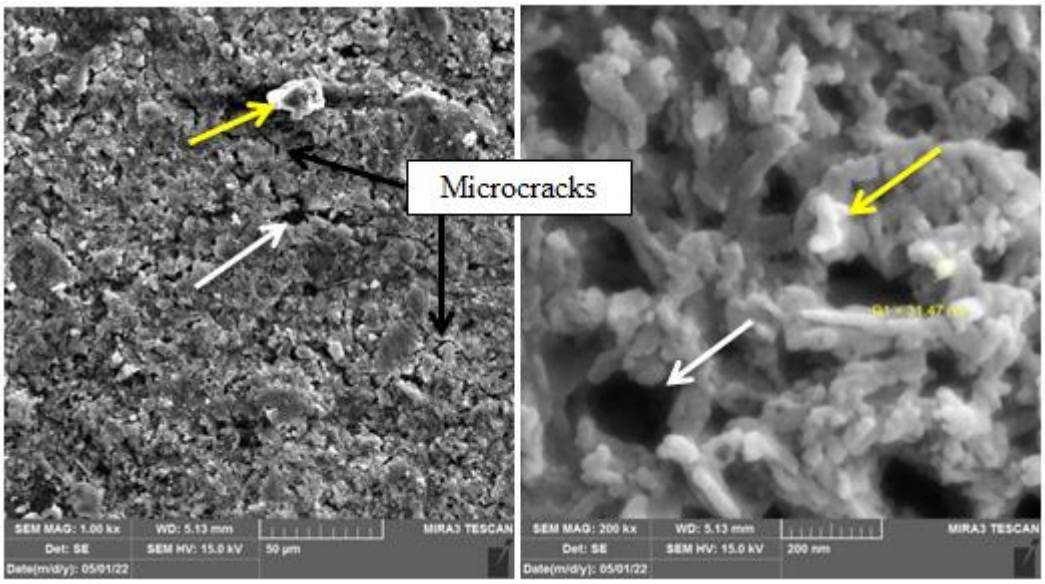


**Figure (4.15):** FESEM Images for CMC Coating (C2-Specimen) after 6 Days Immersion.

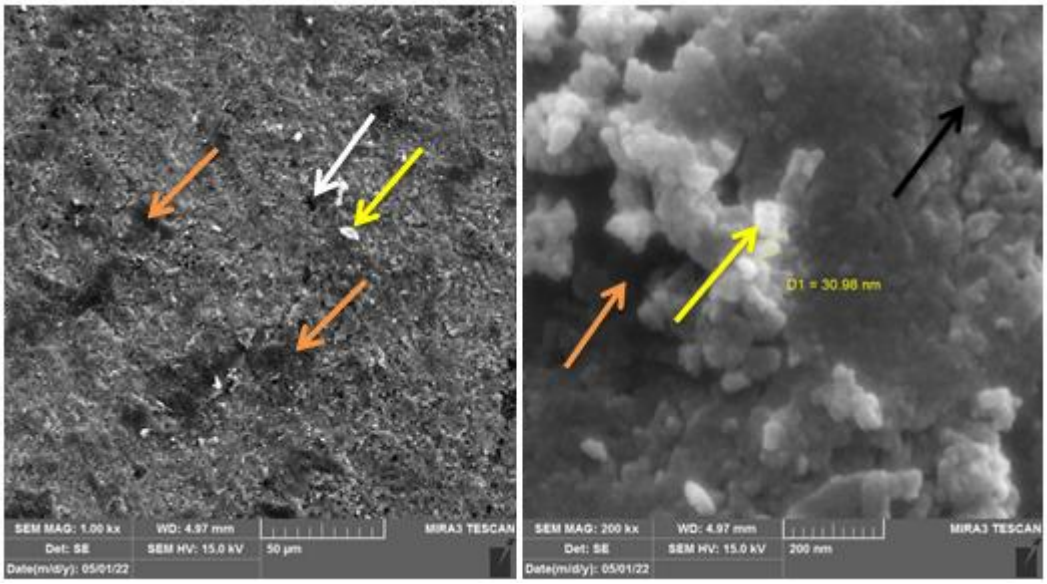


**Figure (4.16):** FESEM Images for Ternary Coating (M2-Specimen) after 6 Days Immersion.

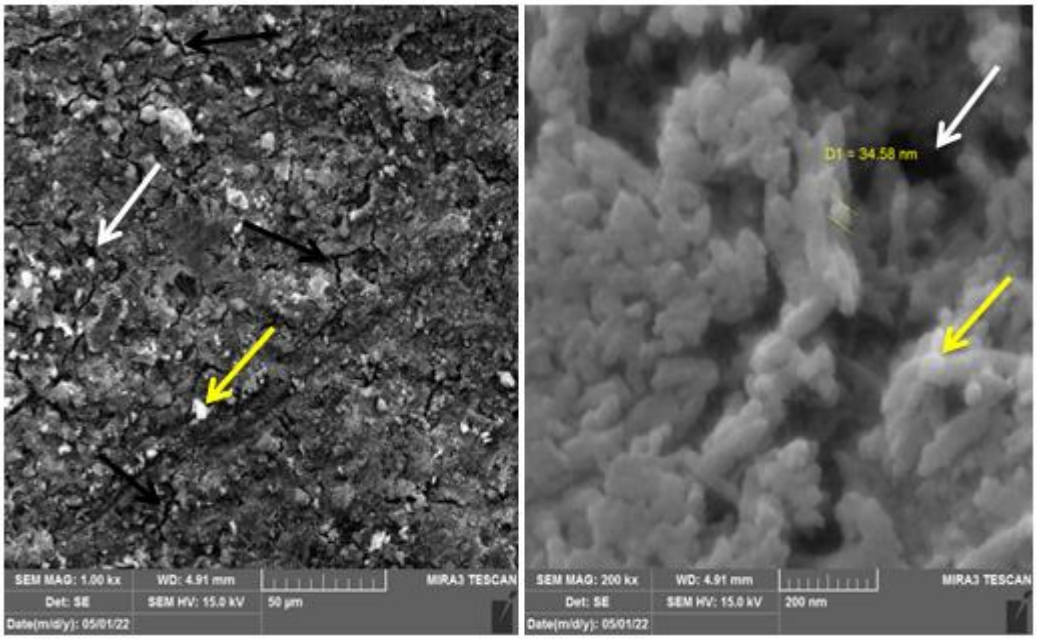


**Figure (4.17):** FESEM Images for HAp Coating (H-Specimen) after 6 Days Immersion.

Figures from (4.18) to (4.21) show the line EDS results for all coated specimens (HAp, HAp-Gr, HAp-CMC, and ternary coating). As can be seen, the results of EDS analysis were relatively close to the percentage of addition because the values gained from EDS analysis do not cover the total area, only the liner where the electron stroke [153]. The results of EDS also supported the above microstructure in terms of the presence and distribution of the additives along the specific microstructure.

In general, the results of EDS proved in all the figures below that the coatings were deposited distinctly and noticeably on the surface of the Ti-13Nb-13Zr alloy, which supports the previous and subsequent results that were made on the surface of these coatings. It was also confirmed that the applied voltage was suitable for depositing the graphene coating homogeneously mixed with hydroxyapatite for 60 seconds and for the rest of the coatings.

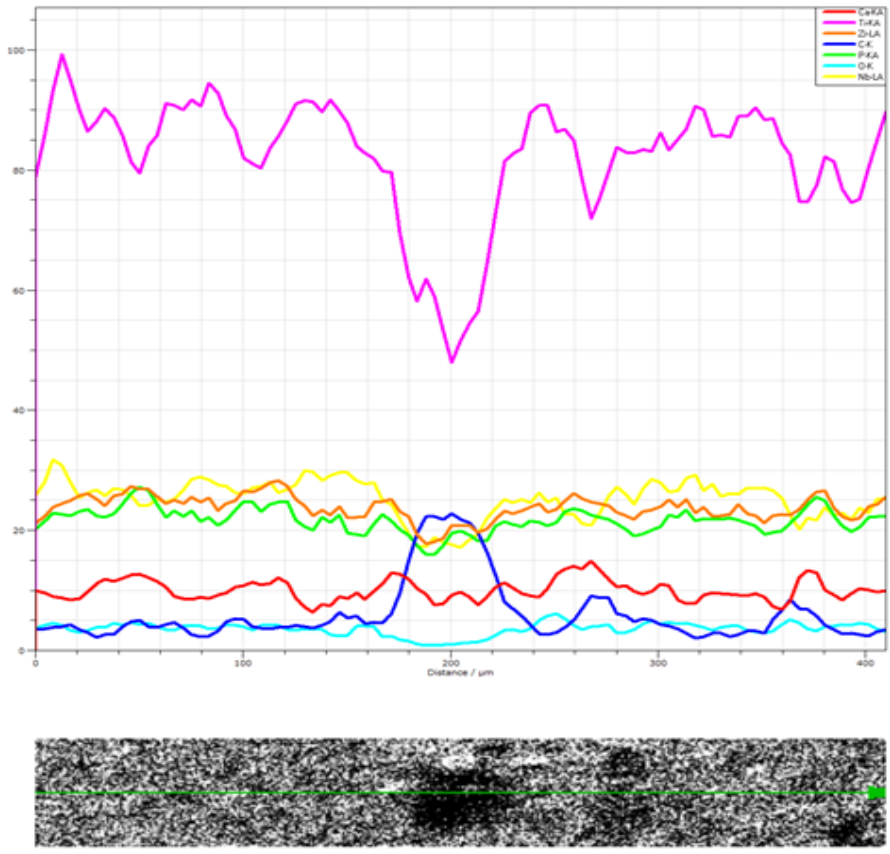


**Figure (4.18):** EDS Spectrum for Graphene Coating (G2-Specimen) after 6 Days Immersion.

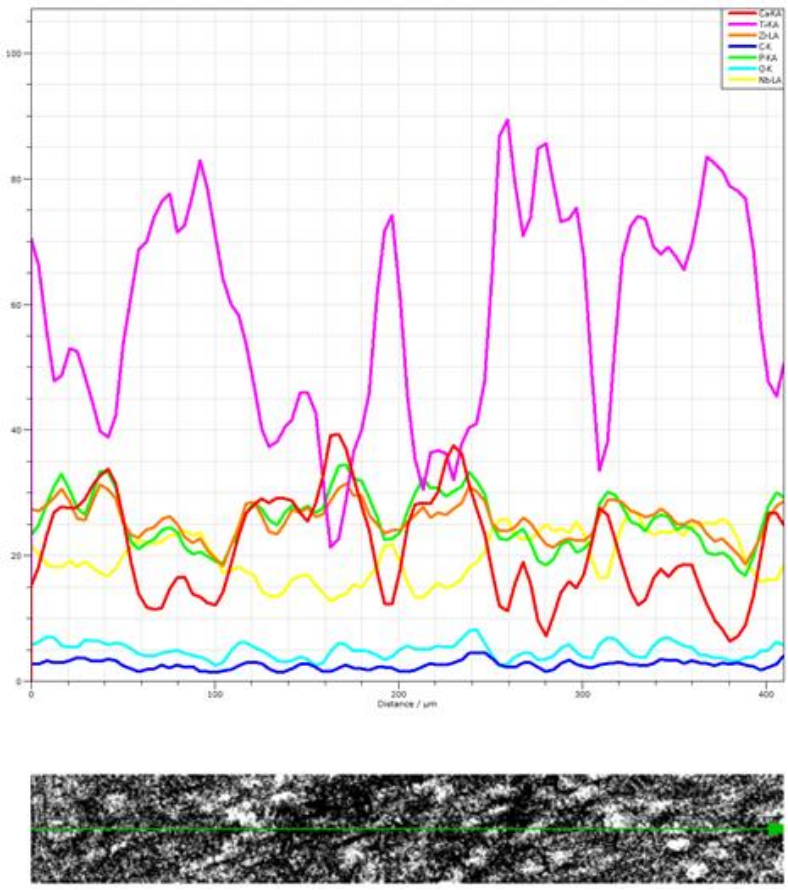


**Figure (4.19):** EDS Spectrum for CMC Coating (C2-Specimen) after 6 Days Immersion.

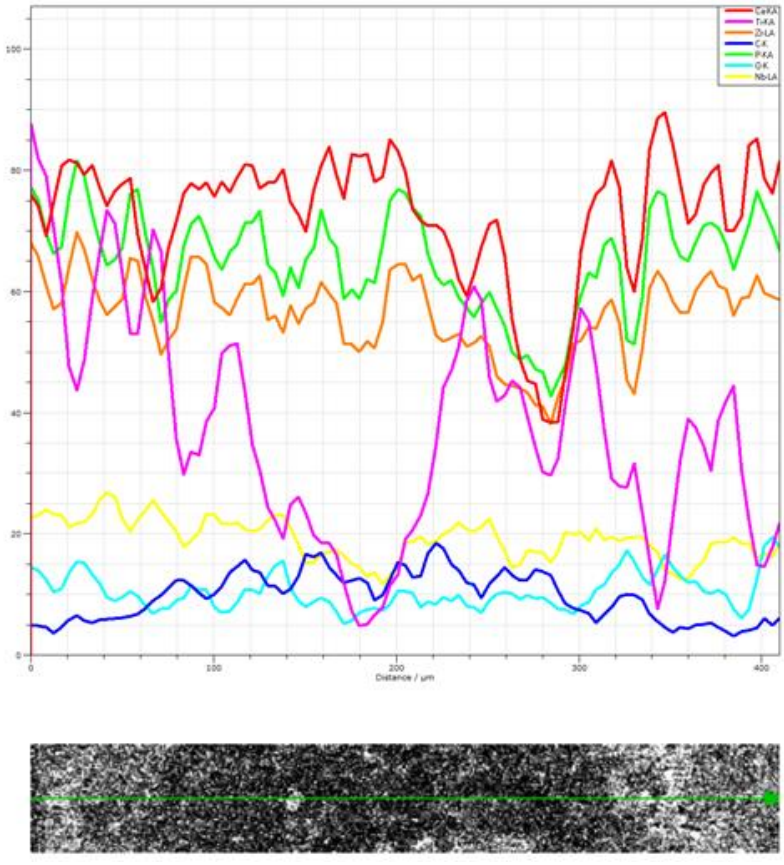


**Figure (4.20):** EDS Spectrum for Ternary Coating (M2-Specimen) after 6 Days Immersion.

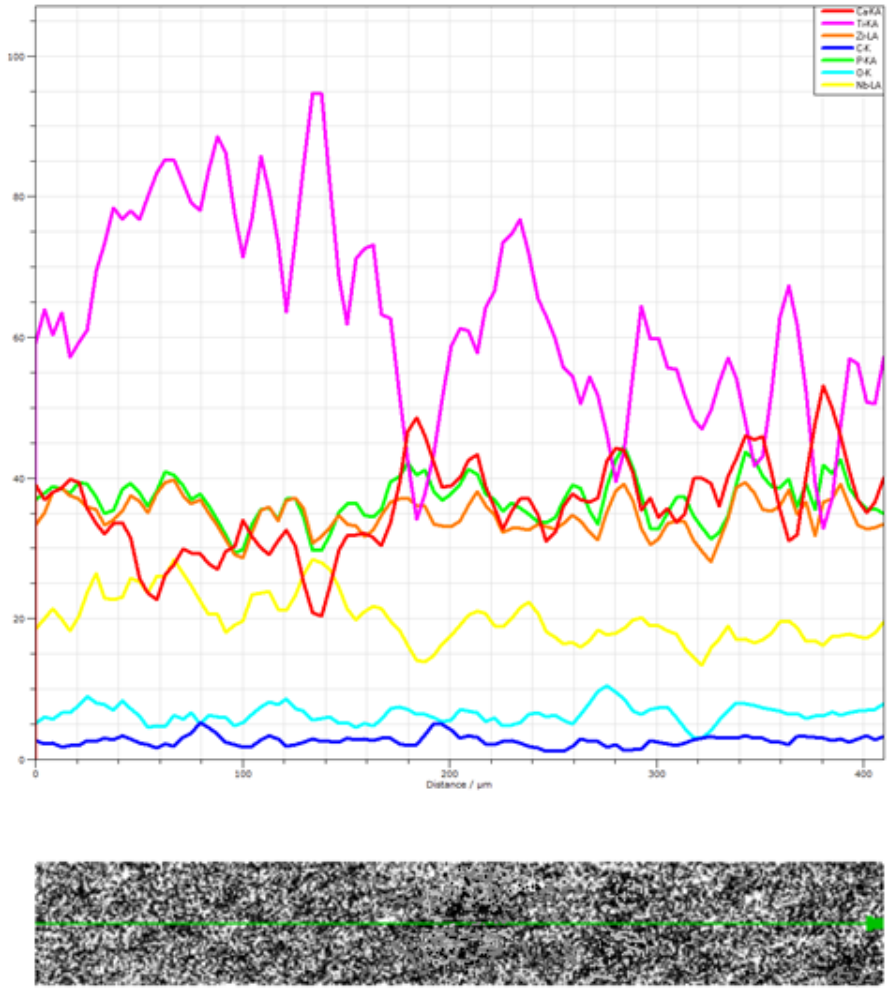


**Figure (4.21):** EDS Spectrum for HAp Coating (H-Specimen) after 6 Days Immersion.

## 4.9 Dry Wear Test

Specimens with a diameter of 13 mm as uncoated, hydroxyapatite-coated, and additive ( graphene, Carboxymethyl cellulose, Ternary coating, and functional gradient) subjected to dry wear test under various loads and for several time.

The loads applied to the samples were selected according to previous experiments and research [154, 155, 156]. The load was 5 N (as a starting or ending point) with different times (5,10, 15, 20, and 25).

**5 Newtons as an ending point**, loads (1, 3 and 5 N) were tested and there was no sensitivity to the weight difference for (1 and 3 N) loads as shown in Figure (4.22).

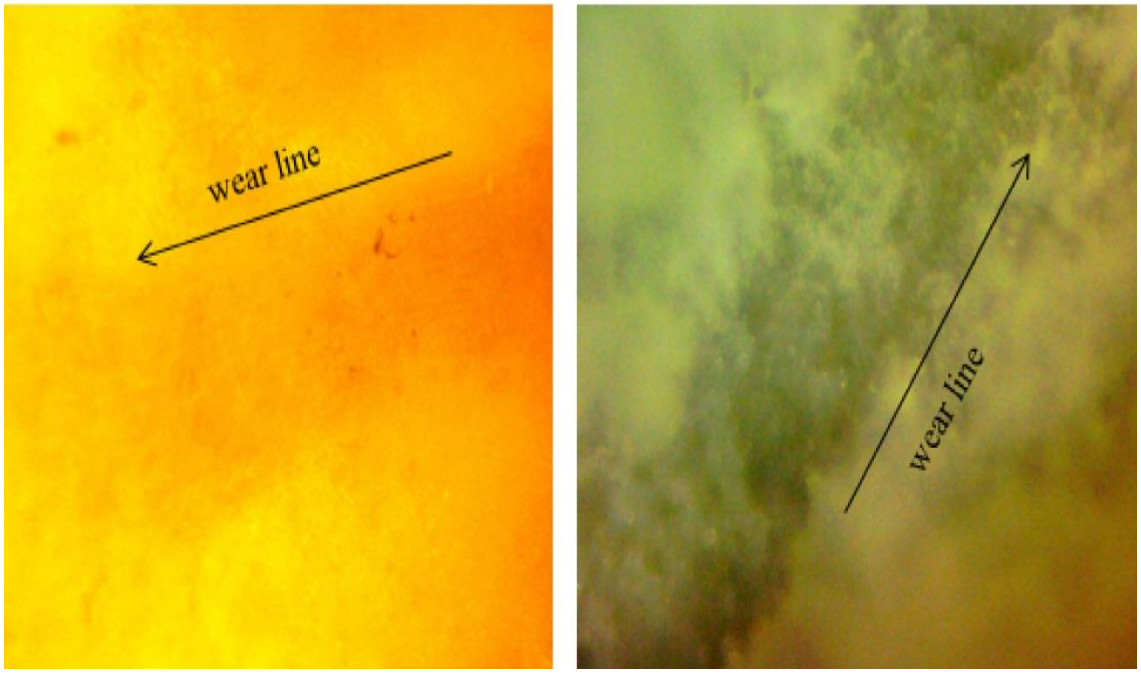


**Figure (4.22):** Optical Microscopy Images of the H Sample for 25 Min (A) 3N and (B) 1N.

**5 Newtons as a starting point**, loads (5, 10 and 15 N) were tested and approved for a slight weight loss as shown in the tables and figures below.

The Figures below show the losses of volume as a function of time. Regardless of the chemical composition and microstructure of alloys, the volume losses of alloys (with and without coating) increases with the increased loads used, but there is clear stability of volume losses for some coated alloys with increasing time for all loads.

From Figures (4.23) It is possible to note the relative stability on volume loss of graphene coating (especially the G4 and F specimens) on Ti-13Nb-13Zr alloys(For all loads ) this indicates the complete protection of the loaded layer over time compared to Ti-13Nb-13Zr alloy uncoated and all coatings (CMC or Ternary coating). This is Attributable to the hardness of this coating which is difficult to remove during time, so, it is subjected to the Archard's law which States "weight loss for materials that is inversely proportional to the material hardness value"[157]. In addition to, the high adhesion of this layer as mentioned earlier, which makes it more stable and cohesive on the surface of the Ti-13Nb-13Zr alloy as shown in the Figures(4.24 … 4.31).

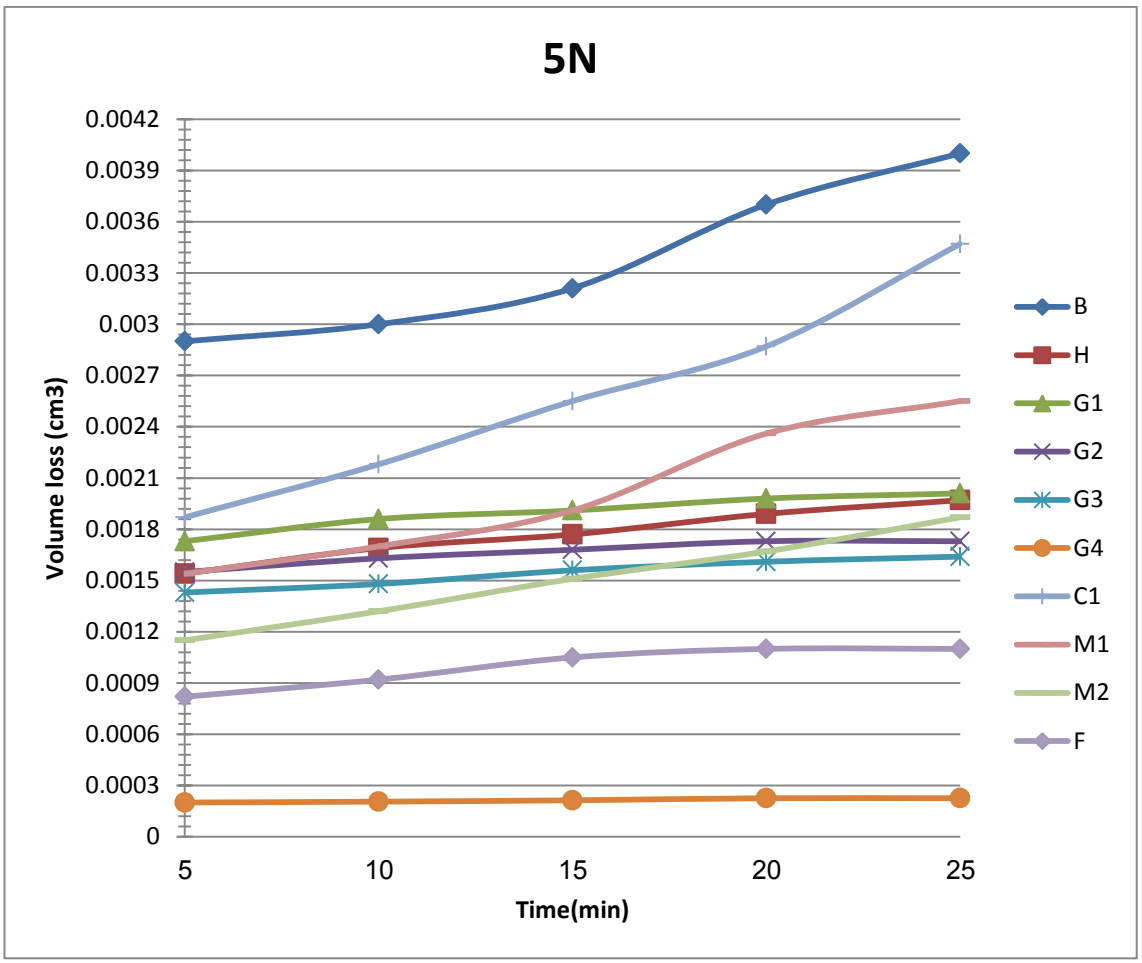
5N
Volume loss (cm3)
0.0042
0.0039
0.0036
0.0033
0.003
0.0027
0.0024
0.0021
0.0018
0.0015
0.0012
0.0009
0.0006
0.0003
0
5
10
15
20
25
Time(min)
B
H
G1
G2
G3
G4
C1
M1
M2
F

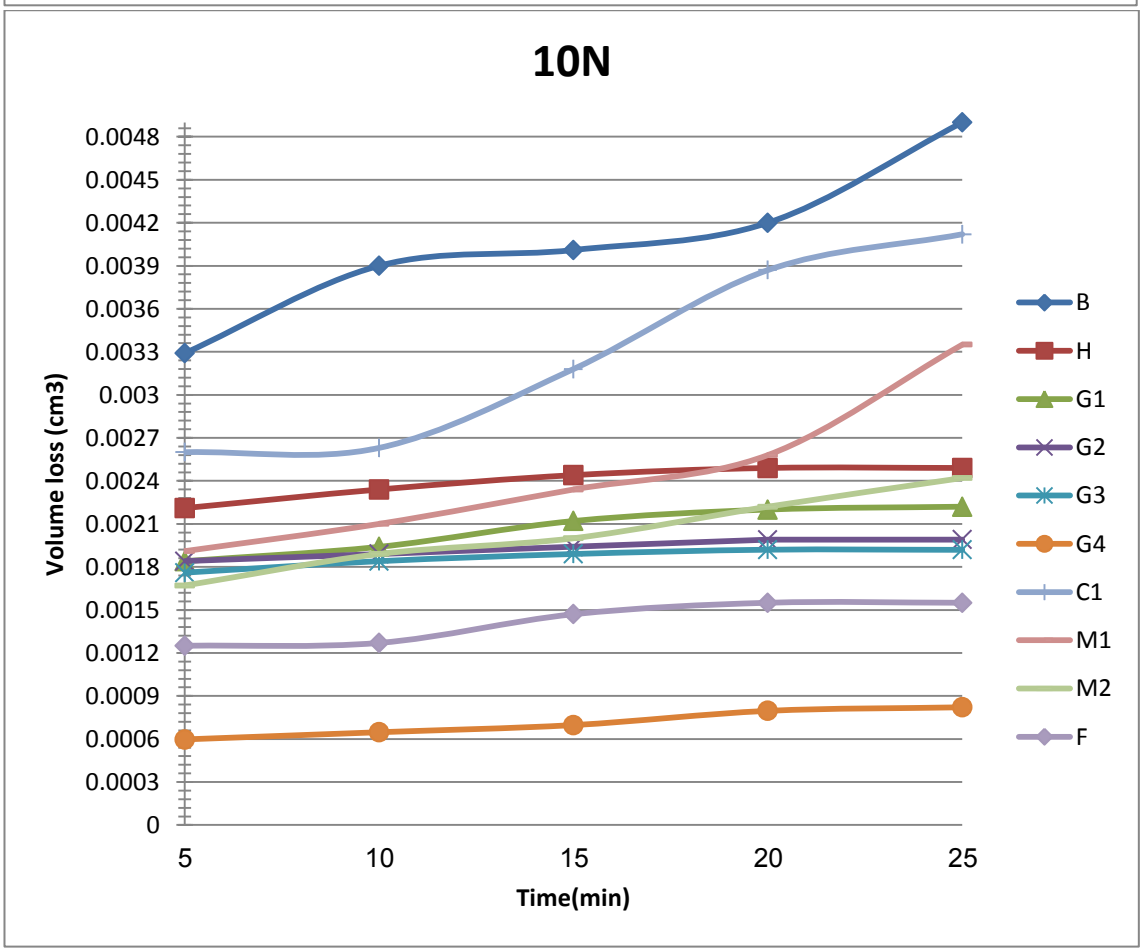
10N
Volume loss (cm3)
0.0048
0.0045
0.0042
0.0039
0.0036
0.0033
0.003
0.0027
0.0024
0.0021
0.0018
0.0015
0.0012
0.0009
0.0006
0.0003
0
5
10
15
20
25
Time(min)
B
H
G1
G2
G3
G4
C1
M1
M2
F

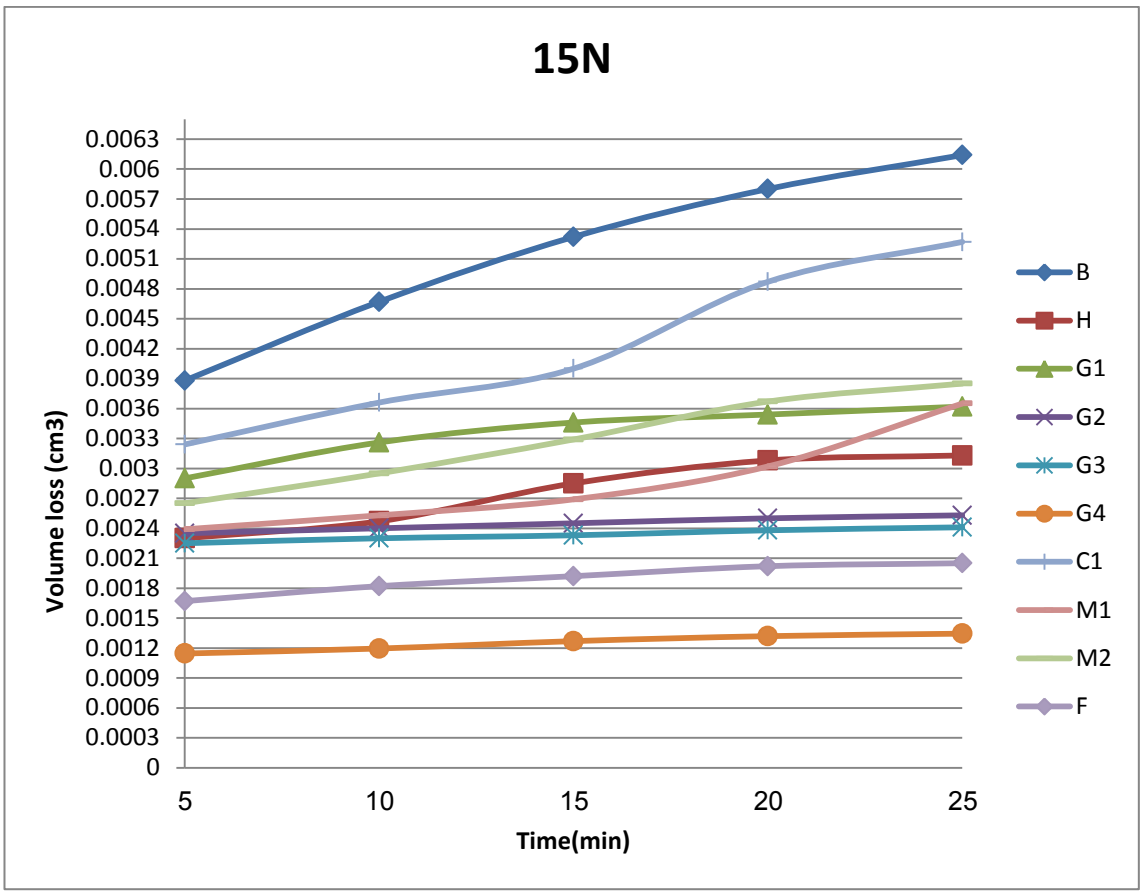


**Figure (4.23):** Volume Losses vs. Time for (B, H, G1, G2, G3, G4, C1, M1, M2 and F) Alloys under (5, 10 and 50N) Loads.

Conversely, the coating (H, C1, M1, and M2), there is an increase in the loss of volume to all loads if it is compared to (Gr and FG) coating, this is due to the decrease in the hardness of this coating compared to other coatings hardness and thus can remove this layers on the surface of the alloy easily as shown in the Figures (4. 32 and 4.33).

Although there is variation in volume loss for (Gr, C1, M1, M2 and F) coatings on the base alloy, all these coatings reduce the volume loss of the Ti-13Nb-13Zr alloy.

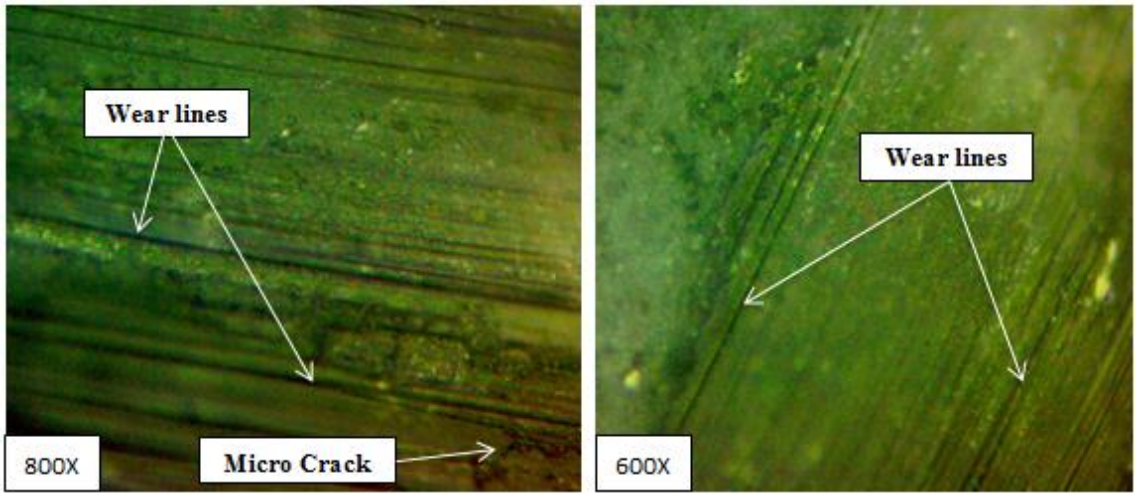


**Figure (4.24):** Microstructure for G4 Specimen by Use (LOM) after Wear Test under 15N Load and 25min Time.

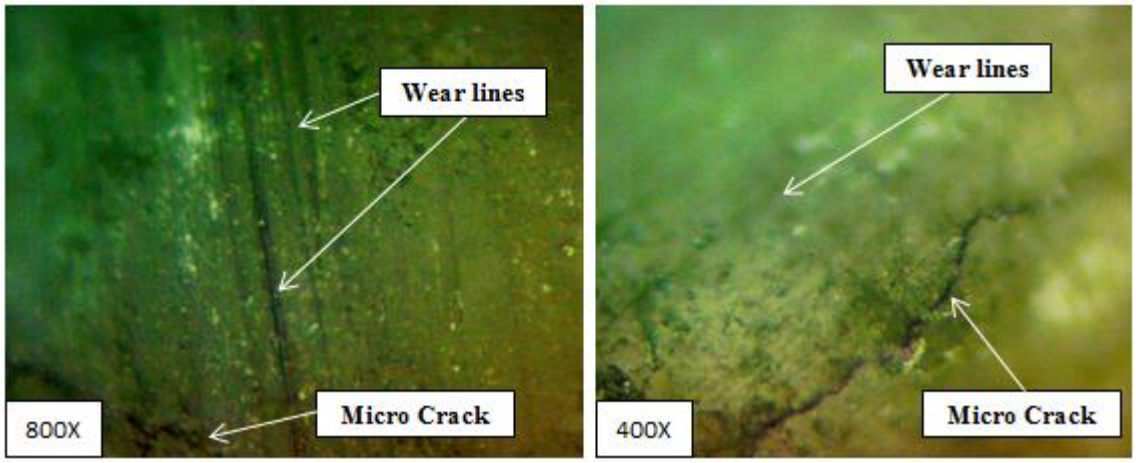


**Figure (4.25):** Microstructure for G3 Specimen by Use (LOM) after Wear Test under 15N Load and 25min Time.

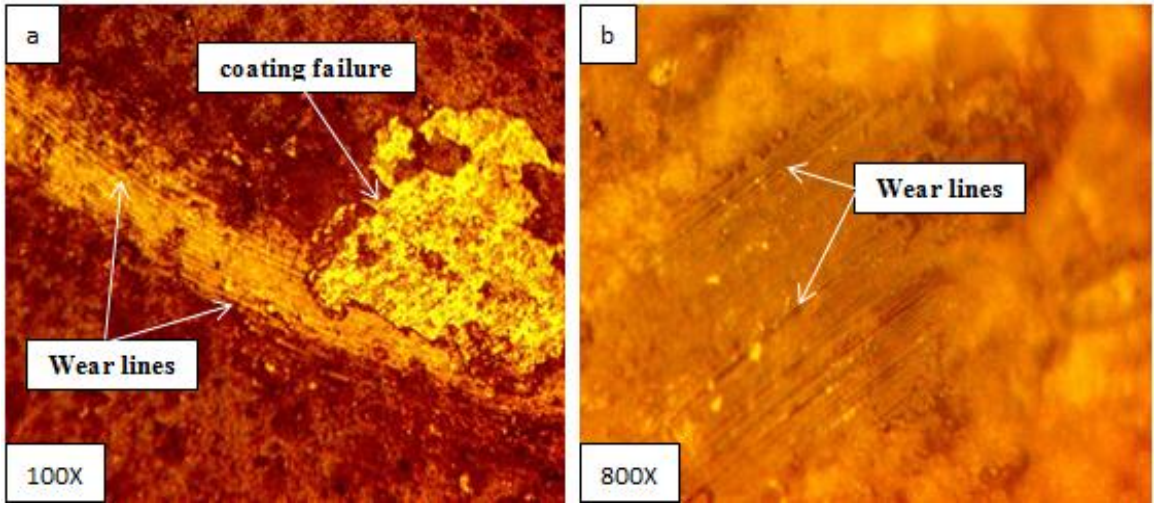


**Figure (4.26):** Microstructure for G2 Specimen by Use (LOM) after Wear Test under (a) 5N, (b) 15N Load at 25min.

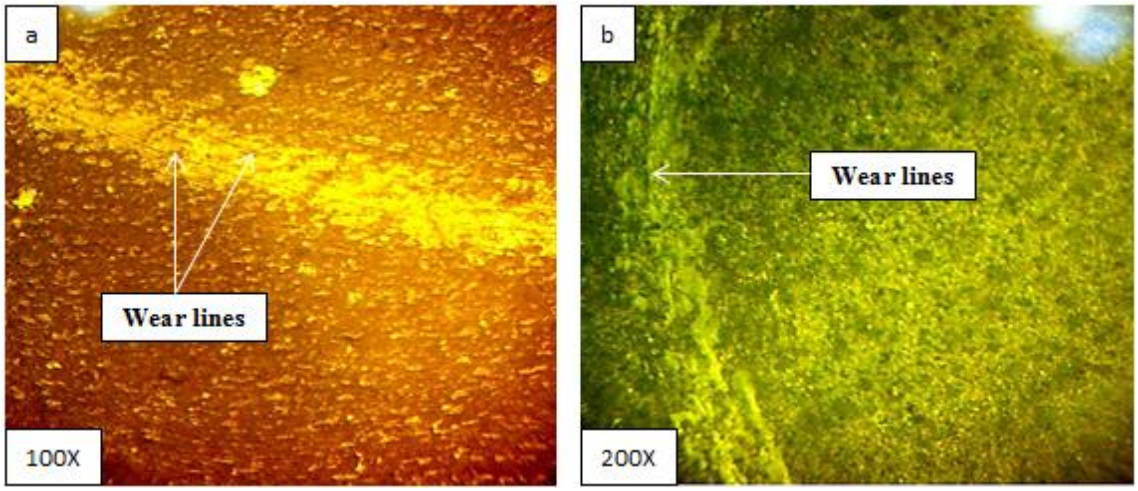


**Figure (4.27):** Microstructure for G1 Specimen by Use (LOM) after Wear Test under (a) 15N, (b) 5N Load at 25min.

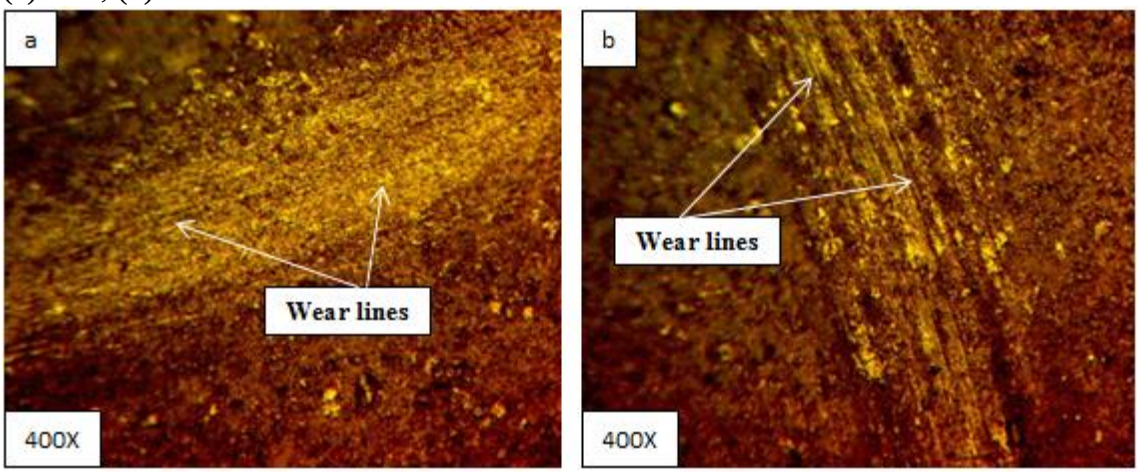


**Figure (4.28):** Microstructure for F Specimen by Use (LOM) after Wear Test under (a) 5N, (b) 15N Load at 25min.

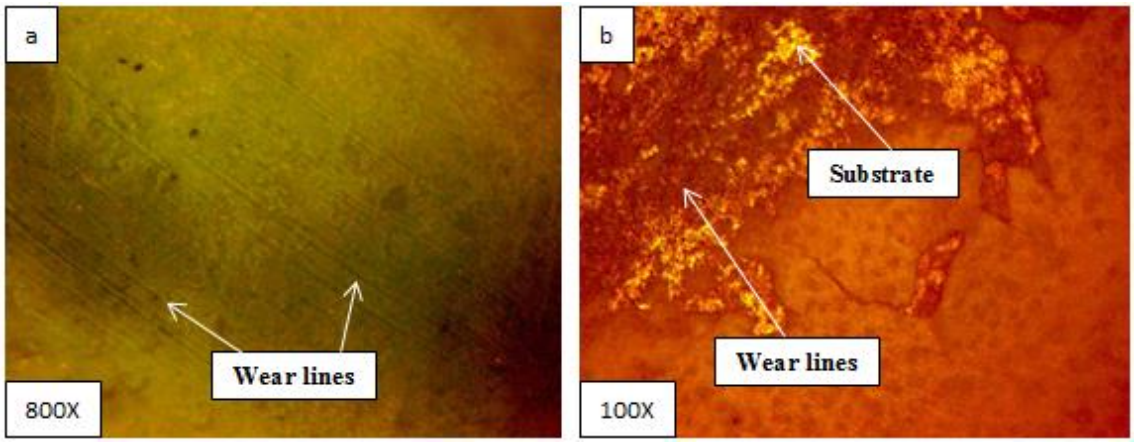


**Figure (4.29):** Microstructure for H Specimen by Use (LOM) after Wear Test under (a) 5N, (b) 15N Load at 25min.

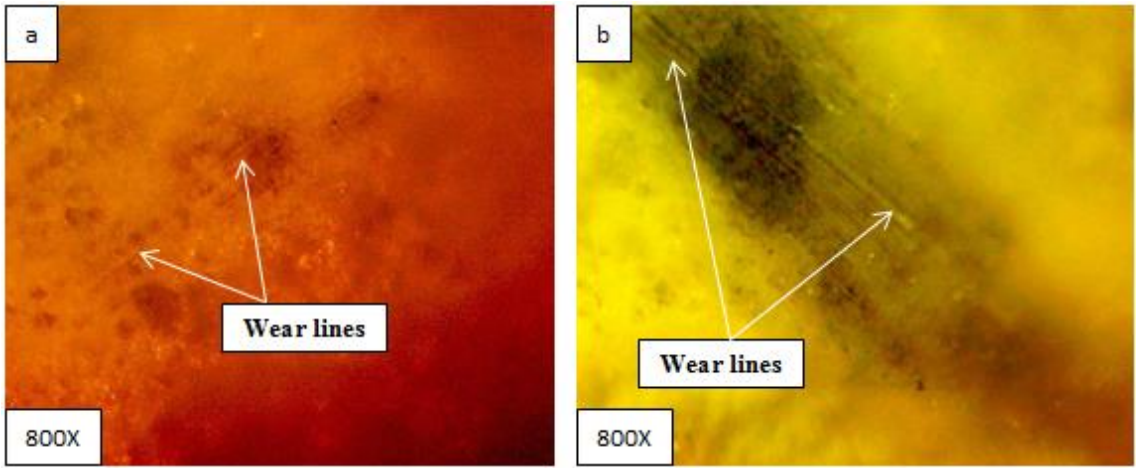


**Figure (4.30):** Microstructure for C1 Specimen by Use (LOM) after Wear Test under (a) 5N, (b) 15N Load at 25min.

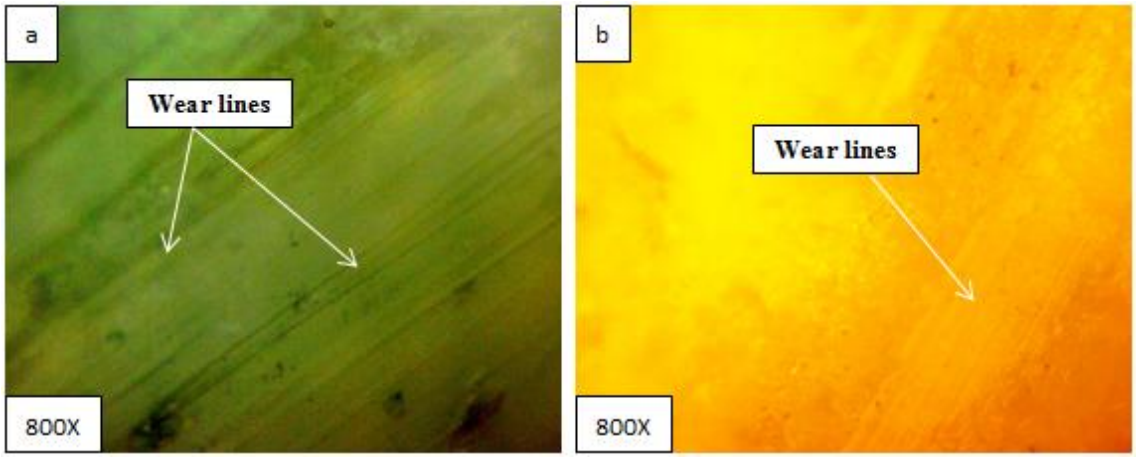


**Figure (4.31):** Microstructure for M2 Specimen by Use (LOM) after Wear Test under (a) 15N, (b) 5N Load at 25min.

The microstructure in the Figures (4.24) ... (4.31) shows the morphology of the worn surface of the tested specimens, where the wear evidence can be seen on the worn surfaces of all the alloys. Where the wear areas, as well as plastic deformation can be seen on the tracks of wear, Which results from the penetration of the solid abrasive ball to the coating surface. The depth of the penetration depends on time, load and the hardness of the tested coating.

For the samples that were not mentioned above (C2, C3, M3 and M4), this is due to the fracture of the coating layer adjacent to the wear line as shown on below Figures (4.32 and 4.33), which can be attributed to the weak adhesion of the coating on the surface of the alloy, which makes this layer vulnerable to breakage and damage when exposed to any applied load. This is agree with the adhesion strength and SEM results

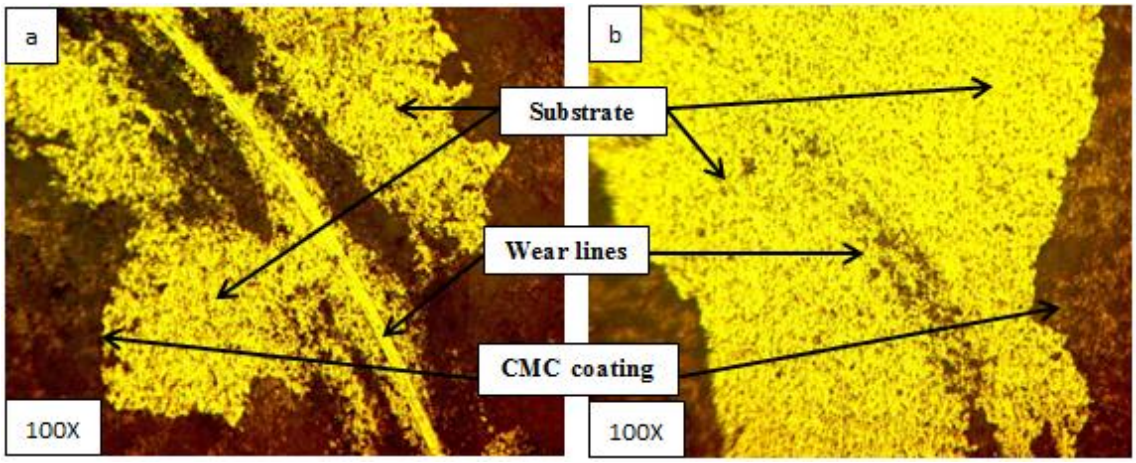


**Figure (4.32):** Microstructure by Use (LOM) after Wear Test for (a) C2, (b) C3 Specimens Under 5N Load at 5min.

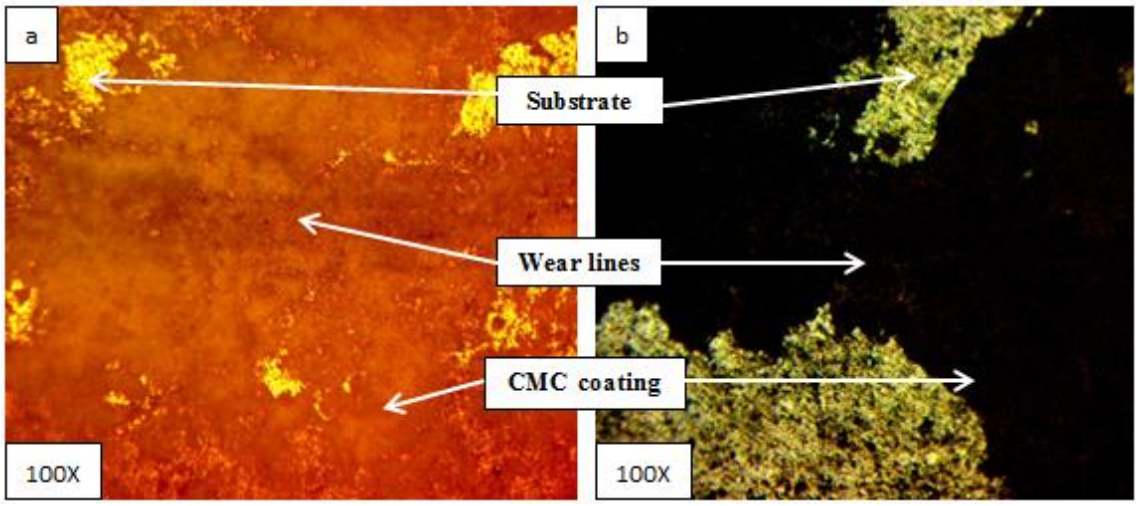


**Figure (4.33):** Microstructure by Use (LOM) after Wear Test for (a) M3, (b) M4 Specimens Under 5N Load at 5min.

## 4.10 Electrochemical Tests

### 4.10.1 Open Circuit Potential (OCP)-Time Measurement

The OCP-time is measured with respect to SCE in Hank's solution at (37)℃±2 for all tested alloys (coated and uncoated). Figures (4.34, 4.35 & 4.36) displays the evolution of corrosion potential of the alloys throughout time. The minimum time period from 0 up to 120 min as shown in specimen (B) and the maximum time period of up to 200 min as shown in specimen (M3)) and with interval of 5 min were potentially reported. The mean values of the OCP were recorded by using two specimens for each coating.

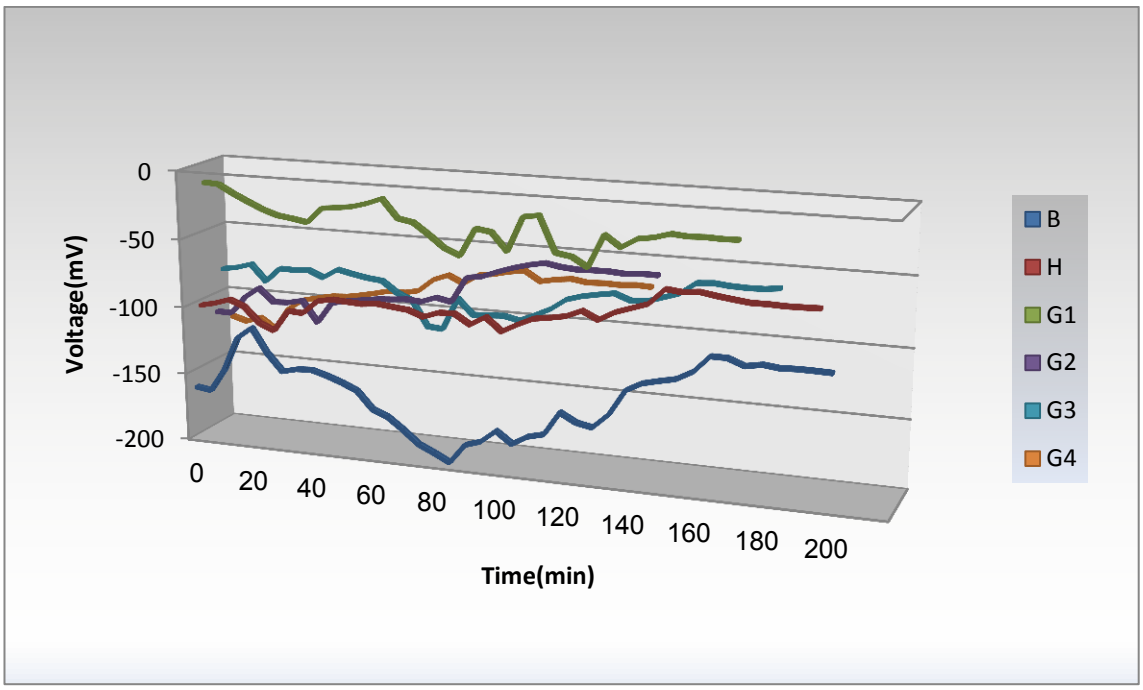


**Figures (4.34):** The OCP-Time for Base, HAp and all Graphene percentage coating in Hank's Solution at(37±2)℃.

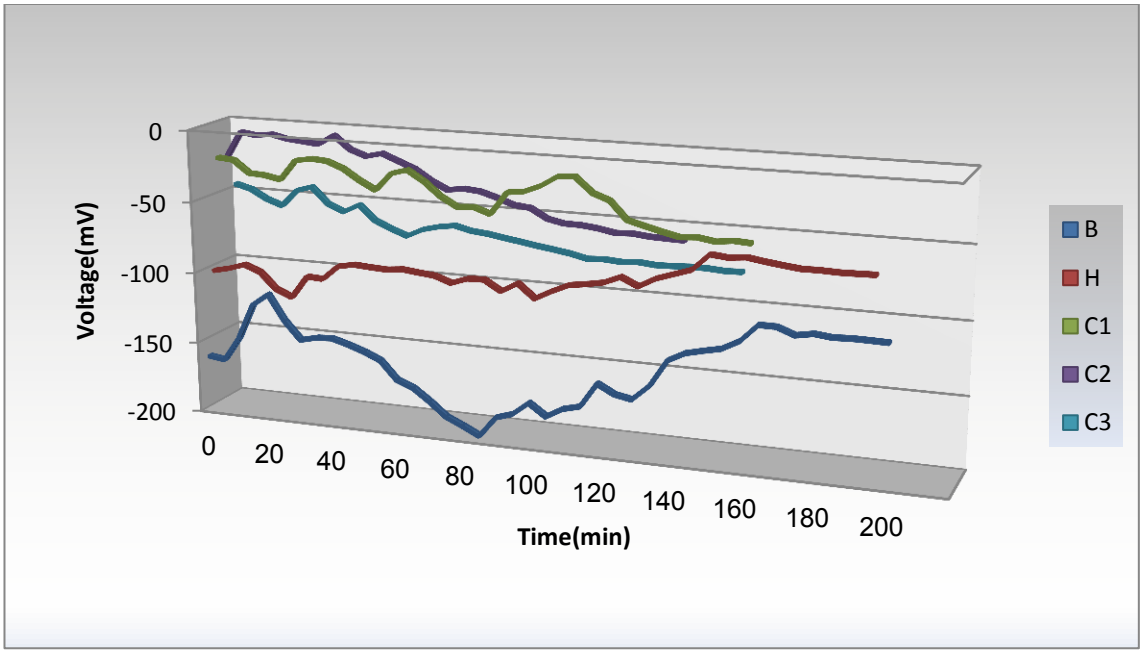


**Figures (4.35):** The OCP-Time for Base, HAp and all CMC percentage coating except for 1g addition, in Hank's Solution at(37±2)℃.

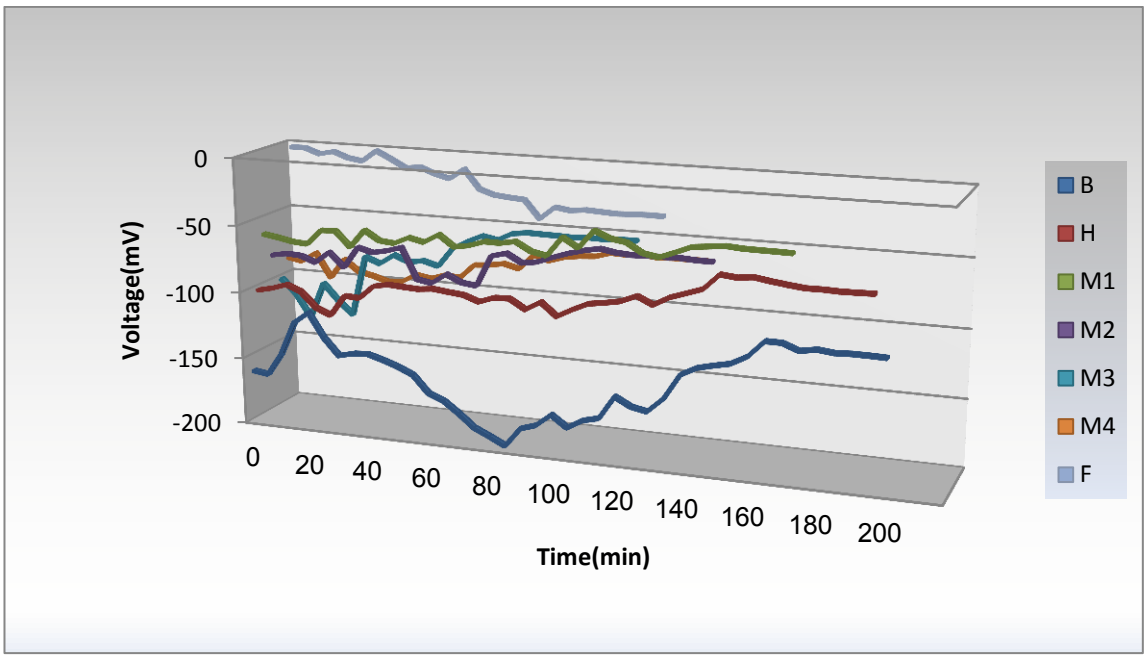


**Figures (4.36):** The OCP-Time for Base, HAp and all mix percentage with functional gradient coating in Hank's Solution at(37±2)℃.

The above Figures can be seen sharp gradients in $E_{ocp}$ for the uncoated alloy followed by the HAp-coated alloy with time compared to Graphene and CMC alloys, Ternary coating and in a functional gradient coating in Hank's solution, where these gradients in $E_{ocp}$ for especially base alloy, are attributed to destruction or inefficiency of the passive layer made by Ti-13Nb-13Zr alloy without coating, with a sign of declining or reducing these sharp gradients after the coating process.

It also notes the values of $E_{ocp}$ for the base alloy and the HAp-coatings are increasing negatively compared to the coated samples that have less negative values of $E_{ocp}$. This proves an increased corrosion resistance to coated alloys unlike the base alloy without coating, it is known that the most negative $E_{ocp}$ values have a high corrosion tendency, (Zarka. M et.al confirmed this in their research) [158]. Therefore, the negatively low values can be considered for the coated samples (especially the graphene coating (single or in function gradient) as shown in the Figure (4.37) below as less corrosive and with a more stable and homogeneous layer and a higher resistance to the aggressive surrounding conditions represented by Hank's solution.

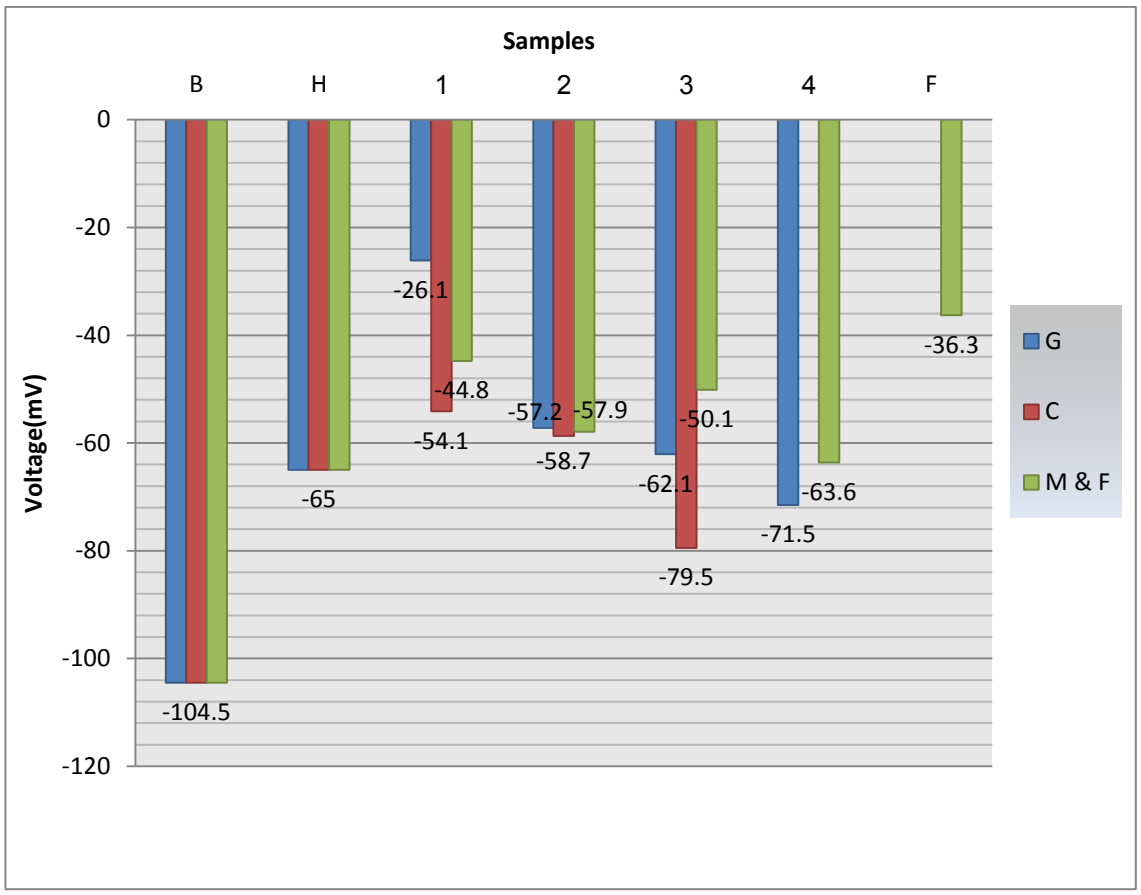


**Figure (4.37):** Shows the Values of $E_{ocp}$ Adopted in the Tafel Test.

### 4.10.2 Potentiodynamic polarization

The corrosion behaviour of all used alloys (coated and uncoated) in Hank's solutions has been studied. In addition, the effect of corrosion on the microstructure has been illustrated in Hank's solutions using Potentiodynamic polarization to give estimation about the corrosion behavior of alloys (coated and uncoated).

The corrosion parameters are corrosion current ($I_{corr.}$), corrosion potential ($E_{corr.}$) and corrosion rate resulted from weight loss test for the specimens in Hank's solution at 37±2℃ were illustrated in Tables (4.5) and (4.6).

Figures (4.38, 4.39, 4.40, and 4.41) shows the corrosion behaviors of the Ti-13Nb-13Zr alloy uncoating and Ti-13Nb-13Zr alloy with H, G, C, M, and F respectively coating evaluated from electrochemical test (Tafel test) and the results are summarized in Table (4.5 and 4.6)

Figure 4.38 shows the potentiodynamic polarization curves obtained from the electrochemical tests of the Ti-13Nb-13Zr alloy with B, H, G1, G2, G3, and G4 coating showing their passivation behaviour with respect to current density passed through the immersed samples. Compared to the Ti-13Nb-13Zr alloy uncoating, Ti-13Nb-13Zr alloy with H, G1, G2, G3, and G4 coating exhibited lower corrosion passivation potential ($E_{corr.}$) and current ($I_{corr.}$) values compared to the another additions ( C, M and F) in Figures (4.39, 4.40 and 4.41) as obtained from the Tafel fit of polarization curves. Moreover, the increases in percent additions of ( Gr, CMC, and Mix) to Ti-13Nb-13Zr alloy resulted in increases in the passivation potential and logarithmic current density, indicating increased polarization resistance (Rp) to elementary ratios for additions only.

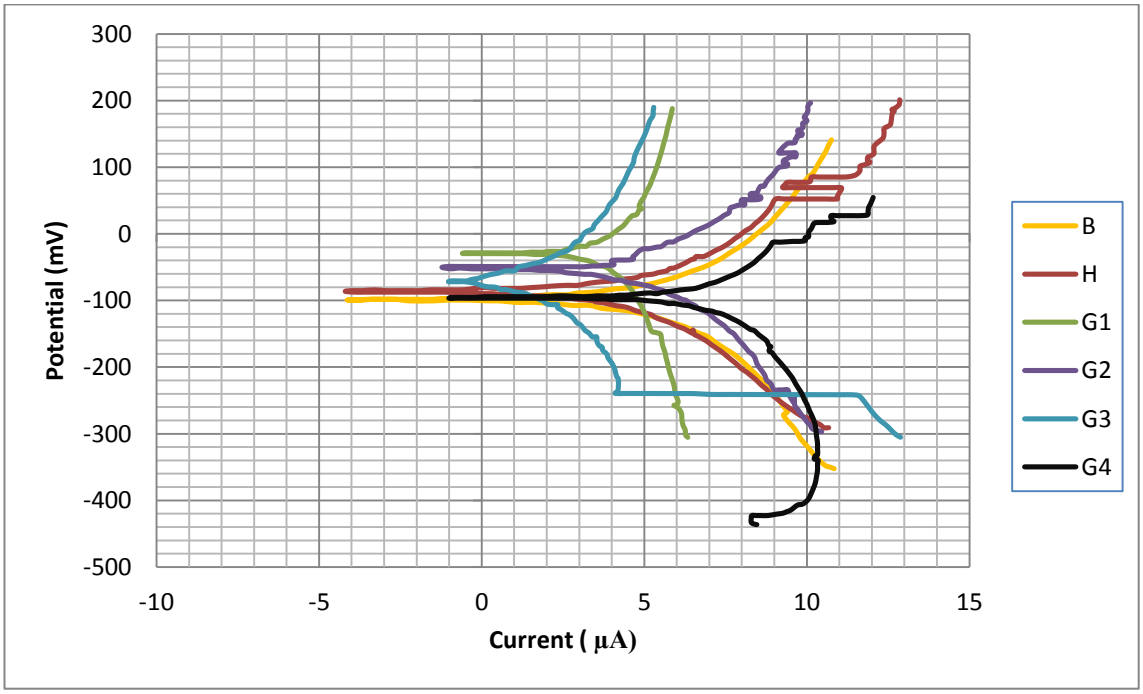


**Figure (4.38):** Potentiodynamic Polarization for B Alloy, H, G1, G2, G3, and G4 Coating in Hank's Solution.

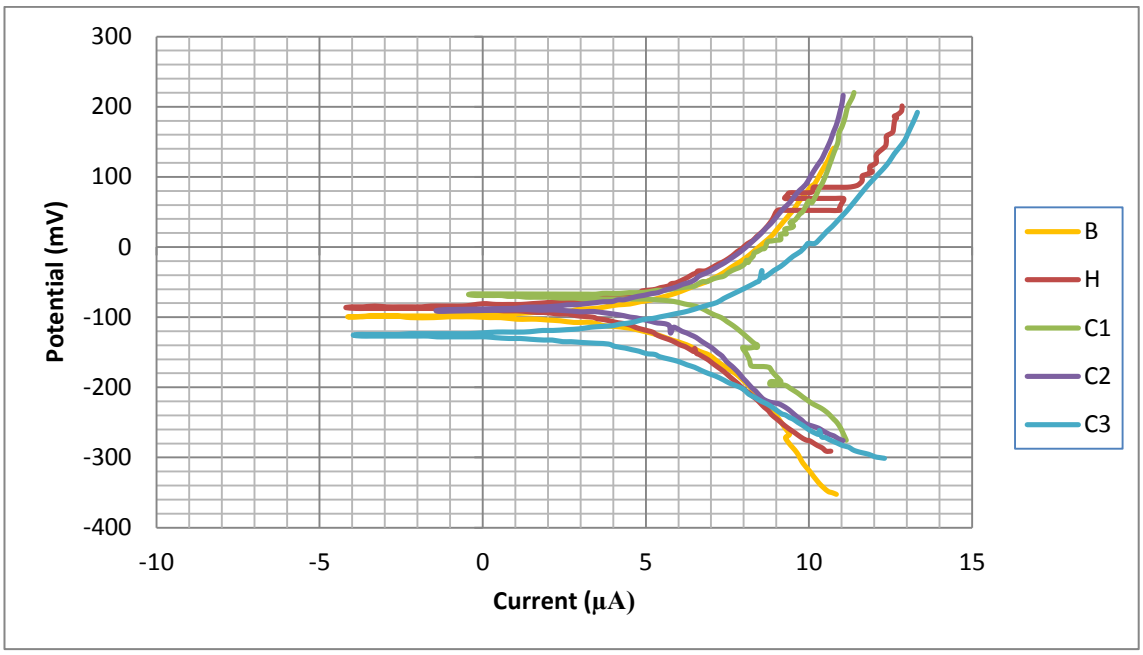


**Figure (4.39):** Potentiodynamic Polarization for B Alloy, H, C1, C2, and C3 Coating in Hank's Solution.

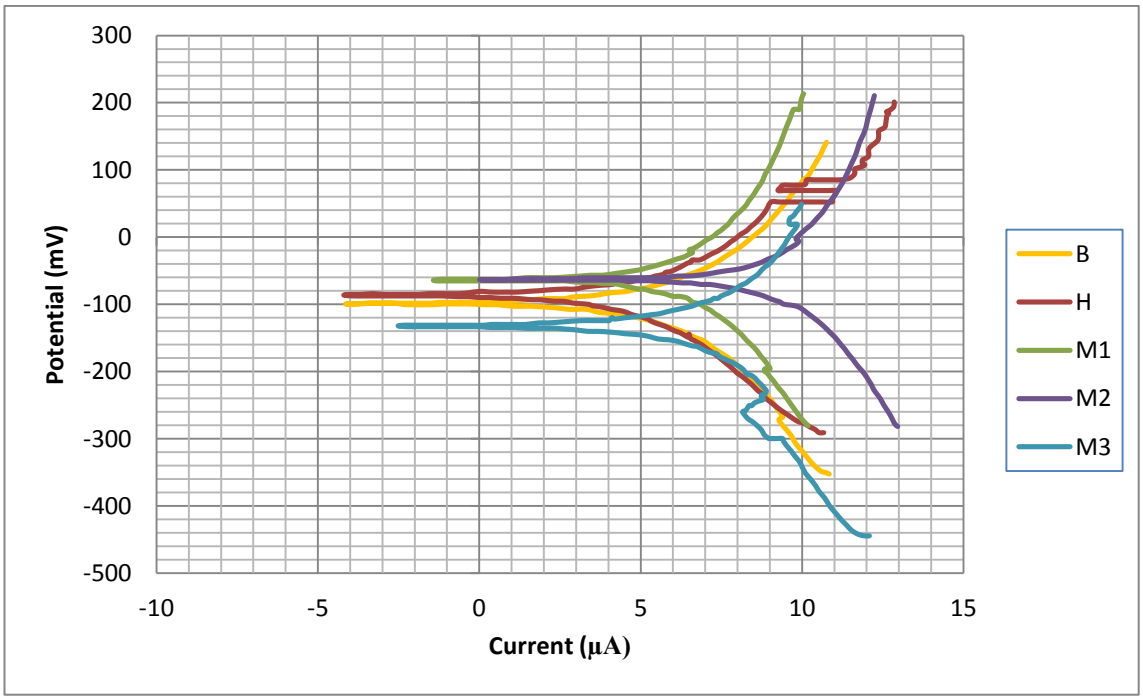


**Figure (4.40):** Potentiodynamic Polarization for B Alloy, H, M1, M2, M3, and M4 Coating in Hank's Solution.

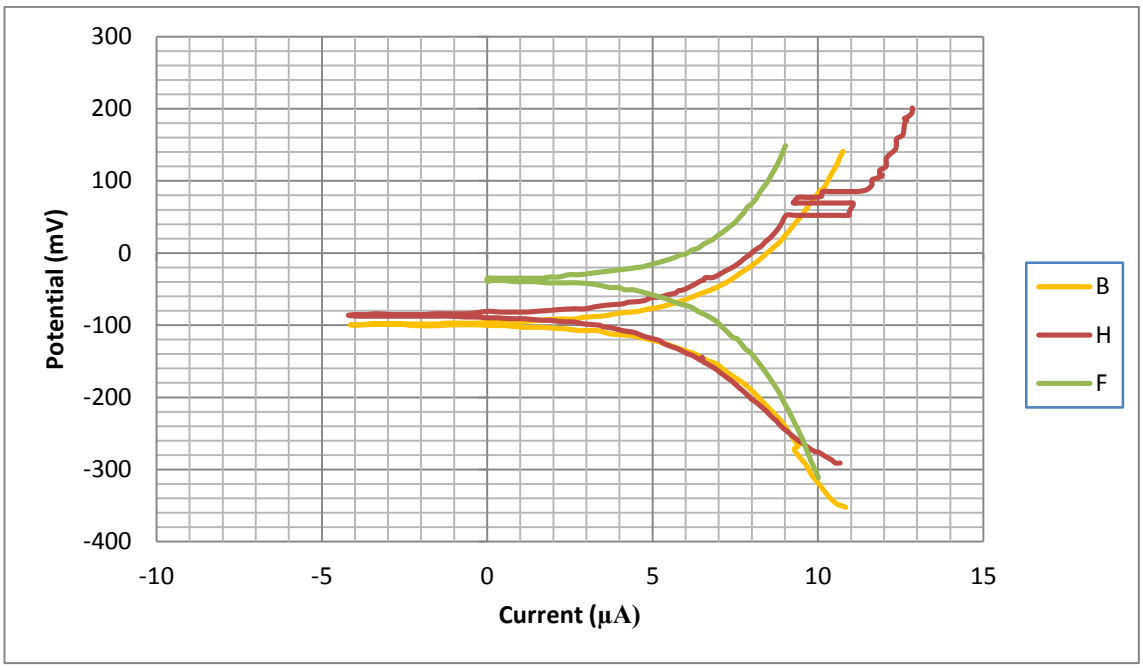


**Figure (4.41):** Potentiodynamic Polarization for B Alloy, H, and F Coating in Hank's Solution.

From Table (4.5), it can be seen that there is very great improvement in corrosion resistance of the B alloy with different additives of Graphene, but this improvement gradually decreases with the increase in the addition of graphene (G1: 96%, G2: 90%, G3: 49%, &G4: 15%) relative to the Base alloy without coating, and this improvement decreases until it reaches below zero when (1) gram is added relative to the HAp coating (G1: 94%, G2: 84%, G3: 21%, & G4: -32%). ($I_{corr.}$) and ($E_{corr.}$) for specimens are graded from (9.03 nA/cm²) (-27.4 mV) for G1 alloy to (792.85 nA/cm²) (-93.4 mV) for G4 alloy which are lower than B alloy which is (1.03 µA/cm²) (-102.8 mV), and which are lower than H alloy which is (763.38 nA/cm²) (-85.4 mV) except added of (1)g from graphene (G4). This increase in the corrosion rate when the addition of graphene is increased can be attributed to the increase in the porosity that allows the corrosion fluid to penetrate to the surface of the base alloy. In general, all the added ratios of graphene significantly improvement the corrosion resistance relative to the Ti-13Nb-13Zr alloy without coating.

The data listed in Table (4.5) shows partial and limited improvement in corrosion resistance of the B alloy with different additives of

Carboxymethyl cellulose (0.08, 0.2, and 0.5 CMC) but this improvement is decreasing sharply with the increase in the addition of CMC to below zero. Relative to the base alloy (C1: 37%, C2: 28%, and C3: -5%) or relative to the HAp coating (C1: 2%, C2: -11%, and C3: -63%). ($I_{corr.}$) and ($E_{corr.}$) for specimens are graded from (699.10 nA/cm²) (-68.5 mV) for C1 alloy to (844.90 nA/cm²) (-91.1 mV) for C2 alloy which are lower than B alloy is (1.03 µA/cm²) (-102.8 mV), it is lower than C3 alloy which is (2.03 µA/cm²) (-125.1 mV). (C1) it is the only percentage that will reduce the rate of corrosion when compared to HAp-coating and base alloy, but if CMC additions compare to graphene, so CMC coating is considered a failure and useless, neither economically nor practically. The reason for the sharp decrease in the values of the corrosion rate when adding CMC can be attributed to the decrease in the adhesion from (7.90MPa) for C1 to (6.63MPa) for C3 compared to the addition of graphene, Mix and functional gradient (FG) (Table 4.3).

**Table (4.5):** The Corrosion Current ($I_{corr.}$), Corrosion Potential ($E_{corr.}$), Corrosion Rate and Improvement percentage for B, H, G and C Specimens in Hank's Solution at 37℃.

| Sample code | $I_{corr.}$ (nA) | $E_{corr.}$ (mV) | Corrosion Rate(mm/y) | Improvement percentage% | |
|---|---|---|---|---|---|
| | | | | relative to the Base | relative to the HAp |
| B | $1.03\times10^3$ | -102.8 | 0.0781 | --- | --- |
| H | 763.38 | -85.4 | 0.0505 | 35 | --- |
| $G_1$ | 9.03 | -27.4 | 0.00312 | 96 | 94 |
| $G_2$ | 385.85 | -55.6 | 0.00799 | 90 | 84 |
| $G_3$ | 436.91 | -68.0 | 0.0398 | 49 | 21 |
| $G_4$ | 792.85 | -93.4 | 0.0665 | 15 | - 32 |
| $C_1$ | 699.10 | -68.5 | 0.0495 | 37 | 2 |
| $C_2$ | 844.90 | -91.1 | 0.0559 | 28 | -11 |
| $C_3$ | $2.03\times10^3$ | -125.1 | 0.0821 | - 5 | -63 |

From Table (4.6) can be noticed that there is a relative improvement in corrosion resistance when using the coating produced by mixing (HAp + Gr + CMC ) ternary coating (M). But this improvement is gradually decreasing at an accelerating pace with the increase in the addition of CMC percent (M1: 41%, M2: 38%, M3: 35%, & M4: 25%) relative to the Base alloy without coating, and this improvement decreases until it reaches below zero for (M3 & M4) relative to the HAp coating (M1: 10%, M2: 4%, M3: -1%, & M4: -17%). ($I_{corr.}$) and ($E_{corr.}$) for specimens are graded from (543.37 nA/cm²) (-63.1 mV) for M1 alloy to (968.76 nA/cm²) (-131.7 mV) for M4 alloy which are lower than B alloy which is (1.03 µA/cm²) (-102.8 mV), and which are lower than H alloy which is (763.38 nA/cm²) (-85.4 mV) except added of (0.5 & 1)g from Ternary coating (M3 and M4). From the above, it was shown that the effect of the CMC is more than of graphene when mixed together, but there is a significant improvement in the rate of corrosion if compared to the coating of the CMC but not to the required level.

**Table (4.6):** The Corrosion Current ($I_{corr.}$), Corrosion Potential ($E_{corr.}$), Corrosion Rate and Improvement percentage for B, H, M and F Specimens in Hank's Solution at 37℃.

| Sample code | $I_{corr.}$ (nA) | $E_{corr.}$ (mV) | Corrosion Rate(mm/y) | Improvement percentage% | |
|---|---|---|---|---|---|
| | | | | relative to the Base | relative to the HAp |
| B | $1.03\times10^3$ | -102.8 | 0.0781 | --- | --- |
| H | 763.38 | -85.4 | 0.0505 | 35 | --- |
| $M_1$ | 543.37 | -63.1 | 0.0457 | 41 | 10 |
| $M_2$ | 747.28 | -63.2 | 0.0487 | 38 | 4 |
| $M_3$ | 902.79 | -102.2 | 0.0511 | 35 | -1 |
| $M_4$ | 968.76 | -131.7 | 0.0589 | 25 | -17 |
| F | 28.27 | -33.8 | 0.00365 | 95 | 93 |

The functional gradation(FG) of graphene on the surface of the Ti-13Nb-13Zr alloy gave significant improvement if compared to the addition of the CMC and the results of mixing (Ternary coating), where the improvement percentage was (F: 95%), which is close to adding 0.08 of graphene, which was (G1: 96%) relative to the Base, (F: 93%) and (G1: 94%) relative to the HAp coating , where this improvement is attributed to the low percentage of porosity resulting from successive layers on each other in addition to the good adhesion. The best results obtained from among the additions can be summarized as follows:

(Ti-13Nb-13Zr) < H < C1 < M1 < F < G1

To prove the above equation, it can be observed Figure (4.42), where it shows the best addition that reduces the corrosion rate to (0.00312mm/y) is (G1), but with an increase in the percentage of this addition the corrosion rate increases until it reaches a value (0.0665mm/y) for (G4), which is higher than the addition of H (0.0505mm/y), but still less than the corrosion rate of the base alloy (B) (0.0781mm/y).

While corrosion rate for sample (F) was (0.00365mm/y) which is relatively close to sample (G1), so these two additions were the best in reducing the corrosion rate to a large degree compared to all the additions, making them more acceptable for implantation inside the human body.

The other additives (CMC and Mixing) reduce the corrosion rate, in specific proportions, as shown in the Figure (4.42), which were almost close to or higher than the corrosion rate for the H sample. In general, all additions reduce the corrosion rate for the base alloy, except for the addition of (0.5 CMC), which increases the corrosion rate over the base alloy.

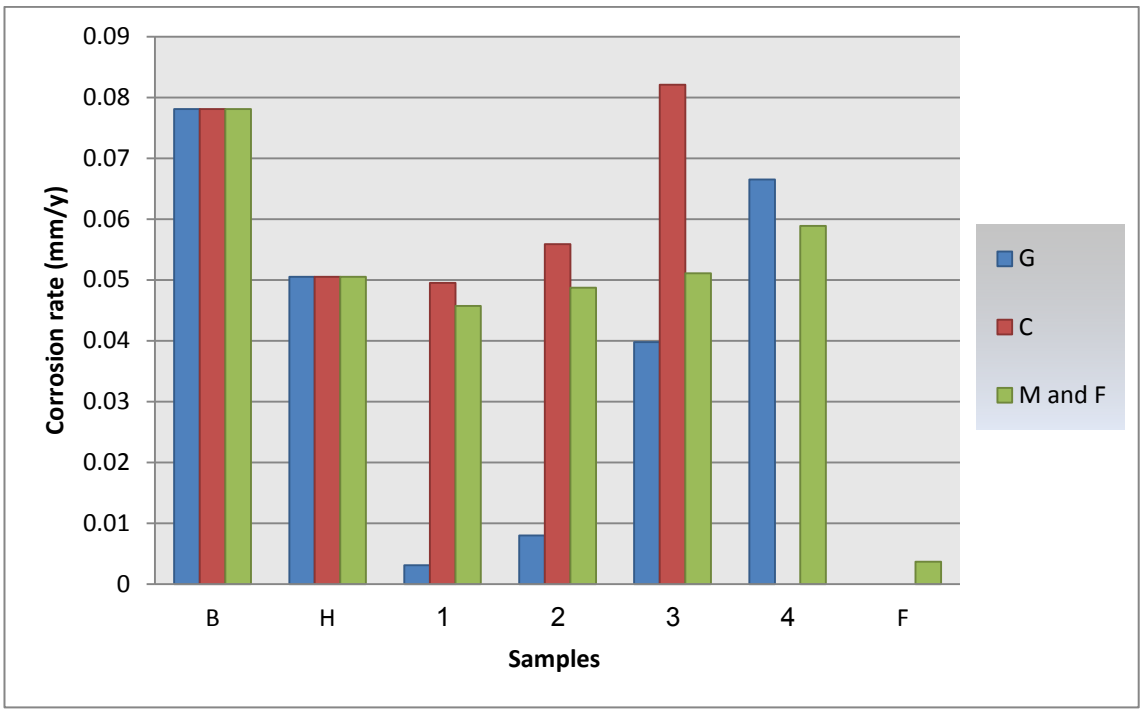


**Figure (4.42):** The Effect of CMC, Gr, Mix Together, and FG- Coating on Corrosion Rate of in Hank's Solution at 37℃.

The microstructure for the corroded surface has been taken in order to study the corrosion effect on the surface of the alloy. As shown in Figure (4.43). The surface of the specimens that were coated by CMC shows few cracks, while in case of Gr coating, presence of dense, homogenous and thicker layer prevents direct contact of corrosive medium with the substrate. As shown in the results, the Gr coating samples have a protective barrier to prevent or reduce the localized corrosion on the surface of the alloy.

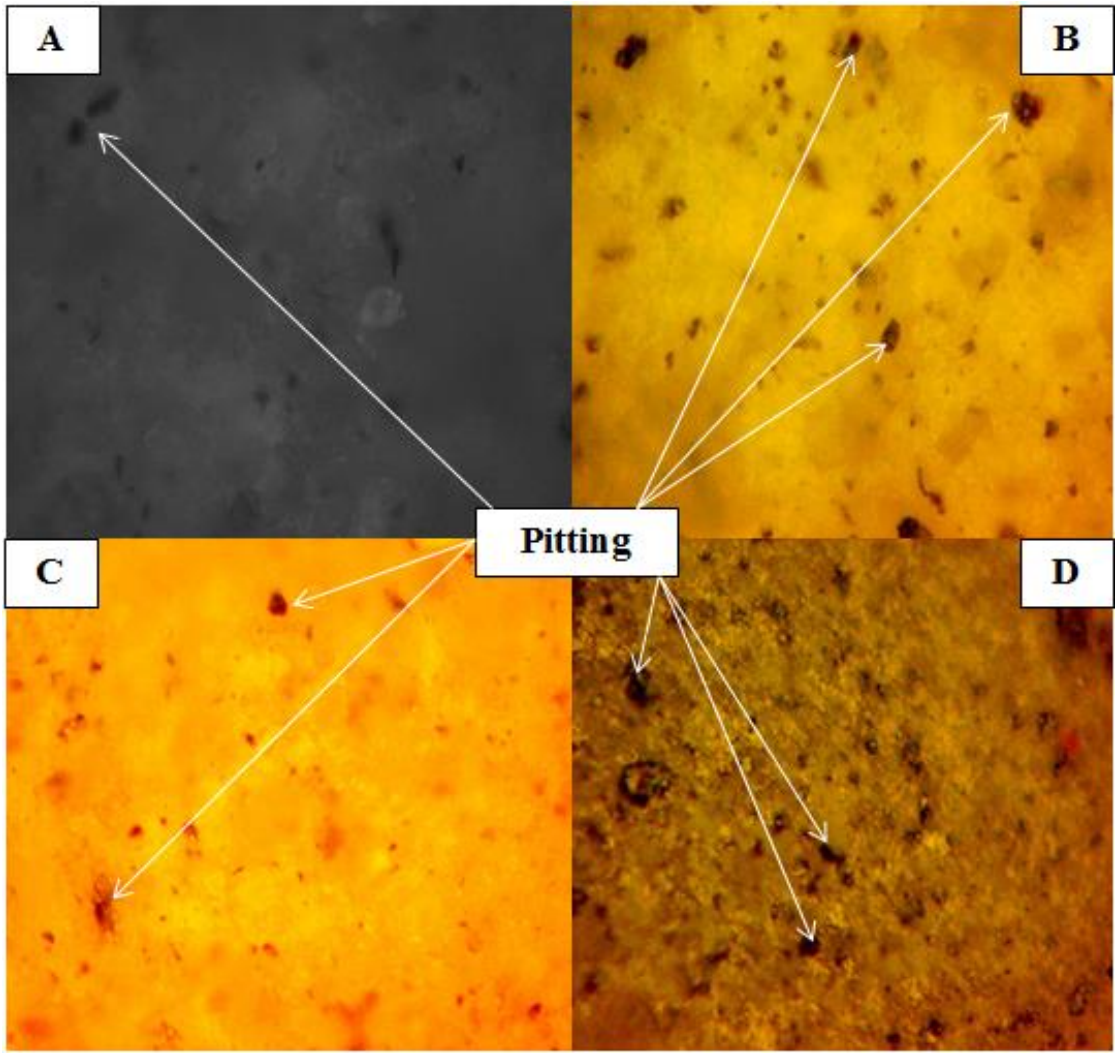


**Figure (4.43):** LOM for (A) Gr Coating, (B) CMC Coating (C) Hap Coatimg and (D) Mix Coating(C1).

Before starting to perform the cycle polarization, antibacterial and cytotoxicity evaluation test and based on the previous tests, the best results can be determined from among the percentages of additives for the used coatings as shown in Table (4.7), in order to reach the optimum coating and initiate cycle polarization test, antibacterial and cytotoxicity evaluation.

**Table (4.7):** The Best Results Obtained Among All Coatings Based on Previous Tests

| Coating | Graphene Coating | CMC Coating | Ternary Coating | Functional gradient (FG) |
|---|---|---|---|---|
| **Best the Result** | G2 | C1 | M2 | F |

Choosing the best percentages of additions mentioned in the above table was not an easy matter, since each of the previous tests gave preference to a specific percentage that differs from the best percentage for the other test, and accordingly, the best results were selected in a way that meets and matches all the tests, which will be approved in the three subsequent tests, cycle polarization test, antibacterial and cytotoxicity evaluation.

### 4.10.3 Cycle Polarization Test

The increased ion release rate due to different forms of localized corrosion, may lead to a series of undesirable biological responses and eventually, implant loosening. Susceptibility to these forms of corrosion is evaluated by cyclic polarization. The parameters obtained from the current-voltage curve can be associated with the localized corrosion mechanism. Typically, the reading starts at the open circuit potential and scans upwards until breakdown is attained. Then the direction of scan is inverted after specific amount of localized corrosion is established and the passive film is damaged. The potential at which stable pit formed is called breakdown potential ($E_b$) or pitting potential ($E_{pit}$). Consequently, the $E_{pit}$ implies the potential over which the pits initiated and developed. If the $E_{pit}$ is high, the material has high resistance to the pitting corrosion. The difference ($\Delta E$) between $E_{pit}$ and $E_{prot.}$ will give an indication to the corrosion resistance of the sample, where the smaller $\Delta E$ value mean the highest corrosion resistance [159].

Figures (4.44 to 4.48) show the polarization curves for specimens (B, G2, C1, M2 & F) in Hank's solution at 37 °C. Significant differences were observed between the curves obtained for each specimen. For substrate specimen, has the lowest $E_{pit}$ and $E_{prot.}$ value compared to the susceptibility to pitting corrosion of the other specimens after coating. The cyclic polarization curves obtained as noted in the Table (4.8), the extent of

the hysteresis loop is highly reduced and therefore, the corrosion mechanism operating on the substrate surface is less active when coating.

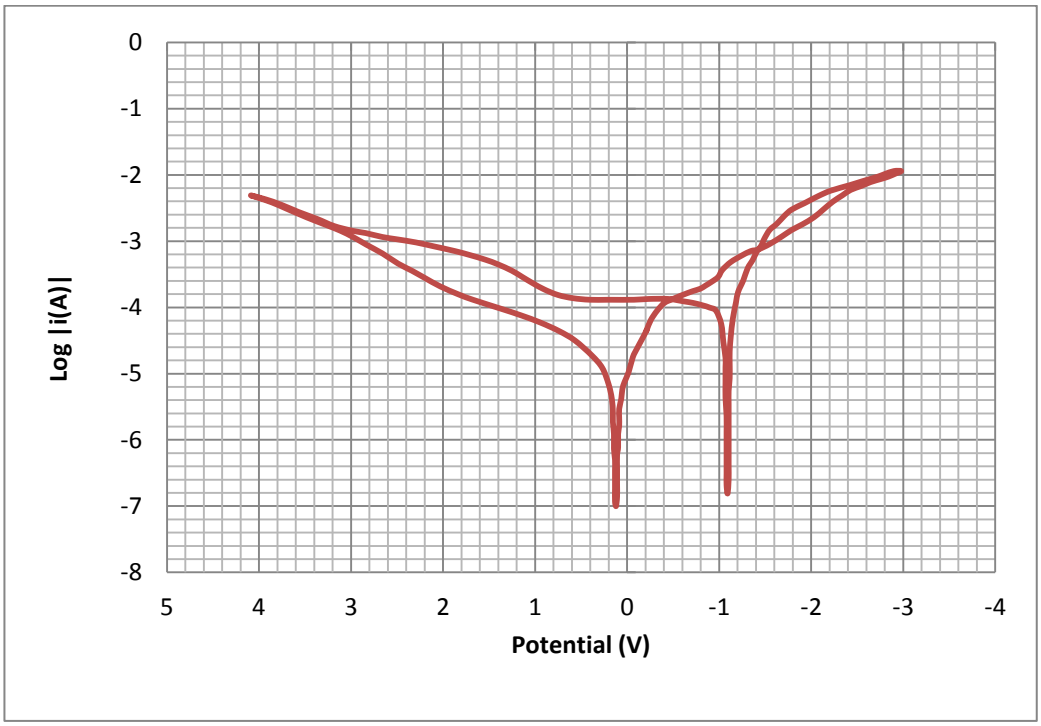


**Figure (4.44):** Cycle polarization curves of B Specimen.

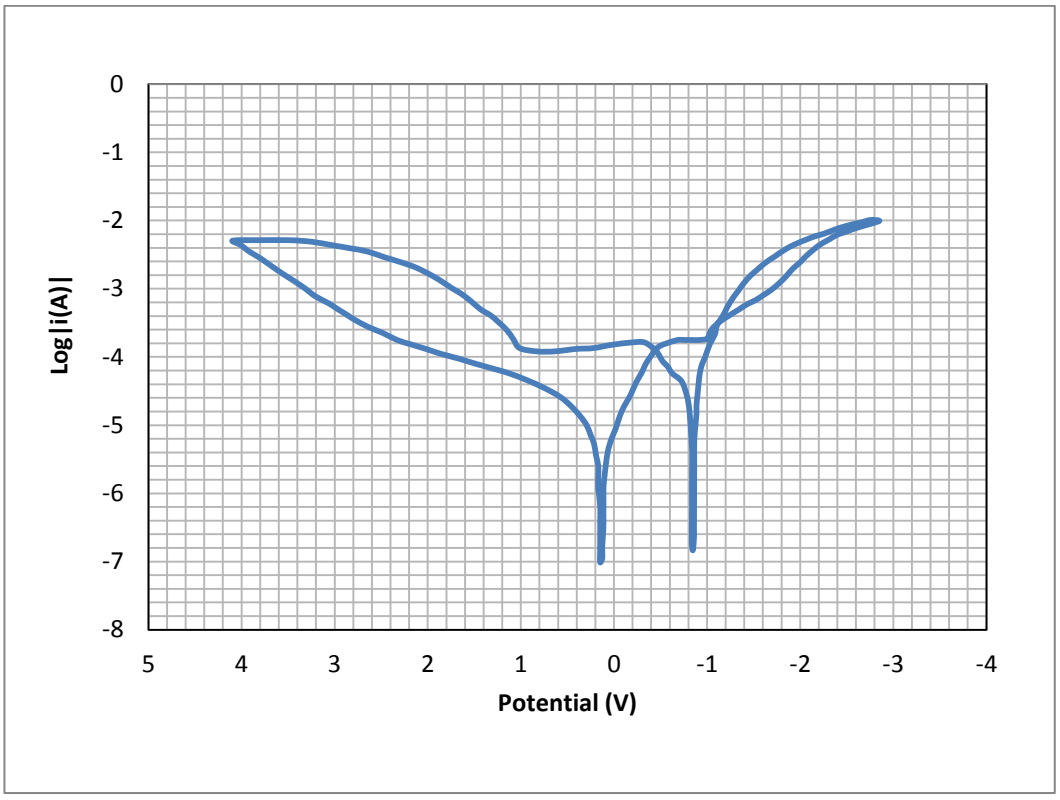


**Figure (4.45):** Cycle polarization curves of G2 Specimen.

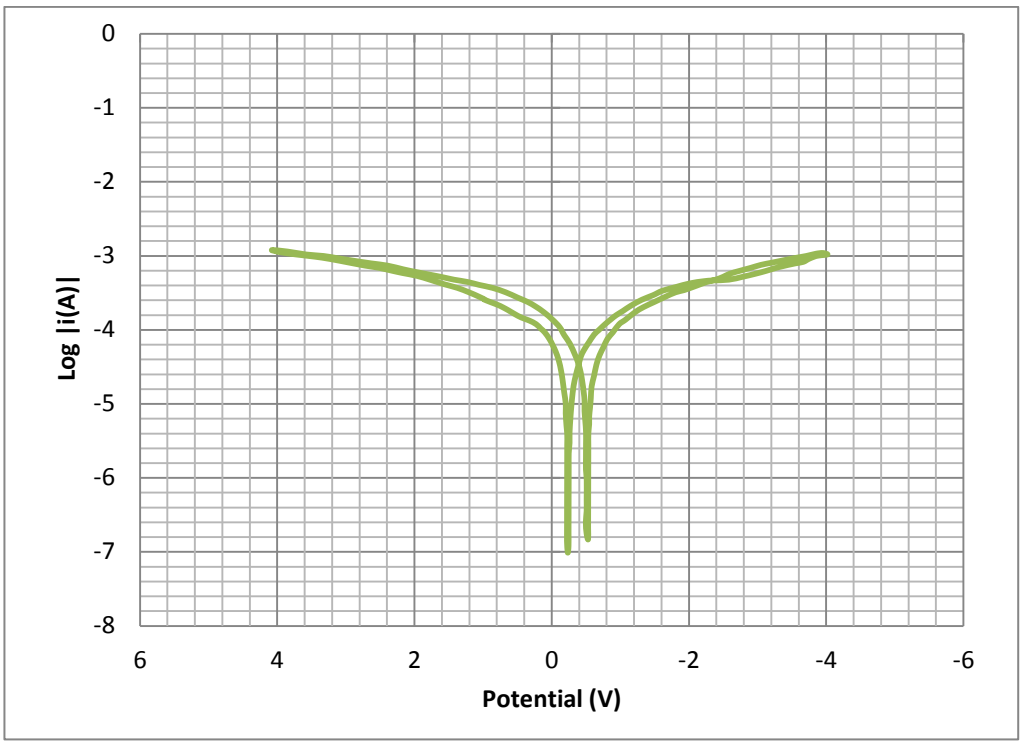


**Figure (4.46):** Cycle polarization curves of C1 Specimen.

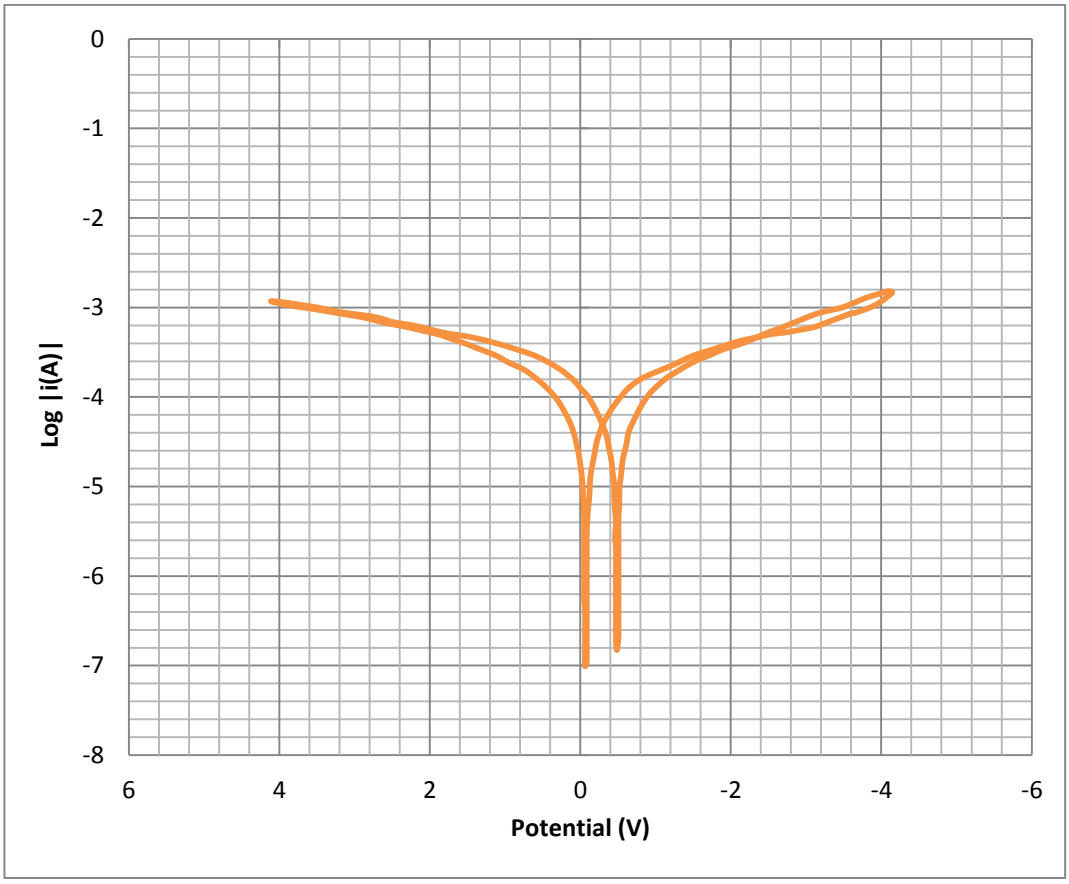


**Figure (4.47):** Cycle polarization curves of M2 Specimen.

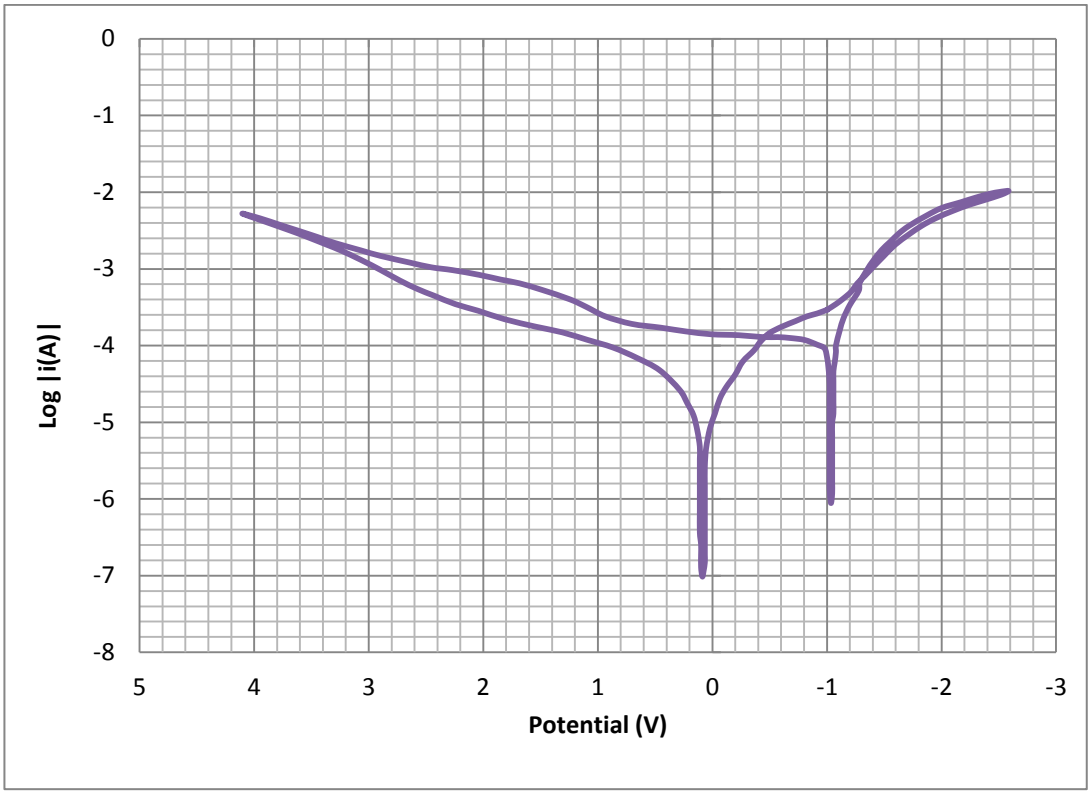


**Figure (4.48):** Cycle polarization curves of F Specimen.

**Table (4.8):** Values of electrochemical parameters of (B, G2, C1, M2, and F) Specimen in Hank's solution from cyclic polarization.

| Specimen | $E_{pit}$ (mV) | $E_{prot.}$ (mV) | $\Delta E=(E_{pit}-E_{prot.})$ (mV) | Improvement percentage (%) |
|---|---|---|---|---|
| B | -1.2 | -1.5 | 0.3 | - |
| G2 | -0.8 | -1 | 0.2 | 33 |
| C1 | -0.7 | -2.5 | 1.8 | -500 |
| M2 | -1 | -2.3 | 1.3 | -333 |
| F | -1.1 | -1.3 | 0.2 | 33 |

## 4.11 Antibacterial Test

The results of the antibacterial property investigations are shown in Figure (4.49). The digital images taken after the test with clear inhibition zone also demonstrated in Figure (4.50). The analysis outcome imparts the increased bactericidal effect toward both negative and positive gram bacteria for the samples coated to (G2, C1, M2, and F) in addition to (Ti-13Nb-13Zr) uncoating alloy.

The formation of clear region around the disc refers to the bacterial inhibition zone. It can be observed that the case exhibited a good antibacterial effect after 24 h of incubation period at 37C°, but the uncoated base (Ti-13Nb-13Zr) alloy does not have an inhibition zone, which indicates that it does not have any antibacterial effect compared to the base alloy coated with the above mentioned coatings.

This examination was conducted for the coated and uncoated samples and the suspended solutions, as shown in Figures (4.49 and 4.50) where it was found that the inhibition zone of the suspended solutions is larger than the coated samples. This can be attributable to the presence of the base alloy that does not have any inhibition towards positive or negative bacteria. It can also cause cracks and porosity to create cavities that help the penetration of liquids inside. It can also be observed that the inhibition zone increased for positive bacteria (S.aureas) compared to negative bacteria (E.coli).

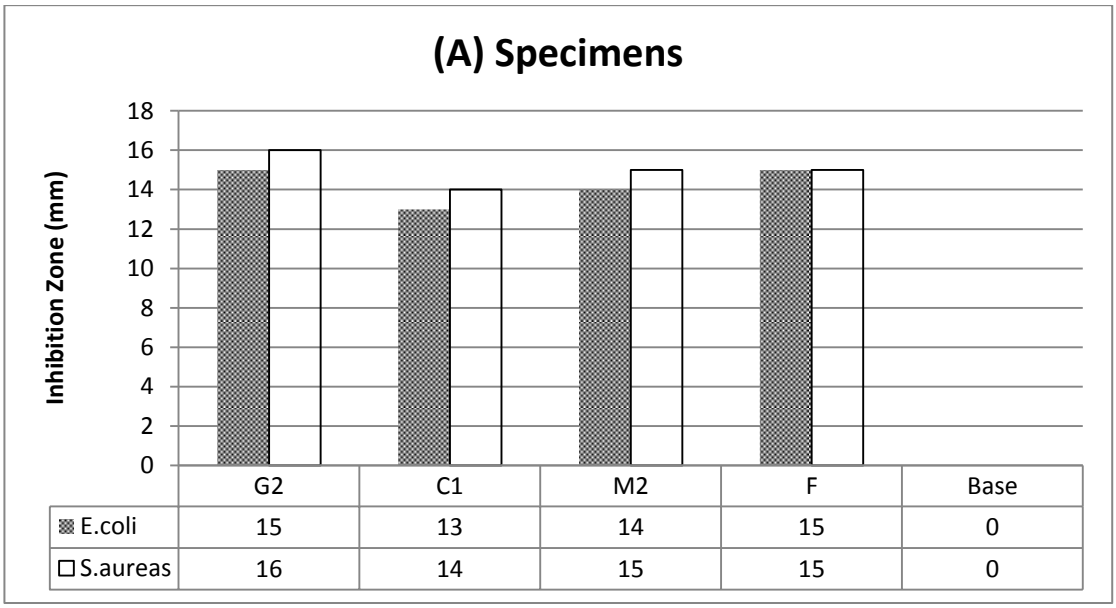


| | G2 | C1 | M2 | F | Base |
|---|---|---|---|---|---|
| E.coli | 15 | 13 | 14 | 15 | 0 |
| S.aureas | 16 | 14 | 15 | 15 | 0 |

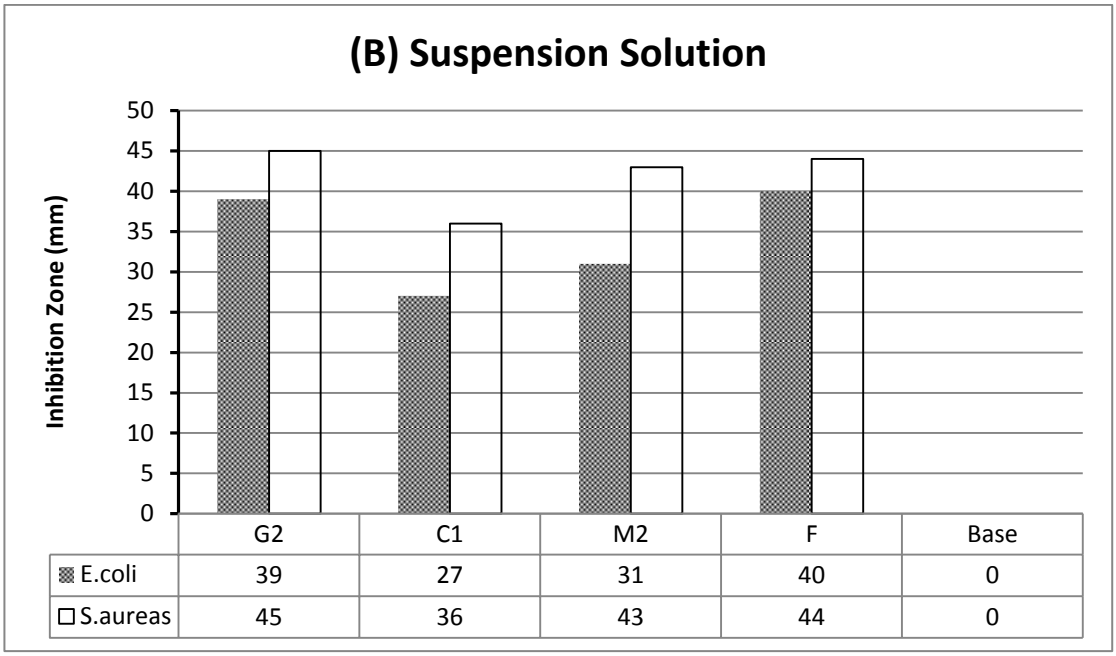


**Figure (4.49):** Diameter of the Inhibition Versus S.aureas (+) and E.coli(-) for (A) Specimen, (B) Suspension Solutions.

The lack of growth of positive and negative bacteria on the surface of the coated samples, as well as the suspension solution of the coatings, is due to the fact that these used materials (CMC and graphene) are biocompatible, as the biological response and cell adhesion improved and this was proven by Podila et al,[160] where the graphene was deposited on the surface of the (NiTi) substrate in several stages using the chemical vapour deposition technique. These substrates were implanted in the endothelial cells of rats where Electron microscopy (SEM) images were obtained that demonstrated the growth of smooth muscle cells of rats.

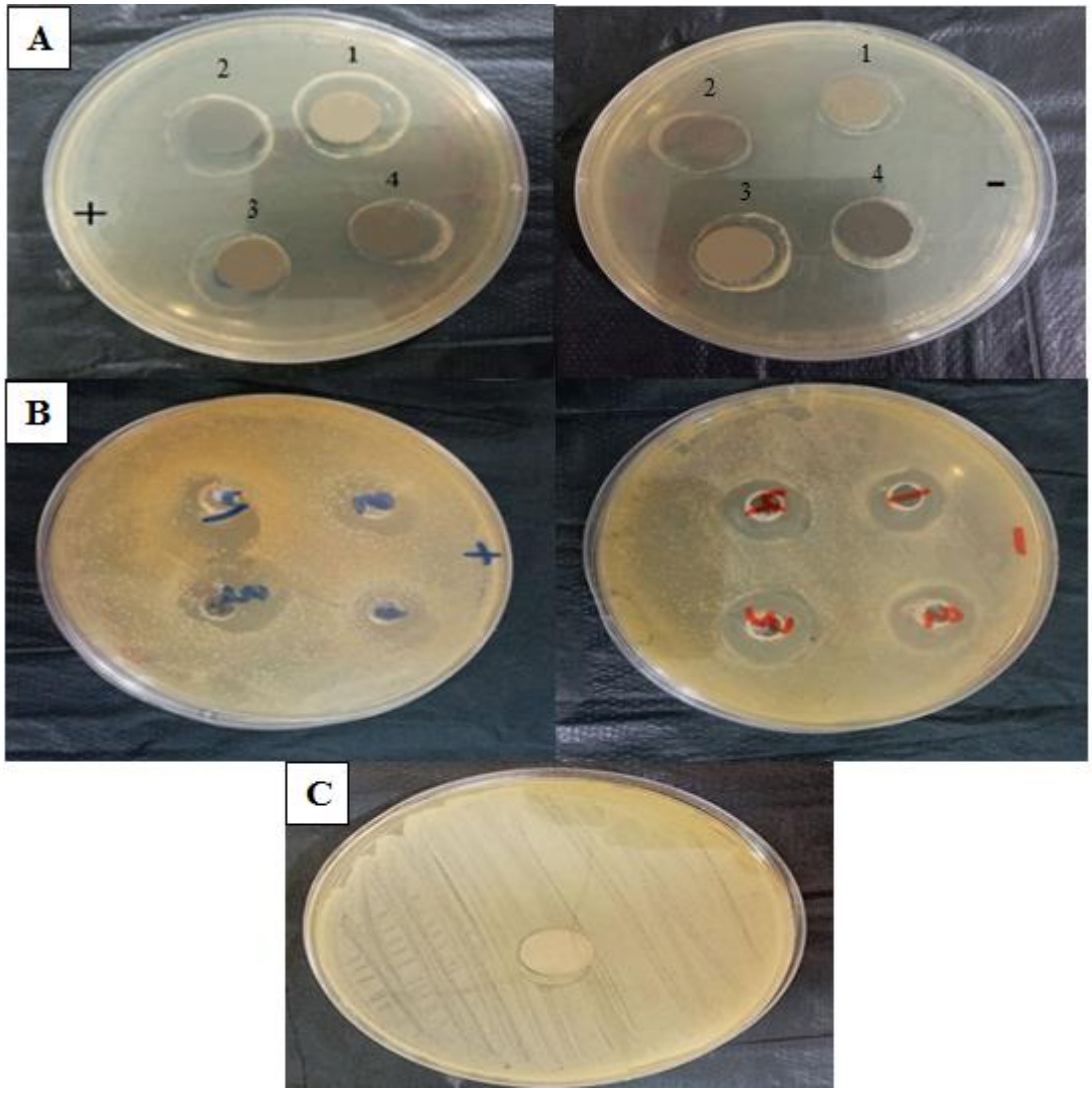


**Figure (4.50):** Antibacterial Activity of Composite Coatings (1) C1, (2) M2, (3) G2, and (4) F on Ti-13Nb-13Zr Alloy, (A) for Specimens, (B) for Suspension Solutions, and (C) Uncoating Alloy Against S.Aureus(+) and E.Coli(-).

The obtained CMC results are consistent with the result of Yadollahi et al.[161], who dealt with the preparation of antibacterial nanocomposite hydrogels by mixing carboxymethyl cellulose (CMC), layered double hydroxides (LDH) and silver nanoparticles (AgNPs), where CMC-LDH and Ag/CMC-LDH nanocomposite were prepared. The results showed an increase in the antibacterial activity of CMC-LDHs especially after addition AgNPs which stabilized for more than one month.

## 4.12 Cytotoxicity Evaluation

MTT assay is the most common method used for assessing the cytotoxicity (loss of viable cells), cells proliferation or viability of

biomedical implants/devices. It is a calorific assay for determining the metabolic cells. The cytotoxicity evaluation of the samples was examined with MTT for 72hr of incubation in the cell culture media. The cell viability quantitative analysis of Ti-13Nb-13Zr without coating, as well as (HAp-Gr (G2), HAp-CMC (C1), Ternary coating (M2), and Functional Gradient (F)) with negative control, is presented in (Figure 4.51). As per ISO 10993-5, the cell viability with more 30% reduction is considered to be the cytotoxicity effect for base alloy without coating. G2 (0.2Gr) specimen exhibited the highest, while (C1) and Ti-13Nb-13Zr alloy without coating specimens presented the least cell viability in comparison to other specimens.

The cell viability for the specimens was obtained in the order of higher to lower G2 > F > M2 > C1 > Base alloy uncoating. G2 (0.2Gr) specimen recorded nearly 100% of the cell viability. From the results, it could be deduced that all the specimens reported sufficient cell viability and can be considered as nontoxic for the biomedical implant applications. These results were also supported by optical fluorescent images (Figure 4.52).

The slight decrease of cell viability compared with the control (100%) could be attributed to the cells adaptation to the interactions with the samples. The osteoblast cell viability values were significantly lower relative to (0.01421%, 0.17826%, 0.1205%, 0.04084%, and 0.28669%) for G2, C1, M2, F and Base alloy without coating, respectively. These results demonstrated that the G2 (0.2 Gr) coating promote the proliferation of osteoblast cells.

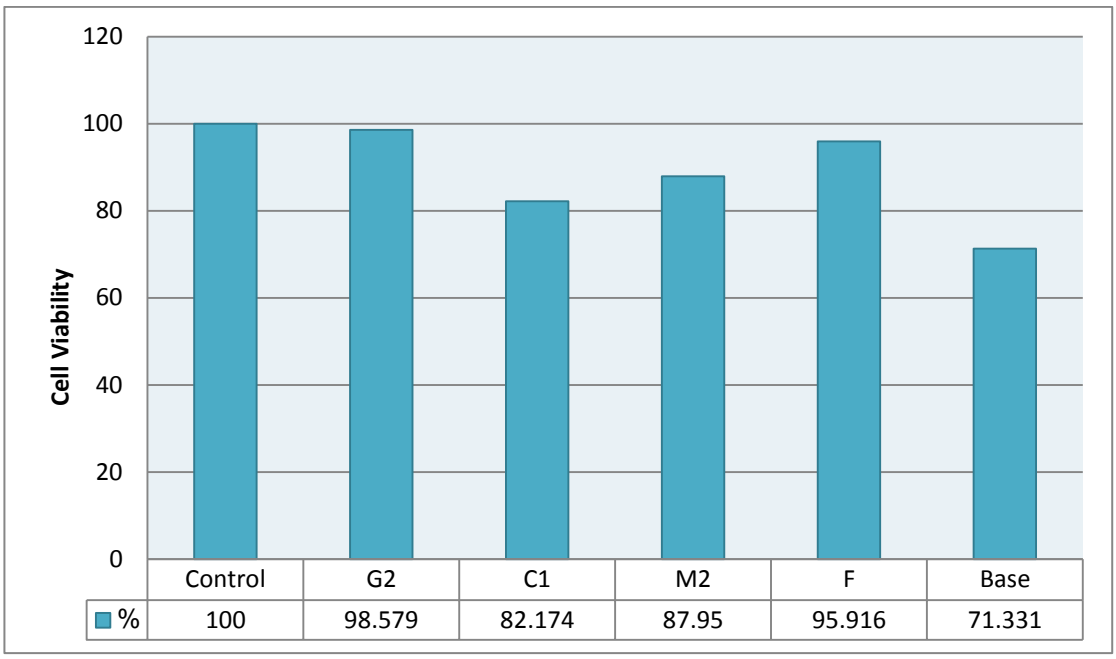


**Figure (4.51):** Cell Viability of Ti-13Nb-13Zr Alloy, G1, C1, and HAp after 72 hr of MTT, 3-(4,5-Dimethylthiazol-2yl)-2, 5-Diphenyltetrazolium Bromide.

Fluorescence microscopy was used to study MG-63 cell behavior on the coating surface for all specimens. (Figure 4.52) shows fluorescence images revealing cell adhesion at different layers of coatings. The fluorescence images confirm that the cells were alive after culturing the cells for 72 h on the samples. A number of cells were well attached to surface layers and all the prepared specimens showed a similar morphology after seeding. in another meaning, the cells were inclose contact with the coated specimens and spread out uniformly over the entire surface. This suggests that all the prepared specimens provide a biocompatible environment for favorable cell attachment, especially coating graphene (G2), which led to results similar nearly to the control.

The results that previously listed for the MTT assay, which showed the biocompatibility of the tested specimens with the body cells represented by the MG-63 cells, agreed with many researches in this regard, where both **Pathak and Pandey [162]** studied the effect of HAp and Fe on the biocompatibility and corrosion properties of zinc, using MTT assay. The cytotoxicity of specimens was evaluated for 24 hours using the metal

extract obtained after 72 hours of incubation of specimens in culture medium.

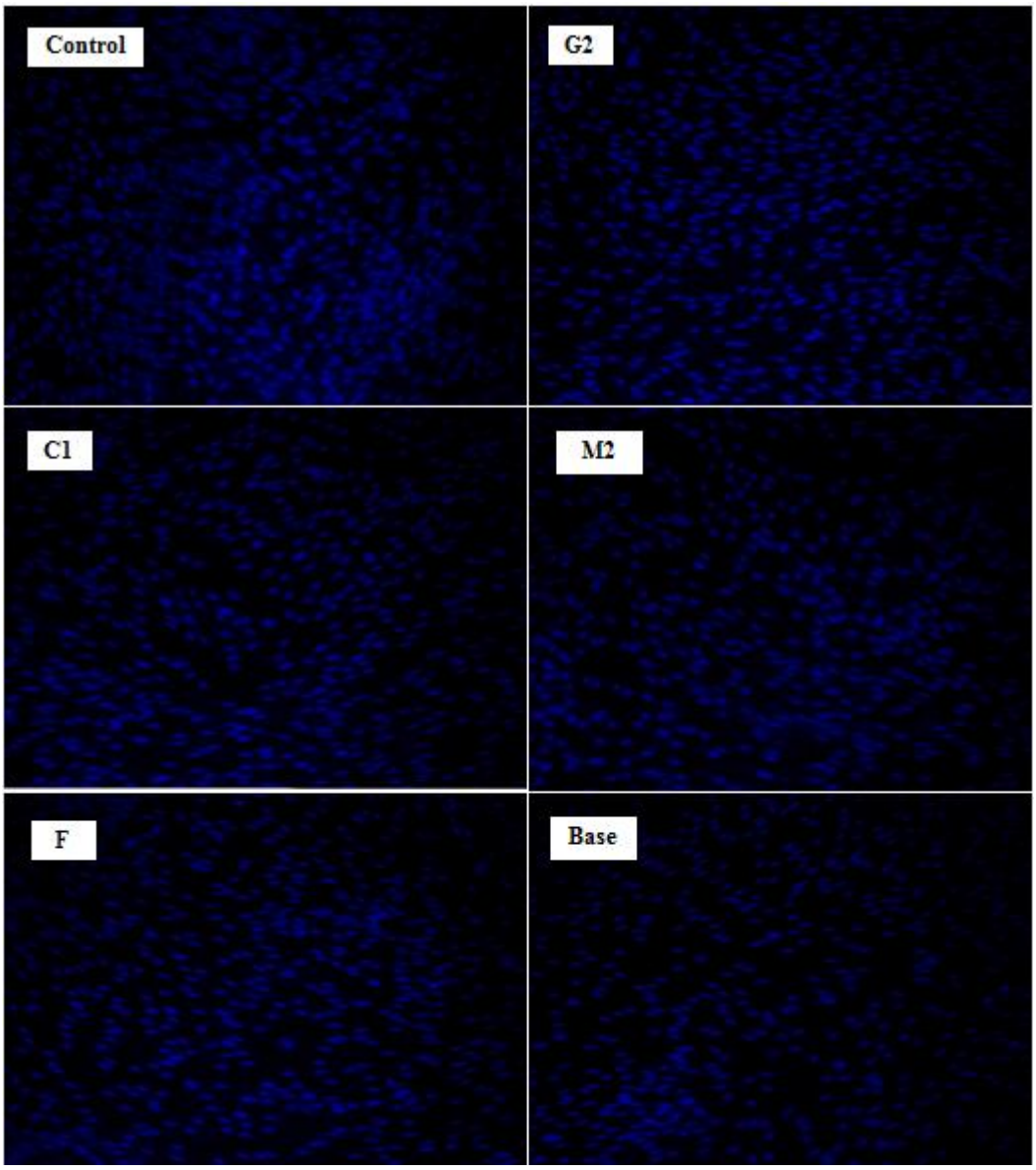


**Figure (4.52):** Fluorescence Images of MG63 Cells for All Specimens Examined.

Zn-3HA specimens exhibited the highest, and Zn-3HA-2Fe samples presented the least cell viability in comparison to other samples. Zn-3HA samples recorded nearly 100% of the cell viability. From the results, it could be deduced that all the samples reported sufficient cell viability and can be considered as nontoxic for the biomedical degradable implant applications. Besides, cell morphology and optical fluorescent images signified the presence of adequate cells in the extract media, which was also an indication of high cell viability for the samples. The developed

composites could be considered as nontoxic and can be used for biodegradable implant applications. **Kumar, et.al, [163]** their work also coincided with the working method of MTT assay, where they studied electrochemical setup is used for coating the hydroxyapatite (HA) powder and nano zinc particle (Zn) on the Ti 6Al-4 V alloy. The electrolyte is prepared by mixing the HA and (Zn) of varying quantity. The cell viability is tested on the surface-modified implants, the cells grown on the cell culture plate were the control sample implant which denoted 0.488 cell viability (OD). The thirteen sample implant plates are designated as a control. The implant coated with 6 g/L HA concentration along with 1.6 g/L of zinc shows the highest cell viability with 0.366, and sample with 14 g/L HA showed least with 0.146.

Despite the different in addition ,the method and results of the mentioned research show the MTT assay is indispensable in coated alloys are implanted inside the human body, which must be friendly to the host cells, and thus the survival of the cell line that was implanted on the surface of the coated specimens is clear evidence that specimens respond to the medium in which they will live for a long time.

# CHAPTER FIVE

# Conclusions and Recommendations

# CHAPTER FIVE
# CONCLUSIONS & RECOMMENDATIONS

## 5.1 Conclusions

According to the obtained results, the following conclusions are made:

1. The use of (316L) alloy as anode was very suitable for the coating process in terms of efficiency and cost when compared to graphite and Ti-13Nb-13Zr alloy electrodes.
2. The use of high conditions such as (90 volts, 90 seconds) makes the coating layer non-homogeneous and has an irregular appearance and thickness, which requires resorting to reducing these conditions to appropriate levels to obtain the best homogeneity and uniformity of the layer coating and the best of these conditions (40 volts, 60 seconds).
3. The pattern of the base alloy in revealed the diffraction of the beta and alpha phases that matched the JCPDS Card No. (044 - 1294). Can notice the emergence of new peaks due to the effect of the additions ratios (HAp, Gr, and CMC ), which also led to a reduction or increase in the angle of the peaks of each of the phases of the titanium alloy (beta and alpha).
4. Positive values of the zeta potential were a clear indicator of the adoption of the cathodic EPD process, The addition of nitric acid ($HNO_3$) to suspension solutions resulted in a fall in pH, which resulted in an increase in the acidity of the solutions and, as a result, an increase in conductivity.
5. The addition of graphene, CMC, ternary coating and the functional gradation of graphene led to an increase in the adhesion strength of the hydroxyapatite layer starting from 4.55MPa for HAp and up to 7.90MPa for C1, 8.28MPa for M1, 976MPa for G4 to 10.12MPa for FG. This was proved when the adhesion strength of the above coating layers was

increased after immersing the coated specimens for a maximum of 6 days.

6. The high roughness, porosity and cracks on the surface of the CMC coating directly reduced the contact angle of this layer from 54.6° for the base alloy to 11.2° for C3, if compared to the rest of the additives that ranged between 14.3° for M4, 20.5° for G4, and 32.3° for FG.
7. The high wear resistance for adding graphene, whose volume losses ranged from 0.00614 $cm^3$ to the base alloy at 25 min to 0.001344 $cm^3$ to G4 at the same time under a load of 15 N. When compared to the other additions, the high hardness of this coating layer may be expected.
8. When compared to the other additions, the greatest value of OCP (-26.1mV) in the negative direction of the G1 addition shows a decrease in the corrosion rate for this coating layer, from 0.781mm/y for the base alloy to 0.0312mm/y for G1.
9. All the additives used (Gr, CMC, Ternary coating, and FG) are anti-bacterial, as the largest zone of inhibition when suspension solution of G2 (45mm) was when attacking the positive bacteria (S. aureas).
10. The cell viability quantitative analysis of Ti-13Nb-13Zr without coating, as well as ( HAp-Gr (G2), HAp-CMC (C1), Ternary coating (M2), and functional gradient (F) ) with negative control. G2 (0.2Gr) specimen exhibited the highest (98.579%), while C1 specimen and base alloy without coating presented the least cell viability (82.174% and 71.331%, respectively ) in comparison to other specimens.
11. The best results were achieved when G2 (0.2Gr) was added to the hydroxyapatite coating (H), hence this ratio is regarded the optimal ratio in this study for the aim of enhancing the surface of the Ti-13Nb-13Zr alloy.

## 5.2 Recommendations

1. Study metals ions release (static immersion tests) and wet sliding wear test of Ti-13Nb-13Zr alloy surface modification via addition ( graphene and Carboxymethyl cellulose) for the same proportions in this thesis by electrophoretic deposition (EPD) process for different parameters
2. Cell culture, antibacterial, and electrochemical behavior of zinc and niobium oxides coating on Ti-13Nb-13Zr alloy for biomedical application.
3. Investigation of corrosion and mechanical properties of Ti-13Nb-13Zr alloy treated by Ultrasonic.
4. Tribological and corrosion behaviour of Ti-13Nb-13Zr alloy surface modification by diffusion treatments of silver for biomedical applications
5. Tribological behaviour for surface modification Ti-13Nb-13Zr alloy using cladding with silver particles.

# References

# References


[1] Wang, X., Xu, S., Zhou, S., Xu, W., Leary, M., Choong, P., Qian, M., Brandt, M. and Xie, Y.M., (2016). "Topological design and additive manufacturing of porous metals for bone scaffolds and orthopaedic implants: A review". Biomaterials, vol. 83, pp:127-141.

[2] Narayan, R., (2012). "Fundamentals of medical implant materials". ASM handbook, vol. 23, pp: 6-17.

[3] Kunčická, L., Kocich, R., & Lowe, T. C. (2017). "Advances in metals and alloys for joint replacement". Progress in Materials Science, vol. 88, pp:232-280.

[4] Nagata, Y. (2007) 'National Institute of Advanced Industrial Science and Technology', Journal of Life Support Engineering, 19(Supplement), pp:65-65.

[5] Hermawan, H., Ramdan, D. and Djuansjah, J.R., 2011. Metals for biomedical applications. Biomedical engineering-from theory to applications, vol. 1, pp:411-430.

[6] Park, J. and Lakes, R.S., (2007). "Biomaterials: an introduction". Springer Science & Business Media.

[7] Cui, C., Hu, B., Zhao, L. and Liu, S. (2011). "Titanium alloy production technology, market prospects and industry development". Materials & Design, Vol. 32, No. 3, pp.1684-1691.

[8] Bodunrin, M.O., Chown, L.H. and Omotoyinbo, J.A., (2021). "Development of low-cost titanium alloys: a chronicle of challenges and opportunities". Materials Today: Proceedings, vol. 38, pp:564-569.

[9] Kurup, A., Dhatrak, P. and Khasnis, N., (2021). "Surface modification techniques of titanium and titanium alloys for biomedical dental applications: A review". Materials Today: Proceedings, vol. 39, pp:84-90.

[10] Allen, M.R. and Burr, D.B., (2014). "Bone modeling and remodeling". In Basic and applied bone biology, pp. 75-90, Academic Press.

[11] Christy, P.N., Basha, S.K., Kumari, V.S., Bashir, A.K.H., Maaza, M., Kaviyarasu, K., Arasu, M.V., Al-Dhabi, N.A. and Ignacimuthu, S., (2020). "Biopolymeric nanocomposite scaffolds for bone tissue engineering applications–A review". Journal of Drug Delivery Science and Technology, vol. 55, p:101-452.

[12] Hu, C., Ashok, D., Nisbet, D.R. and Gautam, V., (2019). "Bioinspired surface modification of orthopedic implants for bone tissue engineering". Biomaterials, vol. 219, p:119-366.

[13] Buikstra, J.E. ed., (2019). "Ortner's identification of pathological conditions in human skeletal remains", book.

[14] Kameo, Y., Sakano, N. and Adachi, T., (2020). "Theoretical concept of cortical to cancellous bone transformation". Bone reports, vol. 12, p:100-260.

[15] Boyle, C. and Kim, I.Y., (2011). "Three-dimensional micro-level computational study of Wolff's law via trabecular bone remodeling in the human proximal femur using design space topology optimization". Journal of biomechanics, vol. 44, No. 5, pp:935-942.

[16] Guglielmi, G. ed., (2013). "Osteoporosis and bone densitometry measurements", Berlin: Springer.

[17] Khan, M.U.A., Haider, S., Haider, A., Abd Razak, S.I., Kadir, M.R.A., Shah, S.A., Javed, A., Shakir, I. and Al-Zahrani, A.A., (2021). "Development of porous, antibacterial and biocompatible GO/n-HAp/bacterial cellulose/β-glucan biocomposite scaffold for bone tissue engineering". Arabian Journal of Chemistry, vol. 14, No. 2, p:102-924.

[18] Li, X., Hung, V.W.Y., Yu, F.W.P., Hung, A.L.H., Ng, B.K.W., Cheng, J.C.Y., Lam, T.P. and Yip, B.H.K., (2020). "Persistent low-normal bone mineral density in adolescent idiopathic scoliosis with different

curve severity: A longitudinal study from presentation to beyond skeletal maturity and peak bone mass". Bone, vol. 133, p:115-217.

[19] Maier, G.S., Kolbow, K., Lazovic, D. and Maus, U., (2016). "The importance of bone mineral density in hip arthroplasty: results of a survey asking orthopaedic surgeons about their opinions and attitudes concerning osteoporosis and hip arthroplasty". Advances in orthopedics, vol. 2016. P: 5

[20] Berridge MJ, (2012). "Cellular processes. In: Cell signalling biology". Portland Press, Cambridge, vol. 136, No. 7, pp 7-1.

[21] Chocholata, P., Kulda, V. and Babuska, V., (2019). "Fabrication of scaffolds for bone-tissue regeneration". Materials, vol. 12, No. 4, p:568.

[22] Hasan, A., Byambaa, B., Morshed, M., Cheikh, M.I., Shakoor, R.A., Mustafy, T. and Marei, H.E., (2018). "Advances in osteobiologic materials for bone substitutes". Journal of Tissue Engineering and Regenerative Medicine, vol. 12, No. 6, pp:1448-1468.

[23] Martinez-Zelaya, V.R., Archilha, N.L., Calasans-Maia, M., Farina, M. and Rossi, A.M., (2021). "Trabecular architecture during the healing process of a tibial diaphysis defect". Acta Biomaterialia, vol. 120, pp:181-193.

[24] Gittens, R.A., Olivares-Navarrete, R., Schwartz, Z. and Boyan, B.D., (2014). "Implant osseointegration and the role of microroughness and nanostructures: lessons for spine implants". Acta biomaterialia, vol. 10, No. 8, pp:3363-3371.

[25] Wong, K., Trudel, G. and Laneuville, O., (2015). "Noninflammatory joint contractures arising from immobility: animal models to future treatments". BioMed research international, vol. 2015, p: 6.

[26] Wang, J., (2019). "Small Joint Transplantation". In Microsurgical Orthopedics, Springer, Dordrecht, pp: 175-183.

[27] Tubbs, R.S., Shoja, M.M. and Loukas, M. eds., (2016). "Bergman's comprehensive encyclopedia of human anatomic variation". John Wiley & Sons.

[28] Mow, V.C., Ratcliffe, A. and Poole, A.R., (1992). "Cartilage and diarthrodial joints as paradigms for hierarchical materials and structures". Biomaterials, vol. 13, No. 2, pp:67-97.

[29] Aihaiti, Y., Tuerhong, X., Ye, J.T., Ren, X.Y. and Xu, P., (2020). "Identification of pivotal genes and pathways in the synovial tissue of patients with rheumatoid arthritis and osteoarthritis through integrated bioinformatic analysis". Molecular Medicine Reports, vol. 22, No. 4, pp:3513-3524.

[30] Sapuan, S.M., Nukman, Y., Osman, N.A. and Ilyas, R.A. eds., (2020). "Composites in Biomedical Applications". CRC Press.

[31] Blue, C.M., (2015). "Darby's Comprehensive Review of Dental Hygiene-E-Book".

[32] Nagay, B.E., Cordeiro, J.M. and Barão, V.A.R., (2020). "Alloy Materials for Biomedical Applications". Alloy Materials and Their Allied Applications, pp:159-189.

[33] Nouri, A. and Wen, C., (2021). "Stainless steels in orthopedics". In Structural Biomaterials, Woodhead Publishing, pp: 67-101

[34] Zhang, X., Huang, Y., Wang, B., Chang, X., Yang, H., Lan, J., Wang, S., Qiao, H., Lin, H., Han, S. and Guo, Y., (2020). "A functionalized Sm/Sr doped TiO2 nanotube array on titanium implant enables exceptional bone-implant integration and also self-antibacterial activity". Ceramics International, vol. 46, No. 10, pp: 14796-14807.

[35] Quinn, J., McFadden, R., Chan, C.W. and Carson, L., (2020). "Titanium for orthopaedic applications: an overview of surface modification to improve biocompatibility and prevent bacterial biofilm formation". Iscience, p:101-745.

[36] Niinomi, M., Narushima, T. and Nakai, M., (2015). "Advances in metallic biomaterials". Heidelberg, DE: Springer.

[37] Niinomi, M., (1998). "Mechanical properties of biomedical titanium alloys". Materials Science and Engineering: A, vol. 243, No. 2, pp:231-236.

[38] Helsen, J.A. and Missirlis, Y., (2010). "Biomaterials: a Tantalus experience". Springer Science & Business Media.

[39] Yang, L. ed., (2020). "Techniques for corrosion monitoring". Woodhead Publishing.

[40] Aslankoohi, N., Mondal, D., Rizkalla, A.S. and Mequanint, K., (2019). "Bone repair and regenerative biomaterials: towards recapitulating the microenvironment". Polymers, vol. 11, No. 9, p:1437.

[41] Abdalla, M., Joplin, A., Elahinia, M. and Ibrahim, H., (2020). "Corrosion Modeling of Magnesium and Its Alloys for Biomedical Applications". Corrosion and Materials Degradation, vol. 1, No. 2, pp:219-248.

[42] Manam, N.S., Harun, W.S.W., Shri, D.N.A., Ghani, S.A.C., Kurniawan, T., Ismail, M.H. and Ibrahim, M.H.I., (2017). "Study of corrosion in biocompatible metals for implants: A review". Journal of Alloys and Compounds, vol. 701, pp:698-715.

[43] Yan, K., Liu, H., Feng, N., Bai, J., Cheng, H., Liu, J. and Huang, F., (2019). "Preparation of a single-phase Mg–6Zn alloy via ECAP-stimulated solution treatment". Journal of Magnesium and Alloys, vol. 7, No. 2, pp:305-314.

[44] Bermea, O.M. et.al (2021). "Mercury in Blood of Children Exposed to Historical Residues from Metallurgical Activity". Exposure and Health, vol. 13, No. 2, pp:281-292.

[45] Pšenková, M., Toman, R. and Tančin, V., (2020). "Concentrations of toxic metals and essential elements in raw cow milk from areas with potentially undisturbed and highly disturbed environment in

Slovakia". Environmental Science & Pollution Research, vol. 27, No. 21.

[46] Bouchard, M.E., Petrosyan, M. and Kane, T.D., (2021). "Case series of metal allergy following Nuss procedure not only for stainless steel bars". Journal of Pediatric Surgery, Vol. 56, No. 11, pp: 1976-1981.

[47] Blom, L. H., Elrefaii, S. A., Zachariae, C., Thyssen, J. P., Poulsen, L. K., & Johansen, J. D. (2021). "Memory T helper cells identify patients with nickel, cobalt, and chromium metal allergy". Contact dermatitis, Vol. 85, No. 1, PP: 7-16.

[48] Liu, D., Nguyen, T., Wang, J. and Huang, C., (2020). "Mechanisms of enhancing the machining performance in micro abrasive waterjet drilling of hard and brittle materials by vibration assistance". International Journal of Machine Tools and Manufacture, vol. 151, PP:103-528.

[49] Mekicha, M.A., de Rooij, M.B., Mishra, T., Matthews, D.T.A., Jacobs, L. and Schipper, D.J., 2021. Study of wear particles formation at single asperity contact: An experimental and numerical approach. Wear, vol. 470, p:203-644.

[50] Park, J. and Lakes, R.S., (2007). "Biomaterials: an introduction". Springer Science & Business Media.

[51] Li, Y. et.al (2020). "Experimental and modelling investigation on the fretting wear of PTFE with and without electron-beam irradiation". Wear, vol. 460, p: 203-459.

[52] Akay, C., Turan, N., Karakış, D. and Angurel, L.A., (2021). "Improvement of flexural bond strength of zirconia-resin cement by surface patterning using sub-nanosecond UV laser". International Journal of Applied Ceramic Technology, vol. 18, No. 1, pp: 51-59.

[53] Rabadia, C.D. et.al (2018). "High-strength β stabilized Ti-Nb-Fe-Cr alloys with large plasticity". Materials Science and Engineering A, vol. 732, pp: 368-377.

[54] Hu, Z., Zhou, X., Liu, H. and Yi, D., (2021). "The formation of microtextured region during thermo-mechanical processing in a near-β titanium alloy Ti-5Al-5Mo-5V-1Cr-1Fe". Journal of Alloys and Compounds, vol. 853, p: 156-964.

[55] Peng Qi, Bolong, Li a, Tongbo Wang, Lian Zhou, Zuoren Nie, (2021). "Microstructure and properties of a novel ternary Ti-6Zr-xFe alloy for biomedical applications". Journal of Alloys and Compounds, vol. 854, p:157-119

[56] Zhou, X., Fu, X., Chen, H., Xiao, Z., Min, L., Zhou, Y., and Zhang, X. (2019). "Evaluation and regulation of the corrosion resistance of macroporous titanium scaffolds with bioactive surface films for biomedical applications". Journal of Materials Chemistry B, Vol. 7, No. 21, PP: 3455-3467.

[57] Zhang, L.C. and Chen, L.Y., (2019). "A review on biomedical titanium alloys: recent progress and prospect". Advanced engineering materials, vol. 21, No. 4, p: 180-1215.

[58] Yadav, P. and Saxena, K.K., (2020). "Effect of heat-treatment on microstructure and mechanical properties of Ti alloys: An overview". Materials Today: Proceedings, vol. 26, pp: 2546-2557.

[59] Brunette, D.M., Tengvall, P., Textor, M. and Thomsen, P. eds., (2012). "Titanium in medicine: material science, surface science, engineering, biological responses and medical applications". Springer Science & Business Media.

[60] Festas, A. J., Carvalho, S., Horovistiz, A., Ramos, A., & Davim, J. P. (2022). Comparative study of titanium alloys machinability used for medical applications. *Proceedings of the Institution of Mechanical Engineers, Part E: Journal of Process Mechanical Engineering*, 09544089221074852.

[61] Peron, M., et.al (2020). "The effect of Equal Channel Angular Pressing on the stress corrosion cracking susceptibility of AZ31 alloy

in simulated body fluid". Journal of the mechanical behavior of biomedical materials, vol. 106, p: 103-724.

[62] Shahin, M., Munir, K., Wen, C. and Li, Y., (2019). "Magnesium matrix nanocomposites for orthopedic applications: a review from mechanical, corrosion, and biological perspectives". Acta biomaterialia, vol. 96, pp: 1-19.

[63] Rabadia, C. D., Liu, Y. J., Jawed, S. F., Wang, L., Li, Y. H., Zhang, X. H., ... & Zhang, L. C. (2018). Improved deformation behavior in Ti-Zr-Fe-Mn alloys comprising the C14 type Laves and β phases. *Materials & Design*, *160*, 1059-1070.

[64] Ozan, S., Lin, J., Zhang, Y., Li, Y. and Wen, C., (2020). "Cold rolling deformation and annealing behavior of a β-type Ti–34Nb–25Zr titanium alloy for biomedical applications". Journal of Materials Research and Technology, vol. 9, No. 2, pp: 2308-2318.

[65] Kumar, P., Mahobia, G.S., Singh, V. and Chattopadhyay, K., (2020). "Lowering of elastic modulus in the near-beta Ti–13Nb–13Zr alloy through heat treatment". Materials Science and Technology, vol. 36, No. 6, pp: 717-725.

[66] Bahl, S., Suwas, S., & Chatterjee, K. (2021). Comprehensive review on alloy design, processing, and performance of β Titanium alloys as biomedical materials. *International materials reviews*, *66*(2), 114-139.

[67] Schneider, S. G., Nunes, C. A., Rogero, S. O., Higa, O. Z., & Bressiani, J. C. (2000). Mechanical properties and cytotoxic evaluation of the Ti-3Nb-13Zr alloy.

[68] Zhang, Y., Cheng, Z., & Feng, H. (2019). Dynamic fracture analysis of functional gradient material coating based on the peridynamic method. *Coatings*, *9*(1), 62.

[69] Li, W., & Han, B. (2018). Research and application of functionally gradient materials. In *IOP conference series: materials science and engineering* (Vol. 394, No. 2, p. 022065). IOP Publishing.

[70] Bhavar, V., Kattire, P., Thakare, S., & Singh, R. K. P. (2017). A review on functionally gradient materials (FGMs) and their applications. In *IOP Conference Series: Materials Science and Engineering* (Vol. 229, No. 1, p. 012021). IOP Publishing.

[71] Jun, T. (2012). Development and application of functionally gradient materials. In *2012 International Conference on Industrial Control and Electronics Engineering* (pp. 1022-1025). IEEE.

[72] Sadollah, A., & Bahreininejad, A. (2011). Optimum gradient material for a functionally graded dental implant using metaheuristic algorithms. *Journal of the mechanical behavior of biomedical materials*, *4*(7), 1384-1395.

[73] Balani, K., Verma, V., Agarwal, A. and Narayan, R., (2015). "Biosurfaces: a materials science and engineering perspective". John Wiley & Sons.

[74] Burakowski, T. and Wierzchon, T., (1998). "Surface engineering of metals: principles, equipment, technologies". CRC press.

[75] Kulkarni, M., Mazare, A., Schmuki, P. and Iglič, A., (2014). "Biomaterial surface modification of titanium and titanium alloys for medical applications". Nanomedicine, vol. 111, p: 111.

[76] Paterlini, T.T., et.al (2017). "The role played by modified bioinspired surfaces in interfacial properties of biomaterials". Biophysical reviews, vol. 9, No. 5, pp: 683-698.

[77] Amani, H., Arzaghi, H., Bayandori, M., Dezfuli, A. S., Pazoki-Toroudi, H., Shafiee, A., & Moradi, L. (2019). "Controlling cell behavior through the design of biomaterial surfaces: a focus on surface modification techniques". Advanced materials interfaces, vol. 6, no. 13, pp: 190-572.

[78] Hu, S., Li, W., Finklea, H. and Liu, X., (2020). "A review of electrophoretic deposition of metal oxides and its application in solid

oxide fuel cells". Advances in colloid and interface science, vol. 276, pp:102-102.

[79] Akhtar, M.A., Mariotti, C.E., Conti, B. and Boccaccini, A.R., (2021). "Electrophoretic deposition of ferulic acid loaded bioactive glass/chitosan as antibacterial and bioactive composite coatings". Surface and Coatings Technology, vol. 405, pp: 126-657.

[80] Sikkema, R., Baker, K. and Zhitomirsky, I., (2020). "Electrophoretic deposition of polymers and proteins for biomedical applications". Advances in Colloid and Interface Science, vol. 284, p: 102-272.

[81] Zhang, X., et.al (2020). "Electrochemical deposition of metal–organic framework films and their applications". Journal of Materials Chemistry A, vol. 8, no. 16, pp: 7569-7587.

[82] Boccaccini, A.R., Keim, S., Ma, R., Li, Y. and Zhitomirsky, I., (2010). "Electrophoretic deposition of biomaterials". Journal of the Royal Society Interface, vol. 7, pp: 581-613.

[83] Sarkar, P., De, D., Uchikochi, T., & Besra, L. (2012). "Electrophoretic deposition (EPD): fundamentals and novel applications in fabrication of advanced ceramic microstructures:. In Electrophoretic Deposition of Nanomaterials. Springer, New York, NY, pp. 181-215.

[84] Besra, L., & Liu, M. (2007). "A review on fundamentals and applications of electrophoretic deposition (EPD)". Progress in materials science, vol. 52, no. 1, pp: 1-61.

[85] Zouzelka, R., Remzova, M., Brabec, L., & Rathousky, J. (2018). "Photocatalytic performance of porous TiO2 layers prepared by quantitative electrophoretic deposition from organic solvents". Applied Catalysis B: Environmental, vol. 227, pp: 70-78.

[86] Moreno, R., & Ferrari, B. (2000). "Effect of the slurry properties on the homogeneity of alumina deposits obtained by aqueous electrophoretic deposition". Materials Research Bulletin, vol. 35, no. 6, pp: 887-897.

[87] Guo, F., Shapiro, I. P., & Xiao, P. (2011). "Effect of HCl on electrophoretic deposition of yttria stabilized zirconia particles in organic solvents". Journal of the European Ceramic Society, vol. 31, no. 14, pp: 2505-2511.

[88] Basu, R. N., Randall, C. A., & Mayo, M. J. (2001). "Fabrication of dense zirconia electrolyte films for tubular solid oxide fuel cells by electrophoretic deposition". Journal of the American Ceramic Society, vol. 84, no. 1, pp: 33-40.

[89] Wang, Y. C., Leu, I. C., & Hon, M. H. (2004). "Kinetics of electrophoretic deposition for nanocrystalline zinc oxide coatings". Journal of the American Ceramic Society, vol. 87, no. 1, pp: 84-88.

[90] Diba, M., Fam, D. W., Boccaccini, A. R., & Shaffer, M. S. (2016). "Electrophoretic deposition of graphene-related materials: A review of the fundamentals". Progress in Materials Science, vol. 82, pp: 83-117.

[91] Hu, S., Li, W., Li, W., Zhang, N., Qi, H., Finklea, H., & Liu, X. (2019). "A study on the electrophoretic deposition of gadolinium doped ceria on polypyrrole coated yttrium stabilized zirconia". Journal of colloid and interface science, vol. 555, pp: 115-123.

[92] Fitriyana, D. F., Nugraha, F. W., Laroybafih, M. B., Ismail, R., Bayuseno, A. P., Muhamadin, R. C., ... & Siregar, J. P. (2022). The effect of hydroxyapatite concentration on the mechanical properties and degradation rate of biocomposite for biomedical applications. In *IOP Conference Series: Earth and Environmental Science* (Vol. 969, No. 1, p. 012045). IOP Publishing.

[93] Sivasankari, S., Kalaivizhi, R., Gowriboy, N., Ganesh, M. R., & Shazia Anjum, M. (2021). Hydroxyapatite integrated with cellulose acetate/polyetherimide composite membrane for biomedical applications. *Polymer Composites*, *42*(10), 5512-5526.

[94] Venkatesan, J., & Anil, S. (2021). Hydroxyapatite Derived from Marine Resources and their Potential Biomedical

Applications. *Biotechnology and Bioprocess Engineering*, *26*(3), 312-324.

[95] Huang, S. M., Liu, S. M., Ko, C. L., & Chen, W. C. (2022). Advances of Hydroxyapatite Hybrid Organic Composite Used as Drug or Protein Carriers for Biomedical Applications: A Review. *Polymers*, *14*(5), 976.

[96] Fiume, E., Magnaterra, G., Rahdar, A., Verné, E., & Baino, F. (2021). Hydroxyapatite for biomedical applications: a short overview. *Ceramics*, *4*(4), 542-563.

[97] Kehoe, S. (2008). *Optimisation of hydroxyapatite (HAp) for orthopaedic application via the chemical precipitation technique* (Doctoral dissertation, Dublin City University).

[98] Haider, A., Haider, S., Han, S. S., & Kang, I. K. (2017). Recent advances in the synthesis, functionalization and biomedical applications of hydroxyapatite: a review. *Rsc Advances*, *7*(13), 7442-7458.

[99] Uysal, I., Yilmaz, B., & Evis, Z. (2021). Zn-doped hydroxyapatite in biomedical applications. *Journal of the Australian Ceramic Society*, *57*(3), 869-897.

[100]Zhang, S. (2013). *Hydroxyapatite coatings for biomedical applications*. Taylor & Francis.

[101] Szcześ, A., Hołysz, L., & Chibowski, E. (2017). Synthesis of hydroxyapatite for biomedical applications. *Advances in colloid and interface science*, *249*, 321-330.

[102] Rashad, M., Pan, F., Tang, A., Lu, Y., Asif, M., Hussain, S., ... & Mao, J. (2013). Effect of graphene nanoplatelets (GNPs) addition on strength and ductility of magnesium-titanium alloys. *Journal of Magnesium and alloys*, *1*(3), 242-248.

[103] Nesovic, K., Abudabbus, M. M., Rhee, K. Y., & Miskovic-Stankovic, V. (2017). Graphene based composite hydrogel for biomedical applications. *Croatica Chemica Acta*, *90*(2), D1-D1.

[104] Chong, Y., Ge, C., Yang, Z., Garate, J. A., Gu, Z., Weber, J. K., ... & Zhou, R. (2015). Reduced cytotoxicity of graphene nanosheets mediated by blood-protein coating. *ACS nano*, *9*(6), 5713-5724.

[105] Plachá, D., & Jampilek, J. (2019). Graphenic materials for biomedical applications. *Nanomaterials*, *9*(12), 1758.

[106] Shoukat, R., & Khan, M. I. (2021). Carbon nanotubes: A review on properties, synthesis methods and applications in micro and nanotechnology. *Microsystem Technologies*, *27*(12), 4183-4192.

[107] Norizan, M. N., Moklis, M. H., Demon, S. Z. N., Halim, N. A., Samsuri, A., Mohamad, I. S., ... & Abdullah, N. (2020). Carbon nanotubes: Functionalisation and their application in chemical sensors. *RSC advances*, *10*(71), 43704-43732.

[108] Qu, Y., He, F., Yu, C., Liang, X., Liang, D., Ma, L., ... & Wu, J. (2018). Advances on graphene-based nanomaterials for biomedical applications. *Materials Science and Engineering: C*, *90*, 764-780.

[109] Ahangari, M., Johar, M. H., & Saremi, M. (2021). Hydroxyapatite-carboxymethyl cellulose-graphene composite coating development on AZ31 magnesium alloy: Corrosion behavior and mechanical properties. *Ceramics International*, *47*(3), 3529-3539.

[110] Zennifer, A., Senthilvelan, P., Sethuraman, S., & Sundaramurthi, D. (2021). Key advances of carboxymethyl cellulose in tissue engineering & 3D bioprinting applications. *Carbohydrate Polymers*, *256*, 117561.

[111] Panahirad, S., Dadpour, M., Peighambardoust, S. H., Soltanzadeh, M., Gullón, B., Alirezalu, K., & Lorenzo, J. M. (2021). Applications of carboxymethyl cellulose-and pectin-based active edible coatings in

preservation of fruits and vegetables: A review. *Trends in Food Science & Technology*, *110*, 663-673.

[112] Rahman, M., Hasan, M., Nitai, A. S., Nam, S., Karmakar, A. K., Ahsan, M., ... & Ahmed, M. B. (2021). Recent developments of carboxymethyl cellulose. *Polymers*, *13*(8), 1345.

[113] El-Sakhawy, M., Kamel, S., Salama, A., & Sarhan, H. A. (2014). Carboxymethyl cellulose acetate butyrate: a review of the preparations, properties, and applications. *Journal of drug delivery*, *2014*.

[114] Vedula, S. S., & Yadav, G. D. (2021). Chitosan-based membranes preparation and applications: Challenges and opportunities. *Journal of the Indian Chemical Society*, *98*(2), 100017.

[115] Jana, S., & Jana, S. (Eds.). (2020). *Functional chitosan: Drug delivery and biomedical applications*. Springer Nature.

[116] Derwich, M., Lassmann, L., Machut, K., Zoltowska, A., & Pawlowska, E. (2022). General characteristics, biomedical and dental application, and usage of chitosan in the treatment of temporomandibular joint disorders: a narrative review. *Pharmaceutics*, *14*(2), 305.

[117] Kumar, P., Mahobia, G. S., Singh, V., & Chattopadhyay, K. (2020). Lowering of elastic modulus in the near-beta Ti–13Nb–13Zr alloy through heat treatment. *Materials Science and Technology*, *36*(6), 717-725.

[118] Ossowska, A., Zieliński, A., Olive, J. M., Wojtowicz, A., & Szweda, P. (2020). Influence of Two-Stage Anodization on Properties of the Oxide Coatings on the Ti–13Nb–13Zr Alloy. *Coatings*, *10*(8), 707.

[119] Jażdżewska, M., Kwidzińska, D. B., Seyda, W., Fydrych, D., & Zieliński, A. (2021). Mechanical Properties and Residual Stress Measurements of Grade IV Titanium and Ti-6Al-4V and Ti-13Nb-13Zr Titanium Alloys after Laser Treatment. *Materials*, *14*(21), 6316.

[120] Kumar, P., Mahobia, G. S., Mandal, S., Singh, V., & Chattopadhyay, K. (2021). Enhanced corrosion resistance of the surface modified Ti-13Nb-13Zr alloy by ultrasonic shot peening. *Corrosion Science*, *189*, 109597.

[121] Mao, X., Shi, A., Wang, R., Nie, J., Qin, G., Chen, D., & Zhang, E. (2022). The Influence of Copper Content on the Elastic Modulus and Antibacterial Properties of Ti-13Nb-13Zr-xCu Alloy. *Metals*, *12*(7), 1132.

[122] Kadhim, M. J., Abdulateef, N. E., & Abdulkareem, M. H. (2018). Evaluation of surface roughness of 316L stainless steel substrate on nanohydroxyapatite by electrophoretic deposition. *Al-Nahrain Journal for Engineering Sciences*, *21*(1), 28-35.

[123] Baştan, F. E., Rehman, M. A. U., Avcu, Y. Y., Avcu, E., Üstel, F., & Boccaccini, A. R. (2018). Electrophoretic co-deposition of PEEK-hydroxyapatite composite coatings for biomedical applications. *Colloids and Surfaces B: Biointerfaces*, *169*, 176-182.

[124] Ryu, S., Kwon, Y. J., Kim, Y., & Lee, J. U. (2020). Corrosion protection coating of three-dimensional metal structure by electrophoretic deposition of graphene oxide. *Materials Chemistry and Physics*, *250*, 123039.

[125] Khanmohammadi, S., Ojaghi-Ilkhchi, M., & Farrokhi-Rad, M. (2021). Development of bioglass coating reinforced with hydroxyapatite whiskers on TiO2 nanotubes via electrophoretic deposition. *Ceramics International*, *47*(1), 1333-1343.

[126] Abbass, M. K., Khadhim, M. J., Jasim, A. N., Issa, M. J., & Khashan, K. S. (2021). Fabrication and Optimization of Electrophoretic Deposition Parameters Using Alternating Current by Taguchi Design. *Al-Nahrain Journal for Engineering Sciences*, *24*(1), 8-15.

[127]Vafa, E., Bazargan-Lari, R., & Bahrololoom, M. E. (2021). Electrophoretic deposition of polyvinyl alcohol/natural

chitosan/bioactive glass composite coatings on 316L stainless steel for biomedical application. *Progress in Organic Coatings*, *151*, 106059.

[128] Maciąg, F., Moskalewicz, T., Kowalski, K., Łukaszczyk, A., Hadzhieva, Z., & Boccaccini, A. R. (2021). The effect of electrophoretic deposition parameters on the microstructure and adhesion of zein coatings to titanium substrates. *Materials*, *14*(2), 312.

[129] Bartmanski, M., Cieslik, B., Glodowska, J., Kalka, P., Pawlowski, L., Pieper, M., & Zielinski, A. (2017). Electrophoretic deposition (EPD) of nanohydroxyapatite-nanosilver coatings on Ti13Zr13Nb alloy. *Ceramics International*, *43*(15), 11820-11829.

[130] Moskalewicz, T., Zimowski, S., Zych, A., Łukaszczyk, A., Reczyńska, K., & Pamuła, E. (2018). Electrophoretic deposition, microstructure and selected properties of composite alumina/polyetheretherketone coatings on the Ti-13Nb-13Zr alloy. *Journal of The Electrochemical Society*, *165*(3), D116.

[131] Singh, S., Singh, G., & Bala, N. (2020). Electrophoretic deposition of hydroxyapatite-iron oxide-chitosan composite coatings on Ti–13Nb–13Zr alloy for biomedical applications. *Thin Solid Films*, *697*, 137801.

[132] Dai, N., Zhang, L. C., Zhang, J., Chen, Q., & Wu, M. (2016). "Corrosion behavior of selective laser melted Ti-6Al-4 V alloy in NaCl solution". Corrosion Science, vol. 102, pp: 484-489.

[133] Budiatin, A. S., Gani, M. A., Nilamsari, W. P., Ardianto, C., & Khotib, J. (2020). "The characterization of bovine bone-derived hydroxyapatite isolated using novel non-hazardous method". In Journal of Biomimetics, Biomaterials and Biomedical Engineering, Trans Tech Publications Ltd, Vol. 45, pp. 49-56.

[134] Zhang, X., Li, Y., Guo, M., Jin, T. Z., Arabi, S. A., He, Q., ... & Liu, D. (2021). "Antimicrobial and UV blocking properties of composite chitosan films with curcumin grafted cellulose nanofiber". Food Hydrocolloids, vol. 112, pp: 106-337.

[135] Jiang, L., Li, Y., Wang, X., Zhang, L., Wen, J., & Gong, M. (2008). "Preparation and properties of nano-hydroxyapatite /chitosan /carboxymethyl cellulose composite scaffold". Carbohydrate Polymers, vol. 74, no. 3, pp: 680-684.

[136] Thiyagu, C., Manjubala, I., & Narendrakumar, U. (2021). "Thermal and morphological study of graphene based polyurethane composites". Materials Today: Proceedings, vol. 45, pp: 3982-3985.

[137] Wang, H., Jürgensen, J., Decker, P., Hu, Z., Yan, K., Gurevich, E. L., & Ostendorf, A. (2020)." Corrosion behavior of NiTi alloy subjected to femtosecond laser shock peening without protective coating in air environment". Applied Surface Science, vol. 501, pp: 144-338.

[138] ASTM. (2011). " Standard Practice for Preparing, Cleaning, and Evaluating Corrosion Test Specimens: G1 – 03" . ASTM International, 100 Barr Harbor Drive, PO Box C700, West Conshohocken, United States, pp: 19428-2959.

[139] Haruna, K., & Saleh, T. A. (2021). "N, N′-Bis-(2-aminoethyl) piperazine functionalized graphene oxide (NAEP-GO) as an effective green corrosion inhibitor for simulated acidizing environment". Journal of Environmental Chemical Engineering, vol. 9, no. 1, pp: 104-967.

[140] Singh, A., Dayu, X., Ituen, E., Ansari, K., Quraishi, M. A., Kaya, S., & Lin, Y. (2020). "Tobacco extracted from the discarded cigarettes as an inhibitor of copper and zinc corrosion in an ASTM standard D1141-98 (2013) artificial seawater solution". Journal of Materials Research and Technology, vol. 9, no. 3, pp: 5161-5173.

[141] ASTM. (2010). " Standard Test Method for Wear Testing with a Pin-on-Disk Apparatus: G99 − 05". ASTM International, 100 Barr Harbor Drive, PO Box C700, West Conshohocken, United States, pp: 19428-2959.

[142] Khanmohammadi, S., Ojaghi-Ilkhchi, M., & Farrokhi-Rad, M. (2021). "Development of bioglass coating reinforced with hydroxyapatite whiskers on TiO2 nanotubes via electrophoretic deposition". Ceramics International, vol. 47, no. 1, pp: 1333-1343.

[143] Gudić, S., Vrsalović, L., Kvrgić, D., & Nagode, A. (2021). Electrochemical behaviour of Ti and Ti-6Al-4V alloy in phosphate buffered saline solution. *Materials*, *14*(24), 7495.

[144] Venugopal, B., Chandran, S., & Ajit, A. (2022). ISO 11137: An Overview on Radiation for Sterilization of Medical Devices and Healthcare Products. *Medical Device Guidelines and Regulations Handbook*, 121-143.

[145] Kumari, S., Tiyyagura, H. R., Pottathara, Y. B., Sadasivuni, K. K., Ponnamma, D., Douglas, T. E., ... & Mohan, M. K. (2021). "Surface functionalization of chitosan as a coating material for orthopaedic applications: A comprehensive review". Carbohydrate Polymers, vol. 255, pp: 117-487.

[146] Pawłowski, Ł., Bartmański, M., Strugała, G., Mielewczyk-Gryń, A., Jażdżewska, M., & Zieliński, A. (2020). "Electrophoretic deposition and characterization of Chitosan/Eudragit E 100 coatings on titanium substrate". Coatings, vol. 10, no. 7, p: 607.

[147] Ke, Z., Yi, C., Zhang, L., He, Z., Tan, J., & Jiang, Y. (2019). Characterization of a new Ti-13Nb-13Zr-10Cu alloy with enhanced antibacterial activity for biomedical applications. *Materials Letters*, *253*, 335-338.

[148]Rad, A. T., Solati-Hashjin, M., Osman, N. A. A., & Faghihi, S. (2014). Improved bio-physical performance of hydroxyapatite coatings obtained by electrophoretic deposition at dynamic voltage. *Ceramics International*, *40*(8), 12681-12691.

[149]Hou, P., Shi, C., Wu, L., & Hou, X. (2016). Chitosan/hydroxyapatite/Fe3O4 magnetic composite for metal-

complex dye AY220 removal: recyclable metal-promoted Fenton-like degradation. *Microchemical Journal*, *128*, 218-225.

[150] Fotsing, P. N., Woumfo, E. D., Mezghich, S., Mignot, M., Mofaddel, N., Le Derf, F., & Vieillard, J. (2020). "Surface modification of biomaterials based on cocoa shell with improved nitrate and Cr (vi) removal". RSC Advances, vol. 10, no. 34, pp: 20009-20019.

[151] Singh, B., Singh, G., Sidhu, B. S., & Bhatia, N. (2019). "In-vitro assessment of HA-Nb coating on Mg alloy ZK60 for biomedical applications". Materials Chemistry and Physics, vol. 231, pp: 138-149.

[152] Chi, J., Zhang, X., Wang, Y., Shao, C., Shang, L., & Zhao, Y. (2021). "Bio-inspired wettability patterns for biomedical applications". Materials Horizons, vol. 8, no. 1, pp: 124-144.

[153] Lkhagvaa, T., Rehman, Z. U., & Choi, D. (2021). Post-anodization methods for improved anticorrosion properties: A review. *Journal of Coatings Technology and Research*, *18*(1), 1-17.

[154] Hee, A. C., Martin, P. J., Bendavid, A., Jamali, S. S., & Zhao, Y. (2018). "Tribo-corrosion performance of filtered-arc-deposited tantalum coatings on Ti-13Nb-13Zr alloy for bio-implants applications". Wear, vol. 400, pp: 31-42.

[155] Cui, W., Cheng, J., & Liu, Z. (2019). "Bio-tribocorrosion behavior of a nanocrystalline TiZrN coating on biomedical titanium alloy". Surface and Coatings Technology, vol. 369, pp: 79-86.

[156] Li, K. M., Song, K. J., Guan, J., Yang, F., & Liu, J. (2020). "Tribocorrosion behavior of a Ti6Al4V alloy electromagnetic induction nitride layer in a fluorine-containing solution". Surface and Coatings Technology, vol. 386, pp: 125-506.

[157] Cvijović-Alagić, I., Cvijović, Z., Mitrović, S., Panić, V. and Rakin, M. (2011). "Wear and corrosion behaviour of Ti–13Nb–13Zr and Ti–

6Al–4V alloys in simulated physiological solution". Corrosion Science, Vol. 53, No. 2, pp: 796-808.

[158] Zarka, M., Dikici, B., Niinomi, M., Ezirmik, K. V., Nakai, M., & Yilmazer, H. (2021). "A systematic study of β-type Ti-based PVD coatings on magnesium for biomedical application". Vacuum, vol. 183, pp: 109-850.

[159] Esmailzadeh, S., Aliofkhazraei, M., & Sarlak, H. (2018). Interpretation of cyclic potentiodynamic polarization test results for study of corrosion behavior of metals: a review. *Protection of metals and physical chemistry of surfaces*, *54*(5), 976-989.

[160] Podila, R., Moore, T., Alexis, F., & Rao, A. (2013). "Graphene coatings for biomedical implants". JoVE (Journal of Visualized Experiments), vol. 73, p: 50276.

[161] Yadollahi, M., Namazi, H., & Aghazadeh, M. (2015). "Antibacterial carboxymethyl cellulose/Ag nanocomposite hydrogels cross-linked with layered double hydroxides". International journal of biological macromolecules, vol. 79, pp: 269-277.

[162] Pathak, D. K., & Pandey, P. M. (2021). Evaluation of in vitro corrosion behavior of zinc–hydroxyapatite and zinc–hydroxyapatite–iron as biodegradable composites. *Journal of Biomedical Materials Research Part B: Applied Biomaterials*, *109*(3), 436-450.

[163] Kumar, R., Thanigaivelan, R., Rajanikant, G. K., Jagadeesha, T., & Das, J. (2021). Evaluation of hydroxyapatite-and zinc-coated Ti-6Al-4V surface for biomedical application using electrochemical process. *Journal of the Australian Ceramic Society*, *57*(1), 107-116.

# Appendices

# Appendix 'A'

Average Atomic Number: 0.00 Loss of Ignition: 1.0006 %

| Z | Symbol | Element | Concentration | Abs. Error |
|---|---|---|---|---|
| 12 | Mg | Magnesium | < 0.029 % | (0.0) % |
| 13 | Al | Aluminum | < 0.0071 % | (0.0) % |
| 14 | Si | Silicon | < 0.0035 % | (0.0) % |
| 15 | P | Phosphorus | < 0.0045 % | (0.0) % |
| 16 | S | Sulfur | < 0.0010 % | (0.0) % |
| 22 | Ti | Titanium | 69.94 % | 0.11 % |
| 23 | V | Vanadium | < 0.038 % | (0.0) % |
| 24 | Cr | Chromium | < 0.0063 % | (0.0) % |
| 25 | Mn | Manganese | 0.0387 % | 0.0075 % |
| 26 | Fe | Iron | 0.1155 % | 0.0067 % |
| 27 | Co | Cobalt | 0.0158 % | 0.0038 % |
| 28 | Ni | Nickel | 0.0148 % | 0.0026 % |
| 29 | Cu | Copper | 0.0432 % | 0.0041 % |
| 30 | Zn | Zinc | 0.0527 % | 0.0023 % |
| 33 | As | Arsenic | 0.00115 % | 0.00052 % |
| 40 | Zr | Zirconium | > 15.22 % | 0.06 % |
| 41 | Nb | Niobium | > 13.45 % | 0.08 % |
| 42 | Mo | Molybdenum | 0.077 % | 0.018 % |
| 47 | Ag | Silver | 0.0038 % | 0.0023 % |
| 48 | Cd | Cadmium | < 0.0013 % | (0.0) % |
| 50 | Sn | Tin | < 0.0018 % | (0.0) % |
| 51 | Sb | Antimony | < 0.0017 % | (0.0) % |
| 74 | W | Tungsten | 0.0041 % | 0.0032 % |
| 82 | Pb | Lead | < 0.0012 % | (0.0) % |

Sum of concentration 99.00 %

**Figure (1):** The Chemical Composition for Ti-13Nb-13Zr Alloy.

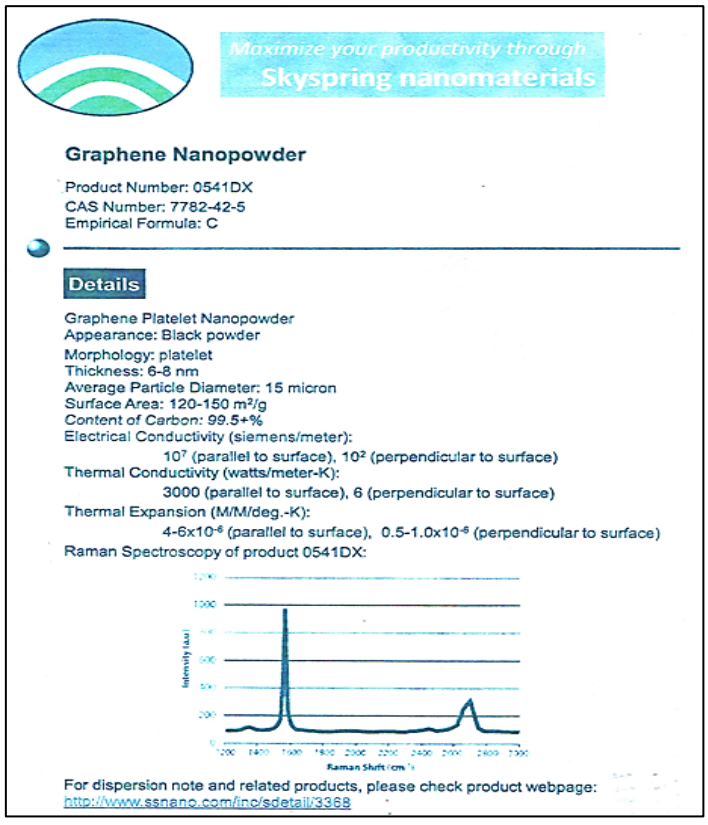


**Figure (2):** Details of Graphene Platelet Nanopowder.

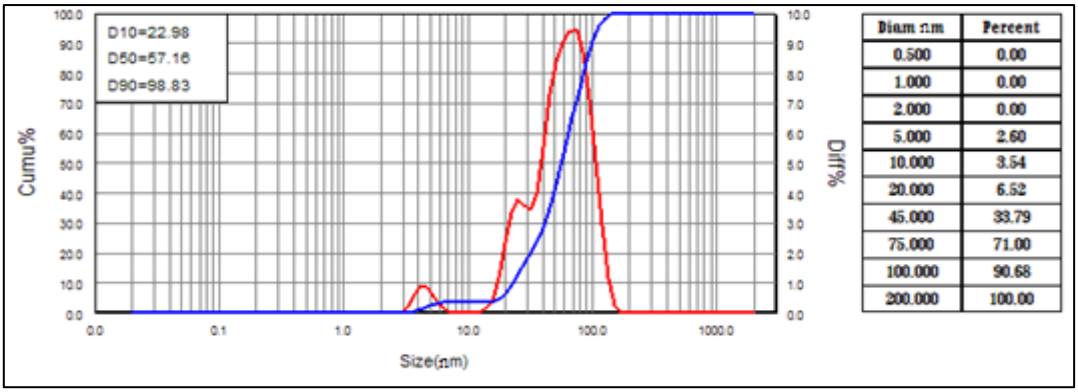


| Diam nm | Percent |
|---|---|
| 0.500 | 0.00 |
| 1.000 | 0.00 |
| 2.000 | 0.00 |
| 5.000 | 2.60 |
| 10.000 | 3.54 |
| 20.000 | 6.52 |
| 45.000 | 33.79 |
| 75.000 | 71.00 |
| 100.000 | 90.68 |
| 200.000 | 100.00 |

**Figure (3):** Particle Size of Chitosan (CH) Material.

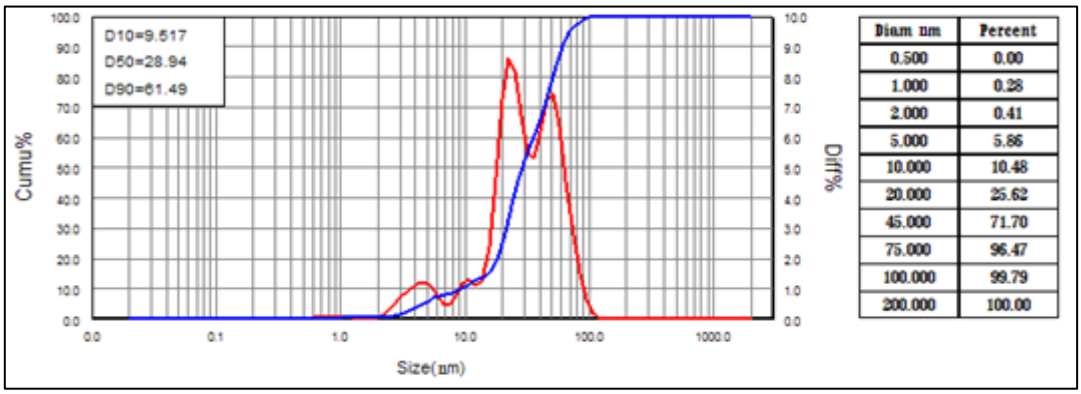


| Diam nm | Percent |
|---|---|
| 0.500 | 0.00 |
| 1.000 | 0.28 |
| 2.000 | 0.41 |
| 5.000 | 5.86 |
| 10.000 | 10.48 |
| 20.000 | 25.62 |
| 45.000 | 71.70 |
| 75.000 | 96.47 |
| 100.000 | 99.79 |
| 200.000 | 100.00 |

**Figure (4):** Particle Size of Graphene (Gr) Material.

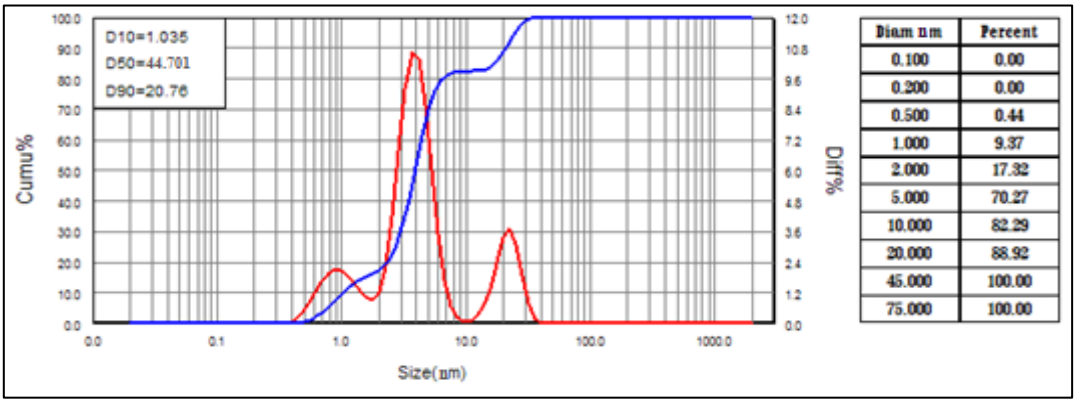


| Diam nm | Percent |
|---|---|
| 0.100 | 0.00 |
| 0.200 | 0.00 |
| 0.500 | 0.44 |
| 1.000 | 9.37 |
| 2.000 | 17.32 |
| 5.000 | 70.27 |
| 10.000 | 82.29 |
| 20.000 | 88.92 |
| 45.000 | 100.00 |
| 75.000 | 100.00 |

**Figure (5):** Particle Size of Hydroxyapatite (HAp) Material.

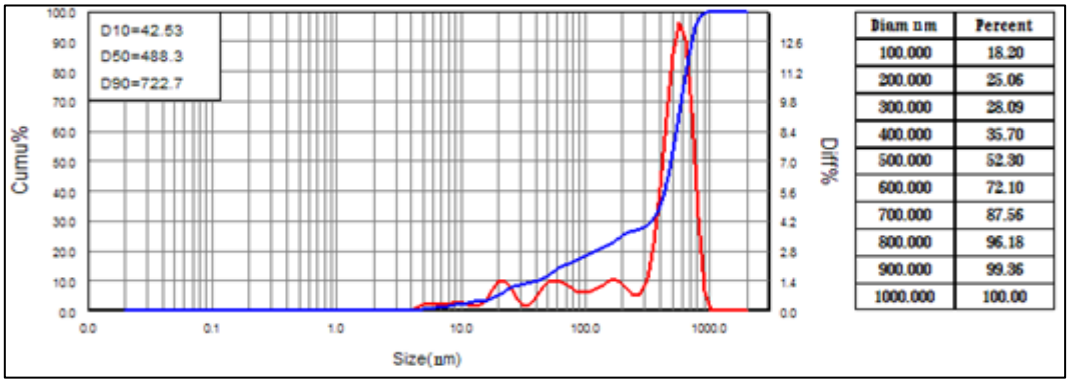


| Diam nm | Percent |
|---|---|
| 100.000 | 18.20 |
| 200.000 | 25.06 |
| 300.000 | 28.09 |
| 400.000 | 35.70 |
| 500.000 | 52.30 |
| 600.000 | 72.10 |
| 700.000 | 87.56 |
| 800.000 | 96.18 |
| 900.000 | 99.36 |
| 1000.000 | 100.00 |

**Figure (6):** Particle Size of CarboxyMethyl Cellulose (CMC) Material.

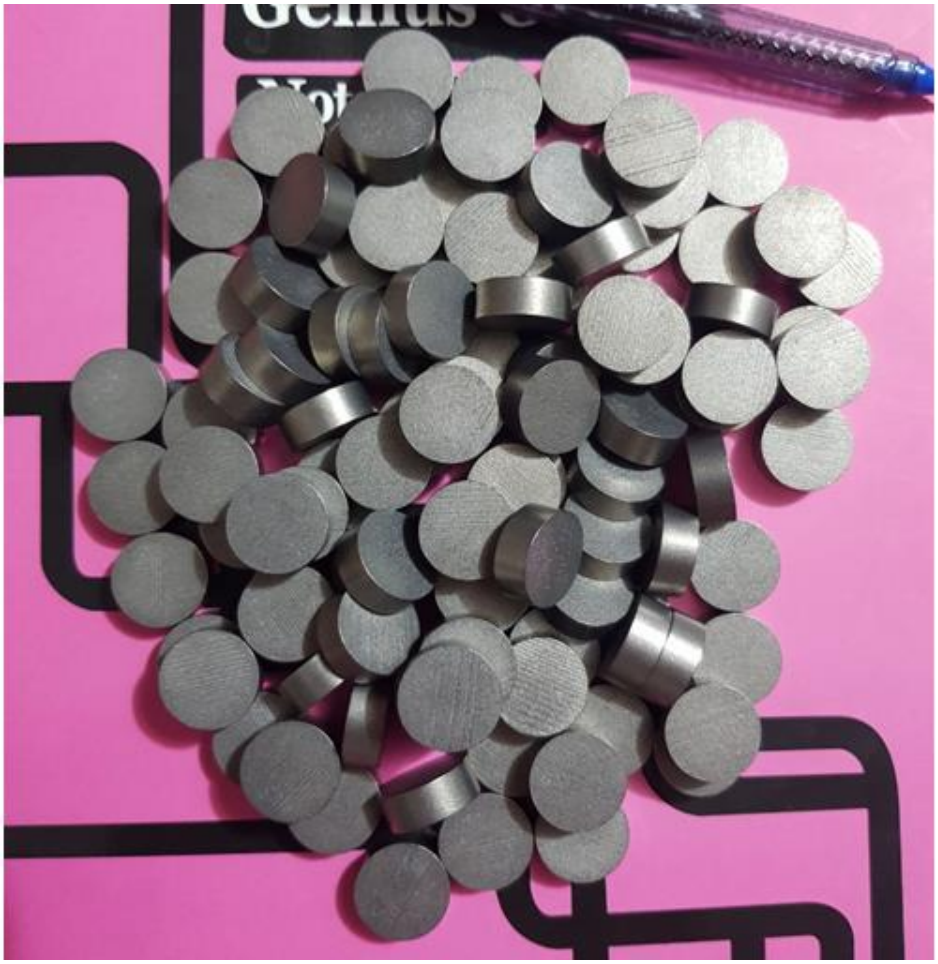

**Figure (7):** Ti-13Nb-13Zr alloy specimens used in the EPD process before grinding and washing

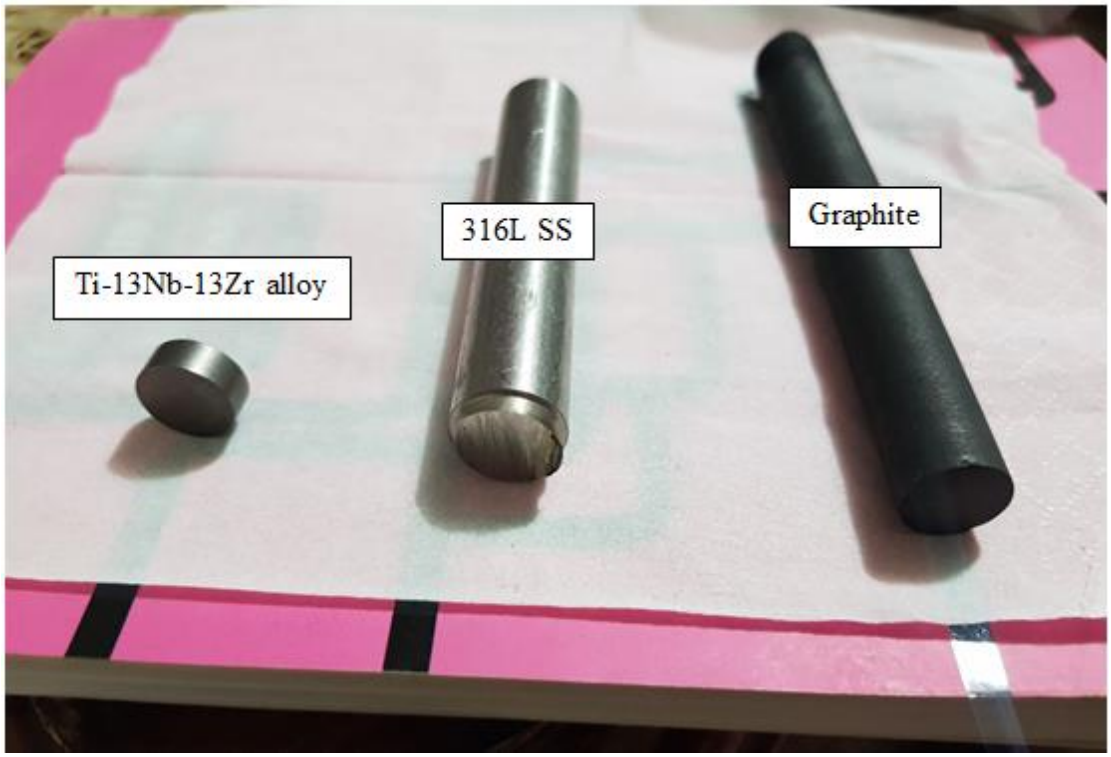


**Figure (8):** Anode electrodes used in EPD process.

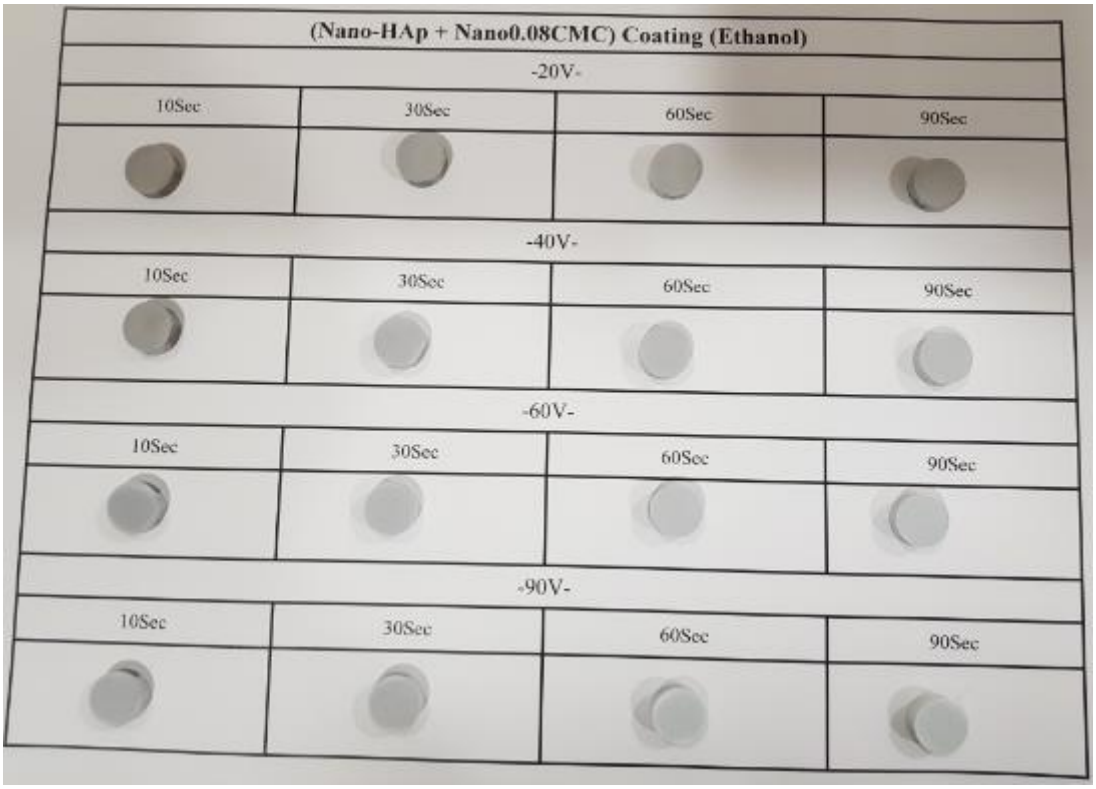


**Figure (9):** 0.08CMC Coating at Different Voltage and Time .

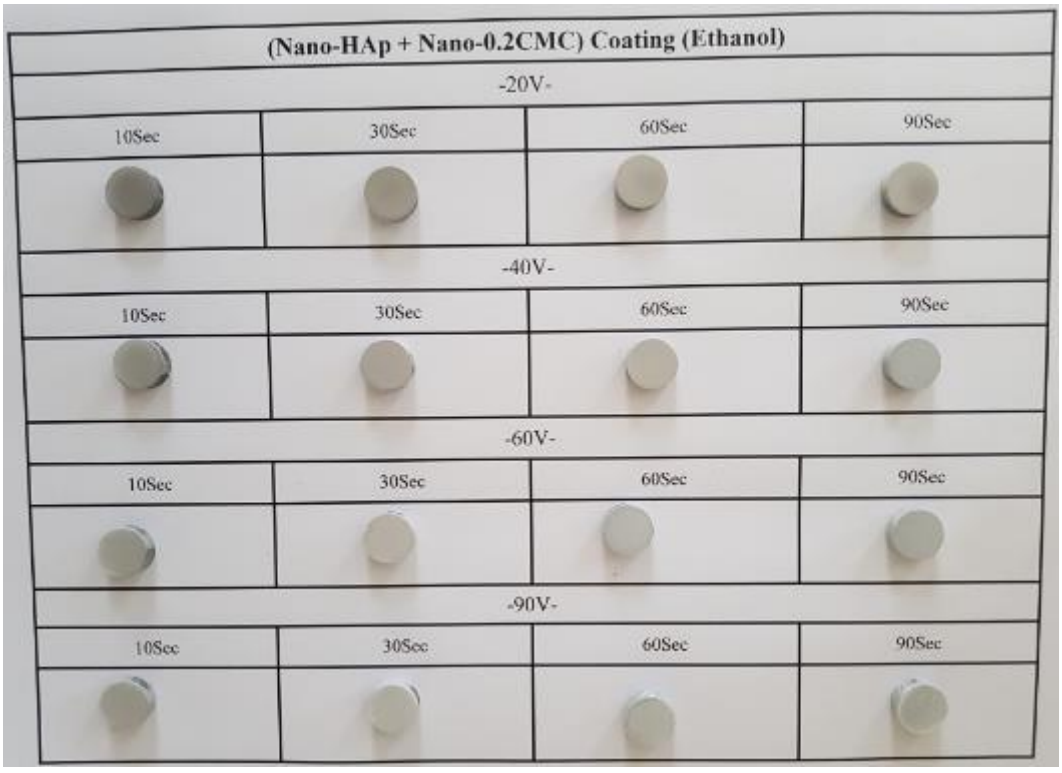


**Figure (10):** 0.2CMC Coating at Different Voltage and Time .

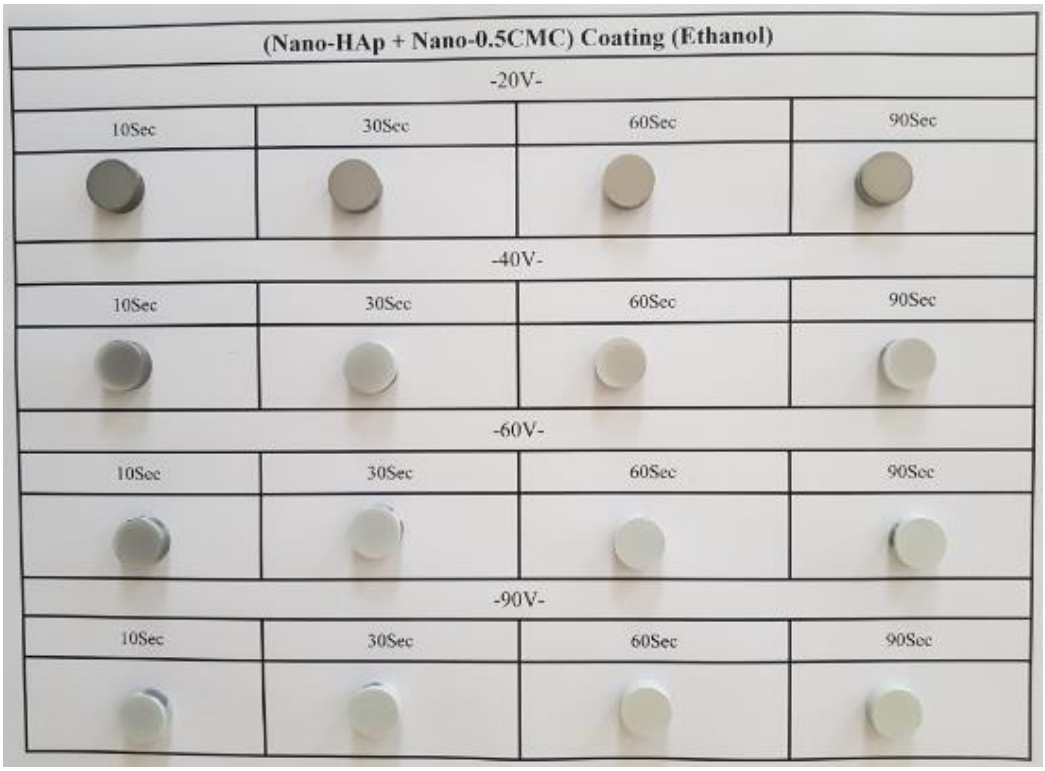


**Figure (11):** 0.5CMC Coating at Different Voltage and Time.

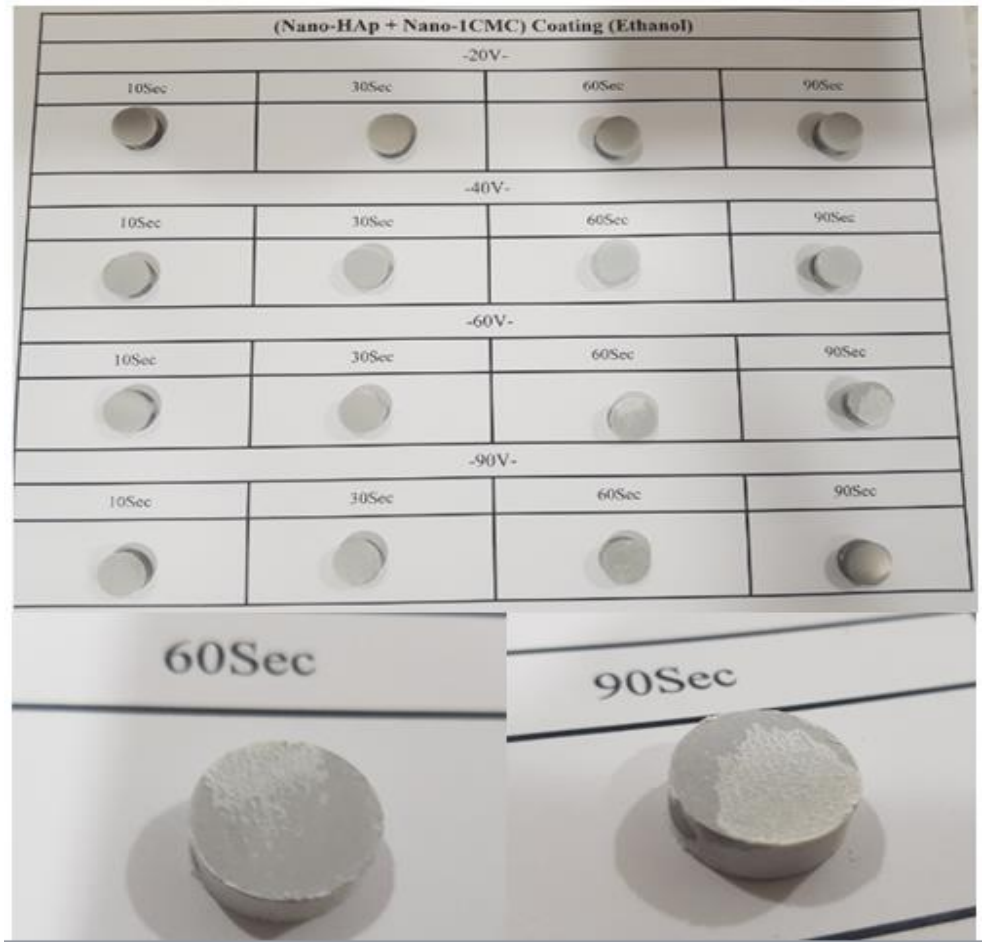


**Figure (12):** 1CMC Coating at Different Voltage and Time.

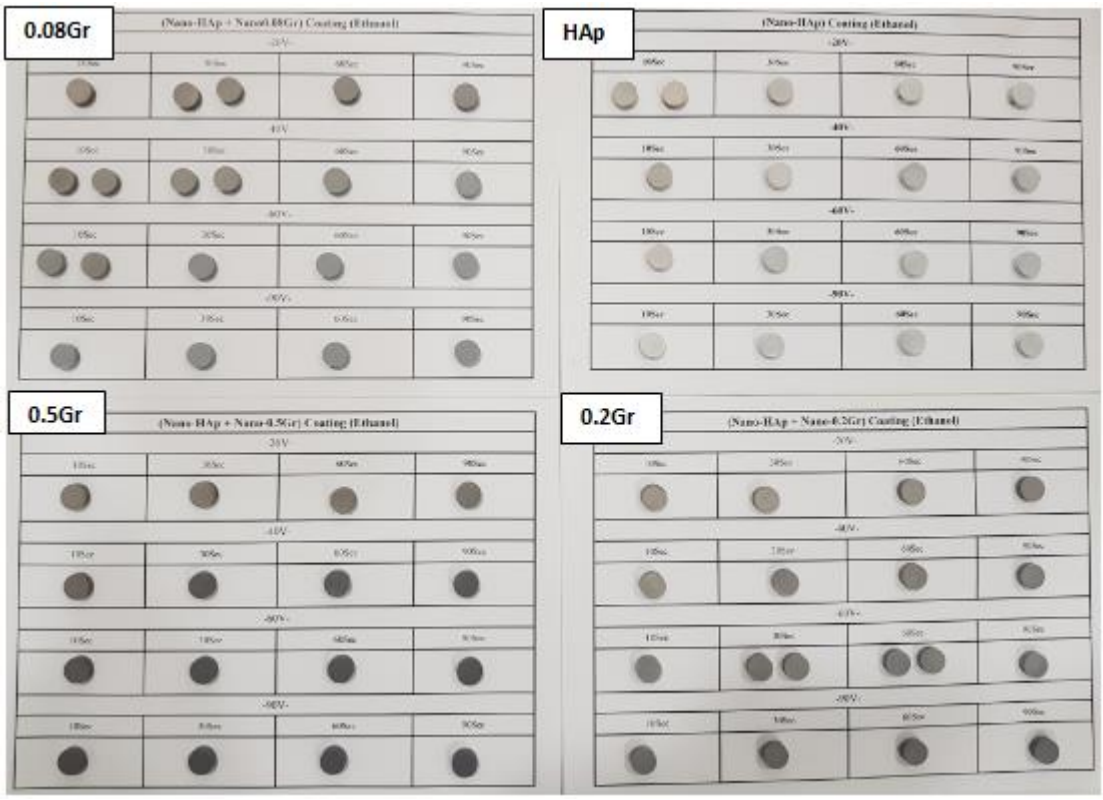


**Figure (13):** Graphene & HAp Coatings at Different Voltage and Time.

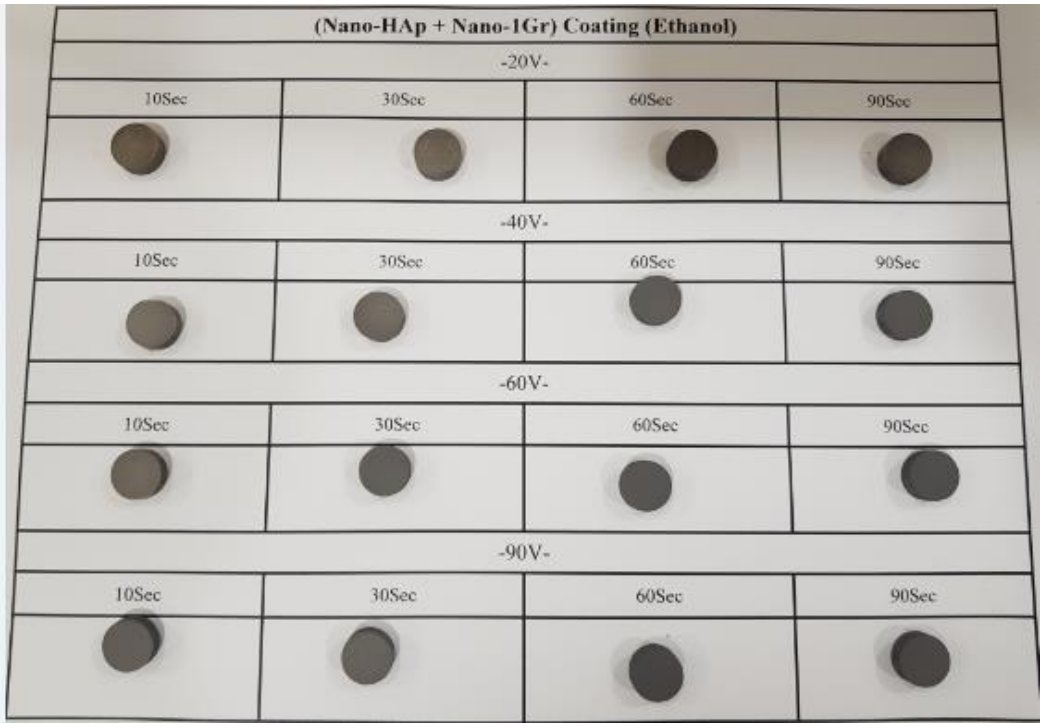


**Figure (14):** 1Gr Coating at Different Voltage and Time.

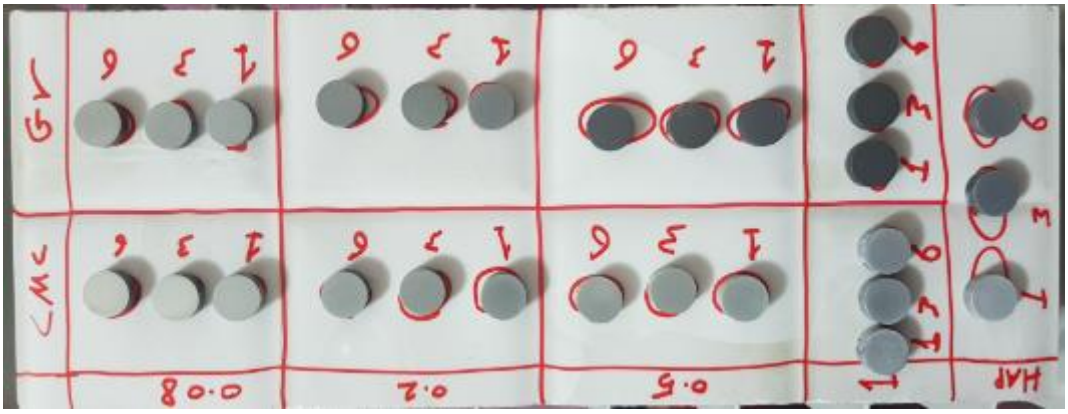

**Figure (15):** The Coated Specimens after Immersion for 1,3 and 6 days at 40 volts and 60 sec.

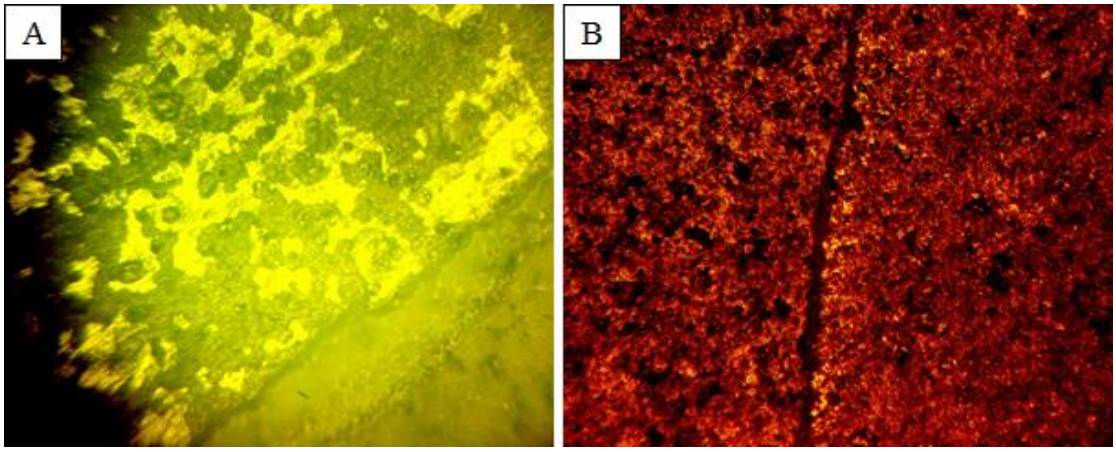


**Figure (16):** LOM after Adhesion Test for Graphene Coating (G1), (A) Before Immersion, (B) After 6 Days Immersion (10X).

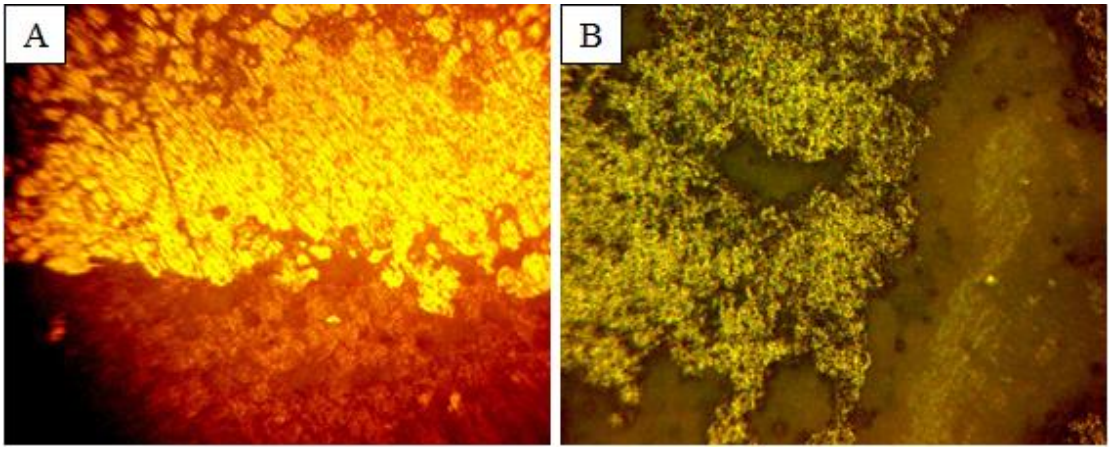


**Figure (17):** LOM after Adhesion Test for CMC Coating (C1), (A) Before Immersion, (B) After 6 Days Immersion, (10X).

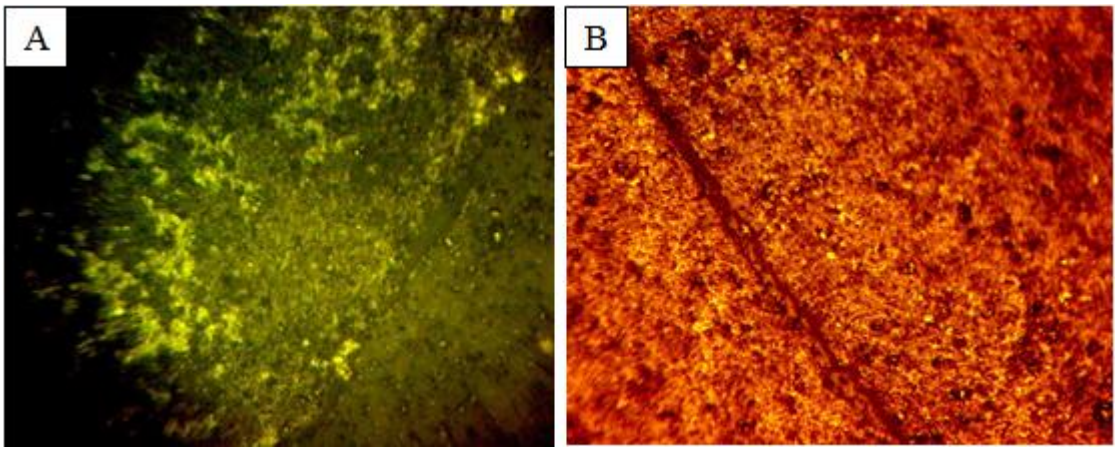


**Figure (18):** LOM after Adhesion Test for FG Coating (F1), (A) Before Immersion, (B) After 6 Days Immersion (10X).

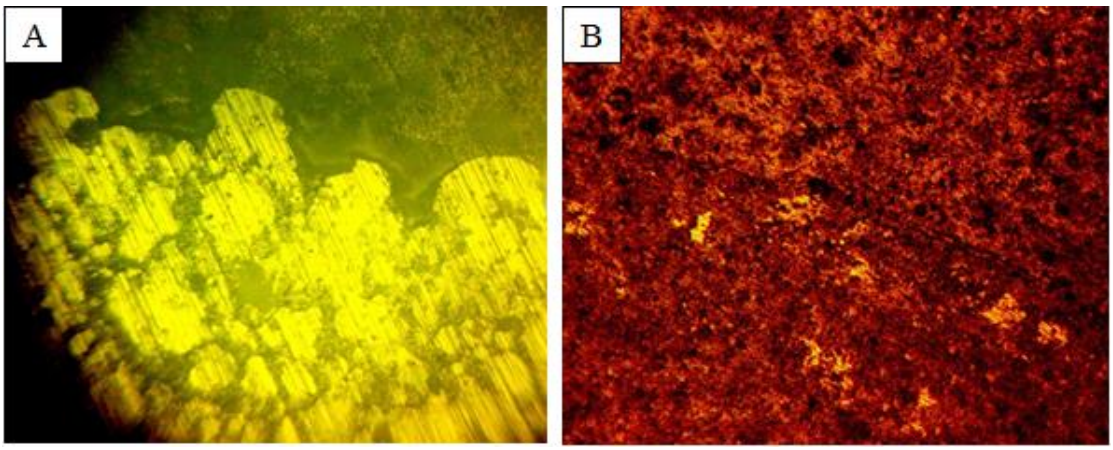


**Figure (19):** LOM after Adhesion Test for Ternary Coating (M1), (A) Before Immersion, (B) After 6 Days Immersion(10X).

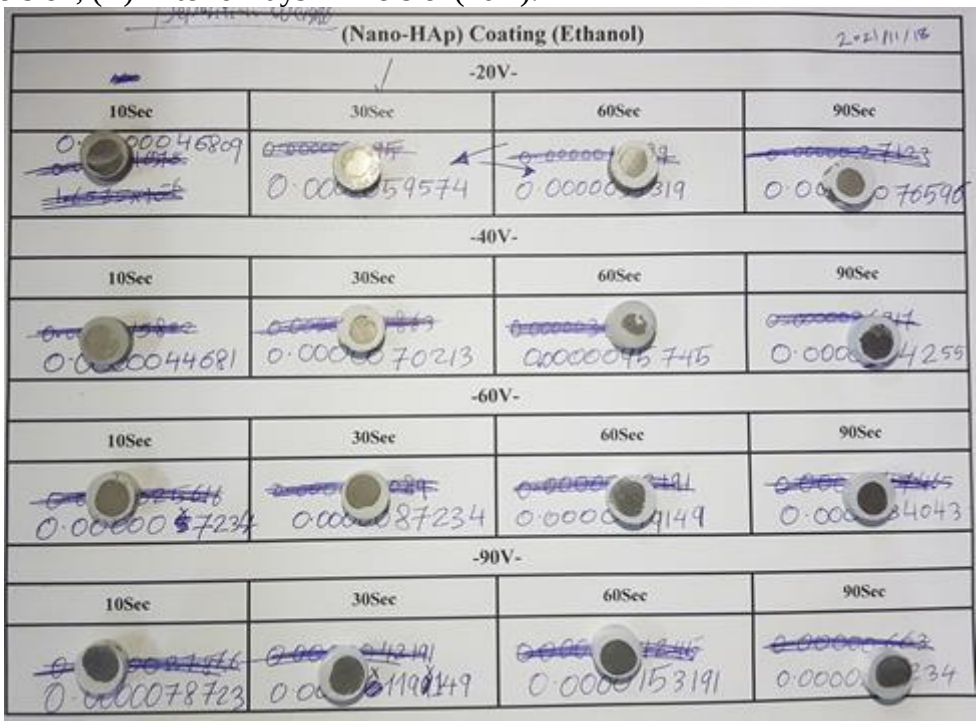


**Figure (20):** Show Different type of Adhesion Test for HAp Coating.

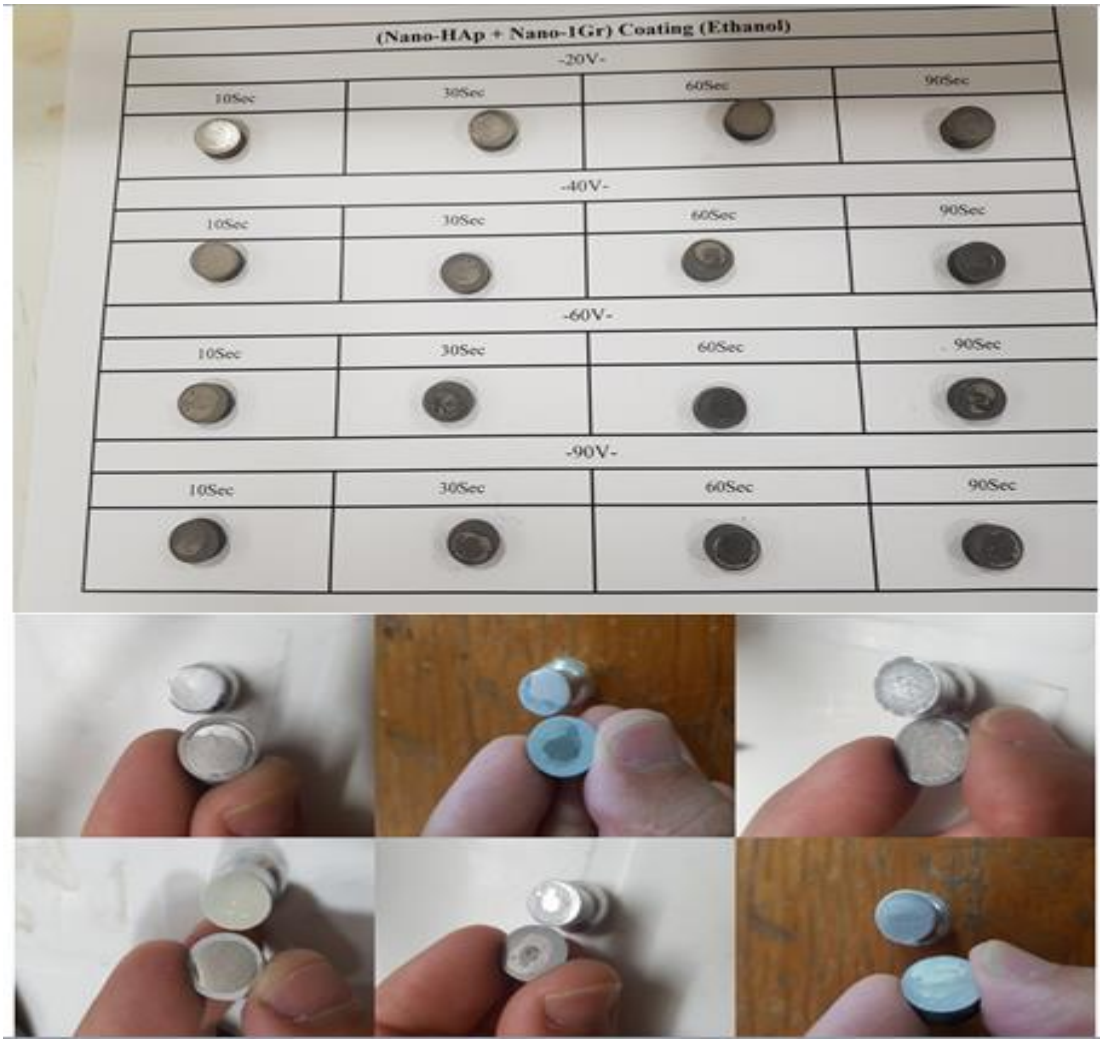


**Figure (21):** Show Different type of Adhesion Test for Graphene Coating.

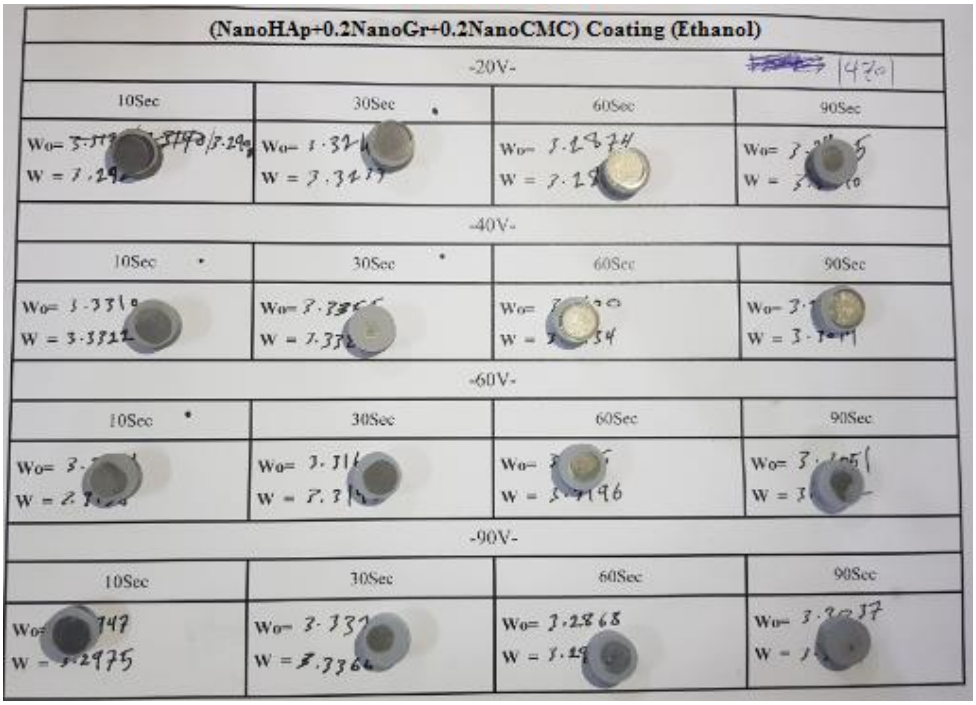


**Figure (22):** Show Different Type of Adhesion Test for Ternary Coating.

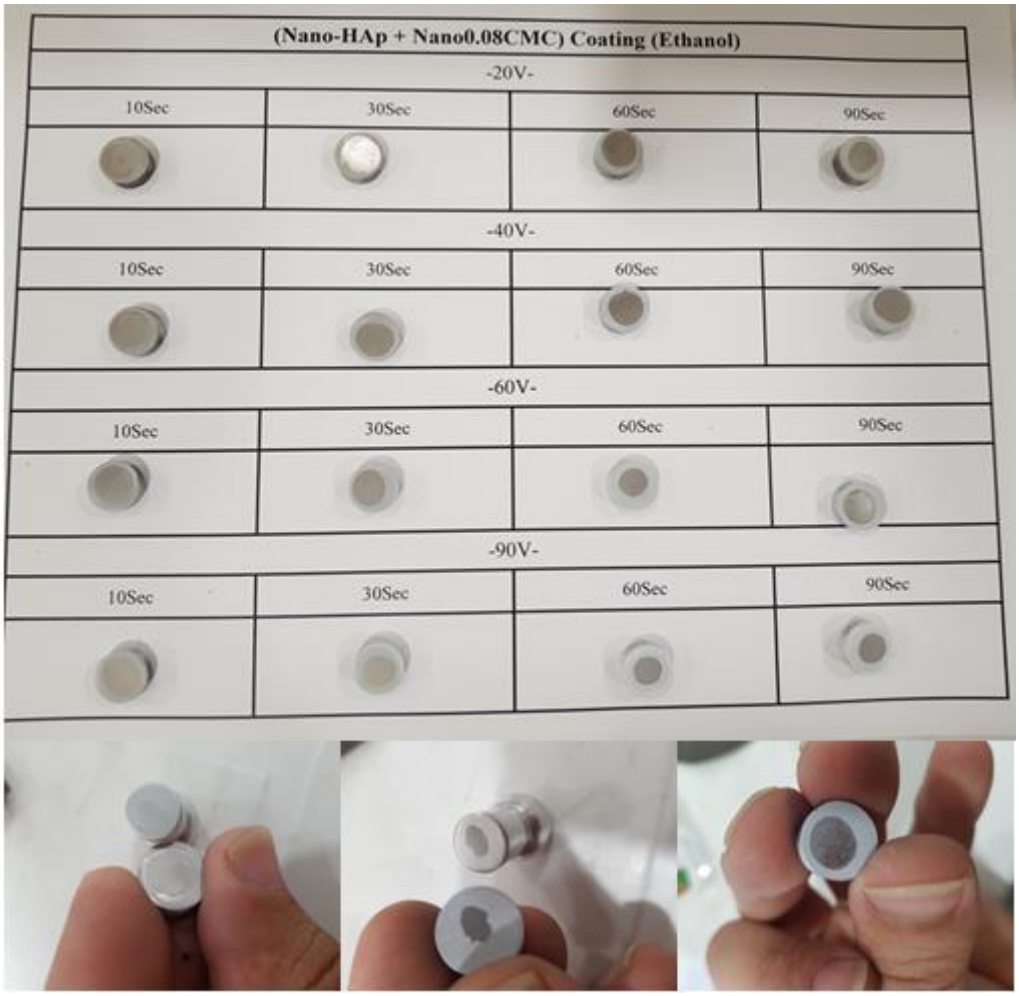


**Figure (23):** Show Different type of Adhesion Test for CMC Coating.

**Figure (24):** Show Adhesion Test for FG Coating.

# الخلاصـــة

سبائك التيتانيوم نوع (بيتا) لها العديد من خصائص التوافق الحيوي والاندماج العظمي ومقاومة التآكل الفائقة ، يتطلع العديد من الباحثين إلى تطوير هذه السبائك لتناسب البيئة العدائية لجسم الإنسان. في هذه الدراسة ، بعد اختيار الظروف المناسبة (قطب الأنود ، الجهد المطبق و وقت الترسيب ... إلخ) ، تمت إضافة (الكرافين (Gr) ، كاربوكسي مثيل سليلوز (CMC) والمادتان معًا) إلى طلاء هيدروكسيباتيت المعلق بالإضافة إلى التدرج الوظيفي (FG) لطلاءات الكرافين المعلقه ، بسبب توافق هذه المواد مع أنسجة جسم الإنسان. ثم تمت دراسة تأثير طبقات الطلاء الناتجة عن هذه المحاليل المعلقة أعلاه على كل من خصائص البنية المجهرية ( XRD، SEM، XRF وLOM) ، الاختبارات الكهروكيميائية (جهد الدائرة المفتوحة والاستقطاب) ، الاختبارات الميكانيكية (اختبار البلى الجاف) ، الاختبارات الفيزيائية (زاوية التماس، الخشونه و الرقم الهيدروجيني(PH)) والنشاط المضاد للبكتيريا وتقييم صلاحية الخلية للتحقق من مدى حماية هذه الطبقات لسطح سبيكة Ti-13Nb-13Zr الحياتية.

كانت القيم الإيجابية لجهد زيتا مؤشرًا واضحًا على اعتماد عملية EPD الكاثودية. كشف نمط السبيكة الأساسية عن حيود المرحلتين (β و α) المطابقين لبطاقة JCPDS رقم (044 - 1294) يمكن ملاحظة ظهور قمم جديدة نتيجة تأثير بنسب الإضافات (5 HAp و 0.5 Gr و 0.5 CMC) مما أدى أيضًا إلى تقليل أو زيادة زاوية القمم لكل مرحلة من مراحل سبيكة التيتانيوم ( بيتا وألفا) ،بالاضافه الى ذلك، ادت إضافة الكرافين و CMC وفي حالات خلطهما معا والتدرج الوظيفي لمحاليل الكرافين المعلقه إلى زيادة قوة الالتصاق ابتداءً من طبقة HAp (4.55 MPa) و طبقة 0.08CMC (7.90 MPa) و( 8.28 MPa) لـطبقة (0.08CMC + 0.2 Gr) و 9.76 ) MPa) لـطبقة 1Gr وانتهاءً بـ 10.12 MPa لـطبقة (FG). تم إثبات ذلك عندما زادت قوة الالتصاق لطبقات الطلاء أعلاه بعد غمر العينات المطلية لمدة اقصاها 6 أيام.

تراوحت قيم زاوية التماس من 14.3 درجة لـ (1CMC+0.2Gr) و 20.5 درجة لـ 1Gr و 32.3 درجة لـ (FG) ، حيث أدت الخشونة المفرطة والمسامية والتشققات على سطح طلاء (CMC) إلى خفض زاوية التماس لهذه الطبقة على الفور من 54.6 درجة لسبيكة Ti-13Nb-13Zr غير المطلية إلى 11.2 درجة لـ 0.5CMC مما يجعلها محبة للماء اكثر اذا ما قورنت ببقية الاضافات. مقاومة البلى العالية لإضافة الكرافين ، مع فقد حجم يتراوح من 0.00614 $cm^3$ إلى سبيكة Ti-13Nb-13Zr غير المطلية عند 25 دقيقة إلى 0.001344 $cm^3$ لطلاء 1Gr في نفس الوقت تحت نفس الحمل (15N)، الصلادة العالية لطبقة طلاء الكرافين يمكن توقعها من مقاومتها العالية للبلى عند مقارنتها بالإضافات الأخرى.

إن أكبر قيمة لجهد الدائرة المفتوحة (OCP) هو (-26.1mV) في الاتجاه السالب لإضافة 0.08 Gr تُظهر انخفاضًا ملحوظا في معدل التآكل لطبقة الطلاء هذه ، بدءً من 0.0781 mm/y لسبيكة Ti-13Nb-13Zr غير المطلية حتى 0.00312 mm/y لطلاء 0.08Gr اذا ما قورنت بالاضافات الاخرى. جميع المواد المضافة المستخدمة (Gr، CMC، المادتين معا و FG) مضادة للبكتيريا ، حيث أكبر منطقة تثبيط هي (45 ملم) عند المحلول المعلق لطلاء (Graphene G2) كانت عند مهاجمة البكتيريا الموجبة (S. aureas). يعتبر اختبار MTT هو الطريقة الأكثر شيوعًا المستخدمة لتقييم السمية الخلوية (فقدان الخلايا القابلة للحياة) ، وأظهرت عينة (0.2Gr) ما يقرب من 100 ٪ من صلاحية الخلية ، وقدمت عينة (C1) والسبيكة الاساس غير المطلية أقل قابلية للبقاء للخلية مقارنة بالعينات الأخرى. تم الحصول على صلاحية الخلية للعينات بالترتيب من أعلى إلى أدنى

السبيكة الاساس غير المطلية < C1 < M2 < F < G2

تم تحقيق أفضل النتائج عند إضافة 0.2Gr) G2) إلى طلاء هيدروكسيباتيت (H) ، ومن ثم تعتبر هذه النسبة هي النسبة المثلى في هذه الدراسة بهدف تعزيز سطح سبيكة Ti-13Nb-13Zr.

جمـــــــهـورية الـعـــــراق
وزارة التعليم العالي والبحث العلمي
جـــامـــعـــة بـــــابـــــل
كـلـيـــة هـنـدســة الـمـواد
قـســم هـنـدســة الـمـعـادن

# التحسين السطحي لسبيكة Ti-13Nb-13Zr بواسطة الترسيب بالهجرة الكهربائية المستخدمة في تطبيقات تقويم العظام

**رسالة**

**مقدمة إلى كلية هندسة المواد/جامعة بابل وهي جزء من متطلبات نيل درجة الدكتوراه فلسفة في هندسة المواد/ المعادن**

**من قبل**

**نبيل محمد عبد الكاظم راضي**

ماجستير هندسة المعادن (٢٠١٩)

**بإشـــــراف**

الاستاذ الدكتور

**جاسم محمد سلمان المرشدي**

**٢٠٢٢ م** **١٤٤٤هـ**